Cronfa
Swansea University's Research Repository

VALUE GENERATION BY RECOVERING BY-PRODUCTS FROM STEELMAKING PROCESSES: DEZINCIFICATION OF BASIC OXYGEN STEELMAKING DUST

Daniel J C Stewart

Swansea University

Prifysgol Abertawe

This thesis is submitted in partial fulfilment of the requirements of the degree of Doctor of Engineering

February 2022

Copyright: The author, Daniel J.C. Stewart, 2022.

This thesis is dedicated to the memory of John Benjamin Wilson, whom I miss every day. Without him, I would have never dreamed any of this possible.

One never notices what has been done; one can only see what remains to be done. –

Marie Curie

DECLARATION

This work has not previously been accepted in substance for any degree and is not being concurrently submitted in candidature for any degree.

Signed: [redacted]

Date:

STATEMENT 1

This thesis is the result of my own investigations, except where otherwise stated. Other sources are acknowledged by footnotes giving explicit references. A bibliography is appended.

Signed: [redacted]

Date: 28/02/2022

STATEMENT 2

I hereby give my consent for my work, if relevant and accepted, to be available for photocopying and for inter-library loans after expiry of a bar on access approved by the University.

Signed: [redacted]

Date: 28/02/2022

STATEMENT 3

The University's ethical procedures have been followed and, where appropriate, that ethical approval has been granted

Signed: [redacted]

Date: 28/02/2022

ABSTRACT

The production of steel through the blast furnace/basic oxygen steelmaking route generates approximately 10kg of ferrous dusts and sludges per tonne of hot metal produced. This ferrous material is readily recyclable via a sinter plant to recover iron units but is difficult to recycle when the material is contaminated with zinc. Historically, excess material has been stockpiled or landfilled which presents an environmental issue but also a commercial opportunity to recover huge volumes of ferrous material from operating and former steelmaking sites.

A review of best available technology for recovery of zinc from steelmaking by-product dusts identified that the Rotary Hearth Furnace (RHF) is the most attractive commercialized option for processing of material at an integrated plant such as Tata Steel Port Talbot, but due to the relatively low value of the ferrous direct reduced iron (DRI) product is still not commercially viable.

A characterization study of basic oxygen steelmaking dust from Port Talbot, Redcar and Scunthorpe steel plants in the United Kingdom was undertaken using a variety of techniques and indicated pyrometallurgical recovery would be the preferred recovery route due to the high metallization and variability of the morphology of the dusts.

Benchmarking of material from Port Talbot material processed in laboratory furnace trials under conditions mimicking the RHF showed that while volatile metal removal and iron reduction performance is adequate for recycling at realistic RHF temperatures and hold times, the high sulfur and gangue content mean the produced DRI would not be valuable enough to offset production costs.

A computational thermochemical study was undertaken using FactSage and identified the possibility of applying next generation RHF technology to produce high value pig iron nuggets from steelmaking by-products.

This possibility was confirmed experimentally, producing pig iron nuggets from BOS dust with complete removal of zinc from the material, at feasible process conditions, by addition of SiO_2 and MgO fluxes.

Alternative reductants for the RHF were also explored, specifically adapting the RHF process to utilize the enormous volume of plastic waste generated from facemasks in the wake of the COVID-19 pandemic. The addition of facemask plastic to a low-volatile coal was found to increase its CO_2 gasification reactivity, which has associated process benefits for direct reduction.

ACKNOWLEDGEMENTS

Firstly, I would like to thank Professor Andrew R. Barron for his guidance, advice, patience, and sense of humor during the production of this work. I'd also like to express my appreciation to the wonderful staff of the Materials and Manufacturing Academy (M2A) at Swansea University for their support and kindness during the course of my research.

I'd like to thank my industrial supervisor Dr David Thomson from Tata Steel UK for his guidance, counsel, and friendship during the course of this research. I would also like to thank Martin Allen of Tata Steel UK for his guidance, as well as his excellent company during a research visit to China. My thanks are also extended to my colleagues at Tata Steel Port Talbot, specifically the BOS labs teams who not only assisted with analyses but also provided a welcoming and fun environment to work within.

My deepest thanks are also extended to the amazing group of researchers I was privileged to be a part of in the Energy Safety Research Institute at Swansea University, specifically Dr Michael Warwick, Dr Katherine Glover, Lucy Fisher, Stephen Shearan, Dr Donald Hill, Dr Dan Jones, and Max Newberry. I will never forget my time spent in the laboratory, the office, and most importantly, in the tearoom with you all.

I'd also like to extend my thanks to Viktor Macha of the Beauty of Steel product for graciously allowing some of his wonderful photography of the steelmaking industry to be reproduced within this thesis.

I'd also like to acknowledge the financial support that was provided by Materials and Manufacturing Academy (M2A) that has been made possible through funding from the European Social Fund via the Welsh Government, Swansea University EPSRC impact acceleration account, the COATED doctoral training centre, and Tata Steel UK. Additional support was provided by the Reducing Industrial Carbon Emissions (RICE) operations funded by the Welsh European Funding Office (WEFO) through the Welsh Government.

Finally, I'd like to thank my mother, Jennifer, and my two sisters, Jessica, and Alison, for their faultless patience and love during my studies, this acknowledgements section could never be enough to express my gratitude for having you in my life.

CONTENTS

1. INTRODUCTION 18
1.1 RESEARCH QUESTION 19
1.2 THE GLOBAL STEEL INDUSTRY AND SOUTH WALES 19
1.3 THE PRODUCTION OF STEEL VIA THE BLAST FURNACE/BASIC OXYGEN STEELMAKING ROUTE 21
1.4 ZINC AND IRON 23
1.5 THE STRUCTURE OF THE THESIS 24
1.6 LIST OF PUBLISHED JOURNAL PAPERS FOR EXAMINATION 25
1.6.1 Chapter 2. Literature Review 25
1.6.2 Chapter 4. The Chemical Suitability for Recycling of Steelmaking By-Products from United Kingdom Facilities 25
1.6.3 Chapter 5. Next Generation RHFs: Pig Iron Nugget Production 25
1.6.4 Chapter 7. Utilization of Facemask Plastic Waste Resulting from the COVID-19 Pandemic in RHF Ironmaking 25
2. LITERATURE REVIEW 27
2.1 INTRODUCTION 28
2.2 THE BASIC OXYGEN STEELMAKING (BOS) PROCESS 30
2.3 BOS DUST 31
2.4 Formation mechanism of basic oxygen steelmaking dust 32
2.4.1 The origin of zinc in the BOS process 34
2.4.2 Off-gas system design 34
2.4.3 Characterization of BOS dust 35
2.4.4 Particle size 35
2.4.5 Morphology 36
2.4.6 Chemical Analysis 37
2.4.7 Phase determination 39
2.4.8 Mössbauer spectroscopy 42
2.5 PYROMETALLURGICAL SEPARATION TECHNIQUES 43
2.5.1 The Waelz Kiln 47
2.5.2 The Rotary Hearth Furnace 49
2.5.3 FASTMET® 51
2.5.4 The INMETCO process 52
2.6 DRyIron ™ process 53
2.7 ITmk3 55
2.8 Hi-QIP 56
2.9 COMET Process 58
2.10 ZINC RECOVERY FOCUSED PYROMETALLURGICAL EXTRACTION PROCESSES 59
2.11 NEXT GENERATION IRONMAKING TECHNOLOGY 61
2.12 FURTHER PROCESSING OF THE CRUDE ZINC OXIDE PRODUCT 62
2.13 CONCLUSIONS 63
3. EXPERIMENTAL METHODOLOGY AND VALIDATION 71
3.1 INTRODUCTION 72
3.2 TOTAL DIGESTION FOR MP-AES 74
3.2.1 Digestion Method 76
3.2.2 MP-AES Operating Method 77
3.3 MP-AES validation against certified reference material 77
3.4 SELECTIVE METALLIC IRON ANALYSIS 79
3.4.1 Validation of Metallic Iron Analysis 81

3.5 CARBON AND SULFUR ANALYSIS 82
4. THE CHEMICAL SUITABILITY FOR RECYCLING OF STEELMAKING BY-PRODUCTS FROM UNITED KINGDOM FACILITIES 83
4.1 INTRODUCTION 84
4.2 EXPERIMENTAL 87
4.2.1 Materials and Chemicals 87
4.2.2 Analytical Techniques 87
4.3 RESULTS AND DISCUSSION 89
4.3.1 Microwave Plasma – Atomic Emission Spectroscopy 89
4.4 Conclusions 111
5. DRI PRODUCTION LABORATORY TRIALS 114
5.1 INTRODUCTION 115
5.1.1 Benchmarking Visit to a Commercial RHF 119
5.2 EXPERIMENTAL METHODS 124
5.3 RESULTS AND DISCUSSION 127
5.3.1 Carbon Analysis of Fired Pellets 127
5.3.2 Sulfur Analysis of Fired Pellets 130
5.3.3 Volatile Metal Removal 134
5.3.4 Powder X-Ray Diffraction of Fired Pellets 156
5.4 THE SEPARATED ZINC PRODUCT 158
5.5 RECYCLING ROUTES – BF, BOF OR SINTER PLANT? 160
5.6 CONCLUSIONS 163
6. NEXT GENERATION RHFS: PIG IRON NUGGET PRODUCTION 165
6.1 INTRODUCTION 166
6.2 COMPUTATIONAL METHODS 168
6.3 THE CONDITIONS OF NUGGET MAKING 169
6.3.1 Low Liquidus Temperature Slag 169
6.3.2 Carbonaceous Reduction of Ferrous and Zinc Oxides 171
6.4 VARYING THE RATIO OF BF DUST TO BOS DUST IN PIG IRON NUGGET PRODUCTION 175
6.4.1 Iron Recovery 175
6.4.2 Carburization 177
6.4.3 Sulfur Control 178
6.4.4 Manganese Recovery 179
6.4.5 Liquidity of the system 180
6.5 INTRODUCTION OF FLUXING AGENTS 183
6.5.1 Flux Additions 183
6.5.2 Recovery of Zinc 188
6.6 PRACTICAL VALIDATION OF COMPUTATIONAL EXPERIMENTS 191
6.6.1 SEM-EDX 195
6.6.2 Oxidative behaviour of Pig Iron Nuggets versus Direct Reduced Iron 199
6.7 CONCLUSIONS 200
7. UTILIZATION OF FACEMASK PLASTIC WASTE RESULTING FROM THE COVID-19 PANDEMIC IN RHF IRONMAKING 203
7.1 INTRODUCTION 204
7.2 INSTRUMENTAL METHODS 206
7.3 MATERIALS AND MILLING PROTOCOL 206
7.4 THERMOGRAVIMETRIC ANALYSIS 211
7.5 KINETIC ANALYSIS 215
7.6 PYROLYSIS EXPERIMENTS AND STRUCTURAL CHANGES 221
7.6.1 SEM analysis 221
7.6.2 Surface Area Analysis 224

7.7 PRODUCING DRI FROM FACEMASK PLASTIC 225
7.7.1 Thermogravimetric Analysis *225*
7.7.2 Tube Furnace Experiments *228*
7.8 DISCUSSION 233
7.9 CONCLUSIONS 236
8. CONCLUSIONS 238
8.1 SUMMARY 239
8.2 RECOMMENDATIONS FOR FUTURE WORK 240
REFERENCES 242
APPENDICES 266

LIST OF TABLES

TABLE 2.1. ELEMENTAL ABUNDANCE IN SAMPLES OF BOS DUST (WT. %). 39
TABLE 2.2. PHASES IDENTIFIED IN BOS DUST BY POWDER XRD 40
TABLE 2.3. COMPARISON OF DRI PRODUCTION PROCESSES WITH TRADITIONAL BLAST FURNACE PRODUCTION. 46
TABLE 2.4. CHEMICAL ANALYSIS (WT. %) OF THE INPUTS AND PRODUCTS OF THE WAELZ KILN PROCESS. 48
TABLE 2.5. PRINCIPAL CHEMICAL REACTIONS OCCURRING IN A ROTARY HEARTH FURNACE. 50
TABLE 2.6. TYPICAL CHEMISTRY OF STEELMAKING BY-PRODUCT INPUT AND DRI OUTPUT OF A FASTMET RHF 52
TABLE 2.7. COMPARISON OF ITMK3 PIG IRON NUGGETS VERSUS BF PIG IRON 55
TABLE 2.8. CHEMICAL ANALYSIS OF HI-QIP IRON PEBBLES 57
TABLE 2.9. CHEMICAL COMPOSITION (WT. %) OF THE BF DUST ALONGSIDE IRON PEBBLES PRODUCED AT 1550 °C 57
TABLE 2.10. TYPICAL ANALYSIS OF COMET DRI 59
TABLE 2.11. TYPICAL ANALYSIS OF HISARNA IRON. 62
TABLE 2.12. KEY INFLUENCING PROPERTIES OF BOS DUST ON RECYCLING PROCESS SELECTION 65
TABLE 2.13. SUMMARY OF THE ADVANTAGES AND DISADVANTAGES OF VARIOUS ZINC REMOVAL PROCESSES. 67
TABLE 3.1. MP-AES OPERATING PARAMETERS 77
TABLE 3.2. CERTIFIED COMPOSITION VALUES FOR CRM 884-1 FURNACE DUST 78
TABLE 3.3. EXPERIMENTAL RECOVERY OF PB, NA, K, ZN, AND FE FROM CRM 884-1. 79
TABLE 4.1. TRACE METAL ANALYSIS RESULTS FOR PORT TALBOT, SCUNTHORPE, AND REDCAR MATERIAL 90
TABLE 4.2. METALLIC IRON ANALYSIS FOR PORT TALBOT, SCUNTHORPE, AND REDCAR MATERIAL 91
TABLE 4.3. XRF ANALYSIS RESULTS FOR PORT TALBOT, SCUNTHORPE, AND REDCAR MATERIAL. 92
TABLE 4.4. CALCULATED BASICITY FOR MATERIAL FROM PORT TALBOT, SCUNTHORPE, AND REDCAR 92
TABLE 4.5. CALCULATED LATTICE PARAMETERS FOR THE SPINEL PHASE IN EACH STEEL BY-PRODUCT DUST SAMPLE 94
TABLE 4.6. PARTICLE SIZING DATA FOR PORT TALBOT BOS DUST, PORT TALBOT BF DUST, SCUNTHORPE BOS DUST AND REDCAR BOS DUST. 103
TABLE 4.7. COMBUSTION ANALYSIS RESULTS FOR PORT TALBOT BOS DUST, PORT TALBOT BF DUST, SCUNTHORPE BOS DUST AND REDCAR BOS DUST 107
TABLE 4.8 RAW MATERIAL AND PRODUCED DIRECT REDUCED IRON CHEMICAL COMPOSITION FOR THE COMMERCIAL KAKOGAWA FASTMET PLANT. 112
TABLE 5.1 CHEMICAL ANALYSIS OF FIRED AND UNFIRED BRIQUETTES FROM COMMERCIAL RHF PLANT. 120
TABLE 5.2. PROPORTION OF BOS DUST TO BF DUST IN EXPERIMENTAL BLENDS 124
TABLE 5.3. CHEMICAL COMPOSITION OF THE BLENDS USED FOR RHF BENCHMARKING. 125
TABLE 5.4. COMPARISON OF COMMERCIAL RHF DRI SULFUR CONTENT. 134
TABLE 6.1. CHEMICAL COMPOSITION OF THE TWO ZINC CONTAMINATED STEELMAKING BY-PRODUCTS BF DUST AND BOS DUST. 169

TABLE 6.2. CALCULATED PIG IRON AND SLAG COMPOSITIONS FOR 100G 37:63 BF DUST TO BOS DUST RATIO AT 1450 °C, WITH THE ADDITION OF 5.4 G SiO_2 AND 1.51 G MGO. 186
TABLE 6.3. COMPARISON OF INPUT MATERIALS AND PIG IRON NUGGET CHEMISTRY USED IN EXPERIMENTAL STUDIES..... 187
TABLE 6.4. SCHEIL-GULLIVER COOLING PROJECTION FOR SLAG PRODUCED BY ADDITION OF 37:63 BF DUST TO BOS DUST WITH THE ADDITION OF 5.4 WT. % SIO2 AND 1.51 WT. % MGO.. 188
TABLE 6.5. COMPARISON OF SECONDARY ZINC CONTAINING DUSTS FROM A WAELZ KILN, RHF AND A LABORATORY STUDY PRODUCING IRON NUGGETS FROM BF DUST. 190
TABLE 6.6. CALCULATED (VIA FACTSAGE) AND EXPERIMENTAL COMPOSITION OF A 37:63 BF DUST:BOS DUST + 5.14 WT. % SiO_2 + 1.51 WT. % MGO..... 195
TABLE 7.1. PROXIMATE ANALYSIS OF THE GCI COAL AND CHARCOAL SAMPLES. 207
TABLE 7.2. CARBON AND SULFUR ANALYSIS OF GCI COAL, CHARCOAL, AND COARSE FACEMASKS..... 207
TABLE 7.3. EDX ANALYSIS OF FACEMASK ASH..... 213
TABLE 7.4. SURFACE AREA (BET) AND PORE VOLUME (DFT) ANALYSIS FOR PRE- AND POST-PYROLYSIS OF SAMPLES CARBON AND CARBON/FACEMASK SAMPLES.. 224

LIST OF FIGURES

FIGURE 1.1: A VIEW OF TATA STEEL PORT TALBOT AS SEEN FROM THE NORTH. PICTURED ARE THE TWO OPERATIONAL BLAST FURNACES, SINTER PLANT, POWER PLANT AND BOS PLANT. 21
FIGURE 1.2. SIMPLIFIED STEEL PRODUCTION PROCESS FLOW FOR THE BF/BOS ROUTE OF PRODUCTION. 23
FIGURE 2.1. GRAPHICAL ABSTRACT SHOWING THE INTER-LINKING BETWEEN ZINC AND THE STEEL MATERIAL CYCLE. 27
FIGURE 2.2. GLOBAL STEEL PRODUCTION BY PROCESS ROUTE OVER THE LAST 30 YEARS.. 30
FIGURE 2.3. SCHEMATIC OF THE BUBBLE BURSTING MECHANISM FOR THE FORMATION OF BOS DUST. 33
FIGURE 2.4. SEM IMAGES OF (A) GLOBULAR SPHEROID PARTICLE, (B) AGGLOMERATED PARTICLE CONSISTING OF SUBMICRON PARTICLES, AND (C) CROSS SECTIONAL VIEW OF GLOBULAR PARTICLE SHOWING METALLIC FE CORE.. 37
FIGURE 2.5. SEM IMAGES OF ULTRAFINE PARTICLES ADHERING TO THE EXTERIOR OF LARGER, GLOBULAR PARTICLES.. 37
FIGURE 2.6. CALCULATED POWDER XRD PATTERNS (USING VESTA SOFTWARE) FOR MAGNETITE AND ZINC FERRITE 40
FIGURE 2.7. PREDOMINANCE DIAGRAM FOR THE ZN-FE-CO-CO_2 SYSTEM AT 1000K. CALCULATED USING FACTSAGE 7.3 (ISOBAR (+) AT 1 ATM). 42
FIGURE 2.8. SIMPLIFIED SCHEMATIC PROCESS FLOW FOR A TWO-STAGE NATURAL GAS DRI PLANT SUCH AS MIDREX® 45
FIGURE 2.9. SCHEMATIC REPRESENTATION OF THE WAELZ KILN PROCESS. 48
FIGURE 2.10. A SCHEMATIC CROSS-SECTIONAL VIEW OF THE ZINC REMOVAL MECHANISM IN THE ROTARY HEARTH FURNACE (RHF). 49
FIGURE 2.11. SIMPLIFIED SCHEMATIC OF THE FASTMET® PROCESS FLOW. 51
FIGURE 2.12 SIMPLIFIED SCHEMATIC OF THE INMETCO PROCESS FLOW. 53
FIGURE 2.13. SIMPLIFIED SCHEMATIC FOR THE DRYIRON™ PROCESS FLOW. 54
FIGURE 3.1. SCHEMATIC OF THE OPERATING PRINCIPLE OF AN MP-AES 73
FIGURE 3.2. THE DIGESTION AND FILTRATION APPARATUS USED IN THIS THESIS. 76
FIGURE 3.3. ACTUAL FE_{MET}/FE_{TOT} RATIOS FOR VALIDATION SAMPLES COMPARED WITH THE FE_{MET}/FE_{TOT} AS DETERMINED VIA MP-AES SELECTIVE METALLIC IRON ANALYSIS... 81
FIGURE 4.1. UK CRUDE STEEL PRODUCTION OUTPUT AND UK LANDFILL TAX TATES. 85
FIGURE 4.2. MAJOR STEELMAKING PRODUCTION FACILITIES IN THE UK SINCE 1980. 86
FIGURE 4.3. POWDER XRD PATTERNS FOR PORT TALBOT BOS DUST, PORT TALBOT BF DUST, SCUNTHORPE BOS DUST AND REDCAR BOS DUST.. 93
FIGURE 4.4. TGA-DSC RESULTS FOR PORT TALBOT BOS DUST, PORT TALBOT BF DUST, SCUNTHORPE BOS DUST, AND REDCAR BOS DUST UNDER AN INERT GAS ATMOSPHERE. 96
FIGURE 4.5. POWDER XRD PATTERN OF PORT TALBOT BOS DUST FOLLOWING TGA-DSC ANALYSIS AT 1,000 °C UNDER AN INERT ATMOSPHERE.. 98
FIGURE 4.6. TGA-DSC RESULTS FOR PORT TALBOT BOS DUST, PORT TALBOT BF DUST SCUNTHORPE BOS DUST, AND REDCAR BOS DUST UNDER A FLOW OF COMPRESSED AIR.. 101
FIGURE 4.7. PARTICLE SIZE DISTRIBUTION INFORMATION FOR PORT TALBOT BOS DUST, PORT TALBOT BF DUST, SCUNTHORPE BOS DUST AND REDCAR BOS DUST. 103
FIGURE 4.8. SEM ANALYSIS OF PORT TALBOT BOS DUST, PORT TALBOT BF DUST (B), SCUNTHORPE BOS DUST AND REDCAR BOS DUST. 105

FIGURE 4.9. CROSS SECTIONAL ANALYSIS OF PORT TALBOT BOS DUST, PORT TALBOT BF DUST, SCUNTHORPE BOS DUST AND REDCAR BOS DUST 106
FIGURE 4.10. MÖSSBAUER SPECTROSCOPY DATA AND ASSOCIATED FITTING PATTERN FOR PORT TALBOT BOS DUST. 108
FIGURE 4.11. MÖSSBAUER SPECTROSCOPY DATA AND ASSOCIATED FITTING PATTERN FOR PORT TALBOT BF DUST..... 109
FIGURE 4.12. MÖSSBAUER SPECTROSCOPY DATA AND ASSOCIATED FITTING PATTERN FOR SCUNTHORPE BOS DUST. 110
FIGURE 4.13. MÖSSBAUER SPECTROSCOPY DATA AND ASSOCIATED FITTING PATTERN FOR REDCAR BOS DUST..... 111
FIGURE 5.1. THE EXPERIMENTAL FURNACE AT MCMASTER UNIVERSITY FOR REPLICATING THE CONDITIONS WITHIN THE RHF. 116
FIGURE 5.2 ELLINGHAM DIAGRAM FOR SELECTED OXIDES OF FE, PB, K, NA AND ZN GENERATED USING FACTSAGE 7.3 118
FIGURE 5.3. UNFIRED BRIQUETTES, SECONDARY RHF OFF-GAS DUST AND METALLIZED DRI PRODUCED VIA A COMMERCIAL RHF..... 120
FIGURE 5.4. SEM MICROGRAPHS OF UNFIRED COMMERCIAL RHF PELLETS AND FIRED DRI. 122
FIGURE 5.5. SEM-EDX ANALYSIS OF RHF OFF-GAS DUST FROM A COMMERCIAL PLANT. 123
FIGURE 5.6. EXPERIMENTAL PROCESS FLOW FOR SAMPLE PREPARATION, HEAT TREATMENT AND ANALYSIS.. 126
FIGURE 5.7. 3D SURFACE PLOTS OF THE CARBON CONTENT (WT. %) OF FIRED PELLETS WITH RESPECT TO HOLD TIME (MIN) AND TEMPERATURE (°C).. 128
FIGURE 5.8 3D SURFACE PLOT OF THE CARBON CONTENT (WT. %) OF FIRED PELLETS HEATED TO REACTION TEMPERATURE AT 20 °C/MIN AND IMMEDIATELY WITHDRAWN AND QUENCHED (T = 0). 129
FIGURE 5.9. 3D SURFACE PLOTS OF THE SULFUR CONTENT (WT. %) OF FIRED PELLETS WITH RESPECT TO HOLD TIME (MIN) AND TEMPERATURE (°C).). 133
FIGURE 5.10. ZINC (WT. %) CONTENT OF PELLET BLENDS C/O = 0.5 - 1.0 FROM 1100 °C - 1350 °C OF FIRED PELLETS HEATED TO REACTION TEMPERATURE AT 20 °C/MIN AND IMMEDIATELY WITHDRAWN AND QUENCHED (T = 0). 136
FIGURE 5.11. FIRED PELLET (1100 °C, 0 MIN, C/O = 0.5) REMOVED AND QUENCHED FROM FURNACE SHOWING WHITE POWDER LAYER CONDENSED ONTO PELLET SURFACE... 137
FIGURE 5.12. EQUILIBRIUM CO % FOR EQUATION 5.3 FOR VARYING PARTIAL PRESSURES OF ZINC VAPOUR AT 1 ATM TOTAL PRESSURE. 138
FIGURE 5.13. 3D SURFACE PLOTS OF THE ZINC CONTENT (WT. %) OF FIRED PELLETS WITH RESPECT TO HOLD TIME (MIN) AND TEMPERATURE (°C).. 141
FIGURE 5.14. POTASSIUM (WT. %) CONTENT AND SODIUM (WT. %) CONTENT OF PELLET BLENDS C/O = 0.5 - 1.0 FROM 1100 °C - 1350 °C OF FIRED PELLETS HEATED TO REACTION TEMPERATURE AT 20 °C/MIN AND IMMEDIATELY WITHDRAWN AND QUENCHED (T = 0). 142
FIGURE 5.15. 3D SURFACE PLOTS OF THE POTASSIUM CONTENT (WT. %) OF FIRED PELLETS WITH RESPECT TO HOLD TIME (MIN) AND TEMPERATURE (°C).. 144
FIGURE 5.16. 3D SURFACE PLOTS OF THE SODIUM CONTENT (WT. %) OF FIRED PELLETS WITH RESPECT TO HOLD TIME (MIN) AND TEMPERATURE (°C).. 146
FIGURE 5.17. LEAD (WT. %) CONTENT OF PELLET BLENDS C/O = 0.5 - 1.0 FROM 1100 °C - 1350 °C OF FIRED PELLETS HEATED TO REACTION TEMPERATURE AT 20 °C/MIN AND IMMEDIATELY WITHDRAWN AND QUENCHED (T = 0). 147
FIGURE 5.18. 3D SURFACE PLOTS OF THE LEAD CONTENT (WT. %) OF FIRED PELLETS WITH RESPECT TO HOLD TIME (MIN) AND TEMPERATURE (°C).. 150

FIGURE 5.19. TOTAL FE CONTENT (A) AND METALLIC FE CONTENT (B) OF PELLET BLENDS C/O = 0.5 - 1.0 FROM 1100 °C - 1350 °C OF FIRED PELLETS HEATED TO REACTION TEMPERATURE AT 20 °C/MIN AND IMMEDIATELY WITHDRAWN AND QUENCHED (T = 0). 151
FIGURE 5.20. METALLIZATION OF PELLET BLENDS C/O = 0.5 - 1.0 FROM 1100 °C - 1350 °C OF FIRED PELLETS HEATED TO REACTION TEMPERATURE AT 20 °C/MIN AND IMMEDIATELY WITHDRAWN AND QUENCHED (T = 0). 152
FIGURE 5.21. 3D SURFACE PLOTS OF THE IRON METALLIZATION % OF FIRED PELLETS WITH RESPECT TO HOLD TIME (MIN) AND TEMPERATURE (°C). 155
FIGURE 5.22. POWDER XRD ANALYSES OF C/O = 0.5 OF FIRED PELLETS HEATED TO REACTION TEMPERATURE AT 20 °C/MIN AND IMMEDIATELY WITHDRAWN AND QUENCHED (T = 0).. 157
FIGURE 5.23. POWDER XRD ANALYSES OF C/O = 1.0 OF FIRED PELLETS HEATED TO REACTION TEMPERATURE AT 20 °C/MIN AND IMMEDIATELY WITHDRAWN AND QUENCHED (T = 0).. 158
FIGURE 5.24. ARRANGEMENT OF INVERTED ALUMINA BOAT RESTED ON TOP OF SI-C CRUCIBLE USED TO COLLECT METAL VAPOUR IN-SITU. 159
FIGURE 5.25. SEM MICROGRAPH (A) AND EDX SPECTRUM (B) FOR CONDENSED ZNO COLLECTED DURING BENCHMARKING EXPERIMENTS. 160
FIGURE 6.1. IRON NUGGETS PRODUCED VIA A LARGE SCALE ITMK3 PILOT PLANT[82].. 167
FIGURE 6.2. TERNARY PHASE DIAGRAM OF THE CAO-AL_2O_3-SIO_2 OXIDE SYSTEM. 170
FIGURE 6.3. LIQUIDUS PROJECTIONS BETWEEN 1000 °C – 1800 °C OF THE CALCULATED TEMPERATURE DEPENDENT CAO-AL2O3-SIO2-FEO SYSTEM AT FIXED FEO MOLE FRACTION COMPOSITIONS OF 0.05, 0.1 AND 0.2. 171
FIGURE 6.4. THE REDUCTION OF IRON OXIDES WITHIN BF DUST FROM 0 °C TO 1800 °C. PIG IRON AND SLAG ARE BOTH LIQUID PHASES. 172
FIGURE 6.5. THE REDUCTION OF ZINC WITHIN BF DUST FROM 0 °C TO 1800 °C. 173
FIGURE 6.6. CALCULATED EQUILIBRIUM COMPOSITION OF BOS DUST FROM 0 °C TO 1800 °C. 174
FIGURE 6.7 CALCULATED EQUILIBRIUM COMPOSITION OF BOS DUST WITH THE ADDITION OF 3 MOL OF CARBON FROM 0 °C TO 1800 °C. 174
FIGURE 6.8. SURFACE PLOT SHOWING $R_{FE\%}$ AT VARYING RATIOS OF BF DUST TO BOS DUST FROM 0 °C TO 1800 °C. 176
FIGURE 6.9. CALCULATED SURFACE PLOT SHOWING FE_{OUT} AT VARYING RATIOS OF BF DUST TO BOS DUST FROM 0 °C TO 1800 °C. 177
FIGURE 6.10. CALCULATED SURFACE PLOT SHOWING THE DISSOLVED CARBON (WT. % [C]) IN THE PIG IRON ALLOY PHASE WITH VARYING BF DUST FRACTION BETWEEN 0 °C – 1800 °C. 178
FIGURE 6.11. CALCULATED SURFACE PLOT SHOWING THE DISSOLVED SULFUR (WT. % [S]) IN THE PIG IRON ALLOY PHASE WITH VARYING BF DUST FRACTION BETWEEN 0 °C - 1800 °C. 179
FIGURE 6.12. CALCULATED SURFACE PLOT SHOWING THE DISSOLVED MANGANESE (WT. % [MN]) IN THE PIG IRON ALLOY PHASE WITH VARYING BF DUST FRACTION BETWEEN 0 °C - 1800 °C. 180
FIGURE 6.13. CALCULATED SURFACE PLOT SHOWING THE FRACTION OF THE SYSTEM PRESENT AS A SOLID WITH VARYING BF DUST FRACTION BETWEEN 0 °C – 1800 °C. 181
FIGURE 6.14. SURFACE PLOTS SHOWING THE FRACTION OF THE SYSTEM PRESENT AS SOLID CARBONACEOUS MATERIAL AND NON-CARBONACEOUS MATERIAL WITH VARYING BF DUST FRACTION BETWEEN 0 °C – 1800 °C. 182
FIGURE 6.15. MELTING PROJECTION FOR THE CAO-SIO2−MGO-AL2O3 SYSTEM AT FIXED 9 WT% AL2O3 BETWEEN 1300 – 1500 °C. 184

FIGURE 6.16. CHANGING MANGANESE, SILICON AND SULFUR CONTENT OF THE PIG IRON PHASE WITH SIO2 ADDITION AT 1450 °C WITH 0 G MGO ADDED AND 1.51 G ADDED (B).. 185
FIGURE 6.17. PIG IRON NUGGET AND FUSED SLAG PRODUCED BY FIRING 37:63 BF DUST: BOS DUST + 5.14 WT. % SIO_2 + 1.51 WT% MGO AT 1450 °C IN AIR FOR 15 MINUTES. 191
FIGURE 6.18. SIZE DISTRIBUTION OF PIG IRON NUGGETS PRODUCED FROM 13.5 G BRIQUETTES. 192
FIGURE 6.19. SEM-EDX MAPS FOR PIG IRON NUGGETS PRODUCED AT 1450 °C FOR 15 MINUTES FROM A BRIQUETTE COMPOSITION OF 37:63 BF DUST:BOS DUST + 5.14 WT. % SIO2 + 1.51 WT. % MGO. 196
FIGURE 6.20. SEM-EDX ANALYSIS OF SLAG PRODUCT FROM PIG IRON NUGGET PRODUCTION, SHOWING ENTRAINED DROPLETS OF METALLIC IRON. 198
FIGURE 6.21. TGA OXIDATION BEHAVIOR OF PIG IRON NUGGETS AND DRI 200
FIGURE 7.1. COMPONENTS OF THE DISPOSABLE MASK. 208
FIGURE 7.2. FTIR SPECTRA FOR UNTREATED FACEMASKS AND FACEMASKS THAT HAVE BEEN HELD AT 250 °C FOR 1 HOUR . 209
FIGURE 7.3. MATERIALS AT VARIOUS STAGES OF THE MILLING PROCESS.. 210
FIGURE 7.4. TGA-DTG CURVE FOR UNTREATED FACEMASKS UNDER A 100 CM3/MIN FLOW AIR, UNTREATED FACEMASKS UNDER. 212
FIGURE 7.5 SEM-EDX ANALYSIS OF ASH PRODUCED BY COMBUSTION OF UNTREATED FACEMASKS 213
FIGURE 7.6. TGA MEASUREMENTS TO 900 °C UNDER AR AND TO 1200 °C UNDER CO2 ATMOSPHERES FOR CHARCOALCOMPARED TO CHARCOAL/20 WT. % FACEMASK BLEND AND GCI COAL COMPARED TO GCI COAL/20 WT. % FACEMASK BLEND. 215
FIGURE 7.7. PLOTS OF A AND DA/DT AGAINST T (°C) FOR DIFFERENT HEATING RATES. 218
FIGURE 7.8. FRIEDMAN PLOTS AND CALCULATED ACTIVATION ENERGY (E_A) AGAINST A FOR THE COMBUSTION OF CARBON AND CARBON/FACEMASK MELT BLENDS IN CO_2 ATMOSPHERE.. 220
FIGURE 7.9. SEM IMAGES OF SAMPLES OF CARBON AND CARBON/FACEMASK MELT BLENDS.. 223
FIGURE 7.10 TGA CURVES FOR Fe_2O_3 COAL AND FACEMASK TREATED COAL (FC) FROM ROOM TEMPERATURE TO 1200 °C UNDER ARGON. 226
FIGURE 7.11. EXPERIMENTAL TGA CURVES VERSUS THEORETICAL CURVES FOR Fe_2O_3-C AND Fe_2O_3-FC. 227
FIGURE 7.12. IMAGES OF Fe_2O_3-FC AND Fe_2O_3-C BRIQUETTES REDUCED AT 650 °C FOR 1 HR UNDER N_2. 228
FIGURE 7.13. SEM MICROGRAPHS FOR REDUCED BRIQUETTES. 230
FIGURE 7.14 POWDER XRD FOR Fe_2O_3-C AS PREPARED, AND HEAT TREATED FOR 1 HR AT 650 °C, 1000 °C, AND 1200 °C.. 232
FIGURE 7.15. POWDER XRD FOR Fe_2O_3-C AS PREPARED, AND HEAT TREATED FOR 1 HR AT 650 °C, 1000 °C, AND 1200 °C.. 233
FIGURE 7.16. PROPOSED PROCESS SCHEMATIC SHOWING THE EFFECT OF THE POLYMER FABRIC OF FACEMASKS ON A COAL PARTICLE AS IT UNDERGOES HEAT TREATMENT. 234

LIST OF ABBREVIATIONS AND ACRONYMS

BF – Blast Furnace

BOF – Basic Oxygen Furnace

BOS – Basic Oxygen Steelmaking

CRM – Certified Reference Material

DRI – Direct Reduced Iron

EAF – Electric Arc Furnace

HM – Hot metal, molten iron or steel

HMD – Hot metal desulfurization

ISF – Imperial Smelting Furnace

ITmk3 – Ironmaking Technology Mark III

RHF – Rotary Hearth Furnace

S-OES – Spark-Optical Emission Spectroscopy

tHM – Tonnes of Hot Metal

tpd – tonnes per day

ULCOS – Ultra low CO_2 Steelmaking

VIU – Value in Use

XRD – X-Ray Diffraction

GLOSSARY OF TERMS

Blast – broad industry colloquialism for the pre-heated air (which may or may not have been subject to oxygen enrichment) that is forced into the bottom of a blast furnace.

Burden – also known as charge, the raw materials added into the blast furnace to produce molten iron.

Charge – (verb), the action of adding material to a furnace e.g. the basic oxygen furnace was charged with 15t of scrap steel.

Desulfurization – a process prior to the basic oxygen steelmaking process where reagent mixtures are injected into hot metal to sequester sulfur from the hot metal in a slag phase, where it can be skimmed and removed.

Gangue – undesirable, low value non-ferrous material associated with iron ores, steelmaking by-product dusts etc.

Hearth – the non-combustible floor of a furnace, upon which the burden sits.

Hot metal – broad industry colloquialism iron in the molten state, can refer to molten steel or molten pig iron.

Pig iron – term for the high carbon content molten iron product of the blast furnace. Named as such due to historic resemblance of the casting of iron ingots to suckling pigs in foundry casthouses.

Tramp element – elements with a deleterious effect on the quality of the steel product, includes Cu, Sn, S among others.

Tuyère – A water-cooled copper nozzle found at the base of a blast furnace, through which the hot blast is forced into the furnace.

LIST OF APPENDICES

APPENDIX 1. RAW DATA FROM RHF BENCHMARKING STUDY IN CHAPTER 5.....267
APPENDIX 2. RAW DATA FROM FACTSAGE CALCULATIONS IN CHAPTER 6.....271

1. INTRODUCTION

1.1 Research Question

The research in this thesis sets out to address three key questions in the field of value recovery from zinc contaminated steelmaking by-product dusts:

1. What chemical, structural, and morphological properties do the dusts typically possess and is this consistent between different plants and operations?
2. What are the currently commercialized solutions for the recovery of these materials, and is the material from Tata Steel Port Talbot suitable for processing via these methods?
3. Can next-generation ironmaking processes be adapted to produce higher value products from the processing of zinc contaminated dusts, or use alternative reductants, than currently commercialized methods?

1.2 The Global Steel Industry and South Wales

Steel is arguably the world's most recycled material. In 2019, nearly half a billion tonnes of scrap iron and steel was granted new life in the worlds electric arc furnaces, basic oxygen furnaces, open hearth furnaces and foundries [1].

Steels infinite theoretical recyclability without degradation in quality, the ability to separate ferrous material cheaply and easily using magnetic separation techniques, and a realistic pathway to net-zero CO_2 emission steel production [2] all make steel a critical material for addressing the global climate emergency.

While much focus is given to post-consumer recycling – the recovery of ferrous units from products that have reached the end of their service life such as cars, rails, and steel used in construction, an important consideration is the pre-consumer recycling rate within steel production.

An integrated steelworks, a plant that produces liquid steel using a blast furnace in tandem with a basic oxygen steelmaking plant is a fantastic example of material usage efficiency and internal recycling. Worldwide material efficiencies in the sector have reached 97.6% in recent years [3] with the exception of CO_2, with minimal material requiring disposal in landfill. The highest volume by-products from steelmaking – ironmaking and steelmaking slag (~80% by weight) find use as aggregates in the construction and civil engineering sector [4].

Internally generated scrap such as off-cuts are recycled through simply charging into the steelmaking vessel, and most of the fine material such as mill scale, and off-gas dusts can be agglomerated via a sinter plant and used as ferrous feedstock to the blast furnace. The ambition for the world steel industry, alongside carbon neutrality in the face of a global climate emergency, is to be a zero-waste industry with no solid material being landfilled as a result of production [5].

Ironmaking in Port Talbot, UK is estimated to span over a millennia, with small amounts of iron being smelted and worked by monks in the area utilizing local ores and coals [6]. The installation that stands there today was formally known as the Abbey Works, and a wall believed to be the remains of a farmhouse from the 16th century still proudly stands by the plants hot strip mill.

Today, the plant is a sprawling works that dominates the skyline of the Welsh town (Figure 1.1), with two operational blast furnaces (BF4 and BF5), a large Basic Oxygen Steelmaking (BOS) plant, and hot and cold strip mills among other supporting facilities. While the capacity for integrated steelmaking in South Wales is only around 5 million tonnes per year, the economic importance of its role in the UK construction and automotive manufacturing sectors cannot be overstated.

The Welsh governments target of a Net Zero CO_2 Wales by 2050 will require fundamental shifts in the way that steel is produced [7] and the valorization of by-products to reduce virgin material requirements will play a key part in the decarbonization process. Specifically in the UK the climate change levy constitutes a commercial penalty for large industrial emitters of CO_2, and as such there are immediate bottom-line implications for industries that continue to emit CO_2 at high rates.

Figure 1.1: A view of Tata Steel Port Talbot as seen from the North. Pictured are the two operational blast furnaces, sinter plant, power plant and BOS plant (partially obscured). Images used with permission courtesy of Viktor Macha[8].

1.3 The Production of Steel via the Blast Furnace/Basic Oxygen Steelmaking route

Globally, the BF/BOS route is the most used process to produce steel and a simplified process flow is shown in Figure 1.2. The BF is fundamentally a massive, counter-current, gas-solid shaft reactor. Iron ore, sinter, coke, and fluxes are charged to the furnace from the top while air, preheated in stoves adjacent to the furnace, is injected at extremely high velocity through tuyere pipes in the furnace's lower regions.

The coke within the furnace is combusted to produce carbon monoxide, which reduces the iron oxides present in the ore to metallic iron as it descends through the furnace shaft towards the hotter, lower portions of the furnace.

The ferrous form of the furnace burden can take several forms, depending on the plant. Iron ore can be charged as lump ore or as pellets, and fine iron bearing material can be agglomerated into sinter via a sintering plant where high temperature, oxidizing conditions create a semi-molten state in the fine materials causing bonds to form between particles to form a solid mass.

Material that is to be charged to the BF requires two key physical properties. Firstly, it must be mechanically strong enough to withstand the weight of the furnace burden above it as it descends the shaft without disintegration, and secondly it must be of a suitable diameter (approximately 10 mm) to allow for permeability of the furnace burden to the reducing gas in the furnace. Low strength and inconsistent size can lead to excessive fines generation, process instability, poor heat exchange and large pressure drops across the furnace burden.

It is important to note that a blast furnace cannot be directly charged with powdered materials. The burden must be both large enough (approximately 5 mm in diameter) to allow for efficient gas flow through the furnace shaft and thus reduce pressure drop across the furnace, and strong enough to support the weight of the material above it.

As the ore descends the shaft, it melts and drips down to the furnace hearth where it accumulates as molten pig iron. Fluxes added combine with siliceous gangue to form a molten slag which partially sequesters tramp elements such as sulfur and phosphorous from the pig iron. The furnace is tapped for the molten iron via drilling into tapholes at the base of the furnace, where the ferrostatic pressure from molten iron above the taphole forces the iron from the furnace. The immiscible, molten slag is skimmed from the surface of the iron mechanically, by way of the difference in material densities and the iron is poured into waiting torpedo railcars for further processing.

The high carbon pig iron must be decarburized to render it usable for most consumer application and this is performed via the BOS process in a basic oxygen furnace (BOF). The pig iron may be subject to pre-treatment in a hot metal desulfurization (HMD) processing station prior to charging to the BOF, depending on customer requirements or raw material quality.

A BOF charge is typically around 30 wt. % recycled scrap, from both internal and external sources. The scrap acts not only as a cheap source of ferrous units but also as a coolant to the extremely exergonic BOS process.

Hot metal from the blast furnace is poured into the BOF following the charge of scrap, and basic fluxes are added to generate a refining slag. Oxygen is then blown at supersonic speeds into the molten steel bath and the high oxygen partial pressure oxidizes carbon and other impurities in the hot metal to produce liquid steel.

The liquid steel is then tapped from the BOF and is treated and refined via secondary steelmaking where the material can be de-gassed, further de-oxidized or further alloy additions made subject to customer requirements.

Once additions have been made and the steel has met the customers chemistry requirements, the steel can be cast into slabs, billets or blooms (slabs in the case of Tata Steel Port Talbot) continuously via a caster. The process until the point where the steel is cast and solidifies is sometimes referred to in the UK as 'heavy end' steelmaking, owing to the extremely high capacity batch-wise processes.

Each step in this process naturally generates co-products. Slags are used for refining purposes and as oxidation protection throughout the process while the metal is still molten, and as slabs cool and oxidize in the atmosphere iron oxide scales can form and break away from the bulk material.

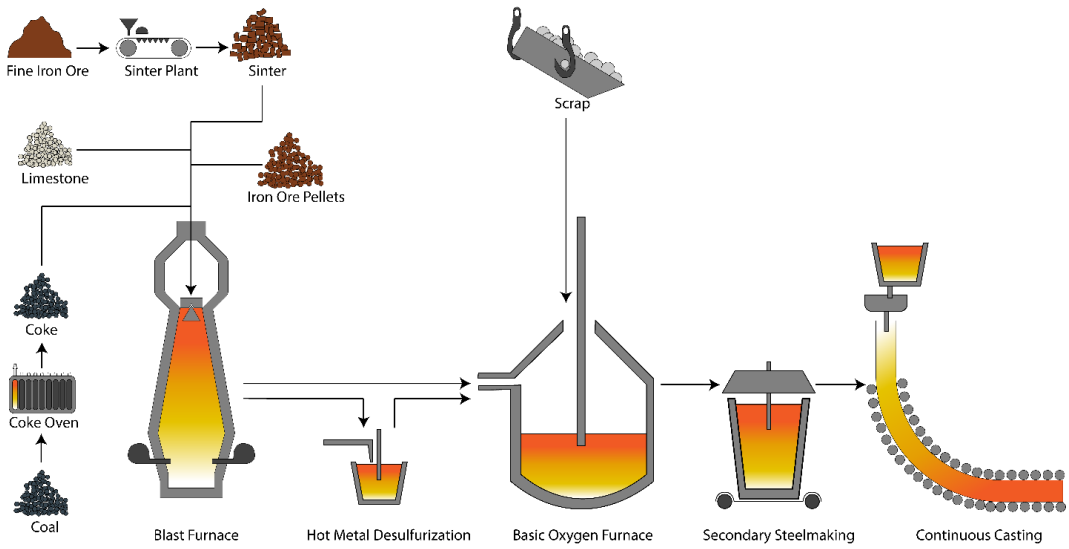

Figure 1.2. Simplified steel production process flow for the BF/BOS route of production.

Fine material generated on the plant such as mill scale or scale produced from continuous casting can be easily reintegrated into the process, and the associated ferrous material recovered, by adding the material into the sinter process [9].

This is often not possible with off-gas dusts from the BF and the BOF due to contamination with zinc, meaning the iron content of the materials is lost from the process.

1.4 Zinc and iron

The partnership of zinc and iron in steelmaking is one that spans centuries. Steel readily corrodes under a large range of conditions, meaning that in many applications additional methods are employed to retard the rate of corrosion to extend the steels usable service

life. These can include anodic protection, cathodic protection, inhibitors, and coatings. One of the most common coatings for this application is zinc, often applied to the steel via hot dip galvanizing.

In hot dip galvanizing, the steel substrate is immersed in a bath of molten zinc to form a continuous surface coating of zinc. This not only provides isolation of the steel substrate from the atmosphere in a manner similar to a non-galvanic coating, but also sacrificial cathodic protection from corrosion should the coating by disrupted by damage [10].

This increased corrosion resistance has led to huge growth in demand for galvanized material, specifically in the automotive sector. Most external panels on modern vehicles are now galvanized for this reason.

While the increased service life of galvanized products has huge benefits, energy savings and emission reductions compared to untreated steel, zinc presents a specific challenge for the steel recycler due to the extremely low tolerances for zinc bearing material in the BF. Once zinc enters into the steel material cycle in can be challenging to fully recycle due to this sensitivity in the BF and hence, historically large amounts of zinc contaminated material have not been recycled and instead stockpiled.

The benefits of galvanizing automotive products are so great that simply avoiding galvanized steel for corrosion sensitive application is environmentally and economically the wrong choice. Instead, the steel industry must adapt to remove zinc from the materials loop of steelmaking and allow it to re-enter the zinc production cycle as an input material. Steel will not be a truly circular material until all the products produced by a steel manufacturer can be effectively recovered and recycled.

1.5 The Structure of the Thesis

This work is divided into several sections.

Chapter 2 forms an in-depth literature review of the best available technology for processing BOS dust, as well as developing technologies that may find application in the future.

Chapter 3 details experimental protocol and validation for the experimental methods used in the thesis.

Chapter 4 is an in-depth characterization study of BOS and BF dusts from three different UK plants, to best advise the type of extractive metallurgical methods to be trialed experimentally.

Chapter 5 is a benchmarking study on the application of the established best available technology, the RHF, to material from Tata Steel Port Talbot to gauge feasibility and effectiveness at zinc removal, iron metallization and sulfur content.

Chapter 6 is a computational thermochemical study into whether next generation RHF technology that produces granulated pig iron nuggets from virgin ore may be successfully applied to removing zinc from BOS and BF dusts to generate a higher value product. The recommendations made via the thermochemical study are also validated experimentally.

Chapter 7 explores the potential for the use of unrecyclable waste plastic in the form of single use COVID-19 facemasks as an auxiliary reductant for the RHF.

Finally, Chapter 8 forms conclusions and recommendations future work based on the research contained herein.

1.6 List of Published Journal Papers for Examination

1.6.1 Chapter 2. Literature Review

1. Stewart, D. J. C. & Barron, A. R. Pyrometallurgical removal of zinc from basic oxygen steelmaking dust – A review of best available technology. *Resour. Conserv. Recycl.* **157**, 104746 (2020). doi: 10.1016/j.resconrec.2020.104746. [First Name Author].

1.6.2 Chapter 4. The Chemical Suitability for Recycling of Steelmaking By-Products from United Kingdom Facilities

The work that formed the basis of this chapter is currently submitted and under review with *Resources, Conservation & Recycling Advances* at the time of writing.

1.6.3 Chapter 5. Next Generation RHFs: Pig Iron Nugget Production

1. Stewart, D. J. C., Thomson, D. & Barron, A. R. The production of high value pig iron nuggets from steelmaking by-products – A thermodynamic evaluation. *Resour. , Conserv. Recycl.* **170**, 105592 (2021). doi: https://doi.org/10.1016/j.resconrec.2021.105592. [First Name Author].

1.6.4 Chapter 7. Utilization of Facemask Plastic Waste Resulting from the COVID-19 Pandemic in RHF Ironmaking

1. Stewart, D. J. C., Fisher, L. V., Warwick, M. E. A., Thomson, D. & Barron, A. R. Facemasks and ferrous metallurgy: improving gasification reactivity of low-volatile coals using waste COVID-19 facemasks for ironmaking application. *Sci. Rep.* **12**, 2693 (2022). [First Name Author].

2. Stewart, D. J. C., Lewis, J., Thomson, D., Barron, A. R. Waste COVID-19 Facemasks as an Auxiliary Iron Reductant in the Rotary Hearth Furnace. *Proceedings of the 8th International Conference on Engineering and Technology (BICET 2021).* **In Press**, (2022). [First Name Author] **.**

2. LITERATURE REVIEW

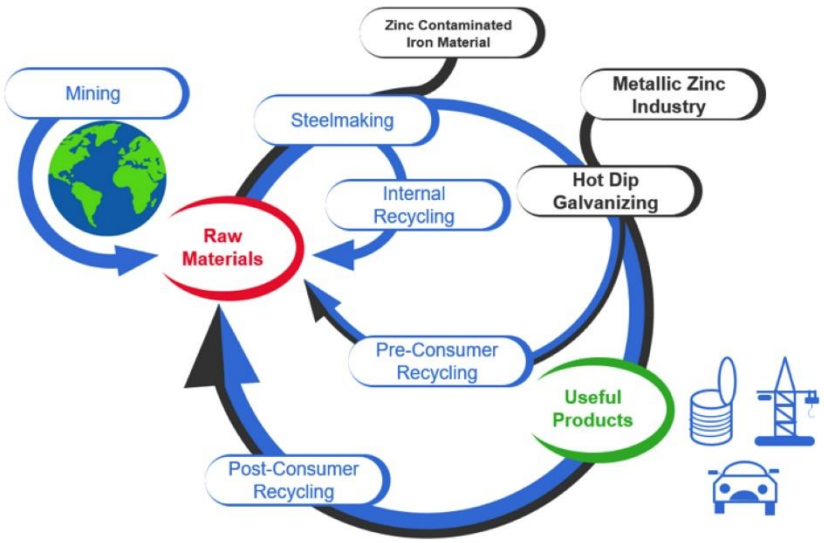

Figure 2.1. Graphical abstract showing the inter-linking between zinc and the steel material cycle.

2.1 Introduction

The most common process for the production of steel is the BOS process, accounting for well over a billion tons of steel produced globally [12]. A significant volume of BOS dust is created as a by-product of the production of liquid steel through the BOS process, which is generally recovered through the off-gas cleaning system. BOS dust is also known as basic oxygen furnace (BOF) dust, BOF fume, or BOS slurry, and varies depending on the origin of the material. For simplicity, this thesis defines BOS dust as the fine ferrous by-product produced during the blowing period in an oxygen converter/furnace at a steelmaking facility, which is wet-scrubbed from the off-gas system of the steelmaking plant and will refer to the material as such when citing references using differing nomenclature.

Typically, BOS dust is highly metalized and has iron content (> 60% Fe_{Tot}) comparable with good quality ores, and therefore could be a valuable secondary source of iron units for an integrated steel plant.

While the recirculation of fine iron-bearing materials back into the blast furnace is commonplace, when these materials are contaminated with zinc, the typical process routes become unsuitable. Because the blast furnace process is remarkably sensitive to volatile metals most critically zinc these, zinc-containing materials have been ordinarily disposed of through ad-hoc stockpiling.

The reason for the sensitivity to zinc is that once charged into a blast furnace, any zinc component is reduced to elemental Zn. Due to the low boiling point of the metal (907 °C) compared to the furnace temperature range (1600–1650 °C), the vapor rises back through the furnace stack and re-condenses [13], leading to condensation of scaffolds (accretions) of zinc on the walls of the furnace. These deposits can affect both solid and gas flow through the furnace negatively impacting productivity and risking damage to the furnace lining through burden slips. Zinc is also known to attack refractories in the upper stack of the furnace and therefore potentially impact on campaign life [14].

As such, the concentration of zinc loaded to a blast furnace is tightly controlled, with levels around 100–120 g/tHM generally permissible (tHM=tonnes of hot metal). In context, for a plant producing 10 mt of liquid steel per annum, this would allow for a maximum 1 kt of zinc to be charged to the furnace per annum if these limits are to be followed. The dilution of zinc bearing wastes and reintegrating them into existing steelmaking processes are therefore not suitable for processing zinc-bearing wastes on a

sustainable scale. The volume of zinc re-entering the steelmaking process through galvanized scrap steel recycling is just too much.

Zinc and iron are routinely married together through the hot-dip galvanization process, with the zinc providing galvanic protection for the steel. It has been postulated that without substantial improvements to the recovery rate of zinc from its industrial uses (principally hot-dip galvanizing) global zinc reserves will be outstripped by demand as early as 2050 [15]. It is therefore clear, that without a go-between process to economically remove zinc from the steel material cycle, the process of hot dip galvanizing will be dependent on depleting global reserves of zinc.

A number of hydrometallurgical techniques, such as alkaline leaching, are often utilized to remove zinc from electric arc furnace dusts [16–18]; however, these are likely inappropriate for recovery of material from BOS dust due to the lower zinc concentration present, in the latter, and extra post-processing steps to utilize the separated iron product. Nevertheless, ammoniacal leaching has been reported to have good results for wastes from BOS furnaces where the zinc content is 2.82 % [19].

There are several emerging novel techniques for the pyrometallurgical separation of zinc from steelmaking dusts, with one of the most promising being rapid microwave carbothermal reduction [20] which has advantages such as rapid reaction times (99.99 % Zn removal in 15 min at 1100 W) and feasible capture of a metallic zinc product. Hybridized pyrometallurgical/hydrometallurgical techniques have also been studied such as chlorination roasting followed by a leaching step [21]. These have advantages in the relatively low processing temperatures required (750 °C) and hence lower energy input when compared to other pyrometallurgical techniques. However, the disadvantages of a poorly valorized ferrous product and comparatively low Zn removal (97 %) mean upscale is unlikely. These technologies are still in their infancy, having not achieved pilot scale operation as of the time of writing, and as such will not form the main basis of this section – instead, focusing more on proven scalable technology and how they might be applied to process BOS dust.

The need to adopt commercial routes to the re-use of zinc waste from BOS dust is part of a broader move to lower the environmental impact of the steel industry [22,23] and ensure its economic sustainability [4,24]. Thus, there are significant incentives to find ways to utilize as much waste material as possible. Herein, approaches to the re- use of BOS dust are reviewed, with particular focus on those that provide the best available technology to supplement an integrated steelworks in processing its zinc-bearing by-products, and to make recommendations to the industry based off viability, technical

feasibility, and environmental considerations. The goal is to ensure that BOS dust is considered a material with potential as a resource rather than a waste.

The objective of this chapter is to provide a short to medium term outlook for the feasibility of pyrometallurgical separation techniques for BOS dusts. The recycling of low zinc bearing materials is routinely performed at most steel plants through dilution in the blast furnace burden. Very high Zn bearing materials such as EAF dusts are very well studied and reviewed [16,25] due to the hazardous nature of the material. Materials that are moderately contaminated with Zn such as BOS dust are comparatively understudied, despite the fact they are produced on a far greater scale.

2.2 The basic oxygen steelmaking (BOS) process

Basic oxygen steelmaking is the most common production route for steel in the world today (Figure 2.2). Immediately following WWII, it became commercially viable to mass produce huge volumes of high purity oxygen for industrial use. This availability of oxygen for use as an oxidizing agent in the steel industry rapidly supplanted the outdated Open-Hearth Furnace, as BOS plants are more productive and require no external heat input due to the extremely exothermic nature of the process.

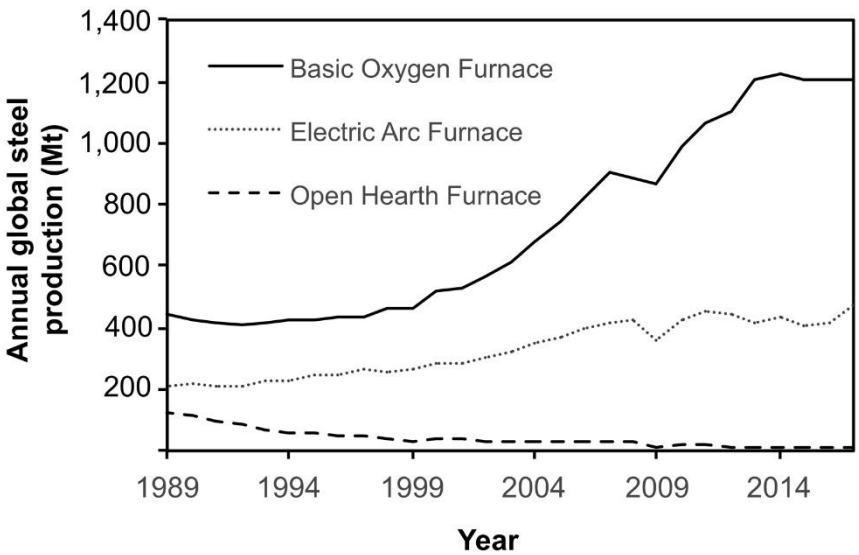

Figure 2.2. Global steel production by process route over the last 30 years. Data adapted from the World Steel Association annual production statistics [12].

In the BOS process, molten pig iron is charged into a converter lined with basic refractory bricks, with scrap steel typically used as an additional iron source and coolant which can make up 25 % by mass of the charge [13]. Oxygen is then blown into the vessel

at supersonic speeds through a water-cooled lance to oxidize impurities within the molten iron, which are then trapped in the molten slag or emitted from the vessel as a gas.

The chemical reactions within the basic oxygen steelmaking process are given in where the state of the reagents is signified by the choice of braces, "{}", to denote a gas phase reactant/product, square brackets, "[]", to denote the reactant/product is dissolved in the bulk Fe(l) phase, and round brackets, "()", denote the reactant/product is dissolved within the liquid slag phase. The oxygen injected by the lance dissociates into the molten iron bath (Equation 2.1) which then acts to rapidly oxidize impurities within the melt such as C, S, Si, Mn and P which are either captured into the molten slag or escape the bath as gas in the case of carbon. Fluxes such as CaO are also added as a processing aid, to promote the removal of S and P from the liquid iron. These equations are an oversimplification of the complex equilibria between the slag and metal interfaces but are useful nonetheless to describe the overall sequestration of unwanted elements in the hot metal to the slag or to the gas phase.

$$\{O_2\} \longrightarrow 2[O] \tag{2.1}$$

$$[C] + [O] \longrightarrow \{CO\} \tag{2.2}$$

$$[Si] + 2[O] \longrightarrow (SiO_2) \tag{2.3}$$

$$2(CaO) + (SiO_2) \longrightarrow (2CaO \cdot SiO_2) \tag{2.4}$$

$$[Mn] + [O] \longrightarrow (MnO) \tag{2.5}$$

$$2[P] + 5[O] + 3(CaO) \longrightarrow (Ca_3(PO_4)_2) \tag{2.6}$$

$$[FeS] + (CaO) \longrightarrow (FeO) + (CaS) \tag{2.7}$$

$$2[P] + 5(FeO) + 4(CaO) \longrightarrow 4(CaO \cdot P_2O_5) + 5[Fe] \tag{2.8}$$

2.3 BOS Dust

The BOS process naturally generates co-products alongside the desired liquid steel, and while the largest by mass of these co-products is steelmaking slag – the glassy mixture of metal oxides used to sequester impurities and refine the liquid steel [4] the volume of ferrous dusts cannot be ignored. As a consequence of the injection of oxygen into the

melt at supersonic speeds as well as the turbulent conditions of the bath caused by so-called 'carbon boil', a significant amount of fine material is ejected from the bath. This fine material is then scrubbed out of the off-gas from the process through either wet venturi scrubber systems[26] or dry electrostatic precipitators[27] before the off-gas is suitable to either collect for caloric recovery or to flare to the atmosphere. The BOS dust is then collected either as a filter baghouse dust or a wet filter cake.

2.4 Formation mechanism of basic oxygen steelmaking dust

The mechanisms of formation of BOS dust have been well researched, as the conditions within an off-gas system can have a significant effect on chemistry of the dust product. In 1944 Kohlmeyer and Spandau theorized that the reaction of gaseous carbon monoxide formed from partial carbon oxidation was reacting with elemental iron to yield iron pentacarbonyl (Equation 2.9) [28].

$$\mathrm{Fe}^0 + 5\mathrm{CO} \longrightarrow \mathrm{Fe(CO)_5} \qquad (2.9)$$

Since $Fe(CO)_5$ decomposes readily back to Fe^0 at comparatively low temperatures (426 °C) [29], and therefore it's unlikely that it would be able to form in the steelmaking environment at a temperature in excess of 1500 °C. It would also be expected that performing a blow using carbon monoxide would also cause the characteristic visible fuming associated with the formation of BOS dust, but in practice, this does not occur [30]. In reality, there are two competing mechanisms at play in the formation of BOS dust, and these are the vaporization or fuming mechanism, and the bubble burst mechanism [31].

Initially the vaporization of iron from a steel bath seems rather counterintuitive because the standard boiling point of iron is 2861 °C and the temperatures in oxygen steelmaking are around 1000 °C lower. Nevertheless, Goetz described the phenomenon of localized 'hot spotting' within the BOS process [32], where the extremely exothermic reactions at the gas/metal interface generate heat so rapidly that it cannot be transported away effectively by convection into the bulk of the bath. Temperatures between 2400-2600 °C, as measured on industrial basic oxygen furnaces using optical pyrometry, have been reported. This localized hotspot formation leads to volatilization and oxidation of iron from the bath in the form of a fine fume.

The second mechanism is the mechanical ejection of metal droplets from the bath due to the collapse of CO bubbles formed *in-situ* (Equation 2.2). This reaction spontaneously forms bubbles of carbon monoxide within the steel bath and is critical to the speed of the BOS process, since it provides excellent bath agitation and mixing. Once these bubbles have formed in the extremely high temperatures found in the molten iron, they are forced upwards due to their relative density before reaching the surface (Figure 2.3a). Upon reaching the surface of the hot metal, the top of the bubble thins (Figure 2.3b) until it's surface tension can no longer contain the hot gas, which break clear of the liquid and escapes to atmosphere (Figure 2.3c). The resulting high pressure at the edges of the now ruptured bubble (Figure 2.3d) form a jet (Figure 2.3e) that ejects droplets of molten iron free of the melt (Figure 2.3f).

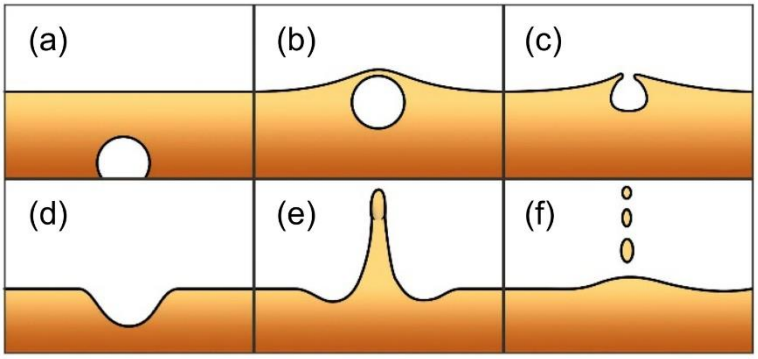

Figure 2.3. Schematic of the bubble bursting mechanism for the formation of BOS dust showing (a) a CO bubble formed in the hot metal, (b) reaching the surface it thins, (c) breaking clear of the liquid and escaping to atmosphere, where (d) the resulting high pressure at the edges forms a jet (e) that ejects droplets of molten iron free from the melt.

From investigations into these two mechanisms, it is abundantly clear that there is a relationship between the carbon content of the iron bath and the volume of fumes generated. It has been shown in lab scale [30,33] and full production scale at the steel plant in Port Talbot, UK [34] that at higher carbon concentrations within the iron bath, the rate of fume generation is higher. However, both mechanisms can be dependent on the carbon levels, so this alone is not enough to determine the predominance of each mechanism. Tsujino et al. devised a method of determining the ratio of so-called ‘bubble burst’ particles to ‘fume’ particles to elucidate the dominant production mechanism [35].

Molybdenum and manganese are both typical alloying elements that may be found as part of the melt in a BOS converter, but have significantly different boiling temperatures, 4612 °C and 1962 °C, respectively. By assuming molybdenum volatilization from the bath is negligible it can be assumed that any molybdenum present within the BOS dust must have been mechanically ejected from the bath via the bubble bursting mechanism rather than volatilized, while the manganese concentration would indicate volatilization. This approach allowed for direct measurement of the ratio of the two particle types throughout the blow and showed that the initial dust produced in the blow was principally through the bubble bursting mechanism, whereas at the conclusion of the blowing period the fuming/vaporization mechanism dominated.
It should be note that the volumes of dust generated from BOS converters are widely variable, usually estimated at around 15–20 kg/tHM. There are clearly many dependent process variables that can affect the composition of BOS dust, including: lance height, oxygen injection pressure, and slag volume [36,37].

2.4.1 The origin of zinc in the BOS process

The use of galvanized strip steel has increasingly found use in automotive body panels, due to its formability, corrosion resistance and good strength/mass ratio. For steelmaking to be truly sustainable, galvanized steel must also be recycled at the end of its useful service life. Should any galvanized steel be included in the scrap charge to the BOS furnace at the beginning of the process, any zinc present will volatilize almost completely from the basic oxygen furnace, upon addition of the pig iron.
Scraps with high zinc content are often cheaper than low zinc content scrap for this reason. EAF dusts are substantially higher in zinc content, along with other tramp elements such as lead, due to their nature of having typically 100 % scrap charges [38].
Integrated plants generally manage BOS dust recycling through careful management of scrap chemistry inputted to the furnace, then reintroducing the material to the sinter plant and then the blast furnace but extremely tight limitations on zinc input mean unexpectedly high zinc material cannot be processed in this manner.

2.4.2 Off-gas system design

One key design feature of a BOS plant’s off-gas system, that can have a substantial effect on the chemistry of the dust product, is whether it is a closed or open hood

design. In a closed hood system, air ingress into the off-gas system is extremely limited and as such degree of oxidation as well as the formation of some spinel phases are suppressed. This is typical for a steel plant with an off-gas recovery system in place, as the gaseous product of the BOS process has substantial caloric value and is utilized as an energy source. BOS dust from these systems typically has a black appearance. In an open hood system, the opposite occurs, the environment of the system is much more oxidative and combustive. As such higher oxidation state iron oxides are expected and the off-gas dust has a more reddish appearance [32].

2.4.3 Characterization of BOS dust

As a potentially valuable ferrous resource, BOS dust from steel plants all around the world has been characterized using several different techniques. Although many different monikers are used to describe the material, it is defined in this work as the fine material that is removed from the off-gas system from a BOS vessel, produced during the blowing period.

2.4.4 Particle size

It has been reported that the distribution of particle size within BOS dust samples is from 0.5 μm up to around 50 μm as determined by laser-based granulometry. Dividing the dust into a fine (< 38 μm) and coarse (> 38 μm) fraction, it was also found that the finer fraction was considerably more Zn rich [39]). Gritzan and Neuschütz subdivided BOS dust into four classifications by size fraction with maxima at 1, 12, 50 and 140 μm, with the largest fraction likely extending past the detection limit of the granulometry technique used (200 μm) [37].

However, it was also found through SEM observations that many of these larger particles were agglomerations of the finer particles [19]. Along with the fine and agglomerated particles, the spheres of iron ejected from the melt were also found to be present around 50 μm[19]. A study on BOS dust particle size distribution between two different, unnamed integrated steelworks in the USA showed differences in the main fractions of the dust, with one plant having a substantially larger fine fraction <75 μm than the other [40].

An investigation on BOS dust produced through the Port Talbot works (UK) showed variation in the particle size analysis throughout the blowing process [41]. A greater proportion of finer particles were generated during the blow than before or after.

These findings were also in agreement with that of Kelebek that showed the finer fraction of BOS dust contained a higher proportion of zinc than the coarser fractions [39]. The implication of this observation combined with SEM measurements observations sheds some light on the interaction of the ferrous material with the zinc vapor present immediately above the BOS vessel.

These observations of Zn enrichment of the finer fraction and zinc being present on the outer surface implies that the iron morphology is dictated by the mechanisms while zinc is still in the gas phase (see above). Once the gas stream has cooled sufficiently, Zn condenses onto the surface of the material as ZnO and then potentially goes on to react to form $ZnFe_2O_4$ at the Fe/Zn interface if the conditions are suitable.

2.4.5 Morphology

Kelebek et al. described the morphology of BOS dust, from scanning electron microscopy (SEM), as comprising a very heterogeneous mixture of particles [39], with sizes ranging from 3 μm to 100 μm (Figure 2.4a). Many of the finer particles are agglomerated to larger particles, differentiated as spheroidal and non-spheroidal (Figure 2.4b). Energy dispersive X-ray spectroscopy (EDS) showed a relatively uniform distribution of zinc across these particles. This information was used to determine that the Zn in BOS dust is localized almost entirely as a coating around an iron core.

This observation was confirmed through a cross-sectional analysis of a particle, showing a metallic iron core, surrounded by iron oxides and zinc oxide/zinc ferrite mixtures (Figure 2.4c). These observations were confirmed by other researchers [42], and are in agreement with the observations of two separate and distinct mechanisms of formation: finer more oxidized particles produced through volatilization of iron and much larger, highly metalized and globular particles generated from the solidification of liquid iron droplets ejected via the bubble burst mechanism.

Using SEM, Heinrich classified three distinct particle groups within Port Talbot BOS dust [41]. The first and most abundant is described as ‘fines’, particles sized around 5 μm. These are consistently produced throughout the blow period, and zinc content is distributed evenly throughout this fraction of the powder. Iron spheres were then described as the next most abundant. These are much larger (up to 500 μm) in diameter and contain less zinc than the finer fraction. The sizing of these particles corresponds well to theoretical calculations of the upper limit of the diameter of a liquid steel droplet to be ejected from steel, which was in the region of 500 μm [43] (Figure 2.5).

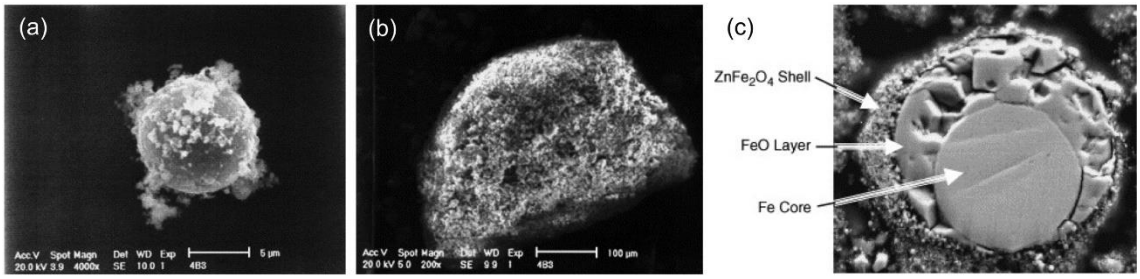

Figure 2.4. SEM images of (a) globular spheroid particle, (b) agglomerated particle consisting of submicron particles, and (c) cross sectional view of globular particle showing metallic Fe core. Adapted with permission from Kelebek et al., copyright Elsevier 2004.

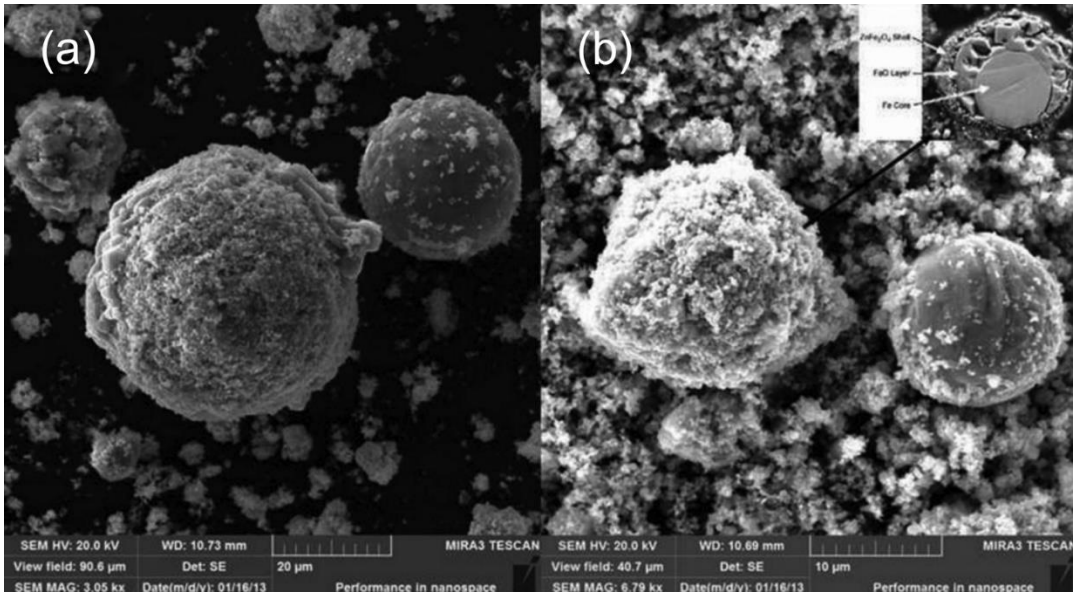

Figure 2.5. SEM images of ultrafine particles adhering to the exterior of larger, globular particles. Adapted with permission from Vereŝ et al., copyright Taylor and Francis 2015.

2.4.6 Chemical Analysis

The determination of the chemical composition of steelmaking materials is carried out via X-ray fluorescence (XRF) spectroscopy or atomic emission/absorption spectroscopy (AES/AAS). XRF is generally used for analysis for non-trace elements, or in siliceous samples such as in ore characterization, but for zinc determination in BOS dust, digestion of samples followed by inductively coupled plasma atomic emission spectroscopy (ICP-AES) is generally the preferred technique due to its sensitivity to low

concentrations and accuracy [44] with detection limits for solid samples as low as 2.5 ppm and 0.01 ppm respectively being achievable.

Typical metal analysis of BOS dust from literature is shown in Table 2.1, from which there is a great deal of variability in the overall composition of samples. This is particularly true in the case of zinc and iron content as these are the two key value drivers of metals recovery of BOS dust. Zinc content of BOS dust can be controlled substantially through the elimination of galvanized scrap's inclusion in the scrap charge to the furnace, will levels capable of reaching 0.1–0.2 wt. % Zn but total elimination of zinc from the material is extremely challenging because of the technical challenges of limiting zinc contamination in merchant scrap and residual levels of zinc within the hot metal itself (~50 ppm).

Table 2.1. Elemental abundance in samples of BOS dust (wt. %).

	Component (wt. %)						
Source	**Ca**	**Fe**	**Mg**	**Mn**	**Pb**	**Zn**	**Ref.**
Unknown	7.40	59.0	2.1	1.48	-	1.48	[45]
Dofasco Hamilton	-	61.0	-	-	-	1.59	[39]
Dofasco Hamilton	-	50.16	-	-	-	2.4	[32]
Tata Steel Port Talbot	-	-	-	-	-	4.8	[46]
Tata Steel Port Talbot	3.0-8.80	50.0-80.0	0.20-5.0	0.40-2.20	0.20-1.80	1.7-6.5	[41]
ArcelorMittal Monlevade (Brazil)	4.18	50.65	1.49	-	0.07	4.37	[47]
U.S. Steel Kosice (Slovakia)	5.5	49.87	2.68	-	0.24	9.37	[42]

EDX analysis also indicates magnesium and calcium are also present within BOS dust, which is likely the result of fine flux additions to the BOS vessel during processing blowing out through the off-gas system and being collected together with the metallic dust [42].

2.4.7 Phase determination

X-ray diffraction (XRD) analysis is a common tool for characterization of the crystalline phases in steelmaking raw materials, products, and wastes. It is a relatively insensitive tool with detection limits of around 1 wt. %. Quantitative analysis can be challenging as the technique is very matrix dependent but is still very effective for rapid crystallographic analysis.

When determining effective recycling solutions for BOS dust an important consideration is the chemical form of the zinc within the material. The two likely candidates are ZnO (zincite) and $ZnFe_2O_4$ (franklinite) and the relative abundance of

these compounds is of great significance. Unfortunately, Fe_3O_4 and $ZnFe_2O_4$ have very similar crystallographic unit cells (Fd 3 m) and the powder XRD patterns are nearly indistinguishable (Figure 2.6), which makes XRD a potentially unreliable measure of the zincite:franklinite ratio present in BOS dust and alternatives need to be explored. Nevertheless, powder XRD can still be a useful tool in exploring the phases present within BOS dust.

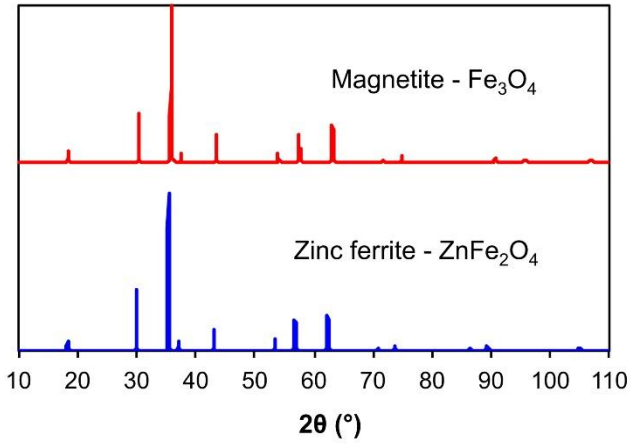

Figure 2.6. Calculated powder XRD patterns (using VESTA software) for magnetite (COD# 1011032 [48]) and zinc ferrite (COD# 9002487 [49]) showing the similarity in diffraction patterns and the difficulty in differentiation.

Table 2.2. Phases identified in BOS dust by powder XRD

Source	Phases present	Reference
Dofasco Hamilton	FeO, Fe_2O_3, $ZnFe_2O_4$	39
Not known	α-Fe, FeO, Fe_3O_4, Fe_2O_3, $CaCO_3$, SiO_2, ZnO	19
ArcelorMittal Méditerranée	Fe_3O_4, Fe_2O_3, $CaCO_3$, C	50
Port Talbot	α-Fe, FeO, Fe_3O_4, Fe_2O_3, $CaCO_3$, SiO_2, ZnO, $ZnFe_2O_4$, C	21
Port Talbot	α-Fe, FeO, $CaCO_3$, $ZnFe_2O_4$	51
Not known	Fe_3O_4, Fe_2O_3, $CaCO_3$, $Ca(OH)_2$, ZnO, $ZnFe_2O_4$	45
U.S. Steel Kosice (Slovakia)	α-Fe, FeO, Fe_3O_4, Fe_2O_3, ZnO, $ZnFe_2O_4$	42

Reports of the phases present within BOS dust are tremendously varied, which reflects how substantially the conditions within the BOS vessel and off-gas system can affect the chemistry of the by-product. Table 2.2 shows a selection of phases identified by different authors from steel plants across the world. It is clear from Table 2.2 that the morphology of BOS dust is drastically variable from plant to plant and even based on the age of the dust that's analyzed and the environment the material was stored in.

The difference between closed and open flue gas hood systems, referred to as suppressed and complete combustion, was investigated using powder XRD [52]. The differences in the crystalline phases present are stark. In closed hood systems the dust is far more metalized, with most of the iron present existing in the metallic form (Fe°) or as FeO (i.e., Fe^{II}), while the calcium is present as $CaCO_3$ (calcite). In the open hood systems, where the BOS gas is combusted fully before dedusting [32], the dust is as expected, much more oxidized. Iron exists principally as Fe^{III} or mixed Fe^{II}/Fe^{III} oxides (Fe_2O_3 and Fe_3O_4, respectively), and the calcium tends to be present as CaO rather than the carbonate. It is likely that the conditions in an open hood off-gas system would favour the formation of $ZnFe_2O_4$ as high temperatures and oxidizing conditions are typical for the production of Franklinite [53].

It has been reported that dust from the Port Talbot (UK) plant, that has been stored outdoors for a number of years, showed significant oxidation of iron to Fe_3O_4 and Fe_2O_3 compared to a more recent sample [21]. Such 'weathering' is to be expected during outdoor storage.

Calcium in the form of $CaCO_3$ and CaO is added as a refining flux to the BOS process and calcium compounds are identifiable in BOS dust as a result. In the heat of the BOS vessel some CaCO3 decomposes to CaO via Equation 2.10

$$\mathrm{CaCO_3} \longrightarrow \mathrm{CaO} + \mathrm{CO_2} \qquad (2.10)$$

In the off-gas system, any CaO reacts with CO_2 present and reforms $CaCO_3$ via the reverse reaction. It is worth noting that this carbonation of CaO happens readily within the off-gas system and not as part of the weathering process during storage. Heinrich evidenced this in-situ carbonization through the use of a novel slurry sampling system that showed calcium in BOS dust produced moments prior was already in the form of $CaCO_3$ [41].

Figure 2.7 shows the calculated dominant phases at 1000 K (approximate BOS gas temperatures within the off-gas system). As the ratio of the partial pressures,

P_{CO}/P_{CO2}, approaches zero as combustion of carbon monoxide nears completion the dominant zinc phase changes from ZnO to $ZnFe_2O_4$.

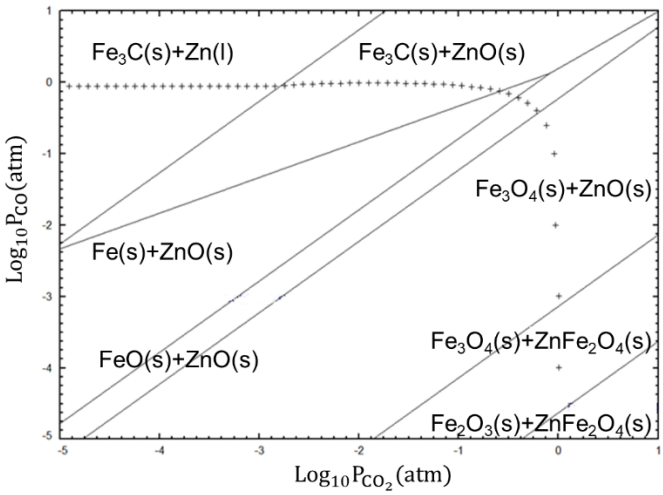

Figure 2.7. Predominance diagram for the Zn-Fe-CO-CO_2 system at 1000K. Calculated using FactSage 7.3 (Isobar (+) at 1 atm).

SiO_2 reported in some samples has likely been introduced into the sample from the splashing of BOS slag during the process [19]. Graphitic phases have been reported in a number of studies [21,50] and these could correspond to the introduction of 'kish' to the sample in the process. As carbon-saturated iron cools the solubility of carbon decreases and a layer of graphite can form on the surface of the liquid in a foliated dendritic structure [54]. This graphite is known in the steel industry as 'kish' and could be introduced into the BOS off-gas system during charging of pig iron, as kish is prone to become airborne due to its low density.

2.4.8 Mössbauer spectroscopy

Mössbauer spectroscopy has historically been used to characterize oxidation states of iron within iron ores [55], as well as a range of other iron containing materials [56–58]. While providing insight into the oxidation state and chemical environment of iron within a sample of BOS dust, its principal use in the study of BOS dust is its ability to indirectly differentiate ZnO from $ZnFe_2O_4$ [42]. This ability to differentiate between ZnO and $ZnFe_2O_4$ has huge implications for metallurgical separation, as $ZnFe_2O_4$ is significantly more refractory to hydrometallurgical recovery [59].

^{57}Fe Mössbauer spectroscopy was used to confirm the chemical environments in which iron was present in the sample. Franklinite was positively confirmed by the

presence of a central doublet in the spectrum [42]. Total Fe and Zn content was confirmed through digestion and subsequent Atomic Absorption Spectroscopy. The ratio of ZnO to $ZnFe_2O_4$ could then be calculated and for the BOS dust used in the study, the sample was 13.47 wt. % $ZnFe_2O_4$ and 7.10 wt % ZnO. This suggests that the ratio of zinc existing in the ZnO:$ZnFe_2O_4$ forms is 60:40; however, it is critical to note that from the work in question it is unclear whether the plant in Slovakia that the dust was generated by has an open or closed hood off-gas system [42].

The abundance of higher Fe oxides and lack of metallic iron present within the sample, would suggest a combustive process, which may lead to a greater degree of zinc existing in the franklinite form.

Mössbauer spectroscopy shows tremendous potential for the analysis of zinc in steelmaking wastes as the ZnO/$ZnFe_2O_4$ ratio has huge implications for extractive process selection, see below.

2.5 Pyrometallurgical Separation Techniques

Based upon a thermodynamic modelling study[60] it was proposed that a range of operating regimes and choice of process were feasible for the pyrometallurgical treatment of BOS dust to remove the zinc (and other volatile elements) and reuse the iron as hot metal, metallized clinker or iron oxide clinker. As such pyrometallurgical processes for removal of zinc from steelmaking by-products are somewhat well established and offer some attractive features such as good scalability and (generally) continuous processing.

Pyrometallurgical separation plants are, however, usually capital intensive, with high setup costs and energy demand. Consequently, in the case of separation of iron and zinc in steel by-product recovery, carbothermal reduction and separation by volatilization is the industry standard. An obvious downside of carbothermal reduction is the production of CO_2 as an intrinsic product of the process, creating greater carbon emissions to an industry already having to struggling to meet the challenges of decarbonization [22,23,61,62]. Pyrometallurgical plants also generally produce a large amount of dust and noise, which must be taken into consideration when assessing plant feasibility.

The relatively high volatility of zinc relative to iron means that it can be physically separated from BOS dust by heating under reducing conditions. Carbon is

gasified through the reverse Boudouard reaction (Equation 2.11) and then ZnO is reduced to elemental Zn vapor by carbon monoxide (Equation 2.12).

$$C + CO_2 \longrightarrow 2CO \tag{2.11}$$

$$ZnO + CO \longrightarrow Zn + CO_2 \tag{2.12}$$

Zinc in the vapor phase readily oxidizes in the presence of CO_2 to reform ZnO via the reverse reaction. Zinc ferrite reduces in a similar fashion, reacting with CO (Equation 2.13) or thermal decomposition of ZnFe2O4 to ZnO (Equation 2.14) between 719 °C and 1050 °C [63].

$$3ZnFe_2O_4 + 4CO \longrightarrow 3Zn + 2Fe_3O_4 + 2CO_2 \tag{2.13}$$

$$ZnFe_2O_4 \longrightarrow ZnO + 2Fe_2O_3 \tag{2.14}$$

Under hot, reducing conditions such as these, reduction of iron oxides also occurs, which is very favorable for ferrous recovery, because a semi-metalized iron product from the separation process has considerable benefits for an integrated steelworks. Direct reduced iron (DRI), or sponge iron, can be directly charged into the iron making process, thus reducing reductant rates within the blast furnace, displacing expensive coke, and improving the process economy [64].

DRI can be produced in a variety of ways, including countercurrent shaft furnaces utilizing reformed natural gas, fluidized beds and others [65,66], but the critical consideration for processing zinc-bearing materials is the direction of gas flow relative to the direction of the oxidizing gradient. To prevent condensation and recirculation of zinc within the furnace, the oxidizing gradient direction must be perpendicular to the material flow direction: to carry condensed zinc oxide away from the ferrous burden. This effectively rules out the counter-current natural gas reduction units such as the Midrex® process often used to produce DRI at mine sites [67]. Figure 2.8 provides an outline of the process [68].

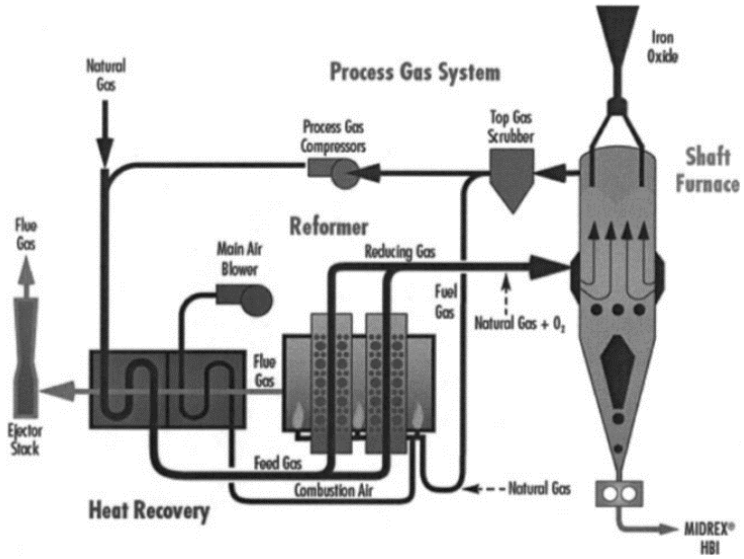

Figure 2.8. Simplified schematic process flow for a two-stage natural gas DRI plant such as Midrex® (reproduced with permission from Fruehan 2005. Copyright Taylor and Francis).

Solid based reduction processes are much more effective in the processing of zinc-bearing by-products. Common reductant sources include coke breeze, pulverized coal, and carbon-bearing revert material such as BF dust [69]. Table 2.3 compares gas direct reduction and solid fuel direct reduction to conventional blast furnace pig iron production. Seeing as both the gas-solid and blast furnace are both unsuitable for Zn bearing by-products such as BOS dust this review will only discuss in detail the solid-solid DRI producing processes that can tolerate high zinc loadings.

Table 2.3. Comparison of DRI Production processes with traditional blast furnace production.

Use	Blast furnace iron making	Gas-solid direct reduction	Solid-solid direct reduction
Reducing agent	Coke, can be supplemented with pulverized coal/tar injection	Reformed natural gas, by-product gases such as coke oven gas (COG)	Coal, coke breeze, carbon-bearing revert material
Ferrous input material	Sinter, ore, DRI. Low volatile metal content is critical	Limited to ore, volatile metal loading similar to a blast furnace	Flexible: ore, waste oxides, etc. Volatile metals are not restricted
Input material form	No fine material, pellets/lump ore. Must have sufficient strength to withstand furnace conditions	Pellets, lump, some processes utilize fine material such as fluidized bed processes	Pellets or fine material, depending on the specific process
Furnace design	Large vertical shaft furnace, charged from the top with a hot blast fed in through tuyeres at base	Typically, a vertical shaft furnace	Rotating kiln or rotary hearth furnace
Product	Molten pig iron	Direct reduced iron	Direct reduced iron or Waelz slag depending on the process
Product quality	Very high quality, complete separation of Fe and gangue. Slag formed has some desulfurizing capacity	Usually excellent quality depending on the quality of the ore and reducing gas	Dependent on feedstock material and coal quality. Usually unsuitable for EAF/BOS use due to high S and gangue content

By-products	Liquid slag, dusts, caloric off-gas which can be reused to heat stoves	Caloric off-gas which can be combusted to heat process, dusts	Off-gas fully combusted in situ, baghouse dust contains ZnO product suitable for sale

2.5.1 The Waelz Kiln

One of the oldest treatments for zinc containing dusts, the Waelz process, involves the heating of dust mixed intimately with a carbon fuel, then heated >1000 °C in a rotating kiln, and fired by a burner at the exit end of the tunnel (Figure 2.9).

A typical Waelz kiln is around 50–70m long with a diameter of 4–5 m. The zinc containing compounds are reduced, volatilized, and consequently re-oxidize in the gas stream, thus, separating the zinc from the ferrous material. The charge for the furnace is prepared by pelletizing and is charged at the top (entry end) of the furnace, as the drum rotates the burden transits down the drum and reacts with the reducing gas generated from the carbon source. The process has several disadvantages, such as long retention times of up to 8 h that lead to very low productivity.

Typically, Waelz kilns found use in the recovery of zinc from EAF dust or zinc ores with a mineral content too low for more traditional mineral dressing [70]. Waelz kiln processing is globally well established with over 1 million tons of capacity for EAF dust in the late 1990s [71,72], which increased to the 3.4 million tons of EAF dust capacity across 35 kilns currently operating globally [73]. However, the Waelz kiln cannot economically process material lower in zinc than around 10 wt. %, due to the relatively low value of the iron-bearing product and the thermal inefficiency of the process.

Table 2.4 shows a typical chemical analysis from a waelz kiln of the input material (EAF dust), the ferrous product and the zinc-rich ‘waelz oxide’ collected through the off-gas dedusting system. Often fluxes are added to the infeed to manage slag chemistry and prevent accretions or ‘slag rings’ forming within the kiln at specific thermal zones. These rings or accretions can reduce productivity through disruption solid material flow through the furnace, attacking refractory and increase maintenance costs. Of course, the addition of fluxes in the form of mineral oxides are not a perfect solution however, as introducing gangue material into the ferrous burden decreases its value in use for recycling purposes.

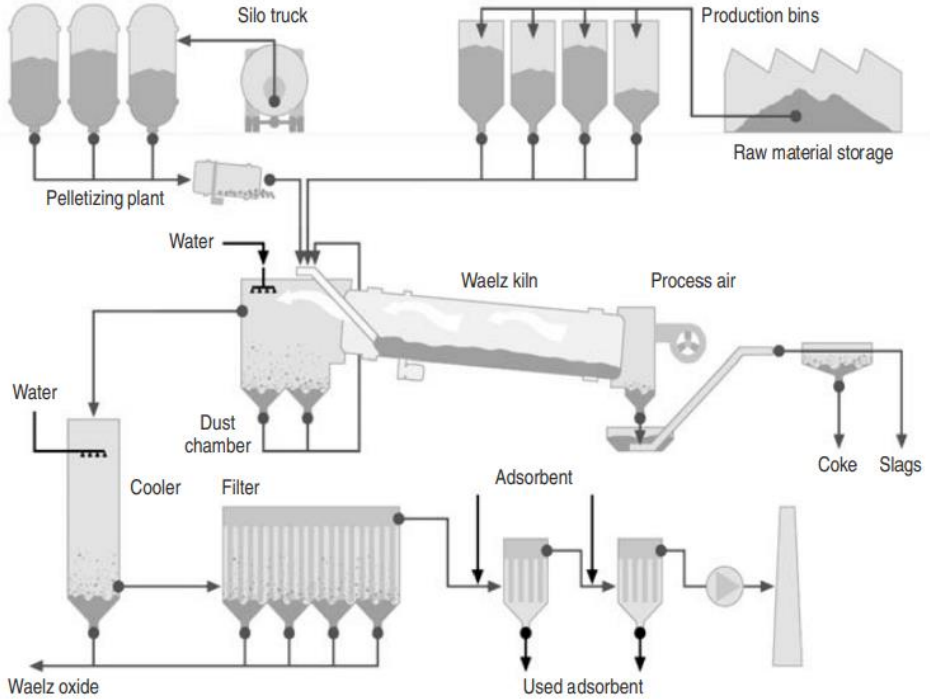

Figure 2.9. Schematic representation of the Waelz Kiln process (Reproduced with permission from Mager et al. [72], copyright Springer-Verlag).

Table 2.4. Chemical analysis (Wt. %) of the inputs and products of the Waelz Kiln process [72].

Element or compound	EAF dust (Wt. %)	Ferrous product (Wt. %)	Waelz oxide (Wt. %)
Zn	18.0 – 25.0	0.2 – 2.0	55.0 – 58.0
Pb	2.0 – 7.0	0.5 – 1.0	7.0 – 10.0
Cd	0.03 – 0.1	<0.01	0.1 – 0.2
F	0.2 – 0.5	0.1 – 0.2	0.4 – 0.7
Cl	1.0 – 4.0	0.03 – 0.05	4.0 – 8.0
C	1.0 – 5.0	3.0 – 8.0	0.5 – 1.0
FeO	20.0 -38.0	30.0 – 50.0	4.0 – 7.0
Fe_{met}/Fe	-	80.0 – 90.0	-
CaO	6.0 – 9.0	15.0 – 25.0	0.7 – 1.2
SiO_2	3.0 – 5.0	6.0 – 12.0	0.5 – 1.0
Na_2O	1.5 – 2.0	1.2 – 1.6	0.1 – 0.2
K_2O	1.0 – 1.5	0.7 – 0.9	0.1 – 0.2

2.5.2 The Rotary Hearth Furnace

Initially patented in the 1960s the rotary hearth furnace process takes advantage of the high reaction speeds afforded through the firing of self-reducing composite pellets of iron oxide and carbon. A rotary hearth furnace (RHF) consists of a circular turntable rotating inside of a refractory lined tunnel (Figure 2.10). Heat is supplied by natural gas or pulverized coal burners, but most of the process heat comes from the combustion of the carbon source within the charge itself. The gas flow is counter-current to the material flow so hot process gases can preheat the freshly charged pellets, resulting in good heat exchange and thermal efficiency.

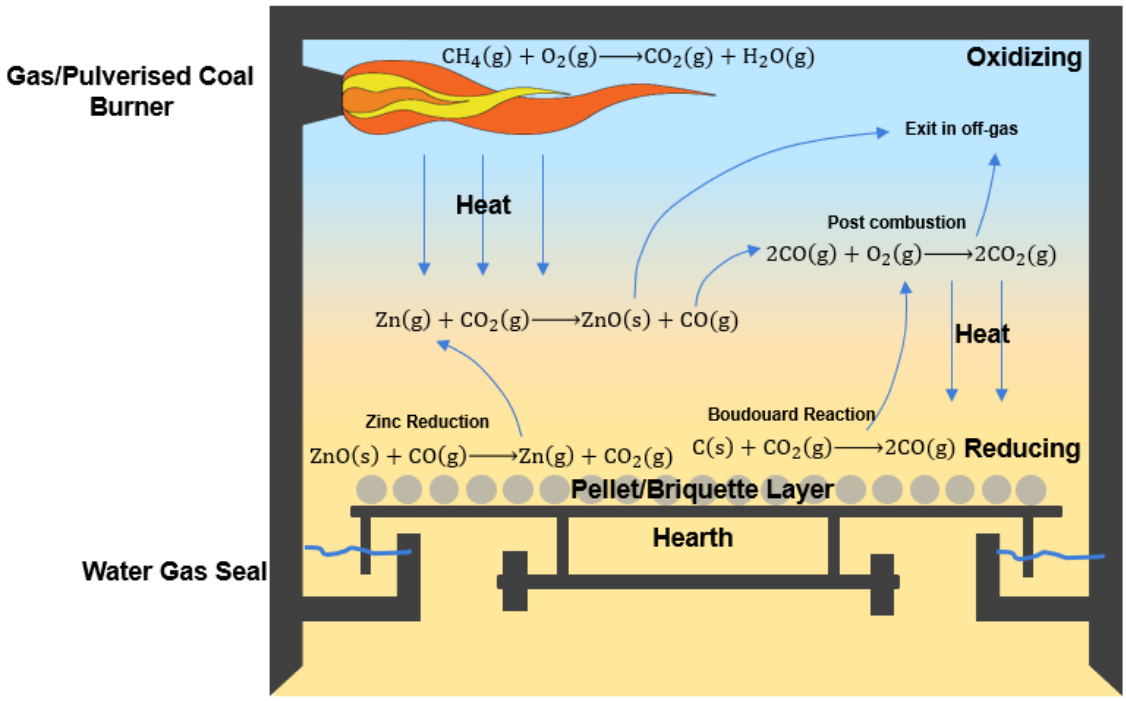

Figure 2.10. A schematic cross-sectional view of the zinc removal mechanism in the rotary hearth furnace (RHF).

RHFs can accommodate a far wider range of materials than a BF, due to the lack of vertical loading of the furnace burden. In the BF, pellets nearer the bottom of the stack must support the mass of the burden above it. Typically blast furnace pellets must have a cold compression strength of >2450 N per pellet to withstand the compressive load of the furnace [74]. In the RHF, the burden layer is at most 3 pellets thick. As such it is permissible to charge materials with far less compressive strength: >40 N per pellet is acceptable to be charged to the furnace.

Table 2.5. Principal chemical reactions occurring in a rotary hearth furnace.

Process stage	Reaction	Equation
Gasification of carbon	Devolatilization of coal	coal $\rightarrow H_2, H_2O, CO, CH_4$
	Combustion	$C + O_2 \rightarrow CO_2$
	Boudouard reaction	$C + CO_2 \rightarrow 2CO$
	Water gas shift	$CO_2 + H_2 \rightarrow CO + H_2O$
Zinc removal	Carbothermal zincite reduction	$ZnO + CO \rightarrow Zn + CO_2$
	Zinc ferrite thermal decomposition	$ZnFe_2O_4 \rightarrow ZnO + 2Fe_2O_3$
	Zinc ferrite reduction	$3ZnFe_2O_4 + 4CO \rightarrow 3Zn + 2Fe_3O_4 + 2CO_2$
	Reduction of zincite by hydrogen	$ZnO + H_2 \rightarrow Zn + H_2O$
Iron reduction	Carbothermal reduction of iron	$Fe_2O_3 + CO \rightarrow 2Fe_3O_4 + CO_2$ $Fe_3O_4 + CO \rightarrow 3FeO + CO_2$ $FeO + CO \rightarrow Fe + CO_2$
	Reduction of iron by hydrogen	$Fe_2O_3 + H_2 \rightarrow 2Fe_3O_4 + H_2O$ $Fe_3O_4 + H_2 \rightarrow 3FeO + H_2O$ $FeO + H_2 \rightarrow Fe + H_2O$
Iron carburization	Gas carburization	$3Fe + 2CO \rightarrow Fe_3C + CO_2$
	Solid carburization	$3Fe + C \rightarrow Fe_3C$

A key advantage of the RHF over the Waelz kiln is an increase in the quality of the ZnO product due to the lower contamination with fine iron material, due to the large pellets not abrading against each other to generate excess iron fines. Excessive contamination of iron is undesirable for zinc reprocessing purposes. The addition of fluxes is usually also unnecessary allowing for increased furnace productivity and a higher value DRI product.

2.5.3 FASTMET®

Developed by Kobe Steel, FASTMET® is one of the most commercially established RHF processes globally, with around a million tons of steelmaking waste processing capacity spread across six plants in Japan [75]. Figure 2.11 shows a schematic of the FASTMET® process flow.

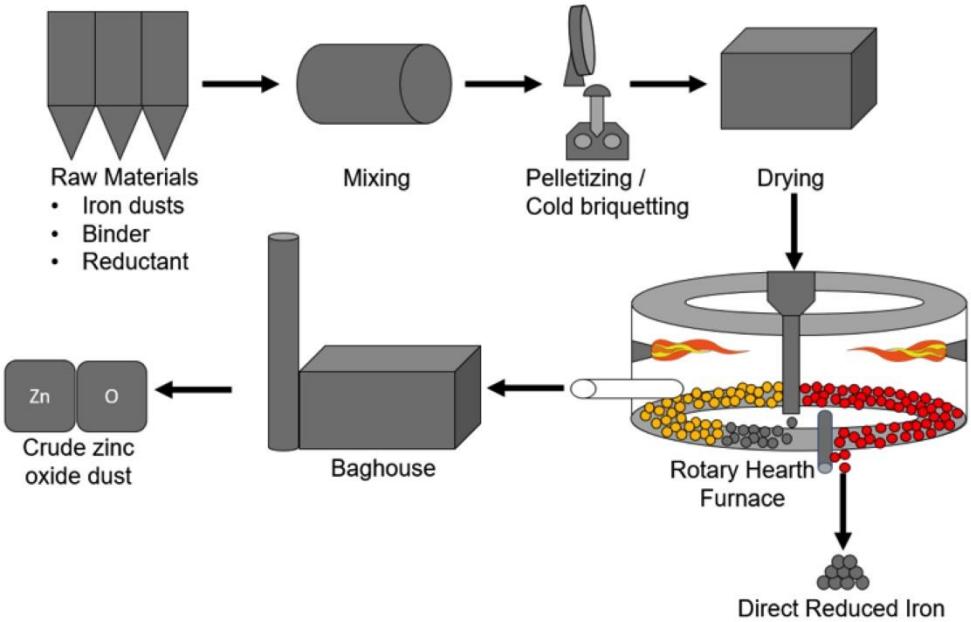

Figure 2.11. Simplified schematic of the FASTMET® process flow.

Pellets are produced by the blending of iron bearing material with a stoichiometric amount of carbon (coal, coke breeze, or carbon-bearing revert material) with a binding agent. These pellets are charged in one or two layers onto the hearth floor. The composite pellets are then heated to around 1300-1350 °C and over the course of 8-16 minutes react and are discharged via a water-cooled rotating screw. Hot DRI is discharged from the exit end of the furnace which can either be held in nitrogen purged canisters for hot charging to the EAF melt shop or turned into hot briquetted iron (HBI). HBI can then be more readily stored for later use in a blast furnace.

An important acknowledgment of the typical product chemistry (Table 2.6) is the sulfur content of the DRI produced from by-product material. Often DRI produced from recycled materials is unfit for recharging directly into the BOF due to sulfur limitations, instead of being routed to the blast furnace. While this does indeed recycle the ferrous material into hot metal, DRI has a lower value in use when charged to the BF than the BOF as a scrap replacement.

Table 2.6. Typical chemistry of steelmaking by-product input and DRI output of a FASTMET RHF [66]

Material	Fe (wt. %)	FeO (wt. %)	C (wt. %)	S (wt. %)	Zn (wt. %)	Fe_{Met}/Fe
BF dust	40.1	19.2	31.0	0.42	0.01	-
BF Sludge	33.0	10.6	31.4	0.49	0.14	-
BOS Sludge	63.2	64.4	0.74	0.1	0.43	-
Fastmet DRI	70.5	-	1.13	0.35	0.004	95%

Variants of FASTMET® such as FASTMELT® incorporate a DRI melting unit to produce hot metal directly using a submerged arc furnace, however these units have an increased energy demand and would likely be uneconomical for use within an integrated works.

2.5.4 The INMETCO process

The INMETCO (International Metals Reclamation Company, Inc.) process is very similar to FASTMET®, in that it also utilizes cold bonded carbon-iron oxide material composite pellets as feedstock to a rotary hearth furnace. Typically for INMETCO 20-25 % volatile content coal is used as a reducing agent.

The process was initially developed to processing stainless steelmaking wastes for Ni and Cr recovery[76], but its scope also extends to Zn recovery from EAF dust. The key point of difference between FASTMET® and INMETCO is the number of pellet layers charged to the furnace simultaneously (Figure 2.12). INMETCO utilizes a multiple layer system around 30 mm in depth (and accordingly has a higher furnace residence time for the material) whereas FASTMET® is operated on a monolayer basis.

Multiple layers of pellets can lead to inhomogeneity of the DRI product, with the top layers reacting substantially quicker than the base layer; however, the thermal load on the furnace hearth is lower than in monolayer processes.

The process is also highly dependent on green pellet strength as not only must the pellets survive the manual handling required to charge them to the furnace, but they must also have sufficient strength to handle the weight of pellets above them as well as the rapid vaporization of the contained moisture and volatiles within the composites.

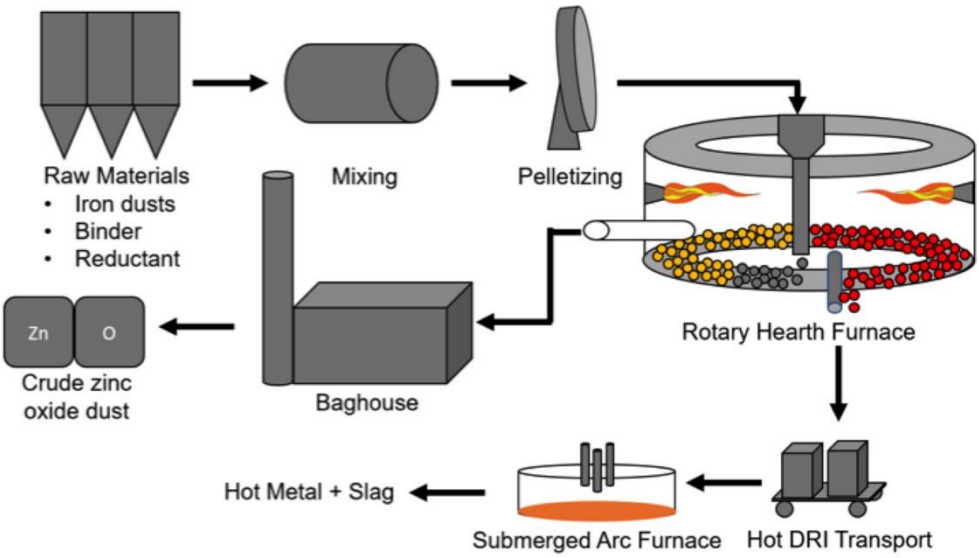

Figure 2.12 Simplified schematic of the INMETCO process flow.

The only commercial plant operating the INMETCO process is in Ellwood City, PA[77] and has been in continuous operation since 1976 processing stainless steel wastes. This plant is integrated into a submerged arc furnace unit that converts the DRI produced into hot metal, which is subsequently cast into ingots suitable as feedstock for the stainless-steel industry. The Ellwood city plant produces 20 kt of pig iron ingots per annum, with a raw material capacity of 50 kt per annum[78]. Zinc is effectively eliminated from the output material partially due to the RHF reduction step and due to the iron smelting step in the submerged arc furnace.

2.6 DRyIron ™ process

The DRyIron™ process is again, very similar to FASTMET® and INMETCO. The fundamental difference is that DRyIron™ is fed exclusively by cold briquetted material (Figure 2.13) and has found commercial use preparing DRI from BOS dust and blast furnace dust. Global capacity for this process is currently around 1.25 mt per annum [79], making DRyIron™ one of the most commercially successful rotary hearth furnace processes. This capacity is almost entirely concentrated in the East Asian steel industry in countries such as South Korea, Japan, and China following the closure of plants in the USA in the early 2000s.

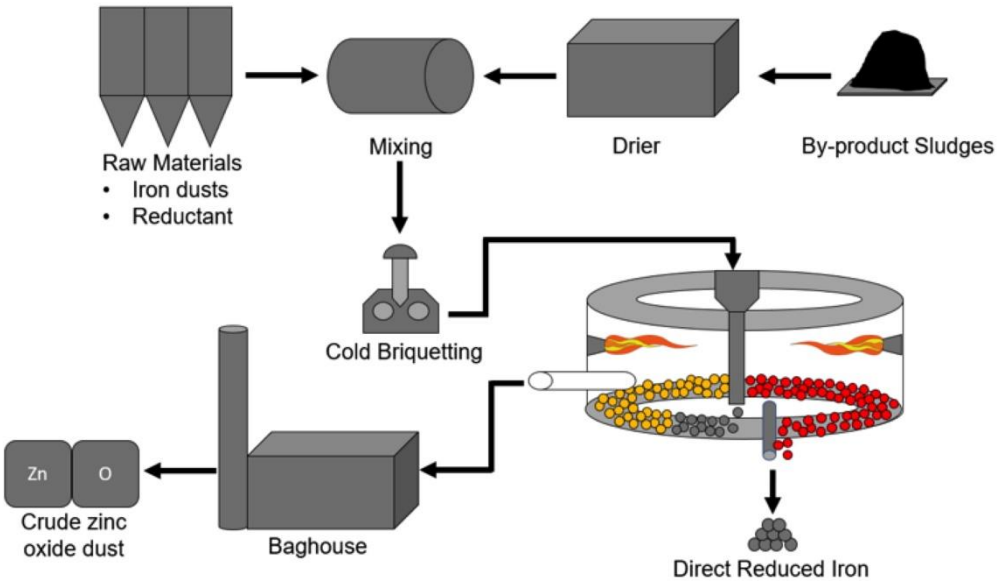

Figure 2.13. Simplified schematic for the DRyIron™ process flow.

The reason for the favorability of the DRyIron™ process for handling of zinc bearing wastes from an integrated steel plant is that cold briquetting processes can utilize exceptionally fine material and produce a product with consistent size and density. With regard to zinc removal, this is critical as a tight size and distribution of in feed material ensures consistent and homogenous zinc removal, which is vital to ensure the recyclability of the DRI produced to the blast furnace.

DRyIron™ also does not utilize a binder in the briquetting process. Binder-less briquetting has two key advantages: reduced preparation costs and reduced gangue in the DRI product. Metallization levels of 95% are achievable in short residence times of 10-15 minutes and residual levels of P and S in the DRI can be managed through reductant selection [66,80].

Unlike the FASTMET® process, material is dried prior to the agglomeration step rather than after forming. This can provide advantages with the consistency of the forming process, as steelmaking by-product dusts can be tremendously variable depending on the method by which they were scrubbed from off-gas (venturi scrubbers versus electrostatic systems) and their storage conditions.

The produced DRI from DRyIron™ is around 80% metallized and are suitable for hot charging to an EAF, or under controlled inert cooling conditions can be subsequently used in the blast furnace depending on raw material selection.

2.7 ITmk3

ITmk3 is an evolution of the FASTMET® and FASTMELT® processes developed by Kobe Steel and is based on the rotary hearth furnace. The fundamental difference between ITmk3 and other rotary hearth furnaces, is that the furnace is run between 1400-1450 °C and through management of slag chemistry, rapid in-situ smelting of iron and generation of a liquid slag occurs. This is a vast departure from the purely solid-state reduction that takes place within FASTMET® and the result is nuggets of gangue free pig iron and a wholly separate slag that is mechanically separable.

There has only been one commercially operating ITmk3 plant worldwide, in Hoyt Lakes, MN, USA through a joint venture between Kobe Steel and Steel Dynamics. This 500 kt per annum plant began operation in 2010 but is under a long-term mothballing as of writing [81]. The Hoyt Lakes plant, known as Mesabi Nugget, was based upon the commercial principal of producing a high value-added iron product at close proximity to the mining site. This provides obvious logistical advantages as the iron nuggets produced are around 50% lighter and 90% more compact than the equivalent ferrous load in ore. As shown in Table 2.7, these iron nuggets are chemically very similar to blast furnace pig iron and were successfully used to displace scrap in electric arc furnaces [82].

Table 2.7. Comparison of ITmk3 pig iron nuggets [81] versus BF pig iron

Material	C (wt. %)	Si (wt. %)	Mn (wt. %)	S (wt. %)	P (wt. %)	Fe_{Tot}
Iron nugget	2.5-4.3	0.2	0.1	0.015	0.06	Bal.
BF pig iron	4.76	0.58	0.3	0.005	0.08	Bal.

The ITmk3 process was developed for use on iron ore but the RHF reactors ability to handle material that contains high quantities of volatile metals such as zinc could mean it is applicable for adding value to steelmaking by-products[83]. There would be several advantages to producing pig iron nuggets versus a DRI product, the gangue content in revert DRI is relatively high and as such it is typically recycled to the BF rather than as a scrap replacement in the BOF.

Another key advantage of utilizing the by-products of an integrated works for this process is that both the carbon source and iron source are effectively free, as BF and

BOS dust respectively could be used. There are also CO_2 emission and energy saving advantages for ITmk3, when compared to a small-scale blast furnace, of 38.6% and 14.3% per ton of pig iron produced, respectively [67]. This saving in energy and emissions are afforded by the total combustion in-situ of the process gas; however, the immensely variable chemistry of by-product materials as well as contamination with very high melting point mineral oxides such as Al_2O_3 could render an ITmk3 process unfeasible for the recovery of iron from BOS dust.

The optimal size of an ITmk3 plant in terms of benefitting from economies of scale appears to be around 500 kt per annum. This is a very large volume with regards to steelmaking dust production considering a 10 mt per annum integrated steelworks would produce approximately 200 kt total BF and BOS dust annually. This lack of supply of ferrous material at a single site for the process could be mitigated through centralizing a large ITmk3 unit in a steel production intensive region such as China's Hebei province where a great deal of BOS and BF dust is generated in proximity. On the other hand, western countries where the steel industry has declined substantially, such as the United Kingdom, has left a legacy of large stockpiles of these materials which were simply unable to be economically recovered. The exact quantity of material in these stockpiles is not accurately known but is estimated to be extensive[84]. Accurate quantification of a region's ferrous assets locked away in these stockpiles will be critical for assessing the feasibility of any zinc separation technology.

2.8 Hi-QIP

The high-quality iron pebble process (Hi-QIP) is chemically speaking very similar to ITmk3, in that it involves direct smelting of iron to generate so called 'pebbles' of iron and a separate slag phase. The key difference, however, is in Hi-QIPs use of a non-agglomerated iron feed material mixed with fluxes and a reducing agent, contained within hollows that are depressed mechanically into a carbonaceous bed on the furnace.

This carbon layer has four key functions; the hearth is protected from direct contact with aggressive molten slags, the thermal load on the refractories is lessened, and it acts as an auxiliary reducing agent. Finally, it also determines the geometry of the iron pebbles through control of the size of the hollows. The primary reactor in the Hi-QIP is also a rotary hearth furnace, heated to around 1500 °C with a residence time of 15-20 minutes. Critically, Hi-QIP has previously been deemed suitable for the processing of BF dusts at an integrated works [85].

A pilot plant operated in Japan in the early 2000's with reasonable results and capacity of 15 tpd. The chemistry of the produced iron pebbles is shown in Table 2.8. They are very chemically similar to ITmk3 pig iron nuggets as well as BF pig iron, but the sulfur level would be a cause for concern for reintroduction to the BOF[85]. It is likely this high sulfur level is the result of reductant selection. The coal used in the study was 0.54 Wt. % sulfur with the intimate contact between the carbonaceous bed and liquid iron causing sulfurization of the hot metal.

Table 2.8. Chemical analysis of Hi-QIP iron pebbles [86].

Material	C (Wt. %)	Si (Wt. %)	Mn (Wt. %)	S (Wt. %)	P (Wt. %)	Fe_{Tot} (Wt. %)
Hi-QIP Pebbles	2.1 – 3.0	0.08	0.01	0.25	0.04	Balance

Table 2.9 shows the chemical analysis of the BF dust used in comparison to the iron pebbles produced [85]. Zn removal was exceptional, with the residual levels of zinc within the iron produced being below the detection limit of the analysis used. This is obviously very promising for the Hi-QIP processes application in managing iron bearing wastes from an integrated works.

More research must be undertaken to reduce the sulfur and phosphorous residual levels within the metal as they would likely render the iron product produced from by-product materials totally unusable as a scrap replacement in the BOS process, which is very sensitive to input sulfur levels.

Table 2.9. Chemical composition (wt. %) of the BF dust alongside iron pebbles produced at 1550 °C for 555 seconds[85].

	Composition (Wt. %)													
Material	**C**	**Fe_{Total}**	**Zn**	**Pb**	**Na**	**K**	**Cl**	**SiO_2**	**Al_2O_3**	**CaO**	**MgO**	**Mn**	**P**	**S**
BF dust	21.3	42.9	2.54	0.64	0.11	1.2	1.13	5.67	3.25	3.12	0.37	0.26	0.07	0.91
Slag	-	5.8	0.02	-	-	-	-	34.0	18.2	34.3	3.42	0.92	-	-
Iron pebble	0.93	Bal.	<0.01	<0.01	-	-	-	-	-	-	-	0.02	0.13	0.72
Off-gas dust	0.68	6.66	47.1	7.02	0.22	1.95	13.2	0.20	-	-	-	-	-	2.34

Unfortunately, there are other drawbacks to the Hi-QIP process relating to the non-agglomeration of the furnace burden. The levels of iron in the collected zinc bearing secondary dust in the process are high (6.66 Wt. %) which may be unacceptable to zinc smelters without further refinement. An agglomerated bed also has poor gas permeability and heat transfer properties, which may offset any productivity bonuses given through denser hearth loading. There is also the potential for yield losses within Hi-QIP due to the separation stage, through solution loss of iron as FeO into the molten slag phase; however, this can be mitigated through increased hold times and reductant levels and iron yields of 97% were shown to be achievable [87].

Reduction temperatures in Hi-QIP are very high (up to 1550 °C), even compared to the relatively high temperature ITmk3 (1450 °C) process. This will obviously have implications on the operational costs of the plant, but the exceptional zinc removal and high value ferrous product may still prove attractive for reintegration of zinc bearing wastes to the iron material cycle.

2.9 COMET Process

The COMET process is another variant on the RHF process developed by the Centre for Research in Metallurgy (CRM), utilizing a non-agglomerated iron ore mixture in alternating layers with a reducing agent and a desulfurizing agent such as limestone[88]. Process temperatures in the COMET process are similar to those in INMETCO and FASTMET®, but typically residence times are higher and productivity therefore lower, in the former, due to the non-agglomeration of the feed.

Following the reduction step, DRI is formed in a sheet of about 10 mm in thickness (relating to the thickness of the ore layer in the original charge), which is broken apart and screened from the other discrete layers. The non-agglomeration provides a few key process advantages, which may make it attractive. Firstly, the removal of the pelletization step removes an element of operational cost from the plant as well as removing the need for a binder. Secondly, the discrete layers allow for the inclusion of a desulfurizing agent such as limestone, which is separable from the DRI product.

As a result, sulfur concentration in COMET DRI is usually very low, and less dependent on reductant selection. This is an advantage for sulfur sensitive DRI end uses such as BOF or EAF steelmaking. The lack of intimate contact between the carbon and iron layers also reduces the overall level of gangue within the direct reduced iron, as

coal ash is not introduced into the material. Table 2.10 shows typical chemical analysis for COMET DRI produced from virgin ore.

COMET DRI is clearly of a superior quality to other coal based RHF processes in terms of sulfur and gangue content, but this advantage comes at a productivity cost, the material in the COMET process has a residence time of approximately 80 min, whereas FASTMET® operates at around a 12 min residence time [89].

COMET is also suitable for processing zinc and lead bearing by-products and the reducing agent layer is also suitable for recycling in an integrated steelworks through a sinter plant. The COMET process has yet to be scaled to commercial operation, it seems unlikely that the benefits of lower sulfur and gangue content in the DRI product, and the lack of an agglomeration stage is substantial enough to offset the reduction in productivity.

Table 2.10. Typical analysis of COMET DRI [90].

Material	C (wt. %)	SiO_2 (wt. %)	S (wt. %)	Fe_{Tot} (wt. %)	Fe_{Met} (wt. %)
COMET DRI	0.2	1.86	0.032	95.8	88.1

2.10 Zinc recovery focused pyrometallurgical extraction processes

All of the above-mentioned processes have focused principally on the removal of zinc from an iron product to allow for the iron to be recovered through steelmaking. As such, zinc in every process discussed thus far is recovered as a crude ZnO, usually slightly contaminated by iron dust. This section highlights technologies designed to produce metallic Zn as a primary product.

Due to the much higher zinc content of EAF dust compared with BOS dust, most of this research on value generation from producing metallic zinc took place on EAF dust; however, the data provides insight to applicability for BOS dust. The principle challenge for the economic recovery of zinc from BOS dust is that the zinc content is so low that many processes designed to maximize the value of the zinc product of separation are simply not viable due to increased processing costs.

Electrothermic processes based on traditional zinc extraction from ore are a commercial reality, however, they typically consist of repurposed facilities retrofitted to handle steelmaking dusts. Due to the low zinc content of steelmaking dusts relative to virgin zinc ores and the capital outlay to set up and maintain them, it is highly unlikely that these types of processes will expand into BOS dust recycling. Typically, these processes are characterized by very high process costs either due to their discontinuous nature, high electricity requirements or complex design.

The Laclede Steel process effectively utilized a modified, electric arc furnace to reduce and volatize Zn from EAF dust. However, what made the process innovative was the inclusion of a splash condenser to capture metallic zinc from the process gas rather than allowing oxidation of the Zn product [91]. The benefit of this is that a lead splash condenser can co-produce lead bullion, and lead is a major contaminant in EAF dust. Yet the process was pained by production problems in relation to the quality of zinc produced, it was not deemed high enough for hot dip galvanizing use internally as intended. Laclede Steel was liquidated in 2002 amidst difficult economic steelmaking conditions.

The Mintek Enviroplas process[92] utilizes a DC arc furnace to produce a metallic Zn product through the condensation of Zn vapor in a lead splash condenser, but the extremely fine nature of the dust particles processed can cause issues with splash condenser efficiency [93].

A hybridized RHF/electrical furnace plant was built in Arkansas (USA) by AllMet around 1998. This plant utilized a standard RHF configuration with crude oxide produced being re-fumed in an electric furnace and condensed using a molten zinc splash condenser but was found to be untenable – the splash condenser was never truly operational and the quality of DRI produced was poor [94].

The Horsehead Resource Development Co., Inc. patented a hydrocarbon-fueled cyclone melting system for treatment of high zinc dusts[95] and a 30,000 t/year plant was established in Texas in 1993. The plant involved injecting fine, dried steelmaking dusts with oxygen enriched air and hydrocarbon fuel into a cyclonic reactor. Reduction of volatiles such as zinc and lead would occur giving a crude Zn oxide product and a ferrous slag.

The Ausmelt process is a two-stage furnace process, involving a smelting vessel and a reduction vessel. Dusts and lump coal are charged to the furnace and enriched air

and powdered reductants are inputted through a cooled lance. ZnO fumes out of the melt and is collected for sale [93].

The iron bearing dust recovery–zinc iron plasma process (IBDR-ZIPP) is another crude oxide producing zinc recovery process. Pelletized dusts and reductants are charged into a furnace where two electrodes generate a high voltage arc. This forms a plasma, which forces the reduction of the raw materials. This process is differentiated from many of the other crude oxide generating processes by the fact it forms molten pig iron suitable for charging directly to a BOS vessel. The IBDR-ZIPP process is energy and capital intensive but produces a stable slag, a useable iron product in the form of pig iron and a saleable zinc oxide meaning no further by-product processing is required within the steelmaking operation prior to sale.

2.11 Next Generation Ironmaking Technology

The ULCOS (Ultra Low CO_2 Steelmaking) project's key technological development in collaboration with Hismelt has been the HIsarna process. This ironmaking technology is a huge paradigm shift from the blast furnace iron production route, and offers numerous potential advantages including dramatic CO_2 reductions, high energy efficiency and, most importantly for the discussion in this thesis, high raw material flexibility[96].

Currently undergoing pilot scale testing at Tata Steel IJmuiden in the Netherlands, the operating concept of this technology is a cyclonic reduction section located directly above a final smelting reactor. Fine material and flux are injected in at high speeds to the top of the reactor where it is pre-reduced by the reactive smelter gases and descends via gravity into the final bath smelter.

This process is designed to alleviate the need for environmentally and economically expensive feed preparation for the blast furnace (sintering, coking) as well as take advantage of the excellent mixing and thermal efficiency of the HIsmelt smelter bath technology[97]. The product of the HIsarna process is hot metal, chemically comparable to that produced via the blast furnace. Typical hot metal chemistry of HIsarna iron from the pilot plant in the Netherlands is shown in Table 2.11.

Table 2.11. Typical analysis of HIsarna iron [97].

	Elemental Composition (Wt. %)							
	C	**S**	**Cr**	**P**	**Mn**	**V**	**Si**	**Ti**
HIsarna Iron	3.7-4.3	0.1-0.2	0.03-0.10	0.02-0.06	0.02-0.05	0.05-0.013	0.003-0.013	0.0-0.002

HIsarna based reactors are not as sensitive to zinc loading as a blast furnace, and a Zn rich dust fraction is produced within the cyclonic section of the reactor. It may therefore be feasible to reintegrate high zinc dusts into a HIsarna based ironmaking process to enrich the zinc content to an extent whereby they become attractive raw materials for zinc recyclers.

The inclusion of high zinc materials such as BOS dust, EAF dust and BF dust into the HIsarna furnace burden has been studied[98] and appears promising. The extremely high temperatures in the cyclonic reactor portion of the plant combined with the reducing atmosphere means that multi-stage enrichment of zinc in HIsarna flue dust may be able to create a dust fraction high enough in Zn for direct sale to zinc processors.

2.12 Further Processing of the Crude Zinc Oxide Product

The product of almost every process described in this review is crude zinc oxide powder, which is extracted from the off-gas system of the heat treatment unit. The exceptions to this such as Enviroplas, which utilize a liquid zinc condenser system to recover zinc in the metallic form.

Theoretically, an Enviroplas plant would be able to sell recovered zinc with minimal further processing to zinc end users. However, these condensers are not currently operated on a large scale and as the product requires almost no post processing, attention should instead be paid to the ZnO product from RHF and Waelz Kiln based processes.

This zinc rich dust generated from most of the technology discussed here is usually referred to as a ‘Waelz Oxide’ and is recyclable through two major pathways; The Imperial Smelting Furnace (ISF), which is in effect a zinc producing blast furnace

[99], and electrolytic zinc production which is by far the dominant production pathway with around 90% of zinc produced globally being produced electrolytically [100].

The primary concern with regard to Waelz oxides recycling into an electrolytic process comes from contamination of the oxide with halides, such as Cl and F. Halide contamination can cause rapid deterioration of electrodes and introduce impurities into the final metallic zinc during processing [101].

Several processes have been developed that are capable of dealing with the high levels of halide impurities found in Waelz Oxide including the Modified Zincex® Process [102] and Zinclor process [103].

The value of the zinc oxide produced must be factored into determining the economics of separating zinc from BOS dust, one key advantage that the RHF has over the Waelz kiln is that without the tumbling action of the burden inside a Waelz kiln, mechanical ejection of iron oxide material into the off-gas system is limited and hence the value of the Waelz oxide produced is greater.

2.13 Conclusions

The reintegration of zinc bearing by-products of steelmaking persists as a key materials efficiency and environmental issue for steel manufacturers. BOS dust in particular presents a challenge as the zinc content renders it unable to be effectively ‘diluted out’ through reintroduction to existing BF/BOS processing but the value of the zinc content is substantially less than in EAF dust meaning many existing processes use to passivate and/or generate value from EAF dust are not commercially viable for the integrated works.

The key commercial drivers for an integrate steelworks with regards to processing this Zn bearing material are;

- High zinc removal, allowing full material reintegration into existing processes.
- Valorization of iron units present within the material.
- High capacity and good economies of scale.

The necessity of a high value iron product effectively rules out hydrometallurgical recovery of Zn as the resulting iron-bearing sludge would be very low, likely to require drying and agglomeration via a sinter plant before the iron content can be recovered through the ironmaking process.

The morphology of the dust and its chemical composition have a large impact on the viability of recycling routes. The main influencing factors are described in Table 2.12.

Although the Waelz Kiln has been surpassed by the RHF, as the principal reactor for the removal of zinc from basic oxygen steelmaking by-products, it is unclear which of the current generation of RHF technologies will dominate in the short to medium term, FASTMET® and DRyIron™ have clear advantages and are readily commercially available and proven technologies. Production unit sizes of around 200-300 kt are ideally sized for managing the BOS dust output from a single plant and can easily feed DRI back into the BF or BOS process.

Table 2.12. Key influencing properties of BOS dust on Recycling Process Selection

Property	Comments
Fe_{Tot} (Wt. %)	A larger proportion of iron compared to non-ferrous minerals makes recycling more attractive due to higher throughput and lower latent heat loss during recycling of the produced DRI in the ironmaking process.
Zn (Wt. %)	For material <0.1 Zn wt. % recycling through dilution may be feasible and for very high Zn content material (>20 wt. %) hydrometallurgical techniques may become commercially viable.
$ZnO:ZnFe_2O_4$	The proportion of zinc present in the ferrite form is critical when selecting a recycling route, $ZnFe_2O_4$ is highly resistant to hydrometallurgical extraction under realistic industrial conditions.
O_{Fe} (Wt. %)	The degree of oxidation of iron present within BOS dust is critical when determining the feasibility of a pyrometallurgical Zn process. The more metallized (and therefore the lower the value of O_{Fe}) the lower the requirement for reducing agents in the process and the shorter the processing time. This leads to a higher Fe_{tot} of process feed as well as reducing raw material costs.
$CaO:SiO_2$	This ratio is often referred to as the 'basicity' of the produced DRI and has major implications for the value in use of the product in blast furnace/basic oxygen steelmaking production, as well as for the mechanical strength of the DRI (Chaung et al.).
Halide Content. F, Cl (Wt. %)	The overall concentration of halides in the material to be recycled has an effect on the value of the separated zinc product due to its deleterious effect on electrolytic zinc production

It seems unlikely that newer steel plants globally will be allowed to operate without a recovery pathway for zinc bearing wastes generated through the process, as legislative pressure to reduce environmental impact and rising landfilling costs render previous disposal routes uneconomical. The fact that RHF technology can utilize other waste products such as the carbon bearing BF dust is another advantage of these reactors, displacing coals with a by-product and thus eliminating BF dusts need for landfilling simultaneously. As high-quality zinc ore deposits become scarcer moving through the 21st century the value of recovered zinc oxides will likely rise, which may make in-situ recovery at a steel plant a more economically attractive option.

The RHF appears set to be the best available technology for the first half of the 21st century, many different variations on this technology have achieved commercial success and their ubiquity, the high value in use of the produced Direct Reduced Iron and lower technical complexity than the obsolete Waelz Kiln make them very attractive for an integrated steel plant.

Zinc focused recovery methods such as the Enviroplas process are unlikely to see widespread use in the short to medium term and are much more suitable for processing EAF dust where the high zinc content can be more effectively valorized. This may change in the far future however as cheap renewable energy becomes more readily available, technology that utilizes electrical energy such as IBDR-ZIPP and Enviroplas could become feasible if the value of the recovered zinc can offset their high capital requirements and energy consumption.

High value-added technologies such as Hi-QIP and ITmk3 have not seen commercial use in recovery of volatile metals from by-product material but may in future, depending on economic conditions. Hi-QIP and ITmk3 are less suitable for smaller scale application such as managing the dust produced at a single integrated works but may potentially be viable for larger scale remediations of post-industrial countries where large legacy stockpiles of materials exist and require remediation, such as the United Kingdom.

In terms of removal of zinc and in the metallization of the product, the molten stage processes such as Hi-QIP, ITmk3 etc. are outstanding, able to reduce zinc content in the ferrous output to trace levels and obtaining complete metallization of the residual iron. The drawback however is the increased reaction temperatures required to drive the carburization and melting reactions and the operational costs that they incur.

Table 2.13. Summary of the advantages and disadvantages of various zinc removal processes.

Process	Products	Process Description	Advantages	Disadvantages
Waelz Kiln	Waelz slag, ZnO	Horizontal rotating cylinder fed by granular feed and fired with natural gas/coal. 6+ hours at >1000 °C.	Well established and proven technology. No need for pelletization of in-feed.	Low productivity Low metallization High Fe content of ZnO produced. High maintenance costs.
FASTMET	DRI, ZnO	RHF fed with pelletized iron oxides and carbon source. 1300 °C for 6-12 minutes.	Most established commercial RHF process High throughput DRI useful in blast furnace	DRI has a higher gangue content than INMETCO etc.
DryIRon	DRI, ZnO	RHF fed with binderless briquettes. 1300 °C for ~15 minutes.	No need for expensive binder. High metallization %.	No binder means unfired briquettes are extremely fragile. Not as established as Fastmet.
ITmk3	Pig Iron Nuggets	RHF fed with pellets, 1450 °C for 10-20 minutes.	Complete metallization and slag separation. Rapid reaction speeds. Extremely high value product.	High refractory and energy operational expenditure. Untested for Zn recovery from by-products. Only one commercial plant

				that no longer operates.
INMETCO	Direct Reduced Iron, ZnO	Pelletized feed charged in 3 layers to an RHF. 1300 °C for >60 min. Can be supplemented with a submerged arc furnace melter.	Proven technology, industrial plant operating. Supplementing with melter unit can increase thermal efficiency by utilizing latent heat of process DRI.	Long residence time and low throughput. Layered structure leads to non-homogeneity of DRI. Melter units are energy intensive.
COMET	Direct reduced iron, ZnO	Non-agglomerated feed charged to an RHF and fired for >60 min at 1300 °C. Can be supplemented with a submerged arc furnace melter.	Addition of limestone layer can give very low sulfur DRI No pelletization required. Can be fueled by coke oven gas. Can produce hot metal with addition of submerged arc furnace.	Low productivity per sq metre of hearth. Limited DRI strength. Melter units are energy intensive.
Hi-QIP	Pig Iron Nuggets, ZnO	Powder feed charged onto a carbon bed within an RHF fired to 1500 °C for 10-20 min. Total separation of Fe and slag occurs.	High value pig iron product Rapid reaction speed Zinc removal has been previously explored using Hi-QIP.	Very high temperature requires expensive. refractories and high energy costs. Not commercially implemented. Requires auxiliary carbon source.

Laclede Steel Process	Hot metal, metallic Zn, lead bullion.	A modified EAF with a zinc/lead splash condenser.	Recovery of both zinc and lead provides high value products.	Very high capital investment and operational costs More suited for EAF dust processing.
Enviroplas	Stabilized slag, metallic Zn.	DC arc furnace with splash condenser.	High value metallic zinc product.	Low value ferrous product More suitable for passivated hazardous EAF dusts than BOS dust.
Ausmelt	Stabilised slag, ZnO	Two stage smelting reduction reactor.	Small process footprint. Not electrically powered.	Low value ferrous product. Only economical for high zinc wastes.
IBDR-ZIPP	ZnO, hot metal, slag	Agglomerated feed of material to a plasma heated reduction smelting reactor.	High value products which can be used within the steel plant.	Very high expenses and capital cost Only economical for high zinc wastes.

It is to be expected that the price of zinc will rise as global high-quality virgin ore reserves dwindle and demand for galvanized steel increases and thus the processing of lower zinc ferrous by-products will become more economically favorable as it has with the higher zinc EAF dusts. As such, the lower boundary of Zn Wt. % in dusts that can be economically processed is likely to fall in time. Legislative pressure may also have an impact, as landfilling fees are also likely to rise in developed countries, making recycling more commercially attractive.

For the iron producer production of a reduced iron product from these by-products also has the economic incentive of displacing expensive reducing agents and iron units in further iron production. Ultimately, the next generation of ironmaking technology, processes such as HISarna will need to alleviate the tight raw material requirements of the blast furnace and allow for high Zn materials to be processed without pre-treatment. The steel industry must overcome these barriers to the circular usage of galvanized steel if it is to become truly sustainable.

Therefore, the key scientific challenge for recovering zinc is not in fundamental scientific concepts, processes exist that can separate zinc from iron at good efficiencies such as FASTMET. The key challenge will be leveraging the value drivers of these processes into a commercially viable process.

In this thesis, that will take the form of assessing the value of processed material from RHF processes, trying to improve the value of the iron product through application of next generation RHF technology such as ITmk3, and introducing novel reductants such as waste plastics to reduce raw material costs.

3. EXPERIMENTAL METHODOLOGY AND VALIDATION

3.1 Introduction

The experimental proportion of this thesis makes extensive use of quantitative chemical analysis to not only characterize the initial starting materials, but to monitor reaction progress and heat treatment efficiencies in direct reduction trials.

Analytical techniques such as microwave plasma atomic emission spectroscopy are powerful and extremely sensitive techniques, allowing for the quantification of metal content down to parts per million (PPM) levels.

MP-AES has a deceptively simple working principle and is shown in Figure 3.1. Fundamentally, a sample solution containing the analyte of interest is drawn into a nebulizer using a peristaltic pump to eliminate interaction of the sample solution with pump components.

The sample is aerosolized with N_2 and introduced into a nitrogen plasma sustained via a high energy microwave source, confined within a quartz torch which is transparent to microwave radiation. The plasma in the center of an MP-AES torch may reach as high as 5000 K [104].

Following introduction of the sample into the plasma torch, the solvent evaporates, and molecular bonds are ripped apart creating free atoms which, in the intense heat of the torch become excited to higher energy states.

As the excited ions relax back to a lower energy state, they emit a photon of a wavelength characteristic to the electronic structure of the element they are emitted from. Emitted photons are focused by an optical lens and are screened using a monochromator and allowed to strike a detector.

The frequency of detected collisions corresponds directly with the concentration of the metal ion in the sample solution, and by producing a calibration curve using standard solutions of known concentrations of the analyte of interest, the metal content of an unknown solution may be determined.

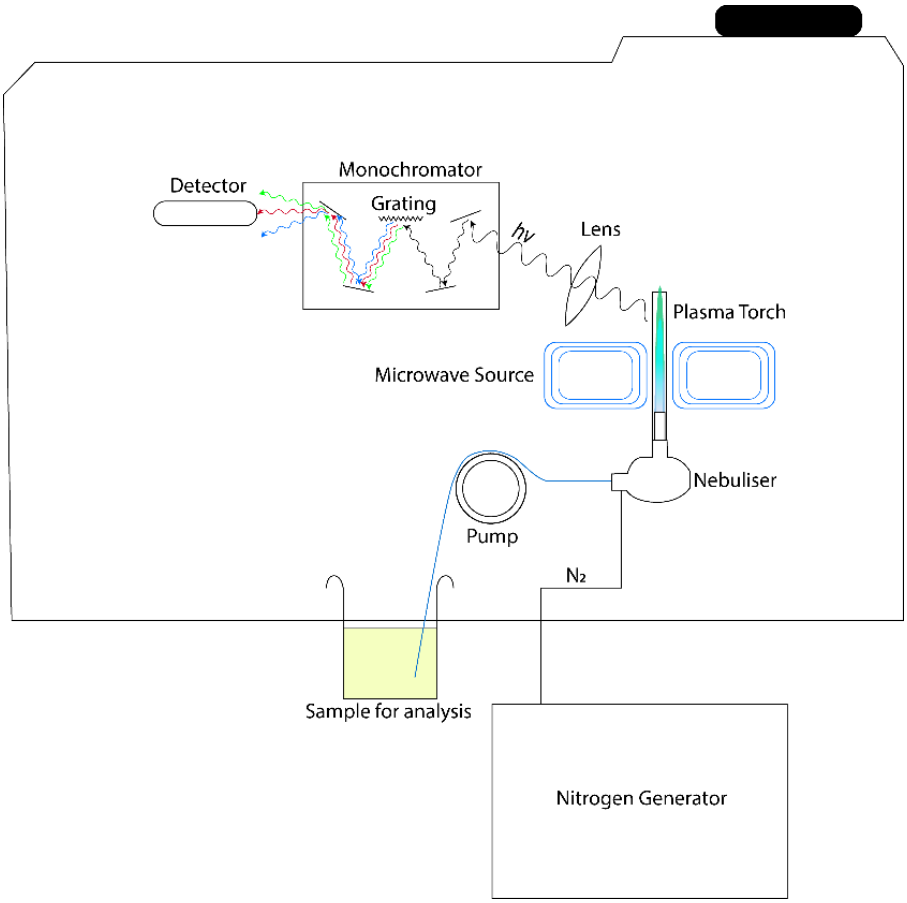

Figure 3.1. Schematic of the operating principle of an MP-AES

To analyze a solid material for trace metals, as in this work, a digestion step is critical. The analytes of interest must be solubilized and enter the aqueous phase before any analysis is possible via MP-AES.

Of key concern are the matrix of the materials that the analytes of interest are contained within, any digestion method must be capable of liberating metals from the solid in their entirety and retaining those metals within the aqueous phase. Many mineral acid digestion methodologies can generate volatile metal compounds, so this is an extremely important consideration to avoid poor recovery of analytes from the sample.

The other key consideration, beside accuracy and precision, is safety. For geological samples, some extremely aggressive chemical methods are typically employed in trace metal analysis.

Common reagents include concentrated HNO_3, HCl, $HClO_4$ and H_2O_2 but in the cases of extremely siliceous samples hydrofluoric acid (HF) may be employed due to the excellent solubility of the hexafluorosillicate (SiF_6^{2-}) ion.

HF is rarely employed on its own due to its comparatively poor oxidizing potential, many salts of alkaline earth metals such as calcium will not dissolve at all in HF hence

it usually employed together with strong oxidizing agents such as nitric acid (HNO_3) or perchloric acid ($HClO_4$).

To validate analytical techniques, in the case of this thesis, the specific digestion protocol for analysis of trace metals by MP-AES, a reference material is required to act as a standard.

This chapter will focus on validation of the experimental methodology used with respect to reference materials where available to ensure the validity of quantitative analyses used herein.

3.2 Total Digestion for MP-AES

Due to the volume of samples required to be digested for analysis in this thesis and the inherent hazards of handling the materials, the use of HF and $HClO_4$ was to be avoided unless found to be critical to the analysis.

HF not only presents a serious safety hazard due to the acute contact toxicity of the material even at extremely low concentrations, but also a serious logistical challenge. HF readily attacks and etches glassware leading to degradation in the accuracy of volumetric glassware and potentially leaching metals from glassware which may act as a source of sample contamination.

Another key consideration is the increased wear on MP-AES components when using HF bearing samples. Most MP-AES instruments run using a quartz torch as standard which is suitable for most sample matrices, but when in contact with even dilute HF solutions for extended use, the damage to the torch can cause plasma instability and affect instrument accuracy.

Disposal of aqueous waste containing HF is expensive and difficult. Neutralization with basic solutions may lead to the formation of water-soluble fluoride salts which can readily reform HF.

Many analytical chemists using HF for digestion will attempt to mitigate the risk of using HF. Evaporating a sample to dryness following digestion is one method of mitigating HF use [105]. Many metal fluorides, specifically silicon tetrafluoride (SiF_4), are extremely volatile. By driving all liquid from the sample and leaving a residue, most of the fluorine will leave the sample in the vapour phase. Of course, some hazardous fluoride salts such as NaF may remain in dried residues and therefore samples must still be handled as though they contain HF.

Specialist fume hoods are usually utilized for digestions where the formation of volatile fluorides is likely, containing filters that can scrub hazardous material from exhaust before venting to atmosphere, polyvinyl chloride liners, and polycarbonate sashes to resist corrosion.

Complexation of free fluoride in digested samples can also decrease the hazards of handling the material, this is typically achieved by reaction with boric acid (BH_3O_3) [106]. However, this reaction is slow, requiring long hold times at high temperature, and samples must still be treated as though they contain HF even following treatment with boric acid.

Perchloric acid presents another set of hazards, especially when heated for use as an extremely aggressive oxidant such as in digestion. Anhydrous perchloric acid can form incidentally when used with a powerful dehydrating agent such as H_2SO_4 and is potentially explosive. Crystalline perchlorate salts that may form in the ductwork of a fume hood are also explosive and extremely sensitive to vibration or percussion [107]. Fume hoods designed for the use of $HClO_4$ typically contain comprehensive washdown capability to ensure perchlorate salt levels cannot build up to dangerous levels.

For this work, a digestion practice was required that used the least aggressive acidic media possible to liberate the analytes of interest from the steelmaking by-product dusts in an aqueous matrix, which could then be analyzed via MP-AES.

To perform the high volume of samples digestions required in this thesis, traditional hotplate digestion was deemed unpractical due to the large amount of labour and supervisor samples require when digested to dryness on hotplates.

A DigiPREP Jr. graphite heating block (Figure 3.2) was utilized for chemical digestions of samples due to its extremely high throughput (24 samples per cycle), consistent temperature between samples, and the fact that the polypropylene digestion tubes double as volumetric glassware and storage tubes. Over temperature control and a temperature feedback probe in a blank sample also allowed for safe unattended operation.

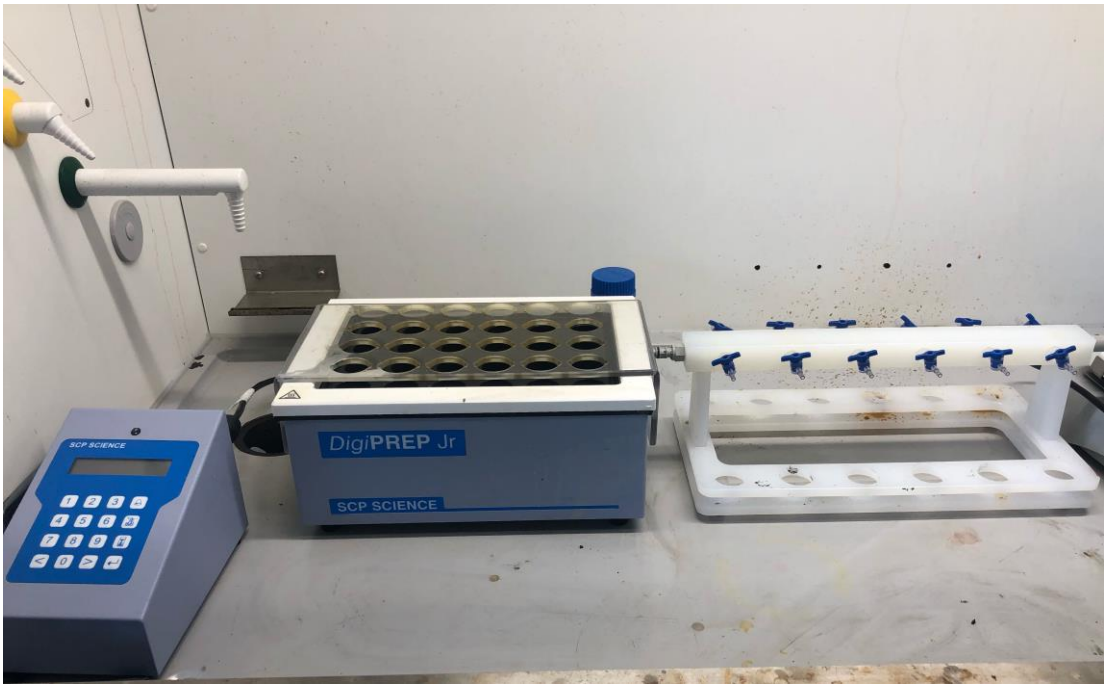

Figure 3.2. The digestion and filtration apparatus used in this thesis, consisting of a programmable controller (left), a graphite digestion block (centre) and a vacuum manifold (right).

3.2.1 Digestion Method

Approximately 200 mg of dried sample pulverized to <250 µm were accurately weighted into clean dry 50 cm^3 digestion tubes. HNO_3 (9 cm^3, 69%) was then carefully added dropwise to the sample allowing any effervescence to subside before continuing the addition. HCl (3 cm^3, 37%) was then added to the tube and covered with a plastic watchglass. Samples were placed into the graphite heating block and heated to 120 °C for a period of 120 minutes before allowing to cool to room temperature.

To oxidize any residual refractory carbonaceous matter such as coke and coal, concentrated H_2O_2 (10 cm^3, 30%) was added extremely cautiously to cooled samples with the sample tubes surrounded by an ice bath.

It was critical that this step was performed slowly and with great care as the addition initiates an extremely exothermic reaction that has the potential to be subject to thermal runaway, whereby the increasing sample temperature increases the speed of oxidation creating a feedback loop and causes samples to boil uncontrollably.

Following the hydrogen peroxide addition, samples were filtered through a 0.45 µm filter before making up to the 50 cm^3 (+/- 0.25 cm^3) mark on the tubes with 18 $M\Omega cm^{-1}$ deionized water.

3.2.2 MP-AES Operating Method

All measurements were taken using an Agilent 4200 MP-AES instrument equipped with a nitrogen generator to act as a carrier gas. Instrument settings are described in Table 3.1.

Standards for MP-AES were prepared volumetrically from CertiPrep™ grade aqueous standards in a 3% HNO_3 matrix. For Fe and Zn analysis, standards were prepared at concentrations of blank, 5, 25, 50, 75, and 100ppm, and for Pb, Na and K analysis standards were prepared at concentrations of blank, 2, 4, 6, 8, and 10ppm.

Calibration standards were remade after 30 days, and recalibration was performed every 30 experimental samples to account for instrumental drift. During calibration, R^2 values above 0.999 were considered acceptable with a linear fit and all measurements were taken relative to a reagent blank.

Table 3.1. MP-AES operating parameters

Parameter	Condition
Pump Speed	15 rpm
Sample uptake time	45 s
Stabilization time	15 s
Sample uptake speed	45 rpm
Replicates	3
Read time	3 s
Rinse time	15 s
Torch	Quartz

3.3 MP-AES validation against certified reference material

To validate the trace metal analyses herein, a certified reference material (CRM) was selected to ensure that the digestion methodology was effectively liberating the analytes of interest (Fe, Zn, K, Pb and Na) into the aqueous media and that reported values are consistent with certified values.

CRM 884-1 Furnace Dust supplied by the Bureau of Accredited Standards (BAS) was selected due to its similar mineralogy to the steelmaking by-product dusts utilized in this study and its certified values are shown in Table 3.2.

Table 3.2. Certified composition values for CRM 884-1 Furnace Dust

Element	Composition (wt. %)	C95 Error (wt. %)
Na	0.585	0.015
K	0.979	0.014
Zn	17.50	0.07
Pb	0.442	0.006
Fe	31.67	0.03

To validate the procedure, the CRM material was digested and analyzed via MP-AES (n=3) and the results and recoveries associated are reported in Table 3.3. Recoveries greater than 95% for all analytes suggests that the digestion technique is sufficient to liberate the metals contained in the reference material into solution and successfully quantify them to an acceptable level of accuracy for this work.

The principal sources of measurement uncertainty in these analyses are uncertainty in the volumetric glassware, uncertainty in the calibration fit used for MP-AES, precision and repeatability of MP-AES readings and recovery of analytes from the solid matrix. Relative uncertainty based on gravimetric and volumetric measurement during weighting and dilution was estimated at ± 0.50% of the measured value for Zn, Pb, K and Na and ± 1.01% of the measured value for Fe due to the serial dilutions required.

However, the principal source of analytical uncertainty for the MP-AES analysis stems, as expected during digestion of solid samples, from recovery of the elements of interest from the solid material and potential losses.

Based on estimations of uncertainty in gravimetric and volumetric measurements as well as recoveries of each element from the CRM, relative uncertainty of approximately ± 5% from the measured value can be expected.

Table 3.3. Experimental recovery of Pb, Na, K, Zn, and Fe from CRM 884-1 using the digestion method outlined in 3.2.1.

Analyte	λ (nm)	Reported composition (Wt. %)			Average recovery (%)	Std Dev (%)
		1	2	3		
Pb	405.8	0.404	0.420	0.467	97.4	0.03
Na	589.0	0.512	0.613	0.606	98.6	0.05
K	766.5	0.931	0.927	0.949	95.6	0.01
Zn	481.0	17.55	17.88	18.01	101.8	0.19
Fe	372.0	31.40	31.70	32.68	100.7	0.52

3.4 Selective Metallic Iron Analysis

A key quality parameter for DRI is the metallic iron content of the produced material. There are several methods for quantifying the metallic iron content selectively of DRI, fundamentally they all involve a selective dissolution step from the solid matrix that only liberates Fe^0 into solution, and then determining the iron content of the solution which then allows the total Fe^0 content of the initial solid sample to be estimated.

Thermogravimetric techniques can also be utilized, by igniting a sample in air to complete oxidation it can be assumed that any metallic iron in the sample is fully oxidised to Fe_2O_3, and the corresponding mass gain can be used to back calculate metallic Fe in the initial sample. However, thermogravimetric assessment is extremely limited by the complexity of the sample. Accurate determinations of Fe^0 content can be made for fine powders with no other oxidizable metal content, decomposable or volatile compounds such as carbonates or fixed carbon content. The ability for Fe to form oxides of widely differing oxidation states under reasonable conditions such as FeO, and Fe_3O_4 may also further obscure results.

Obviously, this is completely insufficient for DRI samples which frequently contain carbonates, other reducible or volatile materials or fixed carbon and thus, a much more selective analysis is required.

Selective dissolution techniques can involve aqueous mercury (II) chloride, aqueous ammonium chloride [108], aqueous copper (II) salts [109] or bromine in ethanol [110] to liberate Fe^0 into solution via redox.

Following selective dissolution, iron determination of the solution can be carried out titrimetrically with potassium permanganate or iodometrically with sodium thiosulphate, but titrimetric determination is extremely time consuming and was deemed to be unfeasible for the number of samples required for the study.

MP-AES offers an extremely accurate and high throughput solution to determining the Fe content of the solution generated by selective dissolution of the Fe^0 present in the initial powdered sample.

Due to the well-known hazards involved in the handling of mercuric compounds [111], selective dissolution by Cu^{2+} salts was selected as the most suitable method due to the reduced toxicity and occupational hazard presented by the handling of large volumes of solution.

For analysis, the methods of Morcali [109] and Xu et al. [112] were adapted for use on the DigiPREP Jr. graphite heating block utilized in Section 3.2.2. Samples were pulverized to <65 μm in a ring and puck mill, and approximately 200 mg of dry sample were accurately weighted into a clean, dry digestion tube.

Samples were then covered with a polypropylene watch-glass and reacted for 90 minutes at 120 °C in $CuSO_4$ solution (20 cm^3, 1 $moldm^{-3}$) where metallic iron in the sample was oxidized to Fe^{2+} by Cu^{2+} via equation 3.1.

$$Cu^{2+}(aq) + Fe^0(s) \longrightarrow Fe^{2+}(aq) + Cu^0(s) \qquad (3.1)$$

Samples were not stirred during this reaction due to their magnetic nature but the vigorous boiling of the samples within the graphite heating block was sufficient to ensure adequate mixing and allowing Cu^{2+} ions to access and react with exposed Fe^0.

Following reaction, samples were filtered while still hot through a 0.45 μm filter. The filtered samples were then acidified to pH 1 using HCl (37%, ~1cm^3) to prevent the precipitation of insoluble iron hydroxides from solution during cooling [113]. Samples were then made up to volume and analyzed via MP-AES in a similar manner to Section 3.2.2 against a reagent blank for iron.

3.4.1 Validation of Metallic Iron Analysis

To validate the metallic iron analysis for accuracy, the methodology of Xu et al. was adapted for use on the DigiPREP heating block [112].

Metallic iron powder of 99% purity, <50 µm mesh size was obtained from Sigma Aldrich and used as a solid standard for reference measurements. Iron (III) oxide (Fe_2O_3) of 99% purity and <5 µm obtained from FisherSci was used to demonstrate the selectivity of the analysis.

Five mixtures were prepared of metallic iron powder and powdered iron (III) oxide, with Fe_{met}/Fe_{Tot} ratios of approximately 0, 0.2, 0.4, 0.6, 0.8 and 1, with the actual masses of Fe_{met} and Fe_2O_3 being accurately recorded. Approximately 200 mg of each blend were accurately weighted and subjected to the experimental protocol in 3.4 and the results are shown in Figure 3.3 as a comparison between values of Fe_{met}/Fe_{tot} as determined by MP-AES and reference values.

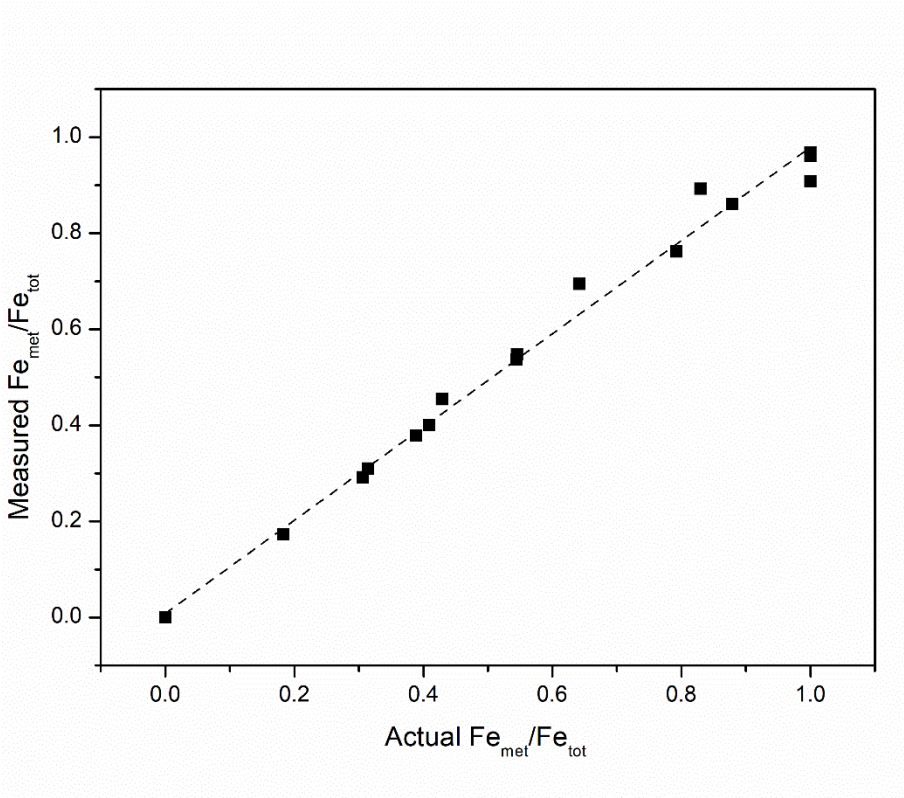

Figure 3.3. Actual Fe_{met}/Fe_{tot} ratios for validation samples compared with the Fe_{met}/Fe_{tot} as determined via MP-AES selective metallic iron analysis.

The linear fit of the data in Figure 3.3 has an R^2 value of 0.990, but a slope of 0.971 suggesting a slight under-reporting of metallic Fe against standard samples. This may be related to degradation of reference materials (metallic Fe powder is hygroscopic and prone to oxidation) but is more likely to

be the incomplete reaction due to surface passivation by the plating out of copper onto the surface of metallic iron particles.

Nevertheless, the agreement between measured and expected values is robust enough for the purposes of this work and thus the experimental protocol as outlined in 3.4 was deemed suitable for the analyses required in this work.

3.5 Carbon and Sulfur Analysis

Carbon and Sulfur were quantitatively determined via an Eltra CS500 C/S analyzer. Approximately 200 mg of powdered sample were accurately weighted into an alumina combustion boat and charged into the horizontal tube furnace of the analyzer.

The furnace was set to 1450 °C and the furnace purged with 4 dm^3min^{-1} O_2. Samples were introduced and fully combusted such that all carbonaceous and sulfurous compounds, as well as C and S dissolved into metallic iron are completely reacted to CO_2 and SO_2 respectively. Typical analysis takes 60 seconds within the instrument.

These exhaust CO_2 and SO_2 is quantitatively analyzed by a set of four infra-red gas cells before capture and abatement in reagent tubes containing CO_2 and SO_2 prior to discharge.

The C and S content are calculated automatically by relating the purge gas flow, CO_2 and SO_2 content of the exhaust gas and the initial sample mass to yield a measurement of C and S in the initial sample.

As a reference material, CRM052 from the South Africa Bureau of Standards was used to validate the analysis, containing 85.79 wt. % C and 0.85 wt. % S. After every 30 analyses, the CRM was re-run 3 times to check for instrument drift. A mean value with error < 2% and a standard deviation < 0.3 % was deemed to be acceptable, with the machine being recalibrated against standards following an unsuccessful drift check.

4. THE CHEMICAL SUITABILITY FOR RECYCLING OF STEELMAKING BY-PRODUCTS FROM UNITED KINGDOM FACILITIES

4.1 Introduction

Steelmaking via the BF/BOS process naturally generates ferrous bearing by-product dusts. These can be formed by abrasion during handling of bulk products, such as ore in the case of iron ore fines [114], abrasion during hot rolling or casting [115] or they are recovered from off-gas systems in the case of flue dusts [116]. Typically, these fine materials sometimes known as 'revert' materials are recycled through integration into the sintering process. This process agglomerates the fine material into a strong lumpy product known as sinter, which is then suitable for charging to the BF where it is then smelted alongside virgin material and the iron content is recovered.

Two key fine materials that are a consistent challenge to recycle are BOS dust and BF dust, sometimes referred to as slurry, filtercake etc. [11]. These materials are scrubbed from the off-gas systems of the BOF and BF respectively and the barrier to their reintegration into the ironmaking process is their contamination with zinc. High zinc loading to the BF has a well-studied detrimental effect of BF performance [117–119] and as such, is tightly controlled to levels around 120-200 g/tHM for most industrial furnace operations. Zinc removal processes for these materials have been thoroughly studied and commercialized over the past 50 years and reviewed recently [11] and the rotary hearth furnace (RHF) is the key emerging technology for removal of zinc from these by-products.

RHF processes such as FASTMET [120], DRyIron [121], and INMETCO [78] utilize self-reducing agglomerates fired in a rotating turntable furnace to temperatures around 1300 °C for 12 – 22 minutes. Zinc is reduced by carbon present in the briquettes and vaporized, the zinc vapour reoxidizes in the hot off-gas and is collected as a crude oxide from the off-gas system of the furnace. The key advantages of a RHF are the iron product discharged from the furnace is highly metallized (>80%) and mechanically strong enough to be charged to the BF. This high degree of pre-reduction can decrease fuel rates within the BF leading to higher throughput and reducing requirements for expensive and environmentally costly coking coals. A case study at Tata Steel India reported a 6% coke rate reduction with the addition of 100-150 kg/tHM 5-18 mm DRI to the BF [66]. Another key advantage of the RHF is the tremendous flexibility in reducing agent selection in the self-reducing briquettes, alternative reductants including steaming coal [89], waste plastic [122], biomass [123] and BF dust [124].

Developments in the field have meant that a solid waste processing solution such as a RHF are becoming more commercially attractive but much of this potentially valuable zinc and iron resource is being landfilled or stockpiled, creating an environmental liability but also a commercial opportunity. This is especially true in westernized economies such as the United Kingdom (UK). Landfill tax rates have increased dramatically in the UK since their inception in 1996 as the government has sought to reduce the environmental impact of industrial activity. The decline of the UK steelmaking industry has also led to large deposits of iron-bearing material left at sites no longer operating as full integrated plants or no longer operating altogether.

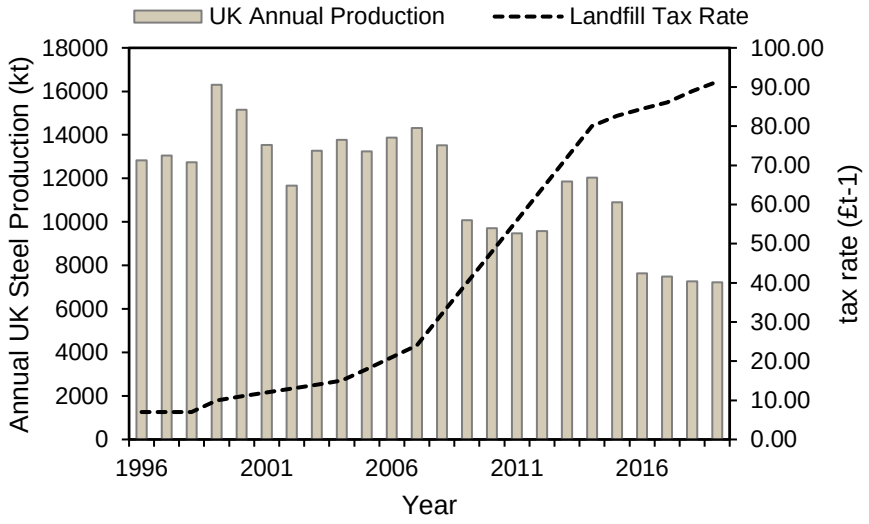

Figure 4.1. UK crude steel production output and UK landfill tax tates. Data adapted from World Steel Association Annual Production Statistics [12] and the UK government respectively [125].

No accurate estimates of the total scale of waste iron oxide stockpiles in the UK exist as of the time of writing, but Mackillop estimates substantial ferrous resource in the form of ad-hoc stockpiles [84]. Figure 4.2 shows key ironmaking sites within the UK. Remediation of land used for ironmaking is an area of key concern for the UK government. Following the closure of the Ravenscraig British Steel plant in Scotland, there was a great deal of controversy surrounding the remediation of the land that the steel plant occupied: an estimated 284,000 m^3 (355,000 – 542,000 tonnes) of stockpiled filtercake dust was left at the site following the termination of production [126].

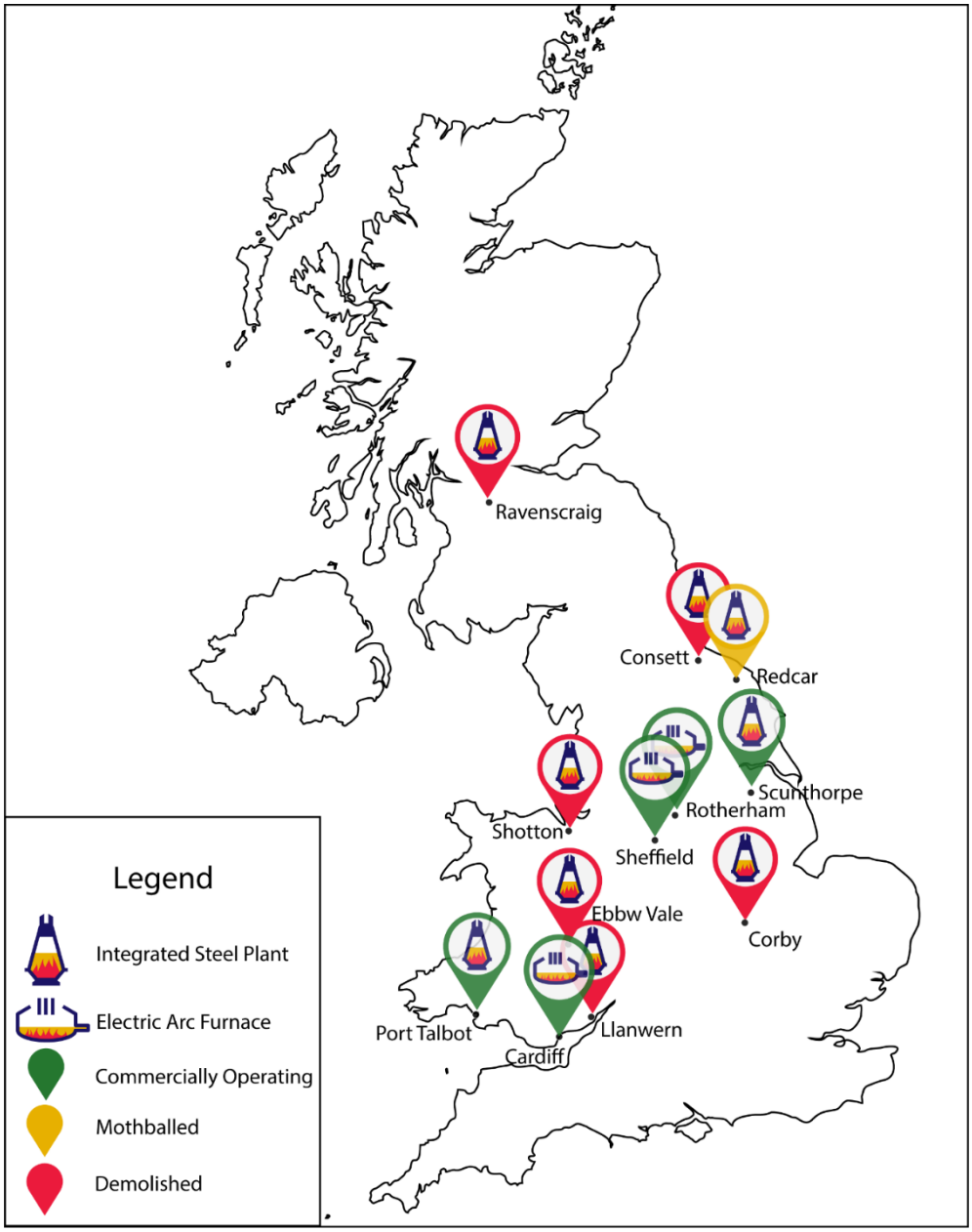

Figure 4.2. Major steelmaking production facilities in the UK since 1980. 'Heavy end' iron production closures occured as follows: Ebbw Vale (1978), Corby, Shotton, Consett (1980), Ravenscraig (1992), Llanwern (2001)[127,128]

To offset the negative environmental legacy of steelmaking, a strategy for dealing with contaminated dusts as they are generated during the ironmaking and steelmaking, as well as the processing of legacy material from plants where ironmaking activity has ended will be critical. The first step in a viable recycling solution of these materials is characterization of them to determine their suitability for recovery through established processes such as the rotary hearth furnace (RHF).

4.2 Experimental

4.2.1 Materials and Chemicals

Samples of basic oxygen steelmaking (BOS) dust were obtained from Tata Steel (Port Talbot), British Steel (Scunthorpe), and the mothballed Redcar steelworks in the United Kingdom. 10 kg of each material were dried at 90 °C and pulverized to <65 μm for analysis.

The 10 kg samples were presumed to be representative of the material stockpiles, however, this is of course quite an assumption. Jaafer demonstrated the material variability of BOS dust material even within the same stockpile [21] and a full excavation study would be needed to fully validate that the material collected was indeed representative. However, constrained by lack of access to the physical stockpiles for sampling activity, it was deemed appropriate to obtain a sample from the plateau of each stockpile that appeared representative and not obviously contaminated with other materials present in the stockpiles.

All reagents used in chemical analysis were of ACS grade.

4.2.2 Analytical Techniques

Chemical analysis and metallic iron analysis via MP-AES was carried out as specified in Chapter 3. The ratio of iron present in the metallic state ($\%_{\text{Metallization}}$) was determined in comparison with the total iron content via Equation 4.1, as determined by complete acid digestion.

$$\%_{\text{Metallization}} = \frac{\text{Fe}_{\text{met}}}{\text{Fe}_{\text{tot}}} \times 100 \qquad (4.1)$$

X-Ray fluorescence analysis was performed by the Basic Oxygen Steelmaking Laboratory team at Tata Steel Port Talbot. Detected elements (Si, Ca, Mg, Ti, P, Al and Mn) were balanced with oxygen to allow for basicity calculations apart from iron due to it routinely existing in multiple oxidation states within ironmaking materials.

Optical basicity is a useful tool for describing the behaviour of molten oxide systems, such as those found in molten steelmaking slags and is therefore commonly referenced in ironmaking. It allows for a description of a molten oxide system that is non-aqueous and non-protic to be described using the lewis approach of acidic and basic oxides,

relating acidity and basicity to the negative charge born on oxygen atoms rather than the ability to donate or accept protons as in the conventional use of acidity and basicity. Basicity was calculated using Equations 4.2 – 4.6.

$$B_1 = \frac{CaO}{SiO_2} \tag{4.2}$$

$$B_2 = \frac{CaO + MgO}{SiO_2 + P_2O_5} \tag{4.3}$$

$$B_3 = \frac{CaO + MgO}{SiO_2 + Al_2O_3} \tag{4.4}$$

$$B_4 = \frac{CaO + MgO}{SiO_2 + Al_2O_3 + P_2O_5} \tag{4.5}$$

$$B_5 = \frac{CaO + MgO + MnO}{SiO_2 + Al_2O_3 + P_2O_5} \tag{4.6}$$

Carbon and sulfur content were quantitatively determined using an Eltra CS500 combustion analyser as outlined in Chapter 3. Powder X-ray Diffraction analysis was performed using a Panalytical Empyrean S3 (Co-K_α λ = 1.7902 Å, 10 – 120 °, s = 0.066 °, t = 20 s). A Hitachi tabletop TM3030 Scanning Electron Microscope was used to provide morphological information. Thermogravimetric information was obtained using an Q600 SDT model TGA-DSC using an alumina crucible, heating rate of 5 °Cmin^{-1} and a flow rate of 100 cm^3min^{-1}. Particle size analysis was undertaken using a Malvern Panalytical Mastersizer 3000 with samples mechanically dispersed in isopropanol.
For transmission ^{57}Fe Mössbauer spectroscopy measurements, acrylic absorber discs with a sample area of 1.767 cm^2 were with each sample. The 14.4 keV γ-rays were supplied by the cascade decay of 25 mCi ^{57}Co in Rh matrix source, oscillated at constant acceleration by a SeeCo W304 drive unit, and detected using a SeeCo 45431 Kr proportional counter operating with 1.785 kV bias voltage applied to the cathode. All measurements were carried out over a velocity range of ±12 mm s^{-1} due to the presence of high-field magnetic splitting and were calibrated relative to α-Fe foil. Spectral data were fitted using the Recoil software package, using Lorentzian line shapes. The ^{57}Fe

Mössbauer spectroscopy measurements and data fitting in this study were undertaken by external collaborators at Sheffield Hallam University.

4.3 Results and Discussion

4.3.1 Microwave Plasma – Atomic Emission Spectroscopy

4.3.1.1 Trace Metal Analysis

Trace metals analysis of the materials indicated sizeable contamination with zinc (Table 4.1). Lead contamination is present in all four samples, although at levels not substantial enough to allow for powder XRD speciation of the lead compounds present. The levels Zn would be too high to recycle any of the dusts at scale via a sinter plant/blast furnace without some form of pre-treatment process to reduce zinc content, typical limitations for a zinc loading to a BF is 100-200 g/tHM [11].

Small amounts of lead were detected in the samples, which appears consistent with results from other studies on similar materials [47,129]. Levels of As, B, Cd, Mo and Sb were found to be below the detectable limit of the analysis and hence not included in Table 4.1.

Table 4.1. Trace metal analysis results for Port Talbot, Scunthorpe, and Redcar Material

	Composition (Wt. %)									
Material	**Ba**	**Cr**	**Cu**	**K**	**Na**	**Ni**	**Pb**	**V**	**Zn**	**Tot.**
Port Talbot BOS Dust	0.020	0.016	<0.005	0.015	0.065	0.006	0.15	0.027	2.74	3.04
Port Talbot BF dust	<0.005	<0.005	<0.005	0.140	0.046	<0.005	0.18	0.013	0.89	1.27
Scunthorpe BOS Dust	<0.005	<0.005	0.01	0.114	0.16	<0.005	0.08	0.017	0.41	0.79
Redcar BOS dust	<0.005	<0.005	0.01	0.065	0.10	<0.005	0.22	<0.005	1.70	2.10

4.3.1.2 Metallic Iron Analysis

Analysis for metallic iron (Table 4.2) showed that as expected the BOS dust materials contain substantial metallic iron.

The BOS dust from Redcar was anomalous to the samples from Scunthorpe and Port Talbot however, in that it was significantly less metallized in terms of iron. There are a few plausible explanations for this, firstly, storage conditions of by-product dusts can have a dramatic effect on material chemistry [21]. The process conditions during the blow in the BOS vessel can have a significant effect on the morphology of the dusts [46]. Finally, the stockpiles that these materials are stored in are heterogenous and can contain many different types of materials, it’s possible that the material from Redcar contains non-BOS dust material as well.

The substantial metallization of the Port Talbot and Scunthorpe BOS dust samples make them especially strong candidates for pyrometallurgical recovery, due to the associated reduction in carbon requirement for iron reduction.

Table 4.2. Metallic iron analysis for Port Talbot, Scunthorpe, and Redcar Material.

Material	Fe_{Met}	$\%_{Metallization}$
Port Talbot BOS dust	14.20	23.63
Port Talbot BF dust	0.76	2.84
Scunthorpe BOS dust	13.50	22.56
Redcar BOS dust	0.60	1.12

4.3.1.3 X-Ray Fluorescence (XRF) Spectroscopy

The results of the XRF analysis indicated some stark differences in the chemical composition of the materials (Table 4.3). It is worth noting that the iron content was highly variable. This is to be expected as the degree of oxidation of the material from its initial condition will depend on variables such as storage conditions and age of the material which is difficult to know for certain.

The BOS dust materials all contained a substantial amount of Ca and Mg, and they are all predominately basic in nature, with oxide basicity greater than 1 as shown in

Table 4.4**Error! Reference source not found.**. 8This is likely owing to the basic nature of the BOS process in which they were produced [52].

BF dust from the Port Talbot site is a clear outlier, it has substantially lower Fe content than the other materials and is much more acidic in terms of the mineral oxides that are present. This is due to the acidic nature of the iron ore used in the blast furnace [55] which is likely the source of the iron within the dust.

Table 4.3. XRF analysis results for Port Talbot, Scunthorpe, and Redcar material.

	Composition (Wt. %)							
Material	**Fe_{Tot}**	**SiO_2**	**Al_2O_3**	**TiO_2**	**CaO**	**MgO**	**P_2O_5**	**Tot.**
Port Talbot BOS dust	60.09	2.31	0.34	0.06	10.67	1.16	0.088	74.72
Port Talbot BF dust	26.79	5.61	2.63	0.14	3.86	0.77	0.159	39.96
Scunthorpe BOS dust	59.83	2.98	0.65	0.08	6.66	1.91	0.133	72.24
Redcar BOS dust	53.73	2.71	0.70	0.07	4.71	1.14	0.159	63.22

Table 4.4. Calculated basicity for Material from Port Talbot, Scunthorpe, and Redcar.

Material	**B_1**	**B_2**	**B_3**	**B_4**	**B_5**
Port Talbot BOS dust	4.62	4.93	4.46	4.32	4.59
Port Talbot BF dust	0.69	0.80	0.56	0.55	0.57
Scunthorpe BOS dust	2.23	2.75	2.36	2.28	2.67
Redcar BOS dust	1.74	2.04	1.72	1.64	1.96

4.3.1.4 Powder X-Ray Diffraction (XRD)

The powder XRD patterns of the four materials show distinct differences in morphology that are not clear through chemical analysis alone (Figure 4.3). All three BOS dust samples were found to contain substantial metallic iron, which is corroborated by the MP-AES analysis results for selective metallic iron in 4.3.1.2.

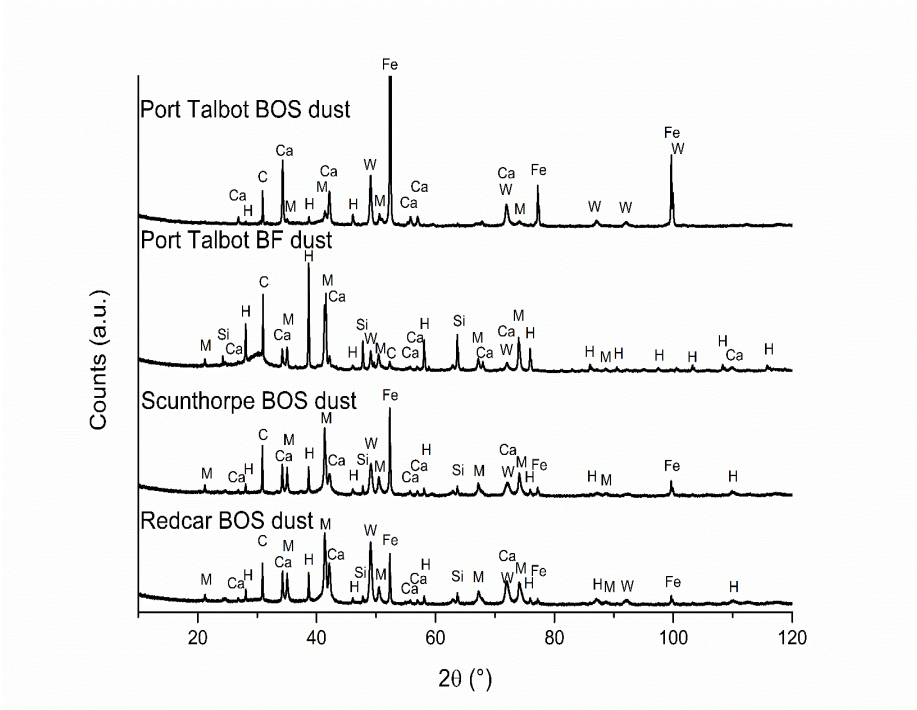

Figure 4.3. Powder XRD patterns for Port Talbot BOS dust, Port Talbot BF dust, Scunthorpe BOS dust and Redcar BOS dust. Ca = Calcite ($CaCO_3$ – COD# 1010962), H = hematite (Fe_2O_3- COD# 9009782), C = graphite (C -COD# 9011577), M = Magnetite (Fe_3O_4 -COD# 9006920), W = Wüstite (FeO – COD# 1011167), Fe = α-iron (Fe – COD# 9006595), Si = quartz (SiO_2 – COD# 500035).

As expected, the BOS dust samples all appear to be significantly reduced. Metallic iron was detected in all three. The XRD diffraction patterns suggest that the BOS dust material from Port Talbot contains iron predominantly in the Fe^0 or Fe^{2+} oxide form, with small amounts of mixed Fe^{2+}/Fe^{3+} and Fe^{3+} oxide. The materials from Scunthorpe and Redcar show a varied mix of iron phases, with comparatively a smaller proportion of Fe^0 and Fe^{2+} oxide relative to the higher iron oxides.
Calculation of the lattice parameter of the spinel phase of each material is shown in Table 4.5.

Crystal lattice parameters for the materials were determined by examination of the position of the spinel peaks on the diffraction patterns at ~21.3 ° and ~35.1 ° due to their lack of overlap with peaks related to other crystalline phases in the materials.
Port Talbot BOS dust showed a cell parameter slightly smaller than anticipated for pure magnetite (a = 8.3708 Å). This result may suggest the spinel phase is slightly deficient in tetrahedral Fe^{2+} occupancy, more similar to a maghemite structure [130], and also suggests that the spinel phase in the material does not contain Zn^{2+} in tetrahedral

occupancy. Port Talbot BF dust (8.3972 Å) was determined to have a cell parameter extremely consistent with pure magnetite (8.394 Å) [131].

Samples from Scunthorpe and Redcar show a slightly elevated lattice constant more consistent with sub-stoichiometric $ZnFe_2O_4$. Specifically, the lattice constant corresponds well with literature examples for $Zn_{0.189}Fe_{2.811}O_4$ (Å = 8.403) [132] and $Zn_{0.35}Fe_{2.65}O_4$ (Å = 8.408) [133] . While this analysis is only qualitative, the levels of zinc removal required for economical recovery of these materials for recycling through the BF/BOS route is very high (~99%) and zinc occupation of tetrahedral sites within the spinel phase of the materials bodes poorly for effective and economical hydrometallurgical processing.

Table 4.5. Calculated lattice parameters for the spinel phase in each steel by-product dust sample

	(202)		(111)		
Sample	**2θ (°)**	**d (Å)**	**2θ (°)**	**d (Å)**	**Cell Parameter (Å)**
Port Talbot BOS dust	35.08	2.9704	21.30	4.8447	8.3708
Port Talbot BF dust	35.12	2.9670	21.29	4.8461	8.3972
Scunthorpe BOS dust	35.11	2.9677	21.28	4.8478	8.4021
Redcar BOS dust	35.12	2.9645	21.28	4.8443	8.4020

4.3.1.5 Thermogravimetric Analysis and Differential Scanning Calorimetry (TGA-DSC)

The TGA-DSC analysis of the four samples under an argon atmosphere is shown in Figure 4.4. Port Talbot BOS dust shown three distinct transitions (Figure 4.4a), a gradual endothermic mass loss between 0 and 200 °C of 2% which likely corresponds to the evaporation of moisture in the sample, an endothermic mass loss around 700 °C which appears consistent with the thermal decomposition of calcite (Equation 4.7) [134].

$$CaCO_3(s) \longrightarrow CaO(s) + CO_2(s) \qquad (4.7)$$

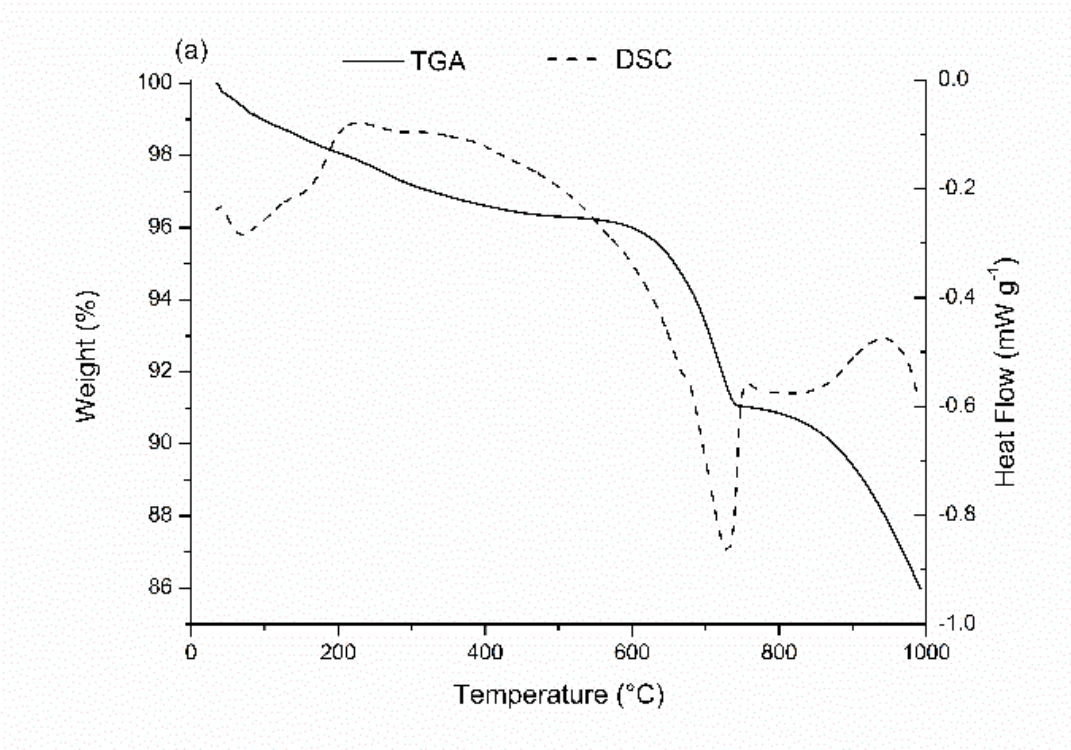
(a)
TGA
DSC
Weight (%)
Heat Flow (mW g-1)
Temperature (°C)
100
98
96
94
92
90
88
86
0.0
-0.2
-0.4
-0.6
-0.8
-1.0
0
200
400
600
800
1000

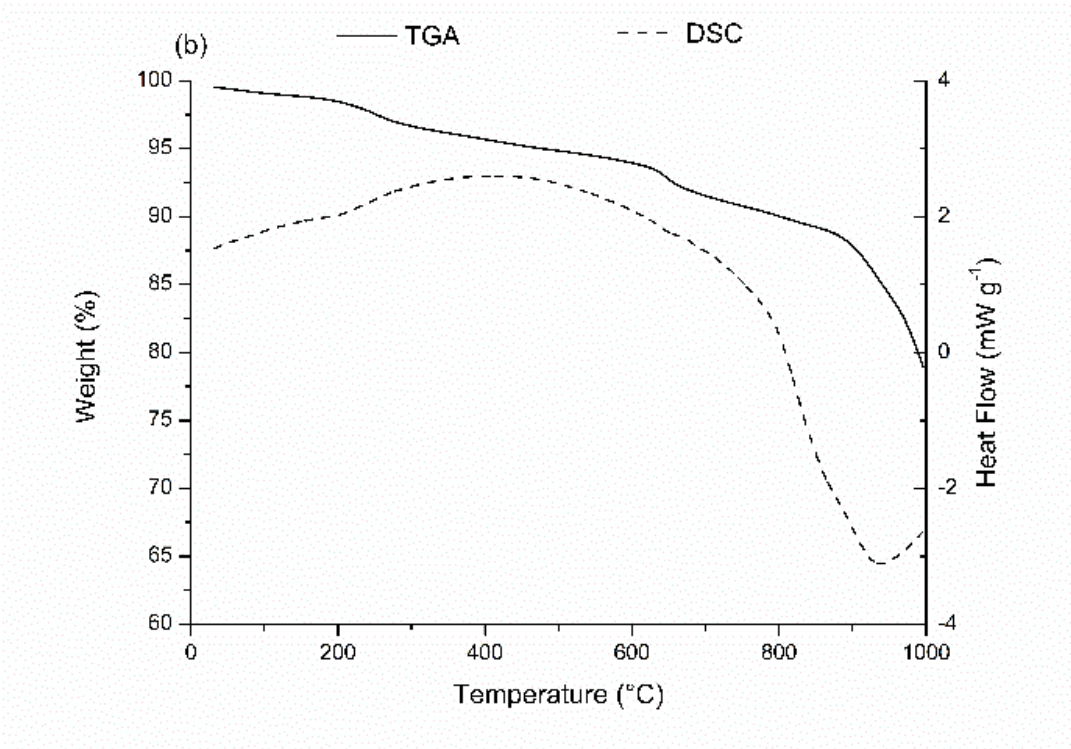
(b)
TGA
DSC
Weight (%)
Heat Flow (mW g-1)
Temperature (°C)
100
95
90
85
80
75
70
65
60
4
2
0
-2
-4
0
200
400
600
800
1000

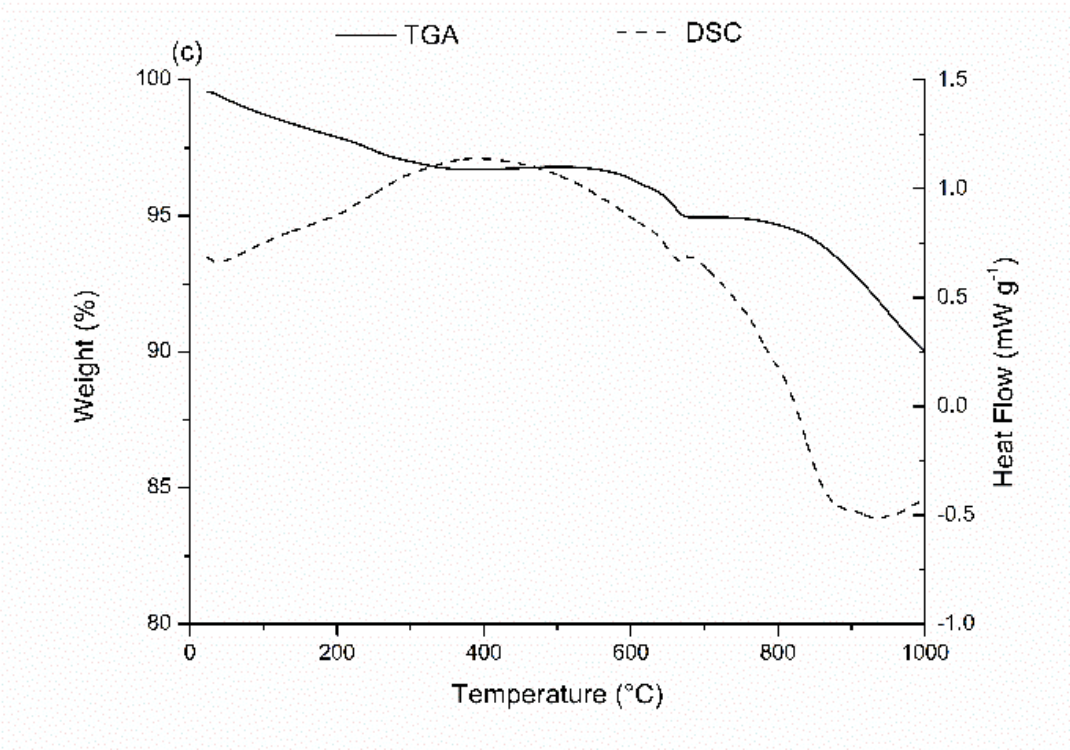

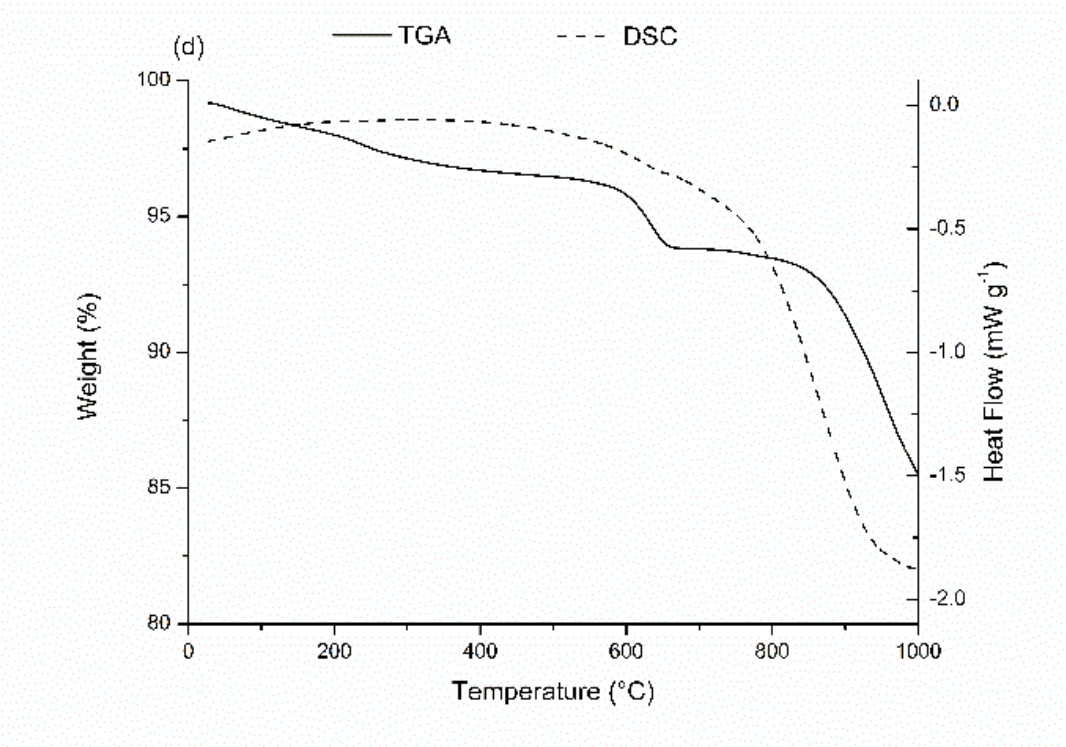

Figure 4.4. TGA-DSC results for Port Talbot BOS dust (a), Port Talbot BF dust (b), Scunthorpe BOS dust (c), and Redcar BOS dust (d) under an inert gas atmosphere. The DSC signals shown are exo-up.

The third transition from 800 °C to 1000 °C of 4% is a little less clear, due to its exothermic nature it is not likely to be pyrolysis of volatile carbon species from the

material. This mass loss is likely attributable to the volatilization of zinc from the material (Bpt = 907 °C)) [135] with metallic iron acting as the reducing agent (Equation 4.8).

$$\mathrm{Fe(s) + ZnO(s) \longrightarrow FeO(s) + Zn(g)} \tag{4.8}$$

This reaction has been studied in detail with respect to the EAF dust with metallic iron added as the reducing agent for zinc oxide [136,137]. Equation 4.9 describes the standard free energy change for this reaction ($\Delta G^0 = 0$ at 1202 °C), and therefore it would be expected to only proceed to the right as that temperature is exceeded. However, it was found that the low partial pressure of zinc vapour caused by the presence of a sweeping gas flow, combined with the reaction promoting effects of CaO mean this reaction is feasible, albeit slow at temperatures as low as 800 °C and Zn(g) partial pressures around 0.001 atm [136].

$$\Delta G^0 = 204{,}070 - 138\ \mathrm{T}\ (\mathrm{J\ mol^{-1}}) \tag{4.9}$$

The observation that this reaction was occurring in the Port Talbot BOS dust was supported by the fact that the metallothermic reduction of zinc oxide by metallic iron is exothermic (Equation 4.9) which is in agreement with the DSC for the material (Figure 4.4a) and by powder XRD of the sample (Figure 4.5), which shows the phase changes after heating to 1000°C. Metallic iron oxidized substantially to iron(II) oxide, which would not usually be expected under anoxic conditions. The presence of brownmillerite [$Ca_2(Al,Fe)_2O_5$] is due to the reaction of CaO formed by the decomposition of calcite at 700 °C, reacting with Fe and Al oxides.

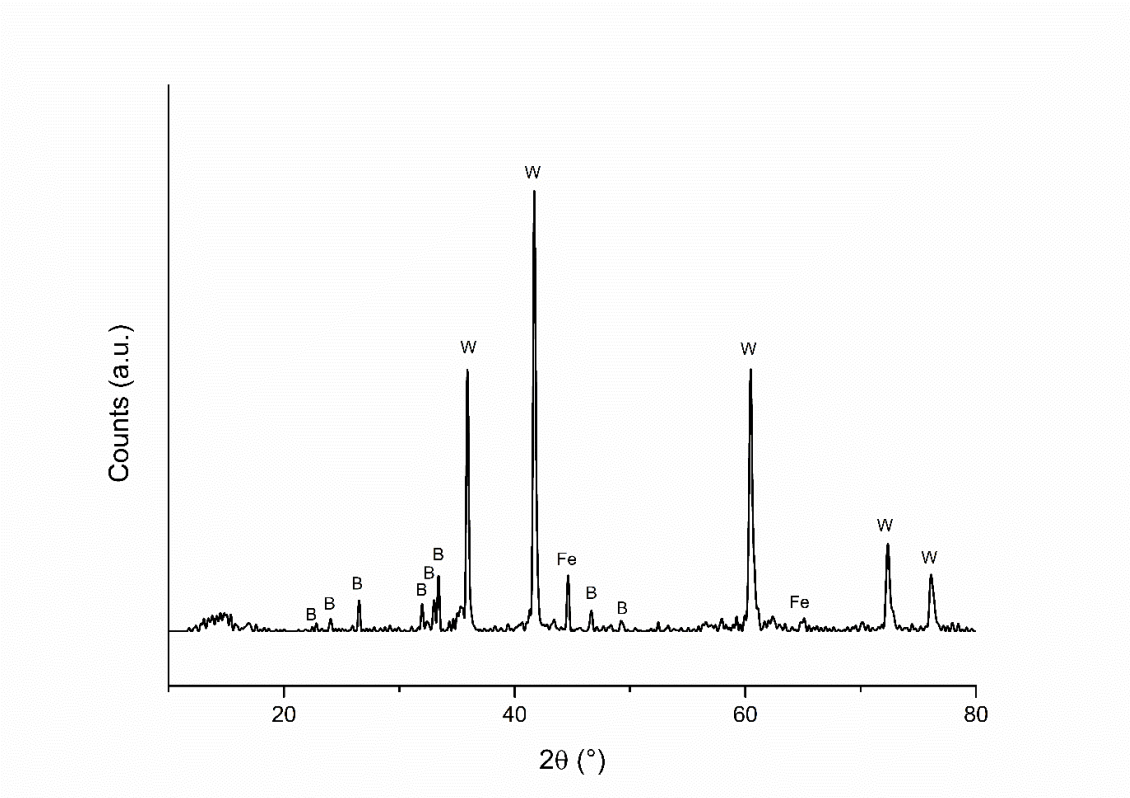

Figure 4.5. Powder XRD pattern of Port Talbot BOS dust following TGA-DSC analysis at 1,000 °C under an inert atmosphere. B = Brownmillerite (Ca2(Al, Fe)2O5 – COD#9014319), W = Wuestite (FeO – COD# 1011167), Fe = α-iron (Fe - – COD# 9006595).

Port Talbot BF dust behaved in stark contrast to Port Talbot BOS dust under inert conditions however (Figure 4.4b), the gradual mass decline from 0 - 600 °C is likely a combination of desorption of water from the material and pyrolysis of organic matter in the material. A slight endothermic mass loss at 700 °C is again characteristic of calcite decomposition. The mass loss from 900 – 1000 °C is not likely to be the metallothermic reduction of zinc oxide as reported for Port Talbot BOS dust due to the lack of metallic Fe available in the sample (Table 4.2) and the peaks endothermic character. This is instead likely to be carbothermal direct reduction of iron oxides in the material (Equation 4.11) [45].

$$2Fe_2O_3(s) + 3C(s) \longrightarrow 2Fe(s) + 3CO_2(g) \qquad (4.10)$$

Scunthorpe BOS dust (Figure 4.4c) behaved quite similarly to Port Talbot BOS dust under inert atmosphere, with decomposition of calcite observed at 700 °C corresponding to a mass loss of 2.5%. The behaviour between 800 °C and 1000 °C is

different to PT BOS dust however, the mass loss is too large to simply be the loss of Zn and is endothermic in nature. It is likely that some carbothermal reduction is taking place between the solid fixed carbon in the sample and the iron oxides as in the case of Port Talbot BF dust.

The Redcar BOS dust sample behaved quite similarly to the sample from Scunthorpe, but the mass loss between 800 – 1000 °C attributed to carbothermal reduction of iron oxides is much more substantial (12% for Redcar BOS versus 5% for Scunthorpe BOS), this is supported by the observation that Redcar BOS material had a higher carbon content (Table 4.7) therefore more carbon available for reduction and thus, a greater mass loss during thermogravimetric analysis.

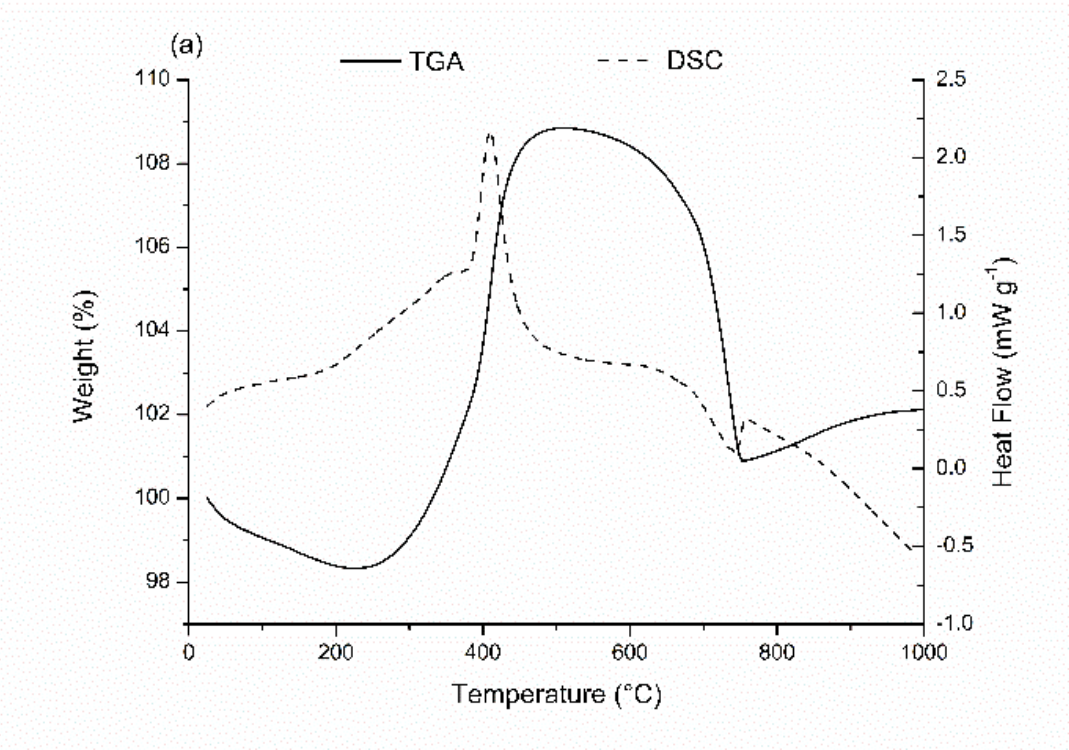
(a)
TGA
DSC
Weight (%)
Heat Flow (mW g-1)
Temperature (°C)
110
108
106
104
102
100
98
2.5
2.0
1.5
1.0
0.5
0.0
-0.5
-1.0
0
200
400
600
800
1000

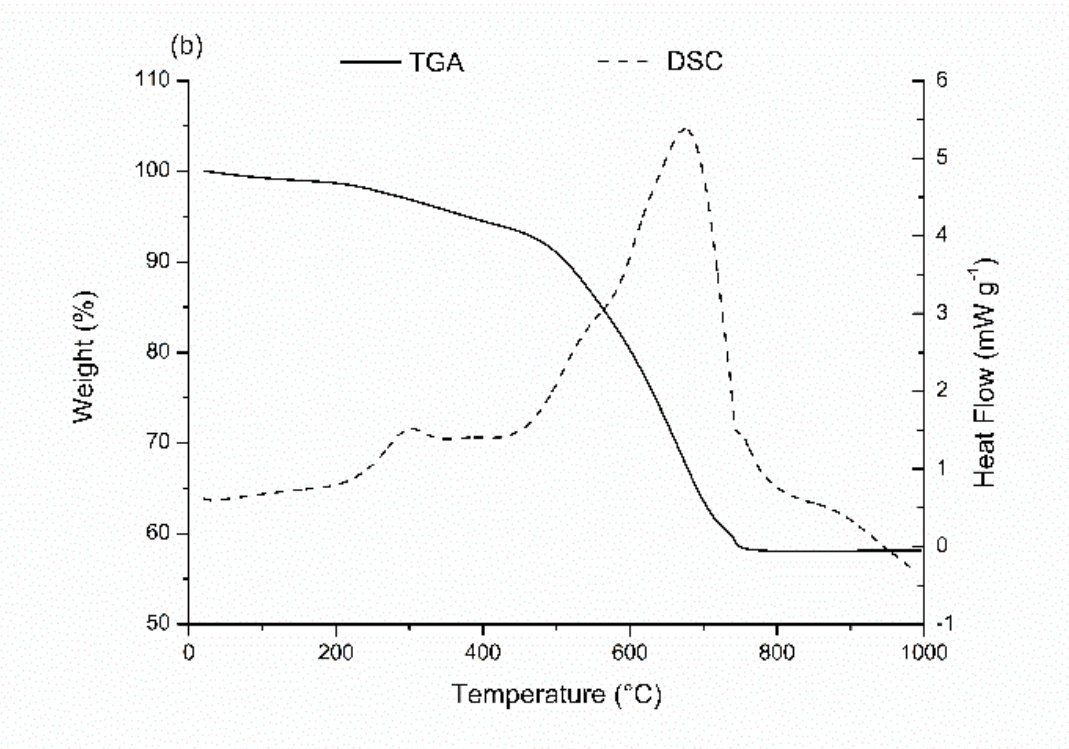
(b)
TGA
DSC
Weight (%)
Heat Flow (mW g-1)
Temperature (°C)
110
100
90
80
70
60
50
6
5
4
3
2
1
0
-1
0
200
400
600
800
1000

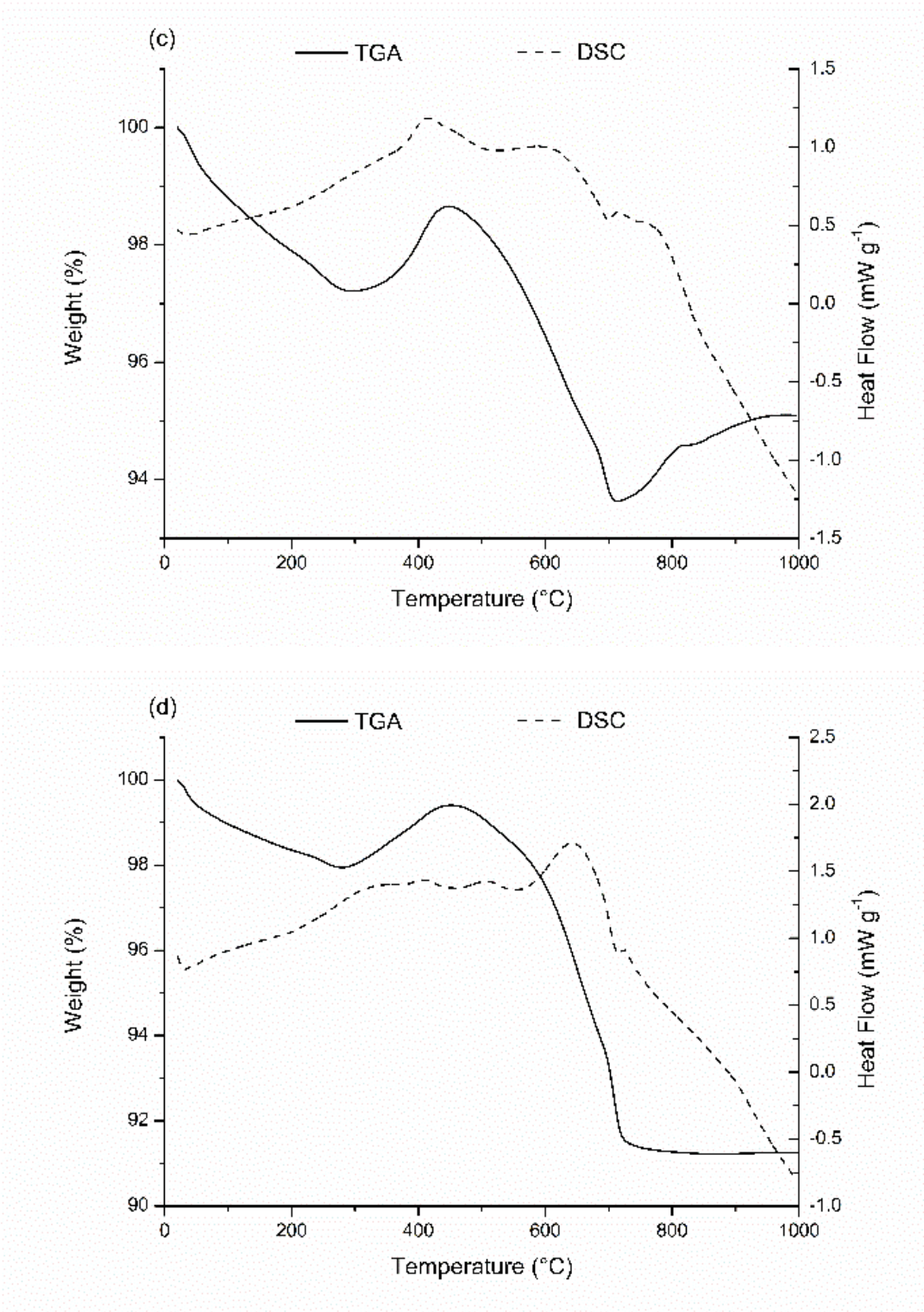

Figure 4.6. TGA-DSC results for Port Talbot BOS dust (a), Port Talbot BF dust (b), Scunthorpe BOS dust (c), and Redcar BOS dust (d) under a flow of compressed air. The DSC signals shown are exo-up.

Figure 4.6a shows that there are three discrete transitions as the Port Talbot BOS dust is heated in air. Between 0 and 200 ˚C the mass loss is likely attributable to

moisture loss, and a large exothermic mass gain of 10% at 400 °C corresponds well with the oxidation of metallic iron and lower iron oxides to Fe_2O_3 [138]. The second transition, at 700 °C, is the endothermic decomposition of calcite, like that observed under inert atmosphere. The sample continues to gain mass as T approached 1000 °C which is likely to be also attributable to oxidation of iron.

Figure 4.6b shows the behavior of Port Talbot BF dust oxidized in air shows two clear exothermic transitions at 400 °C and 710 °C. The exothermic transition at 400 °C is likely to be combustion of volatile organic matter, while the much larger exothermic transition at 710 °C is combustion of fixed carbonaceous matter. The decomposition of calcite seen in the material under an inert atmosphere is likely also present in Figure 4.6b but is masked by the much larger combustion mass loss.

The TGA-DSC analysis for Scunthorpe and Redcar (Figure 4.6c and Figure 4.6d) are quite similar. An initial mass loss between 0 and 200 °C is likely to be volatilization of water or breakdown of hydroxide materials. This transition is followed by an exothermic oxidation of iron at around 400 °C. A broad exothermic mass loss occurs for both samples between 450 °C and 700 °C which is likely to be combustion of organic and carbonaceous matter in the materials. Again, it is also likely that within this region of the data an endothermic carbonate decomposition, as can be seen by a small endothermic signal on the DSC for both samples at 700 °C.

Scunthorpe BOS dust continued to increase in mass between 700 °C and 1000 °C which is likely to be further oxidation of iron. This is not observed in the Redcar BOS dust sample, which agrees with metallic iron analysis of the materials showing very low levels of metallic Fe in the material from Redcar. The results suggest an inconsistent amount of metallic iron between samples, which is of significance for pyrometallurgical recovery as higher initial Fe content reduces the demand for additional carbon in the separation process.

4.3.1.6 Particle Size Analysis

Laser diffraction particle size distributions of the four materials are shown in Figure 4.7. with D10, D50 and D90 particle diameter sizes shown in Table 4.6. It can be seen from the particle size analysis data that Port Talbot BF dust material is very fine, with 90% passing 37.9 μm, an observation in reasonable agreement with analyses performed on similar material [139].

Table 4.6. Particle sizing data for Port Talbot BOS dust, Port Talbot BF dust, Scunthorpe BOS dust and Redcar BOS dust.

Sample	D10 (µm)	D50 (µm)	D90 (µm)
Port Talbot BOS Dust	0.75	12.54	118.2
Port Talbot BF Dust	1.465	11.70	37.9
Scunthorpe BOS dust	1.742	30.08	161.04
Redcar BOS dust	1.724	34.33	135.07

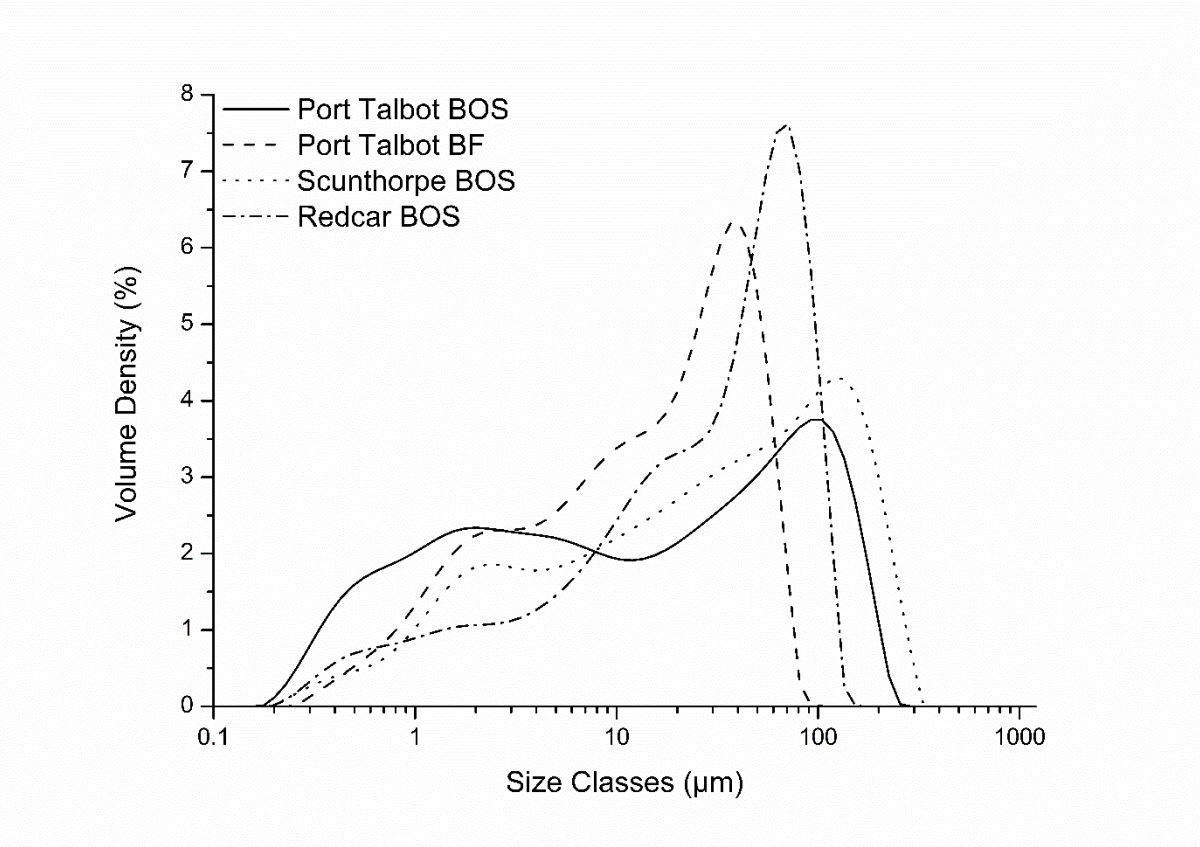

Figure 4.7. Particle size distribution information for Port Talbot BOS dust, Port Talbot BF dust, Scunthorpe BOS dust and Redcar BOS dust.

The BOS dust samples from Port Talbot, Scunthorpe and Redcar showed a different particle size distribution as expected. The BOS dust samples appeared to show two discrete particle types, extremely fine particles < 5 µm and then a large number of particles close to the 100 µm threshold, with the analyses indicating a bimodal distribution of particle size.

The slight differences in size distribution between BOS dust samples may be related to a number of factors, BOS vessel process parameters such as oxygen blowing

velocity are known to have a direct effect on the materials physical properties, and the particle size distribution is known to change throughout the progress of a single blow [46]. Storage condition may also be a factor, some agglomeration of finer particles is to be expected. A study by Jaafar on material from Port Talbot showed that outdoor weathered BOS dust material from stockpiles had a substantially higher D90 value than fresh material even after grinding [21].

The optimal particle size for the production of high compressive strength DRI from self-reducing briquettes as in a RHF is around 100 μm [140] and a fine particle size is desirable for the purposes of accelerating the reduction and zinc removal reactions within the RHF as the reactions are surface area dependent [141].

4.3.1.7 Scanning Electron Microscopy (SEM)

Scanning electron microscopy was utilized to observe the physical structure of BF dust and BOS dusts from the three plants. shows the structure of the dusts under scanning electron microscopy. In the three BOS dusts (Figure 4.8a, c and d) globular particles are clearly visible, and often coated with extremely fine particles. Larger agglomerations of ultrafine particles are also visible. In Port Talbot BF dust spheroidal particles are not observed, instead extremely fine angular particles are visible, including substantial amounts of carbon which appears as dark, flaky particles.

Interestingly, in samples from Scunthorpe and Redcar these dark, flaky carbon particles can also be observed, but not in the BOS dust from Port Talbot.

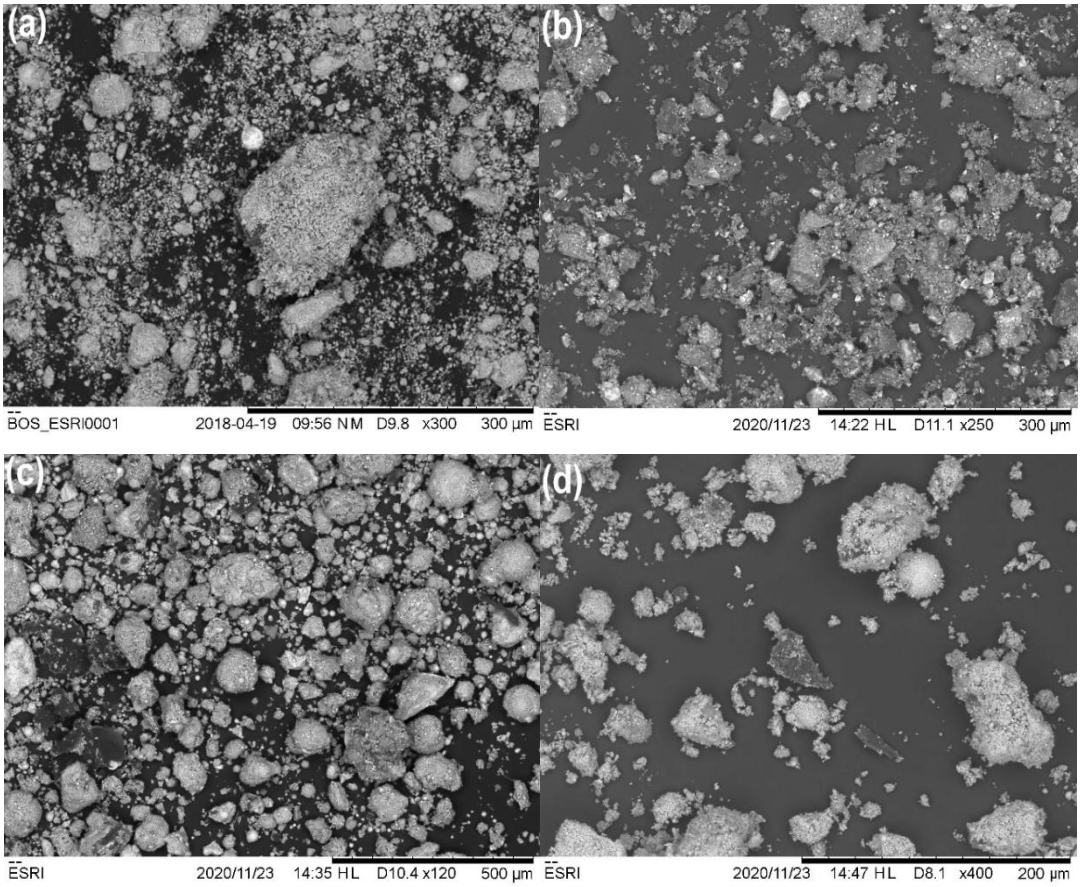

Figure 4.8. SEM analysis of Port Talbot BOS dust (a), Port Talbot BF dust (b), Scunthorpe BOS dust (c) and Redcar BOS dust (d).

Cross sectional SEM analysis (Figure 4.9) on each of the four materials show that the three BOS dust samples contain globular iron particles. These spheroids are formed by the ejection of droplets during the blowing period in a basic oxygen steelmaking vessel [43]. Through the cross-sectional analysis of the materials, the metallic iron core of these spheroidal particles can be imaged. This result is in excellent agreement with the work of Kelebek [39] who first demonstrated this metallic iron core observation in BOS dust, and it can be seen in all three BOS dust samples in this study but not in the BF dust.

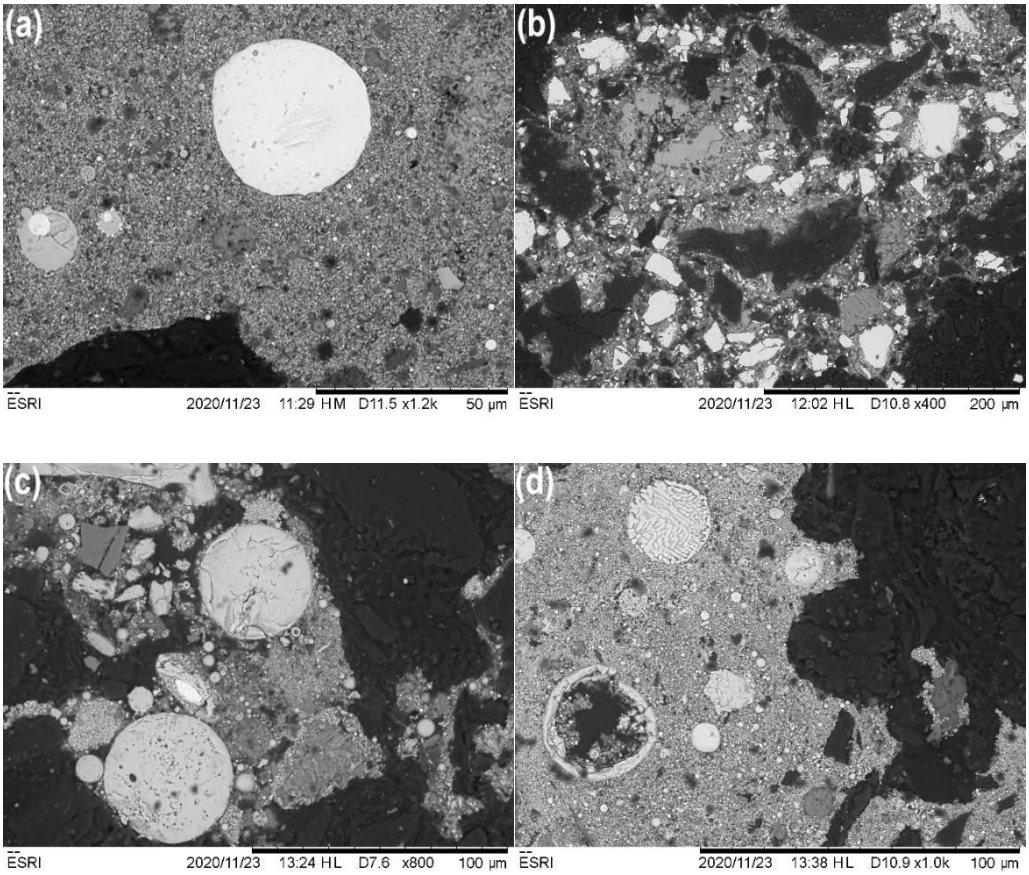

Figure 4.9. Cross sectional analysis of Port Talbot BOS dust (a), Port Talbot BF dust (b), Scunthorpe BOS dust (c) and Redcar BOS dust (d).

The angular shape of the material in the Port Talbot BF dust suggests a formation mechanism primarily consisting of abrasion, whereas the spheroidal particles present in all three BOS dust samples they share a similar, fluid ejection-based formation mechanism.

4.3.1.8 Combustion Analysis

Table 4.7 shows the results of combustion analysis for the four materials. As expected, the BOS steelmaking dust samples contain little carbon relative to the BF dust from Port Talbot. Fixed carbon is difficult to approximate for revert materials such as these, proximate analysis such as those performed thermogravimetrically for coals are inappropriate due to the reducible metals content of the material.

An approximation of carbon in the form of carbonate is given in Table 4.7 based on the carbonate decomposition loss at around 700 °C observed during TGA-DSC experiments.

The results indicate that the majority of carbon present in Port Talbot BF dust is available for reduction as expected. What was less expected however is that all three BOS dust samples showed significant carbon content that is not associated to carbonates and therefore may be useful as a reductant. It is unclear whether this carbon was introduced to the material as it was produced or whether it is the result of contamination and mixing during the stockpiling of the material.

Table 4.7. Combustion analysis results for Port Talbot BOS dust, Port Talbot BF dust, Scunthorpe BOS dust and Redcar BOS dust

	Composition (Wt. %)		
Material	**C**	**S**	**$C_{carbonate}$**
Port Talbot BOS dust	3.95	<0.001	2.18
Port Talbot BF dust	40.49	0.62	0.71
Scunthorpe BOS dust	6.74	0.005	0.75
Redcar BOS dust	9.69	0.014	0.75

Sulfur levels were expectedly low in samples produced during steelmaking, since hot metal has usually been desulfurized prior to charging into the BOS vessel. The level of sulfur in BF dust from Port Talbot was substantially higher, likely from the abraded coke and coal particles present in the material.

4.3.1.9 Mössbauer Spectroscopy

^{57}Fe Mössbauer spectroscopy was used to investigate the chemical environment of Fe species within the material. Samples were shown to be extremely chemically complex, with iron nuclei in many different oxidation states and environments. While it was not possible to assign all sites used in the data fitting with the appropriate level of confidence, important structural information can be gleaned and compared to observations in XRD analysis through spectra fitting.

Previous work in the literature suggested that ^{57}Fe Mössbauer spectroscopy can be utilized to detect and differentiate the small amounts of $ZnFe_2O_4$ that can be found in steelmaking dusts from spinel more easily than using powder XRD [142,143].

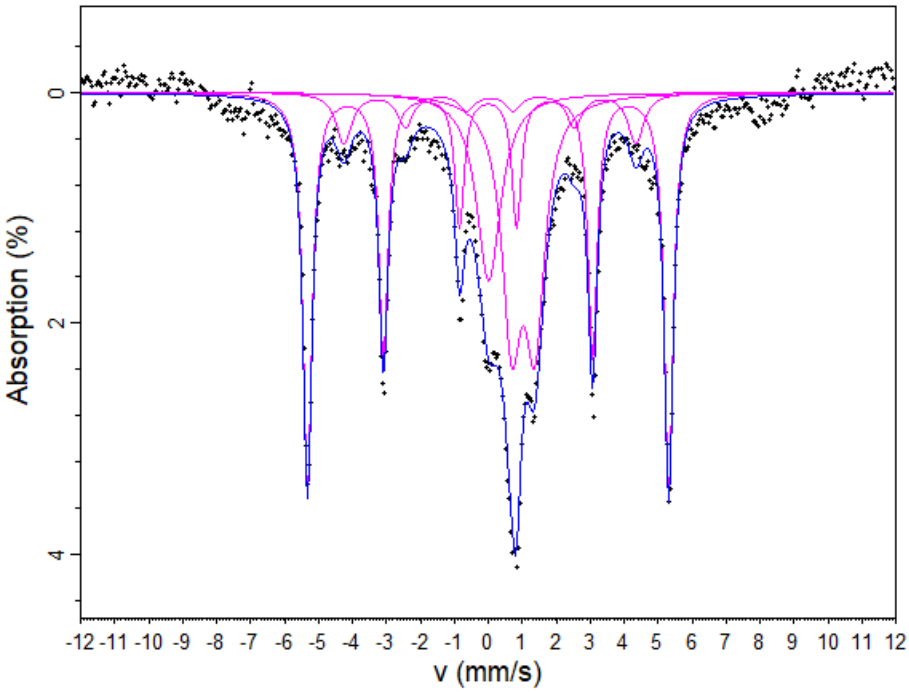

Figure 4.10. Mössbauer spectroscopy data and associated fitting pattern for Port Talbot BOS Dust. Data fitting is illustrated as a solid pink line.

Fitting of the data for the Port Talbot BOS dust shows a few easily assigned features (Figure 4.10). The sextet fitted with zero quadrupolar splitting and chemical shift likely corresponds to metallic α-Fe and the doublet (CS = 1.04 mm/s, QS = 0.67 mm/s) likely corresponds to Fe^{2+} in Wüstite (FeO) [143]. This is in good agreement with powder XRD analysis which also indicated the presence of metallic Fe and FeO.

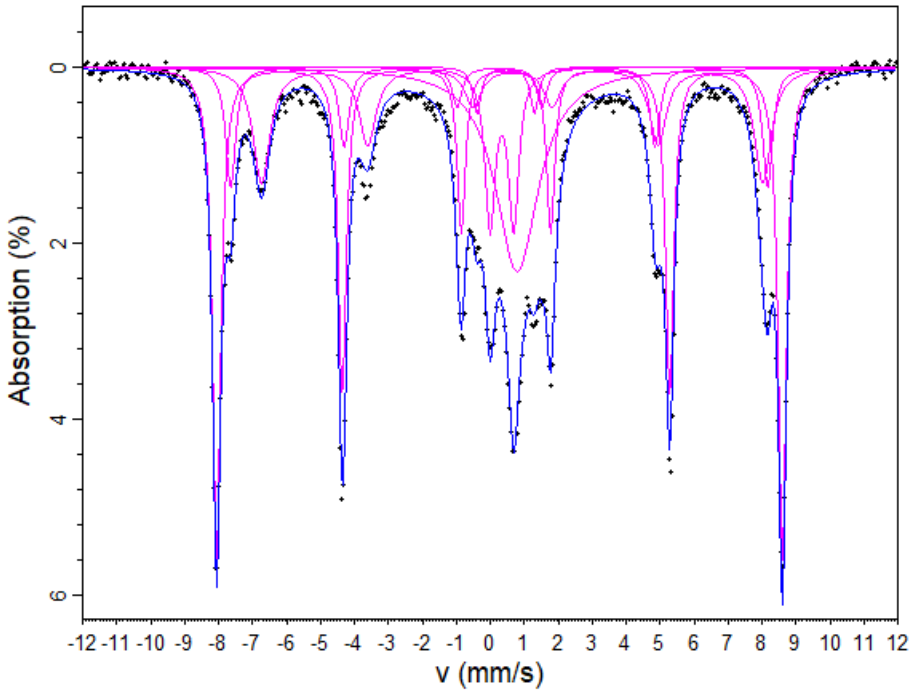

Figure 4.11. Mössbauer spectroscopy data and associated fitting pattern for Port Talbot BF dust. Data fitting is illustrated as a solid pink line.

For Port Talbot BF dust (Figure 4.11), a sextet (CS = 0.37 mm/s, QS = 0 mm/s) suggests the presence of hematite (α-Fe_2O_3), while a second sextet (CS = 0.66 mm/s, QS = 0 mm/s) indicated the presence of magnetite (Fe_3O_4) [144]. Again, this is in good agreement with powder XRD and metallic iron analysis which suggested Port Talbot BF dust was substantially more oxidized than the BOS dust samples.

Scunthorpe BOS dust (Figure 4.12) shows an exceptionally complicated spectral fit, due to the mineralogical complexity of the material. A sextet (CS = 0 mm/s, QS = 0 mm/s) corresponds well with metallic Fe as expected from the powder XRD pattern of the material, likewise a sextet (CS = 0.38 mm/s QS = 0 mm/s) likely corresponds to hematite (a-Fe_2O_3). A doublet (CS = 0.99 mm/s, QS = 0.69) suggests the presence of FeO.

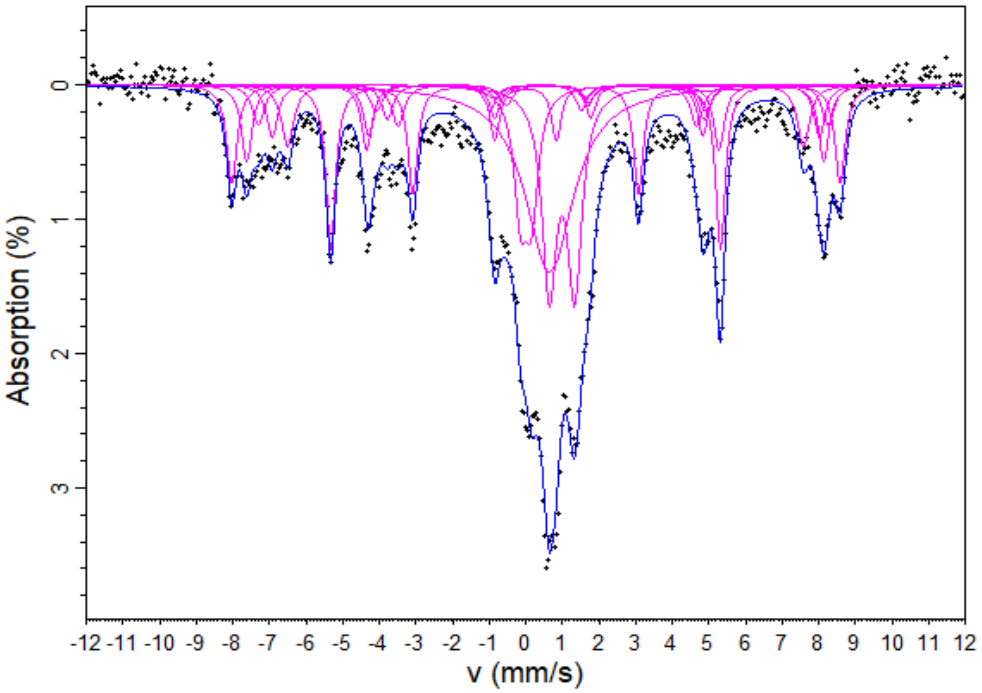

Figure 4.12. Mössbauer spectroscopy data and associated fitting pattern for Scunthorpe BOS dust. Data fitting is illustrated as a solid pink line.

Redcar BOS dust (Figure 4.13) also shows a great deal of complexity in the fitting of the data. Sextets correspond to hematite α-Fe_2O_3 (CS = 0.37 mm/s, QS = 0 mm/s), magnetite Fe_3O_4 (CS = 0.3 mm/s, QS = 0 mm/s), and metallic iron (CS = 0 mm/s, QS = 0 mm/s) while a doublet (CS = 1.03 mm/s, QS = 0.65 mm/s) suggest the presence of FeO.

It is worth noting that franklinite was not detected in any of the four samples via ^{57}Fe Mössbauer spectroscopic analysis. It is possible that a small amount of sub stoichiometric franklinite is present in the samples and is masked by overlapping signals around the region a characteristic hyperfine paramagnetic doublet would be expected (CS = 0.31 mm/s, QS = 0.70 mm/s) [143].

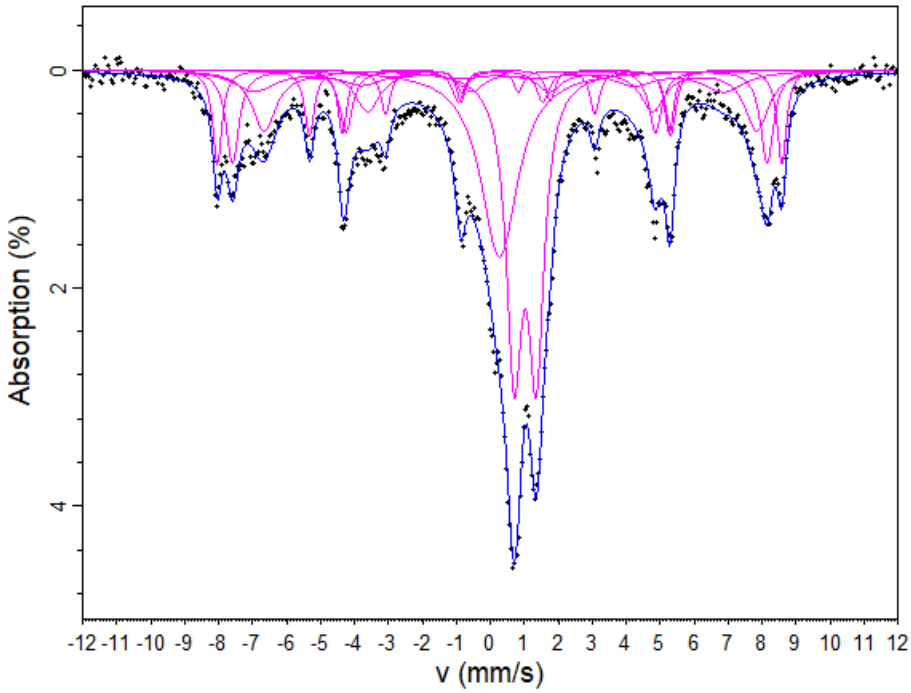

Figure 4.13. Mössbauer spectroscopy data and associated fitting pattern for Redcar BOS dust. Data fitting is illustrated as a solid pink line.

Overall, the results from the ^{57}Fe Mössbauer spectroscopy are in good agreement with powder XRD analyses but unfortunately, the complicated chemical environments that iron is present in within all four samples make parsing the region of the spectra where franklinite may be located is difficult and as such, for the two most complicated Redcar and Scunthorpe BOS dust samples the result is inconclusive.

4.4 Conclusions

Analysis of the samples from Port Talbot, Scunthorpe and Redcar has made clear that the materials are not suitable for direct recycling into the steelmaking process in their current condition. While the BOS dust materials are metallized and contain substantial Fe content, the zinc content is too high to consider agglomeration via sintering and charging to the blast furnace as a viable recycling route.

Crystallographic analysis via XRD diffraction suggested that material from Scunthorpe and Redcar may contain a small amount of sub-stoichiometric zinc ferrite. While ^{57}Fe Mössbauer spectroscopic analysis was unable to differentiate any franklinite spinel from the complicated mineralogy of the samples if it is indeed present. The observation that the Redcar and Scunthorpe material may contain some zinc in the

spinel form means hydrometallurgical processing may present process challenges such as lower zinc removal rates than expected.

These materials would be a prime candidate for recovery through pyrometallurgical processing that is not sensitive to volatile metal loading, such as a rotary hearth furnace. Pyrometallurgical processing has the primary advantage that it is much less sensitive to zinc mineralogy in the feedstock material than hydrometallurgical processing [50].

They are highly metallized meaning reductant use and subsequent CO_2 emission is minimized and a high productivity for the plant. A furnace process such as FASTMET [120], DRyIron [121] or INMETCO [78] would be suitable for recovery of the ferrous material as DRI.

The Port Talbot BF dust could be utilized as a supplementary reductant in a rotary hearth furnace to displace coal to reduce the environmental impact of the process. Processing of BOS dust with BF dust is not a new concept, McClelland et al. reported on the chemistry of typical input and output material to Kobe Steel's Kakogawa FASTMET plant [120]. The study estimated that FASTMET production costs for DRI with chemical composition as shown in Table 6, from BF dust, EAF dust and BOS dust was between $150 - $200 per tonne of DRI, and the similarities between the raw materials used are clear.

Table 4.8 Raw material and produced direct reduced iron chemical composition for the commercial Kakogawa FASTMET plant.

	Composition (Wt. %)								
Material	**Fe_{Tot}**	**Fe_{Met}**	**C**	**S**	**SiO_2**	**Al_2O_3**	**CaO**	**MgO**	**Zn**
Kakogawa BF Dust	31.8	-	37.6	0.70	4.10	-	3.1	-	1.2
Kakogawa BOS dust	53.6	-	0.70	0.17	6.18	0.315	5.0	0.185	2.54
Kakogawa FASTMET DRI	68.0	57.8	2.00	0.52	5.95	-	4.35	-	-

The major disadvantage of the use of BF dust as a reductant is inclusion of sulfur into the metallized product. The produced DRI is metallized enough to be directly integrated as a scrap substitute into a basic oxygen steelmaking vessel but the high levels of sulfur in the material would limit its use and value. Instead, so-called revert

DRI (DRI produced from recycled steelmaking by-product materials) is usually recycled to a blast furnace, which is less sensitive to high sulfur loading but with a lower cost benefit than recycling to the BOS vessel [145].

The United Kingdom would be an excellent candidate for a large scale pyrometallurgical processing plant for zinc bearing wastes due to the suitability of material for integration into the process, the relative ease of material acquisition due to the countries geographic size as well as the fact that steel producing sites typically have excellent rail and sea freight infrastructure for movement of material to a centralized processing site.

5. DRI PRODUCTION LABORATORY TRIALS

5.1 Introduction

To assess the suitability of RHF processing of zinc contaminated dusts from Port Talbot, a laboratory study was undertaken using benchtop heat treatment equipment. RHF processing as described in 2.5.2 is extremely broad, with subtle differences between different processing routes.

While in the literature, iron reduction and zinc removal are relatively well explored, the behaviour of other elements such as sulfur [146], alkali metals such as sodium and potassium, and lead [147] are comparatively under-reported but of interest to the steel by-product recycler.

The composition of the reducing gas present within RHF processes at the hearth layer is surprisingly under-reported. Self-reducing agglomerates, which is a commonly used term for intimate mixtures of carbon and iron oxide briquetted or pelletized for reduction, generate their own shell of reducing gas in the immediately vicinity of the pellet and as such can undergo reduction under conditions that are overall rather oxidizing due to a localized reducing atmosphere surrounding the pellet.

Due to the gradient of oxidizing potential between the furnace hearth where the pellets are located, and the burners which supply heat to the process (Figure 2.10), it is difficult to dynamically predict the gas atmosphere composition surrounding individual pellets at a given point of the reduction process.

Much of the literature in the field of self-reducing agglomerates used to feed the RHF utilize heat treatment under an inert gas atmosphere to remove the influence of high oxygen activity on the reactions and also impede reoxidation during cooling [124,148–152]. While this does allow for high reproducibility in experimental analyses, the critical issue with assessing the performance of self-reducing agglomerates under an inert purge gas in comparison to real world RHF operation is that the continuous disturbance caused by a continuous flow of inert purge gas of the reducing gas shell formed on the outside of the pellet during heat treatment means that solid-solid reactions between carbon and metal oxides tend to dominate leading to discrepancies between laboratory and process measurements.

Ideally, to effectively replicate the RHF a combustion furnace similar to the experimental rig at McMaster University would be utilized (Figure 5.1) [153]. By supplying heat to the furnace through a gas burner rather than via electric resistance heating, much more realistic process conditions can be achieved as the pellets interact with the combustion products as well as each other in the commercial process. Detailed

and multi-point off-gas analysis also provides an excellent window into the gas-solid interactions within the furnace.

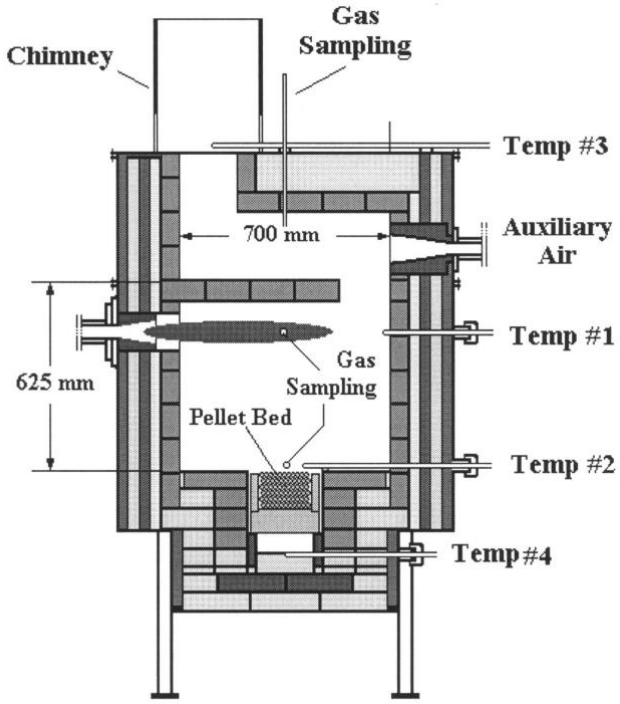

Figure 5.1. The experimental furnace at McMaster University for replicating the conditions within the RHF [153]. Adapted with permission copyright Taylor & Francis.

However, due to the exceptional equipment costs and the complicated engineering that the construction of a combustive furnace such as the one in Figure 5.1 an electric resistance box furnace was selected as the heat treatment method for trials.

Rather than opting to run experiments in inert gas, running samples in air within an electric resistance chamber furnace with no purge gas was selected for several reasons.

Firstly, the lack of purge gas allows for more realistic carbon oxidation and development of a reducing gas shell around the self-reducing agglomerates and allows for a more realistic diffusion of reactive gases into and out of the pellet. This becomes especially significant with regards to volatile metal volatilization reactions which are rapidly reversible.

Additionally, by heat treating samples in a chamber furnace, samples can be hot discharged from the furnace and gas quenched to halt all reactions. This ability to rapidly cool samples allow for more effective sampling and is also more representative

of the RHF where hot DRI is typically discharged via a water cooled rotating screw at extremely high temperatures (> 1200 °C) and cooled rapidly [154].

Under inert atmosphere, it is a reasonably safe assumption that the carbon depleting from the pellet is almost entirely reacting with reducible oxygen bound to metals within the agglomerate. However, in real world RHF operation carbon is consumed by competing reactions, carbon can react with O_2 present within the furnace, directly with oxides, or with CO_2 via the reverse Boudouard reaction. The actual carbon requirement for effective zinc removal and iron reduction may therefore be somewhat higher than under inert conditions, as carbon is also required to sustain the reducing gas shell which enables the reduction to take place.

Finally, operating in an air atmosphere allows for study of the issue of reoxidation in DRI. It is widely accepted that reduction in the RHF proceeds from the boundary of agglomerates inwards [90], with metallic iron forming and carbon in the pellet gradually depleting. Of course, once the boundary layers are reduced and depleted of carbon, the porous boundary layer of iron is at an extremely high temperature and relatively high surface area and therefore kinetically and thermodynamically vulnerable to reoxidation, should the reducing gas shell around the pellet become CO deficient.

This would constitute an undesirable loss of value in the DRI product and therefore understanding the conditions that may lead to overfiring and therefore reoxidation of Fe at the boundaries of the pellet is worthwhile.

Ellingham diagrams are a useful tool for predicting the conditions in which reduction of metals will take place. By plotting the standard Gibbs free energy change (ΔG^0) against T for metal oxide formation reactions, it's possible to visualize the conditions in which a given metal will be reduced by carbon, hydrogen, carbon monoxide or other metals. The point at which the line for a metal-metal oxide formation reaction crosses the line for the formation of CO from C is the temperature at which CO can reduce the metal oxide to its elemental form.

It can be seen from the Ellingham diagram (Figure 5.2) that at RHF temperatures of 1200 °C the reduction of iron oxides to metallic iron is thermodynamically feasible by CO and by solid C. The reduction of Pb, Zn, K and Na is also seen to be feasible at these temperatures.

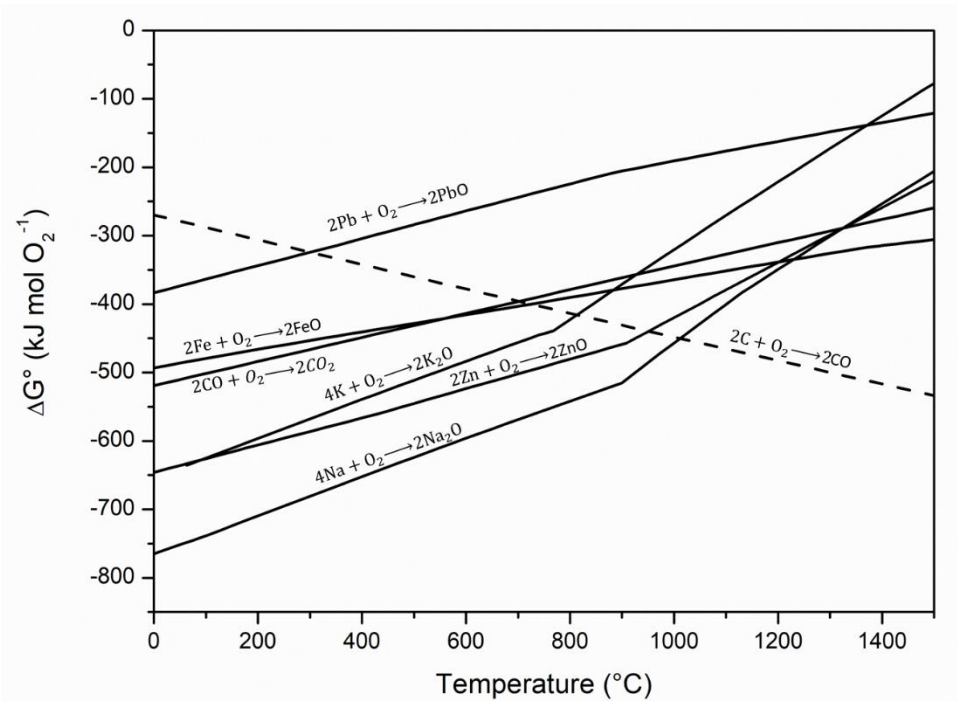

Figure 5.2 Ellingham diagram for selected oxides of Fe, Pb, K, Na and Zn generated using FactSage 7.3

The boiling points of Zn, K and Na can be seen on the Ellingham diagram in Figure 5.2 as a change in the slope of the line for Gibbs free energy change (the slope of the line showing Gibbs free energy change of a reaction against temperature is equal to the change in entropy ΔS°). The boiling points of those metals is 907 °C, 759 °C, and 883 °C respectively therefore under RHF conditions carbothermal reduction of Zn, K and Na to generate metallic vapour is thermodynamically feasible and is a viable method of separating those elements from iron in the furnace feed.

Metallic Pb does not boil until 1749 °C, well above economical RHF operational temperatures but at 1200 °C the vapour pressure of Pb is approximately 0.025 bar [155] which while seemingly negligible may lead to substantial reduction and separation of lead from RHF pellets given the reducing conditions and sweeping horizontal gas flow removing metal vapors from the reaction zone.

It is the experimental aim of this chapter to attempt to explore the RHF reduction of self-reducing agglomerates in a wider context than just iron and zinc reduction. Na, K, Pb and S content of fired pellets are all of relevance for the recycling of fired pellets back into the steelmaking process and therefore this is a research avenue worth exploring. As many literature examples utilize inert atmospheres for reduction, an interesting comparison will also be provided by the study of Zn and Fe reduction in air as in this study compared to previous, inert atmosphere experimentation.

5.1.1 Benchmarking Visit to a Commercial RHF

As of the time of writing, there are no active RHF plants operating within Europe to process zinc bearing by-product dusts and sludges into a recyclable DRI product. Therefore, to effectively benchmark DRI produced from UK material against actual commercial production a visit was undertaken to a 200,000 t/year rotary hearth furnace at a large integrated steel plant in southern China.

The furnace was fed with cold-bonded agglomerate mixtures of BF dust, BOS dust, and an unspecified amount of additional coal, briquetted into pillow shapes using a starch-based binder to allow for sufficient strength to charge into the furnace (Figure 5.3a). Briquettes were then air dried using recirculated hot air from the furnace, before charging to the RHF.

The briquettes were heated from ambient temperature to 1275 °C in a single layer with a total hold time within the furnace of 18 minutes before discharge via water-cooled screw. The removed zinc was collected via bag filter as a crude oxide (Figure 5.3b) for sale to zinc refiners and the produced DRI (Figure 5.3c) was air cooled and charged to the BF.

Figure 5.3. Unfired briquettes (a), secondary RHF off-gas dust (b) and metallized DRI (c) produced via a commercial RHF

Chemical analysis of the fired and unfired briquettes is shown in Table 5.1 as determined via the methods described in Chapter 3 supplemented with XRF analysis performed at Tata Steel BOS Labs, it can be seen that zinc removal performance is high with 94.9% removal rates during the reaction time, but iron metallization is surprisingly low. It's likely that this DRI was charged back to the BF rather than the BOF due to the high levels of gangue and poor metallization. Excessive gangue in the BOF is not desirable due to increased slag generation and higher flux requirements [90].

Table 5.1 Chemical analysis of fired and unfired briquettes from commercial RHF plant.

	Composition (Wt. %)										
Material	**Fe_{tot}**	**Fe_{met}**	**SiO_2**	**Al_2O_3**	**CaO**	**MgO**	**Na**	**K**	**Zn**	**C**	**S**
Unfired Briquette	46.26	BDL	3.10	1.41	8.41	2.93	0.18	0.10	1.17	12.07	0.02
DRI	66.34	29.50	6.09	2.64	11.04	3.42	BDL	BDL	0.06	0.30	0.04

The production economics of including DRI in the BF charge is immensely complicated and reliant on global factors such as ore prices as well as local factors such as energy prices [156], it seems that the operators of the RHF benchmarked herein deemed

that the increased energy expenditure of producing more metallized DRI was not worth the process benefits to the BF. As such it appears the operators simply processed the material as minimally as possible, just until the Zn is below tolerable limits for the BF before carrying out the rest of the reduction within the BF itself and therefore benefiting from the process economy of large-scale BFs (5 mt per year) at the plant.

It's likely these value-in-use considerations would have to be made on a case-by-case basis depending on the location and production costs of any new RHF.

It is notable that the amount of sulfur present in both the fired and unfired briquettes are extremely low (0.02 and 0.04 wt. % respectively), far lower than what would be expected for a similar briquette produced from UK material (Table 4.7). It may be the case that the BF dust produced at the plant used for benchmarking is lower in sulfur due to differences in locally available coke and coal used in the BF, but this is speculative. The unknown quantity of additional coal supplied might also play a role, as while expensive, extremely low sulfur coal is available commercially.

SEM analysis of the unfired and fired briquettes shows angular, dark particles of carbon derived from the BF dust within the pellet mixture coated in the fine iron oxides typical of BF and BOS dusts (Figure 5.4). The fired pellet contains the porous, open structure of directly reduced metallic iron [157] but some unreduced Wüstite which appears granularly in the lower left corner of the image.

The angular particles of carbon present in the unfired pellet are not observed in the fired pellet, due to the participation of carbon in the reduction reactions in the process. This is supported by the chemical analysis of the fired pellet in Table 5.1 showing very little residual carbon in the pellet (0.30 wt. %).

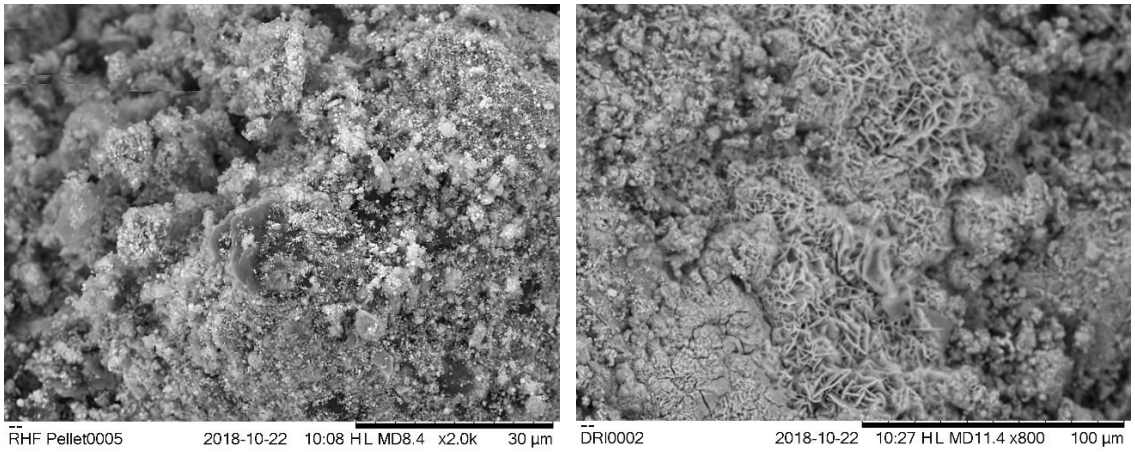

Figure 5.4. SEM micrographs of unfired commercial RHF pellets (left) and fired DRI (right).

Analysis of the secondary dust produced by the commercial RHF via SEM-EDX shows an agglomeration of extremely fine particles (Figure 5.5). The material is extremely rich in zinc, but also contains small particles of Pb, K and Na, all of which can volatilize at RHF temperatures. These metals appear to exist as a mixture of oxides and chlorides which is consistent with literature examples [72].

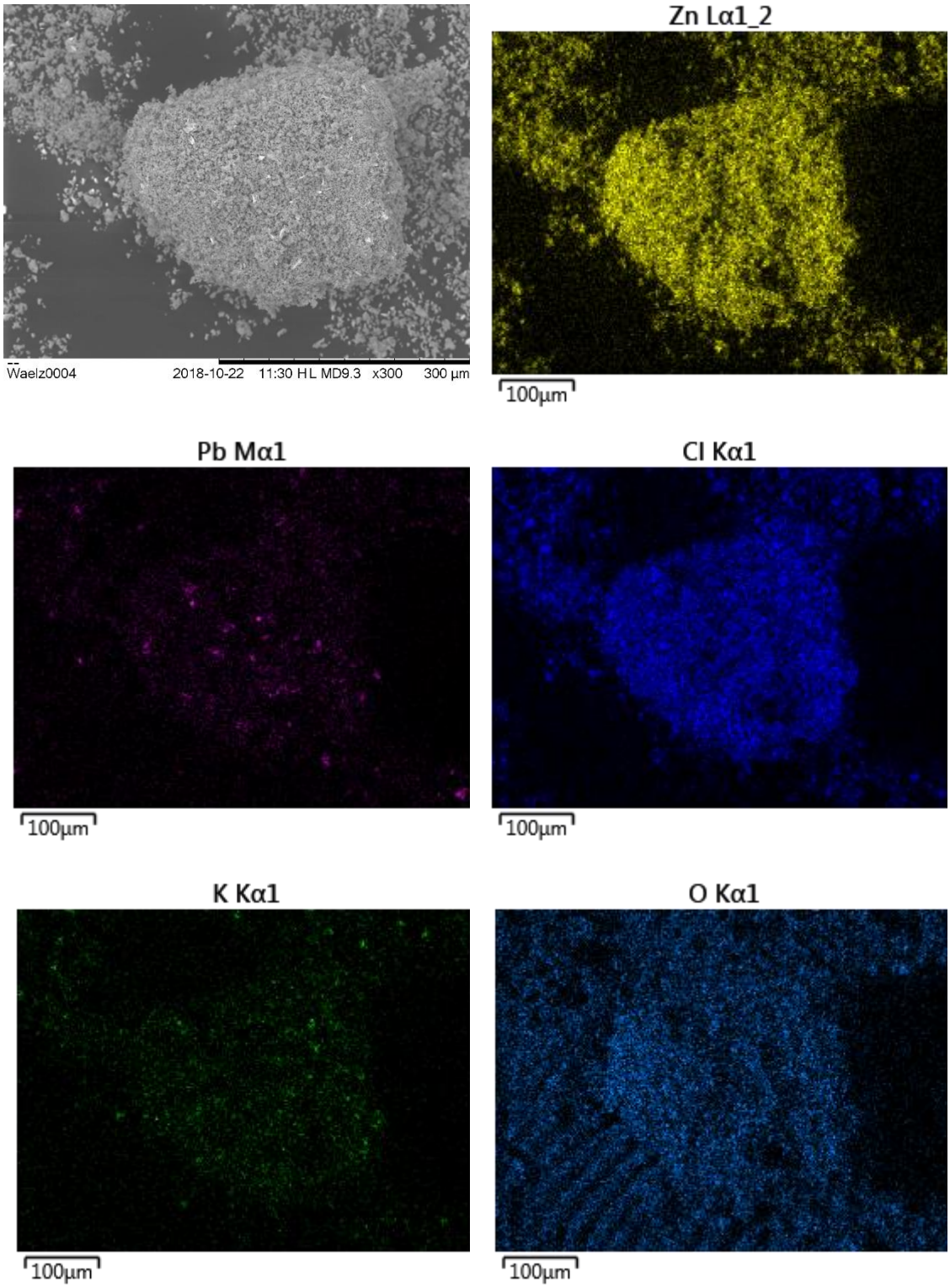

Figure 5.5. SEM-EDX analysis of RHF off-gas dust from a commercial plant.

EDX analysis of the dust indicated a composition of approximately 46.5% Zn, 39.3% O, 9.2% Cl, 1.7% Pb, 1.1% K and 0.8% Fe, which is in reasonable agreement with literature examples of RHF off-gas dusts and waelz oxides [100,158].

The presence of a small amount of lead within the off-gas dust may potentially present a hazard due to the metal's acute toxicity to humans. It seems likely that this lead was introduced into the process via the BOS dust used within the pellet. Consumer scrap can be contaminated by lead through leaded paint coatings, lead based solder or as an impurity in galvanized coatings [159]. Some recovery methods for zinc from waelz oxide or RHF off-gas dust are able to simultaneously reduce and recover lead as well as zinc [99,160,161] so the presence of Pb in the dust does not preclude it from recycling. It may however have some impact on the design of any plant in the UK, to minimize airborne dust hazards.

Based on the trace metal analysis shown in Table 4.1 earlier in the thesis, small amounts of lead are present within the BOS dust and BF dust material from the UK, therefore concentration of lead within the off-gas dust produced in the benchmarking study is worth monitoring.

5.2 Experimental Methods

BF dust from Port Talbot was selected as the reducing agent for benchmarking, based on the use of BF dust in the commercial RHF in 5.1.1. Dried BF dust from Port Talbot was mixed with BOS dust from Port Talbot to prepare six blends with varying molar ratios of fixed carbon and reducible oxygen (C/O).

Blend proportions are shown in Table 5.2 to give six blends with chemical compositions shown in Table 5.3, dried BF dust and BOS dust were weighted individually into the drum of a rotary mixer in the proportions listed to give a total blend weight of 500 g. Samples were mixed dry at 30 rpm within the mixer for 1 hr to ensure homogeneity.

Table 5.2. Proportion of BOS dust to BF dust in experimental blends

	Composition (Wt. %)	
C/O ratio	**BOS Dust**	**BF Dust**
1.0	66.5	33.5
0.9	69.5	30.5
0.8	72.3	27.7
0.7	75.5	24.5
0.6	78.5	21.5
0.5	81.7	18.3

Blends were apportioned into 13.5 g (dry basis) measures based on the observation that green briquettes from Section 5.1.1 were 13.5 g on a dry basis and deionized water (8 wt. %) was added and mixed manually until coarsely granulated using a spatula.

Briquettes were then prepared by compression of a weighted measure of blend in the 32 mm die of a Retsch PP 25 pellet press (120 bar, 60 s residence time). Green pellets were then dried in a laboratory oven at 90 °C before storing in a vacuum desiccator prior to heat treatment.

Table 5.3. Chemical composition of the blends used for RHF benchmarking.

Blend C/O ratio	Composition (Wt. %)									
	Fe_{Tot}	SiO_2	Al_2O_3	CaO	MgO	Na	K	Zn	C	S
1.0	58.12	3.41	1.11	8.39	1.03	0.12	0.14	2.07	13.56	0.21
0.9	59.54	3.31	1.04	8.59	1.04	0.12	0.13	2.13	12.35	0.19
0.8	60.86	3.22	0.97	8.78	1.05	0.12	0.13	2.19	11.22	0.17
0.7	62.37	3.12	0.90	9.00	1.07	0.12	0.13	2.26	9.92	0.15
0.6	63.78	3.02	0.83	9.21	1.08	0.12	0.12	2.32	8.71	0.13
0.5	65.29	2.91	0.76	9.42	1.09	0.12	0.12	2.39	7.41	0.11

For heat treatment, dried cool pellets were charged to a 200 ml clay bonded silicon carbide (Si-C) crucible with an inner diameter of 60 mm before placing into the work chamber of a Carbolite RHF1600 16/8 chamber furnace.

Clay bonded Si-C was selected for experimentation preferentially to Al_2O_3 which suffers from poor heat transfer properties as well as a lack of inertness to iron oxide at reaction temperatures due to the formation of iron aluminates [162]. Si-C was also preferable to clay-graphite due to the much-improved oxidation properties of Si-C at the extreme reaction temperatures used [163,164].

The furnace was then ramped from room temperature at a rate of 20 °C per minute to the working temperature between 1100 °C and 1350 °C (50 °C step size), before dwelling for a period of 0 to 60 (15-minute step-size) minutes. Following the dwell time at working temperatures, crucibles were hot discharged from the furnace

using a set of steel crucible tongs. The hot pellets were then purged under a flow of 2 L/min of argon for a period of 120 seconds to cease chemical reactions and prevent reoxidation.

For analysis, samples were pulverized to < 150 µm using a Fritsch Pulverisite 6 ball mill at 500 rpm and stored in a desiccator before digestion MP-AES analysis, metallic iron determination, combustion analysis and powder x-ray diffraction analysis as set out in Chapter 3.

A process flow for the sample preparation and analysis is set out in Figure 5.6. The large dried samples of BOS dust and BF dust from Port Talbot characterized in Chapter 4 were stored in sealed drums (Figure 5.6a) prior to blending (Figure 5.6b) and pelletizing in the hydraulic press (Figure 5.6c), unfired pellets were then heat treated (Figure 5.6d) to yield pellets of fired DRI (Figure 5.6e) and pulverization in the ball mill (Figure 5.6f).

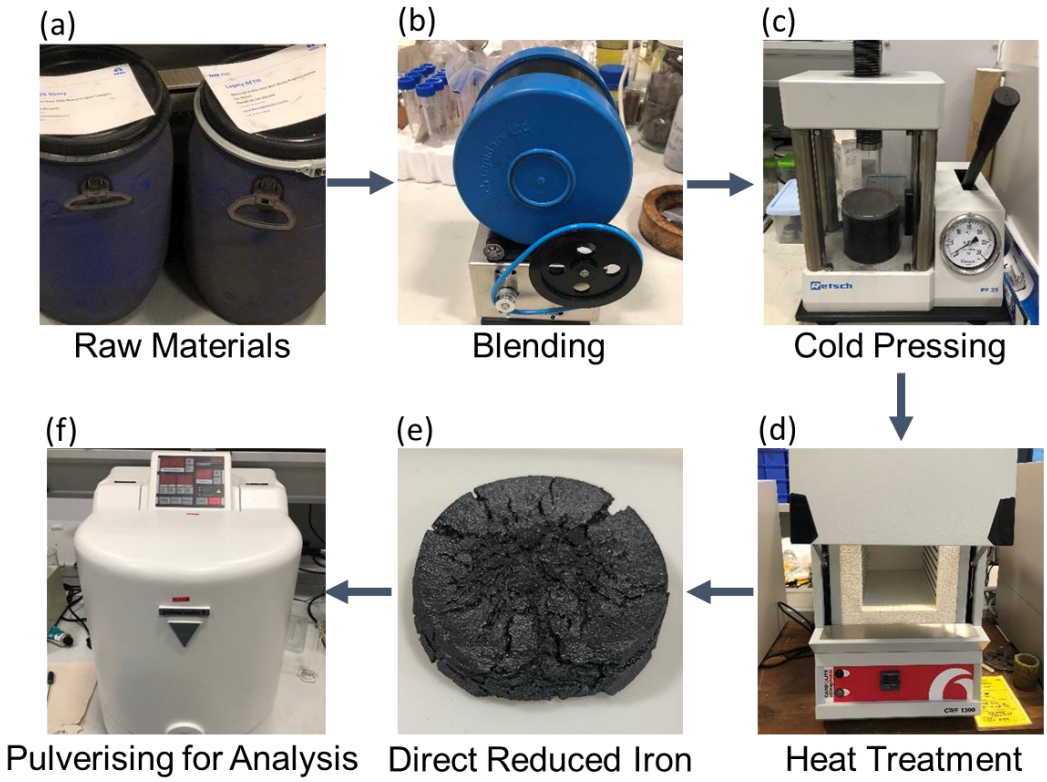

Figure 5.6. Experimental process flow for sample preparation, heat treatment and analysis. Raw materials stored in drums (a), benchtop rotary mixer (b), hydraulic press (c), box furnace (d), pellet of fired DRI as retrieved from the furnace (e), and the ball mill used to pulverize samples prior to chemical analysis (f).

5.3 Results and Discussion

5.3.1 Carbon Analysis of Fired Pellets

Carbon's role in the RHF is twofold, it acts as the reducing agent for the reducible metals and therefore drives zinc removal and iron reduction, but it also acts as sacrificial cover for the freshly reduced iron. Once the available carbon in the pellet has depleted, it stands to reason that some reoxidation of the DRI produced will occur.

Figure 5.7 shows the carbon content of fired pellets for each of the six different blends at varying hold time and temperature. As expected, increased temperature and hold time leads to a depletion of carbon within the pellets but relatively little carbon depletion appears to occur at temperatures < 1100 °C. For the C/O = 1.0 blend, the level of carbon in the pellet remains above 1 wt. % at all temperatures until t = 60 min.

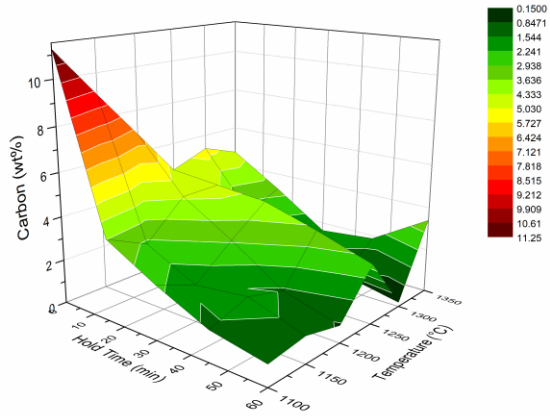

(a)

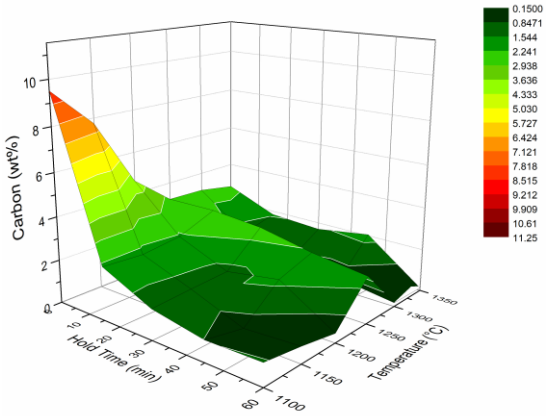

(b)

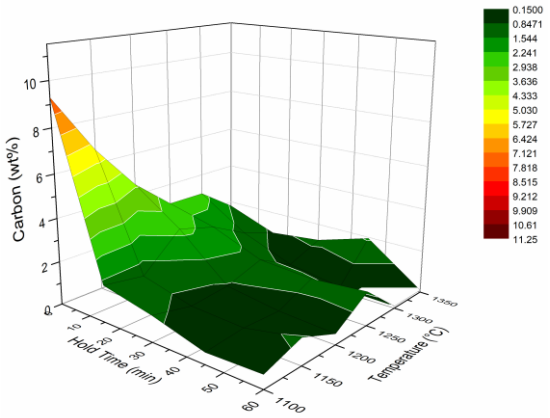

(c)

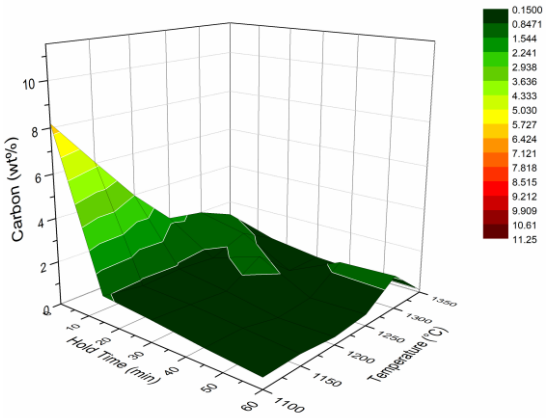

(d)

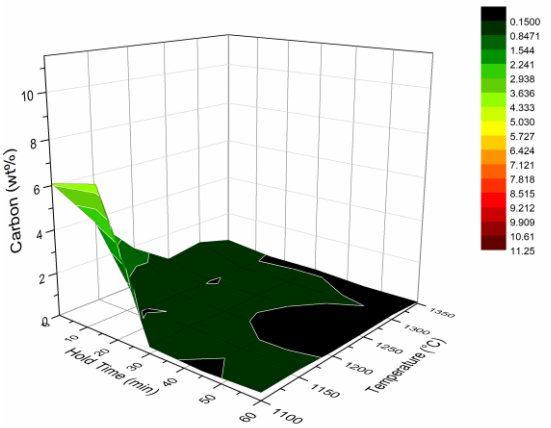

(e)

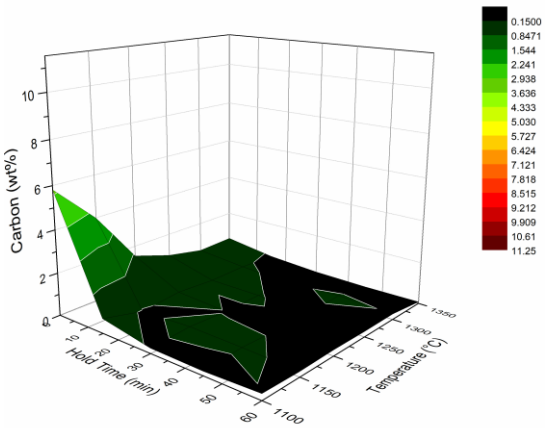

(f)

Figure 5.7. 3D surface plots of the carbon content (wt. %) of fired pellets with respect to hold time (min) and temperature (°C). C/O = 1.0 (a), C/O = 0.9 (b), C/O = 0.8 (c), C/O = 0.7 (d), C/O = 0.6 (e), and C/O = 0.5 (f).

For lower carbon blends (C/O = 0.5 – 0.7) a near total carbon depletion is observed at T > 1200 °C and t > 30 min. It would therefore be expected that reduction reactions would cease under those conditions and reoxidation of the freshly reduced iron becomes a possibility as the oxidizing atmosphere of the furnace attacks the surface of the pellet.

The carbon content of pellets removed from the furnace as soon as the reaction temperature was reached (t = 0) is shown in

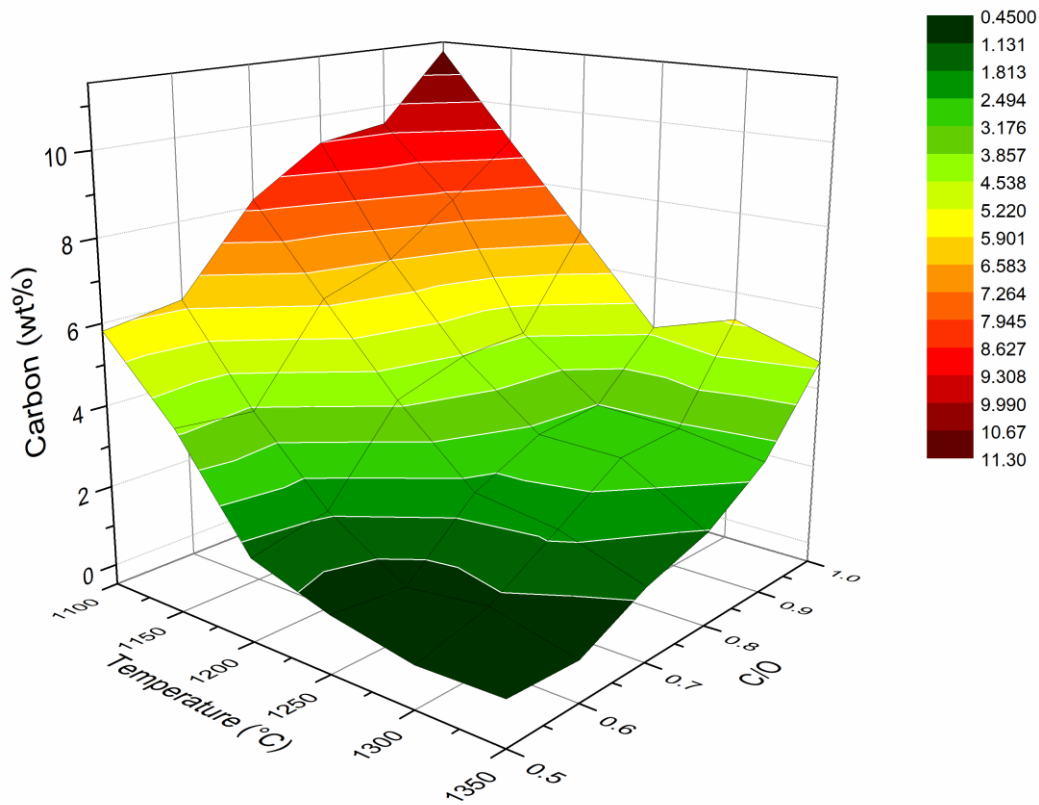

Figure 5.8, and shows that for the blends with low initial carbon levels (C/O = 0.5 – 0.6) the ramping period within the furnace is sufficient to almost completely burn out carbon in the pellet by the time the furnace reaches 1350 °C.

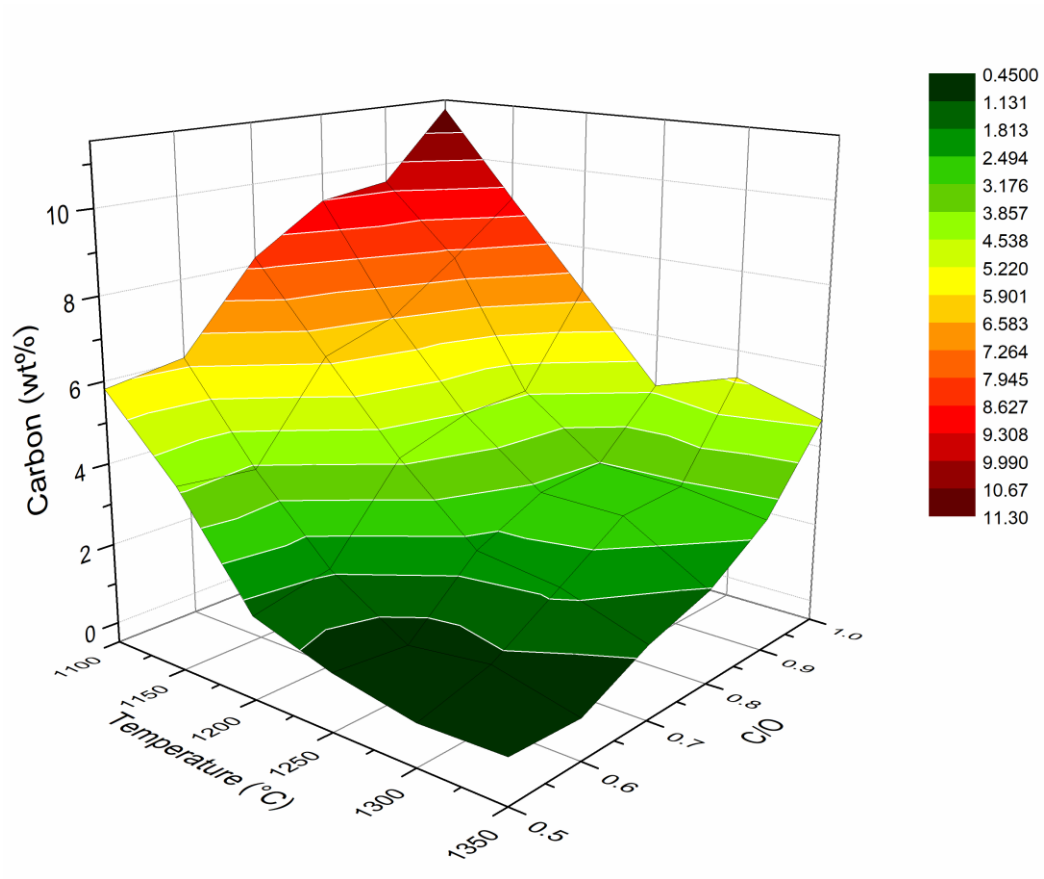

Figure 5.8 3D surface plot of the carbon content (wt. %) of fired pellets heated to reaction temperature at 20 °C/min and immediately withdrawn and quenched (t = 0).

An important caveat of this data is that the carbon analysis utilized herein is measuring total carbon within the material, with no distinction between organic carbon (unreacted coal), carbon dissolved in the reduced iron and also inorganic carbide compounds such as Fe_3C which is common in gas DRI [165]. Powder XRD can distinguish between metallic iron and iron carbide (Fe_3C) and will therefore be a useful tool in exploring these results further.

An extremely important observation based on the literature is that while maintaining carbon levels is significant for driving forward reduction reactions in the RHF and carbon dissolved within solid reduced iron is favorable from a steelmaking perspective [66], excess unreacted carbon present in the pellet post-reaction is highly undesirable. Lee et al described the relationship between initial carbon level, final carbon level and the mechanical strength of fired pellets [166] and noted a marked loss in pellet strength at residual carbon levels above 1 wt. % in the fired pellets due to increased void space and reduced sintering of metallic iron and bonding phases.

Should the DRI produced via an RHF be destined for the BF as a recycling route as in Section 5.1, mechanical strength of the product becomes an extremely important consideration due to the requirement of pellets in the BF to support the burden above them in the furnace. This observation is supported, anecdotally however, from experiences handling hot pellets during their removal from the furnace using a set of tongs – 'underfired' pellets reacted at 1100 °C were significantly more delicate to handle than their counterparts reacted at higher temperatures.

Excessive carbon input is also undesirable due to the increase in sulfur loading to the pellet, which is an undesirable tramp element that's predominately sourced from the BF dust used as a reductant rather than the BOS dust.

It's likely a compromise will have to be struck about supplying enough carbon to the pellet to complete the zinc removal reactions and drive high metallization of iron but without introducing unnecessary sulfur or compromising the fired pellets mechanical strength in a way that may preclude its introduction to the BF.

5.3.2 Sulfur Analysis of Fired Pellets

Sulfurs presence in steelmaking and ironmaking raw materials is generally considered undesirable due to its negative effect on steels mechanical properties and associated expense in its removal [167]. The S content of the fired pellets will have a significant impact on the value in use of the produced DRI.

The sulfur in the unfired pellets is primarily confined to the coal, coke and char particles originally sourced from the BF dust utilized as a reductant (Figure 4.8b). Figure 5.9 shows the change in the S content of fired pellets for each blend of BF dust and BOS dust with respect to temperature and hold time. As expected, the initial content of sulfur in the blends is an extremely significant factor in the residual sulfur post-reaction. Due to the multiple simultaneous gravimetric reactions occurring (oxidation of carbon, loss of oxygen from oxide material, volatilization of Zn, Na etc.) the S content of the fired pellets is seen to increase from initial values at 1100 °C and t = 0 min for all blends as S concentrates into the reducing mass of the pellet as it undergoes reduction.

Interestingly, long hold times at relatively low temperatures of 1100 °C is seen to dramatically desulfurize the DRI with samples at T = 1100 °C, t = 60 min for each blend being reduced to < 0.05 wt. % which is not observed for higher temperatures. A possible explanation for this may be that sulfur readily dissolves in metallic iron, and

tends to accumulate on the boundary layers between reduced iron and the residual carbon particles during direct reduction [146]. It may be the case that at these low temperatures, there is not sufficient metallic iron within the pellet for the newly liberated sulfur to dissolve into. The solubility of sulfur within Wüstite (FeO) is so low as to be reported at zero in some studies [168] and therefore if metallization of Fe is low at T = 1100 °C, t = 15 – 60 min then as carbon depletes from the pellet sulfur may be vacating the pellet via the gas phase as SO_2 as there is not sufficient available metallic iron to dissolve into.

A similar phenomenon is observed for the lower carbon blends at higher temperatures and hold times (C/O = 0.5 – 0.7, T = 1350 °C, t = 15 – 60 min), where sulfur levels are seen to dramatically decrease with extended hold time.

Based on the carbon analysis in Figure 5.8, this may be a result of burnout of carbon in the pellet under those conditions, leading to an increased oxygen activity at the surface of the pellet exposing freshly reduced iron to oxidizing gases. Sulfur dissolved within iron with readily react with atmospheric oxygen at high temperatures to form SO_2 which may go on to further oxidize to SO_3 via Equation 5.1 and 5.2 and vacate the pellet via the gas phase:

$$[S] + \{O_2\} \longrightarrow \{SO_2\} \tag{5.1}$$

$$2\{SO_2\} + \{O_2\} \longrightarrow 2\{SO_3\} \tag{5.2}$$

The behaviour of sulfur in the RHF is not widely reported in the literature. Inaba and Kimura examined the behaviour of sulfur within coal-iron oxide agglomerates under a mixed N_2-H_2 gas atmosphere [146] but at the time of writing no comprehensive study of the behaviour of S within coal-iron oxide agglomerates under a combustive or oxidizing atmosphere appears to exist in the literature.

Inaba and Kimura stipulated that increased hydrogen content in the reducing gas stream and increased temperatures lead to relatively effective desulfurization of coal-iron oxide pellets, with a 30% - 70% H_2-N_2 atmosphere leading to a 50% decrease in pellet sulfur content during heat treatment at 1300 °C for 8 min. Under the hydrogen reducing atmosphere, sulfur was removed from the pellet as H_2S gas, vastly differing from the proposed mechanism herein for experimentation without a controlled gas atmosphere.

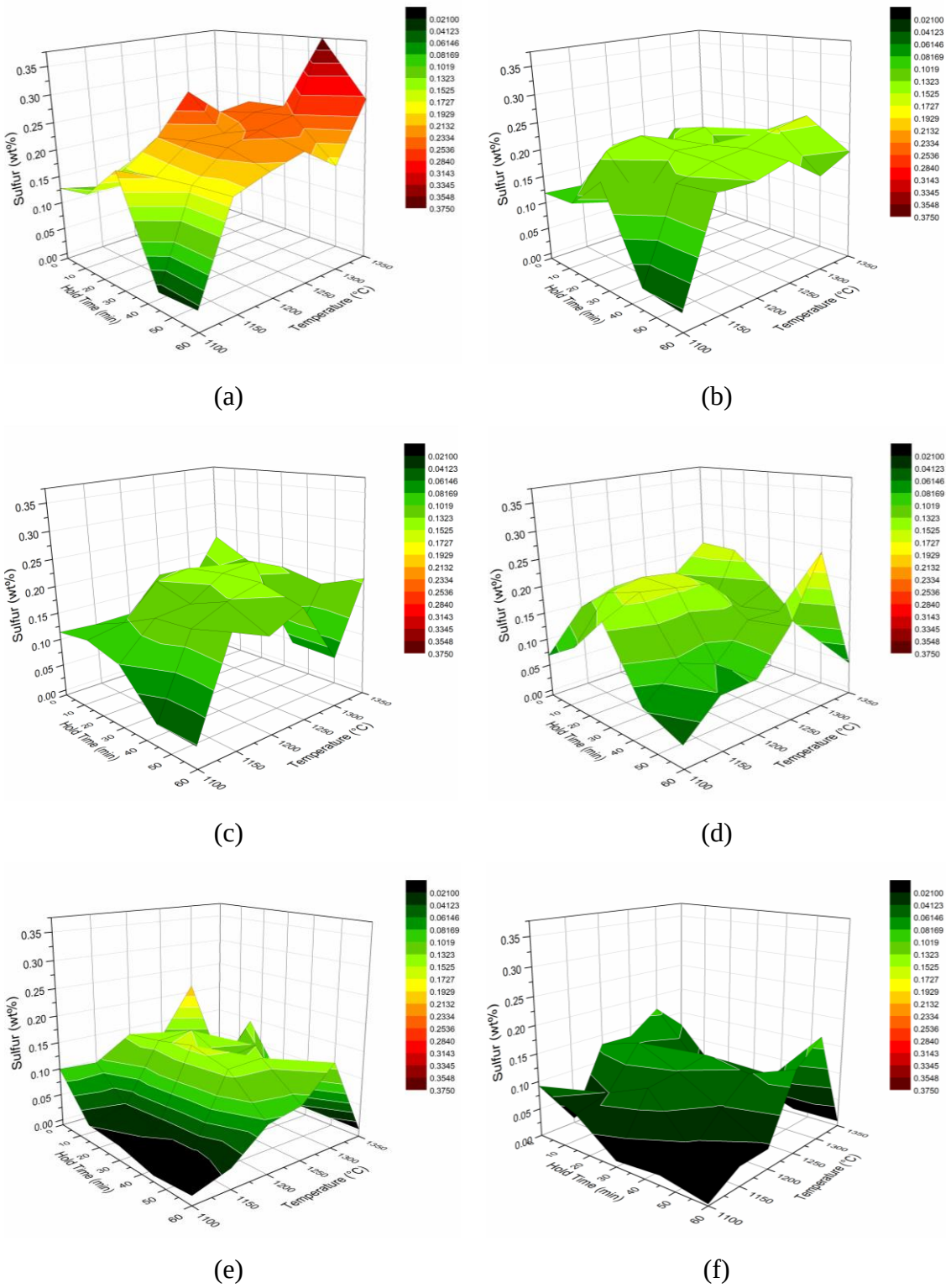

Figure 5.9. 3D surface plots of the sulfur content (wt. %) of fired pellets with respect to hold time (min) and temperature (°C). C/O = 1.0 (a), C/O = 0.9 (b), C/O = 0.8 (c), C/O = 0.7 (d), C/O = 0.6 (e), and C/O = 0.5 (f).

Some data on sulfur content in unfired and fired pellets from production RHFs is available in the literature, although limited to analyses of pre and post RHF process analysis, this data is provided for comparison in Table 5.4. The concentration effect of S in the produced DRI was observed in the FASTMET DRI, in good agreement with the experimental data in Figure 5.9.

Table 5.4. Comparison of commercial RHF DRI sulfur content.

Plant	Sample	Process details	S (wt. %)	Ref
Not specified	Unfired DRI	FASTMET RHF	0.29 0.44	169
Kobe Steel Kakogawa	DRI	FASTMET RHF	0.52	120
Not specified	DRI	DRyIron – Low Sulfur coal	0.04	80

Based on this experimental analysis, the levels of produced sulfur from DRI for each blend at realistic RHF temperatures and hold times of 1250 °C and 15 min would be between 0.1 and 0.15 wt. %.

Assuming a modest sized plant running 10,000 300 t BOF heats per year and based on these results, a 200 kt/annum RHF would supply around 20 t of DRI per heat to the BOF and therefore an additional 20 - 30 kg of input sulfur per heat. Depending on the grade of steel being produced, the available scrap mix and the quality of the hot metal to the BOF this may or may not preclude the use of the DRI produced from BOS dust and BF dust via an RHF in the BOF. Should this additional sulfur input be found to be too large to be diluted by BF hot metal sufficiently to meet grade specification then some proportion of the RHF DRI would need to be diverted to the BF for recycling.

5.3.3 Volatile Metal Removal

5.3.3.1 Zinc Removal

The removal rate of zinc with respect to temperature, hold time and carbon content of the BF dust: BOS dust blends is of course of vital importance, with the high zinc content of the material being the primary reasoning being poor material utilization historically.

The zinc content as determined by MP-AES analysis as in Chapter 3 of pellets of each blend (C/O = 0.5 – 1.0) ramped from 1100 °C – 1350 °C where the hold time t = 0 is shown in Figure 5.10, and significant zinc reduction in each blend can be observed even through the ramping period within the furnace. Blends with C/O = 1.0 – 0.6 were reduced to ≤ 0.1 Zn wt. % with no hold time just from the heating period between 1100 – 1300 °C (10 minutes at 20 °C min-1 heating rate).

The levels of zinc in pellets fired at 1100 °C with no hold time at reaction temperature show discrepancies with the levels of zinc in the unfired blends (

Table 5.3) appearing inflated, but this appears to be merely the result of the simultaneous gravimetric reactions occurring simultaneously within the pellet such as carbon oxidation and iron reduction concentrating Zn in the pellet prior to reduction and removal of Zn occurring. A possible method of accounting for the simultaneous gravimetric reactions occurring during heat treatment would be to normalize the zinc content against the total pellet mass but this proved impractical, as complete removal of pellets from reaction crucibles was made challenging due to pellet sticking at high temperatures and pellet disintegration during recovery leading to inadequate recovery.

While pellets with C/O ratios 0+8of 0.6 – 1.0 appeared to perform extremely similarly with regards to zinc removal in the 1100 – 1300 °C process window, the C/O = 0.5 blend performed dramatically worse. The Zn content of C/O = 0.5, T = 1350 °C, t = 0 min was 0.48 wt. % which is too high for recycling via the BF. Based on the carbon content of pellets fired under these conditions (Figure 5.7) the carbon within the C/O = 0.5 pellets has almost entirely burnt out (< 0.6 C wt. %) at 1300 °C, t = 0 which would effectively halt the zinc removal reaction.

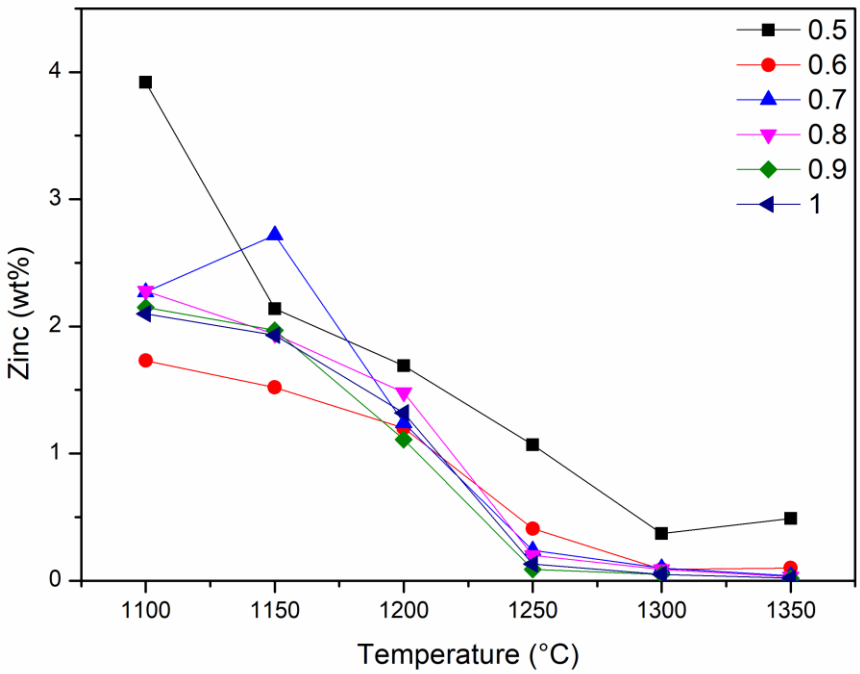

Figure 5.10. Zinc (wt. %) content of pellet blends C/O = 0.5 - 1.0 from 1100 °C - 1350 °C of fired pellets heated to reaction temperature at 20 °C/min and immediately withdrawn and quenched (t = 0).

The carbothermal reduction of zinc becomes feasible at temperatures below 1100 °C but no significant zinc removal is observed in t = 0 samples until higher temperatures are reached.

This may be related to heat transfer from the surface of the pellet inwards, Coatee et al. and Moon identified large thermal gradients between the exterior and interior of self-reducing briquettes during reduction of similar dimensions to those used in this work of >100 °C even after 5 minutes of equilibration time inside of a reaction furnace [170,171].

However, during experimentation it was observed that for pellets held at t = 0 and T = 1100 °C, upon removal from the furnace a white solid would rapidly condense onto the surface of the pellet (Figure 5.11). This observation suggested that the reverse reaction of Zn vaporization may be extremely significant in the removal of zinc from the pellet. Reduction reactions occurring inside the pellet generate Zn vapour as a product of the reduction but as these generated vapors diffuse toward the edges of the pellet it appears critical that the conditions surrounding the pellet are sufficiently

reducing to allow the Zn(g) to diffuse physically away from the pellet and into the exhaust of the furnace.

Figure 5.11. Fired pellet (1100 °C, 0 min, C/O = 0.5) removed and quenched from furnace showing white powder layer condensed onto pellet surface.

The reduction equilibrium for ZnO by CO gas to yield Zn vapour and CO_2 is shown in Equation 5.3 with the standard Gibbs free energy change for the forward reaction shown in Equation 5.4

$$\mathrm{ZnO(s) + CO(g) \rightleftharpoons Zn(g) + CO_2(g)} \tag{5.3}$$

$$\Delta G_T^\circ = 178.3 - 0.111T \tag{5.4}$$

ΔG_T° is related to the temperature dependent equilibrium constant K_T via Equation 5.5

$$\Delta G_T^\circ = RT\ln(K_T) \tag{5.5}$$

Assuming that the vapour pressure of ZnO is zero, K_T can be expressed as Equation 5.6 where P_{Zn}, P_{CO2} and P_{CO} are the partial pressures of Zn(g), CO_2(g) and CO(g) respectively

$$K_T = \frac{P_{Zn} + P_{CO_2}}{P_{CO}} \tag{5.6}$$

Rearranging 5.6 to give equation 5.7, which is an expression for the equilibrium ratio of the partial pressures of CO and CO2 in a system with a fixed partial pressure of Zn.

$$\frac{P_{Zn}}{K_T} = \frac{P_{CO}}{P_{CO_2}} \tag{5.7}$$

Fixing P_{Zn} allows for a visualization of the equilibrium CO/CO_2 ratio at 1 atm total system pressure for a given partial pressure of zinc, that is, the required ratio of CO to CO_2 in the gas phase at a given temperature required to retain zinc vapour in the gas

phase rather than generating ZnO(s) via oxidation of Zn(g) by CO_2 is shown in Figure 5.12.

The partial pressure of zinc vapour surrounding the pellet is likely low relative to the total system pressure but at 1100 °C a partial pressure CO/CO_2 ratio of 0.58 is required to prevent ZnO condensation due to the backward reaction from Equation 5.3. Should either the temperature of the pellet or the reducing capacity of the gas environment decrease, the system will tend back toward equilibrium by oxidation of a corresponding amount of zinc vapour to zinc oxide and regenerating CO.

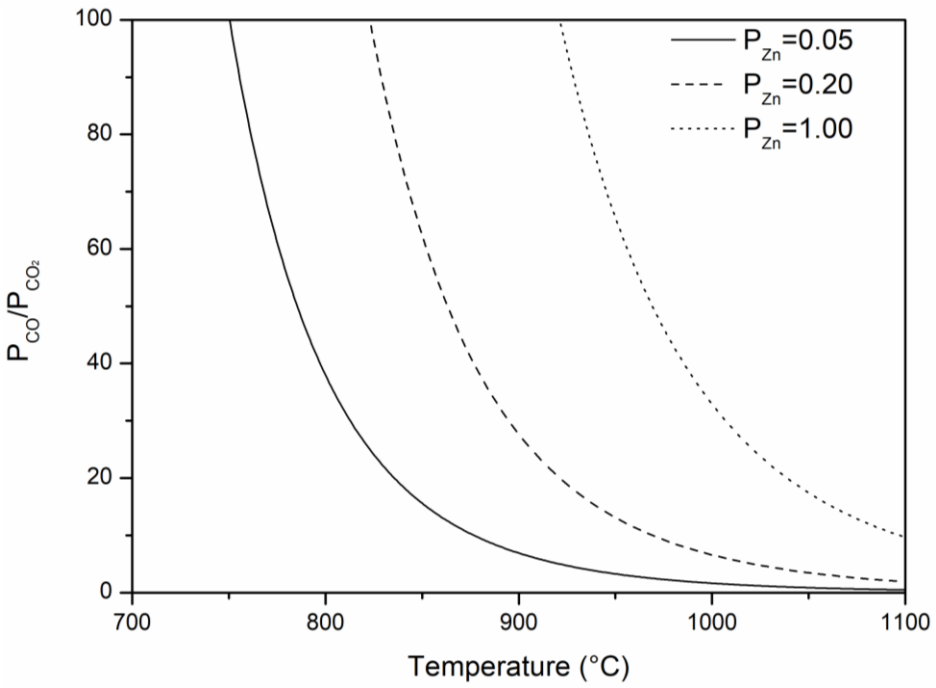

Figure 5.12. Equilibrium CO % for Equation 5.3 for varying partial pressures of zinc vapour at 1 atm total pressure.

The kinetics of the backward reaction of Equation 5.3 are extremely rapid, Cox and Fray studied the kinetics of zinc reoxidation by CO_2 for the purposes of understanding zinc vapor's behavior in the shaft of the Imperial Smelting Furnace [161]. Extremely rapid Zn deposition rates of 1.2×10^{-7} $molcm^{-1}g^{-1}$ of were observed in the 850 – 1000 °C temperature range when the partial pressure was greater than the equilibrium value as dictated by the gas atmosphere in the experiment.

This may explain the observations in Figure 5.11, zinc reduces and begins to diffuse away from the pellet as the carbothermal reduction reaction initiates but is still present in a boundary gas layer surrounding the pellet as the P_{CO}/P_{CO_2} ratio in the pellet boundary layer increases with heat transfer into the pellet and more carbon in the pellet is gasified to CO.

Upon removal from the furnace, the immediate drop in temperature will also cease the carbon gasification reaction, reducing P_{CO}/P_{CO_2} and initiating rapid reoxidation of Zn to ZnO on the available surface on the pellet which provides ample surface area to act as a nucleation site.

Of course, a major disparity between laboratory examination of this phenomena versus a production scale RHF is that this work considers a pellet as an isolated chemical system. In an RHF the volume of reducing gas in the immediate proximity to the pellet is far greater due to the presence of hundreds of other self-reducing pellets in proximity and therefore the generation of aggregated, localized reducing atmosphere within the pellet bed would be likely.

The effect of additional hold time with respect to furnace temperature and C/O of the blend is shown in

Figure **5.13** and exceptional zinc removal performance can be seen, reducing the levels of zinc to < 0.1 wt. % within 15 minutes of hold time at 1200 °C. Zinc removal from the more carbon deficient blends with C/O = 0.5 – 0.7 can be seen to plateau in terms of zinc removal even at extensive hold times > 30 minutes, which is well above typical RHF processing hold times. This appears consistent with the observations made in 5.3.1 about the depletion of carbon in fired pellets with a low initial carbon content at extensive hold times, and supports the notion that the zinc removal cannot continue even at extremely high temperatures of 1350 °C without sufficient carbon to reduce the oxides of zinc present to its elemental form and volatilize it.

The results of this analysis suggest a pellet of C/O = 0.8 is optimal for zinc removal, as relatively modest thermal conditions of 1250 °C for 15 minutes is sufficient to reduce the zinc of the fired pellet to 0.01 wt. % which is acceptable for charge to the BOF or the BF without supplying excessive carbon which has the drawback of increased sulfur content in the fired product and potentially compromising the fired pellets structural integrity.

It is certainly clear from these results that zinc removal performance in self-reducing pellets, even without the protective cover of an inert gas atmosphere is still extremely efficient and in fact is comparable with studies on self-reducing agglomerates performed under inert atmosphere. In the work of Xia et al. a zinc removal % of 99.25% was achieved for a pellet of C/O = 1.1, t = 30 min and T = 1300 °C [172], in this study reduction at 1300 °C, C/O = 1.0 t = 30 min was sufficient to reduce Zn levels in the fired pellet to below the detectable limit of the analysis (<0.005 wt. %) which corresponds to a zinc removal % of 100 ± 0.24 %. The ramp rate of the tube furnace

used to perform the experiments in that study is not specified, which as shown in t = 0 trials in this study may be significant, but nevertheless for zinc removal to be observed as comparable in a furnace open to atmosphere to inert conditions suggests the role of a reducing gas shell forming around the pellet is extremely significant in zinc removal.

Peng et al. performed similar work in a controlled atmosphere furnace with a simulated RHF gas input (mixed N_2-CO_2 atmosphere) with samples preheated at 1000 °C before pushing into the reaction zone of the furnace with a rod. Zinc removal rates in this experimental setup were seen to be remarkably similar to those seen in this work, with 15 minutes at T ≥ 1250 °C found to be sufficient to remove the vast majority of zinc (> 95% zinc removal) [173].

The results suggest that extended hold times > 15 minutes offer little in the way of increased zinc removal and therefore would not be economical or recommended for commercial scale due to the excessive energy use and associated decrease in plant capacity.

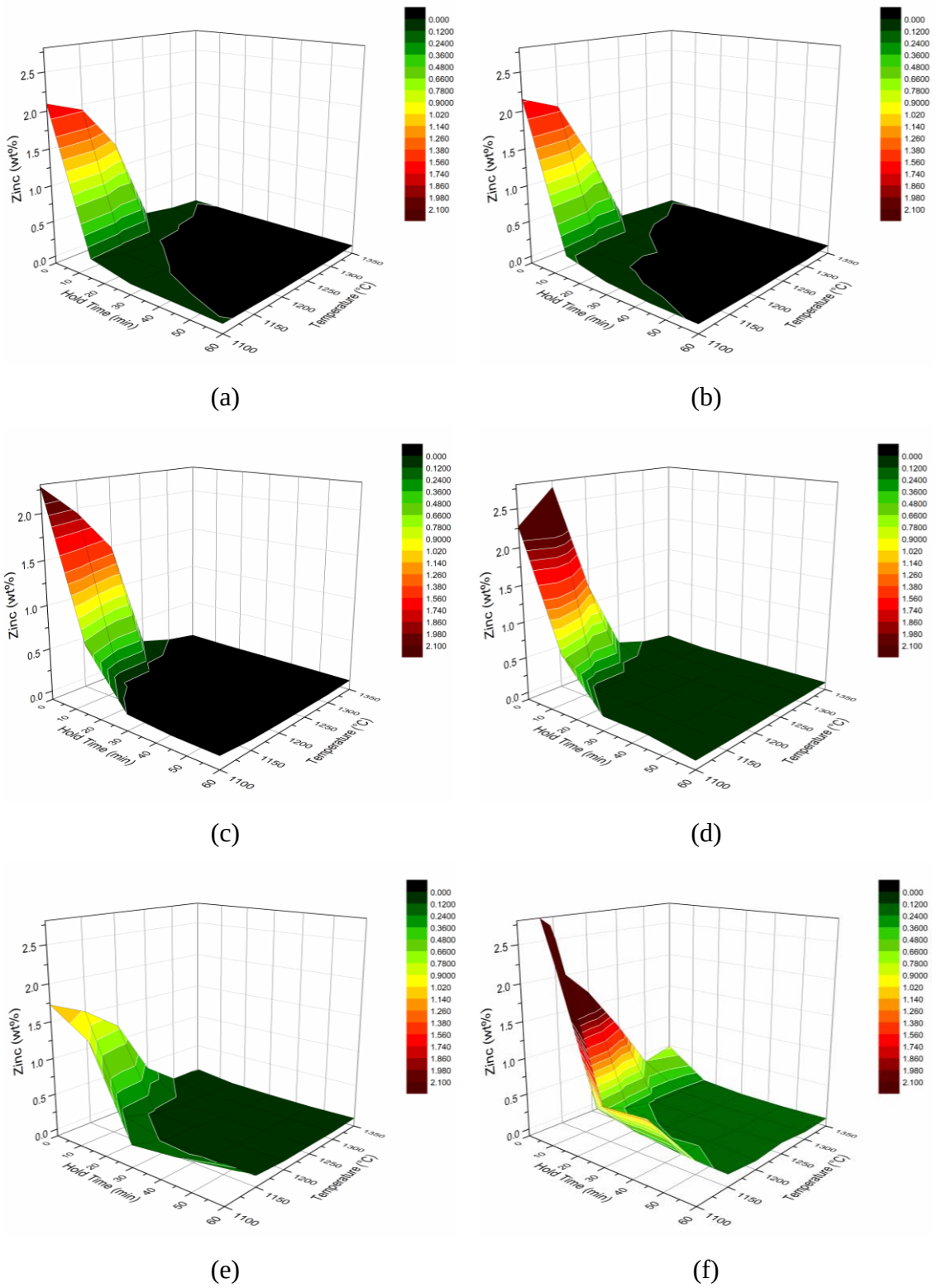

Figure 5.13. 3D surface plots of the zinc content (wt. %) of fired pellets with respect to hold time (min) and temperature (°C). C/O = 1.0 (a), C/O = 0.9 (b), C/O = 0.8 (c), C/O = 0.7 (d), C/O = 0.6 (e), and C/O = 0.5 (f).

5.3.3.2 Sodium and Potassium Removal

Na and K are also deleterious to BF performance, albeit not to the same extent as Zn, due to their catalytic effect on the CO_2 gasification reactivity of coke in the furnace burden, therefore their removal is also desirable during RHF processing. Na and K are much more easily discharged from the furnace due to their greater propensity for dissolution in the slag of the BF [174] and many furnace operations set limitations on Na and K input as a sum of the two elements due to their similar chemical behavior within the furnace and therefore they are considered simultaneously herein.

Removal of K and Na from pellets heated from 1100 °C to 1350 °C (Figure 5.14) at 20 °Cmin^{-1} without additional hold time at reaction temperatures was seen to not show a clear trend, with significant noise in the data. This may be related to the low initial levels of Na and K and relative uncertainty in the analyses.

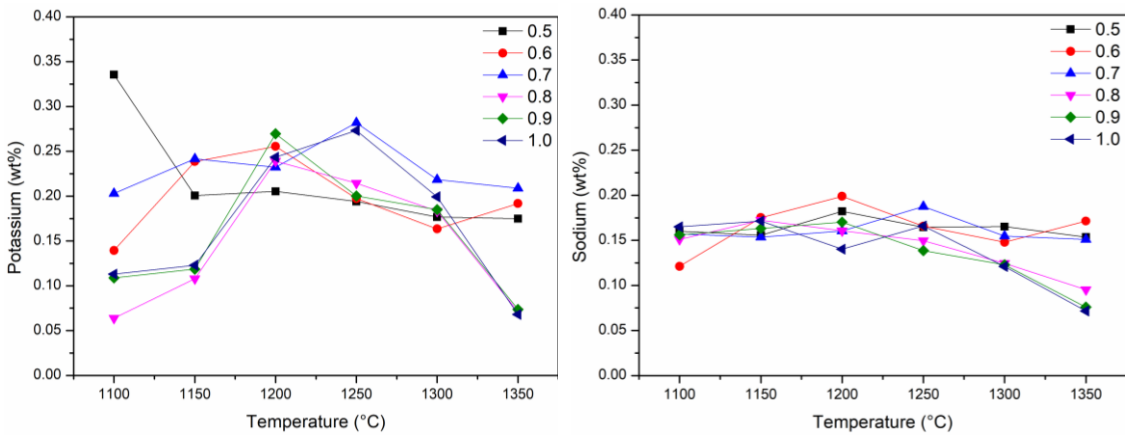

(a) (b)

Figure 5.14. Potassium (wt. %) content (a) and sodium (wt. %) content (b) of pellet blends C/O = 0.5 - 1.0 from 1100 °C - 1350 °C of fired pellets heated to reaction temperature at 20 °C/min and immediately withdrawn and quenched (t = 0).

Variation of the K content of fired pellets with hold times > 0 min at reaction temperature show a noteworthy deviation from the expected removal rates and is shown in Figure 5.15. As anticipated and in good agreement with zinc removal results, higher carbon blends remove K more efficiently.

However, an unusual observation was made for samples held for extended periods of 45 – 60 minutes at temperatures ≥ 1300 °C, the levels of potassium in the pellets began to rapidly increase and exceed the initial levels in the pellets.

Clearly, this could not be explained via concentration of K in the pellets caused by gravimetric changes in the pellet alone, and therefore an alternative explanation was sought. Following repeated measurements to ensure the values were not erroneous and the result of poor analytical technique, the next obvious avenue of investigation was the material the crucibles utilized for experimentation were made from.

High fire clay, typically used in refractories and crucibles such as the ones utilized in this study to act as a binder contains a substantial amount of Na and K bound within the clay matrix [175], and samples treated at 1350 °C for 45 – 60 minutes showed significant coalescence and softening upon discharge suggesting at least a partial formation of a semi-molten slag phase.

As discussed at the beginning of this section, Na_2O and K_2O are soluble in molten SiO_2-CaO-Al_2O_3-FeO slag and therefore it appears based on these results that at extended hold times and high temperatures that the pellets become reactive to the crucible substrate and diffusion of Na and K from the clay binder into the pellet becomes possible.

It appears the effect of this alkali stripping effect becomes more significant and lower pellet carbon contents in the experimental blend as can be seen in Figure 5.15c – f. There are two potential explanations for this; firstly, that the residual carbon present in C/O = 0.9 – 1.0 pellet blends are sufficient to suppress concentration of K in the pellets during heat treatment via reduction and diffusion away by the resultant metal vapour.

Secondly, the fluidizing effects of FeO on the SiO_2-CaO-Al_2O_3-FeO system are well documented [176] and due to the carbon depletion in C/O = 0.5 – 0.8 pellets fired at 1350 °C for extended periods (Figure 5.7) there may be a higher proportion of FeO remaining within the pellets which are promoting the softening and partial melting and thus exacerbating the dissolution of K from the crucible substrate.

This interaction between refractory and pellet is highly undesirable from a process perspective, not least due to increased K content in fired pellets but due to possible issues arising due to degradation of the hearth refractories in the RHF [177] and pellet sticking.

The results suggest not only that refractory material selection is significant for the purposes of potentially introducing undesirable elements into DRI produced via the RHF but that overfiring of pellets at extremely high temperatures and hold times can produce undesirable interactions with refractories causing damage and potential losses to productivity.

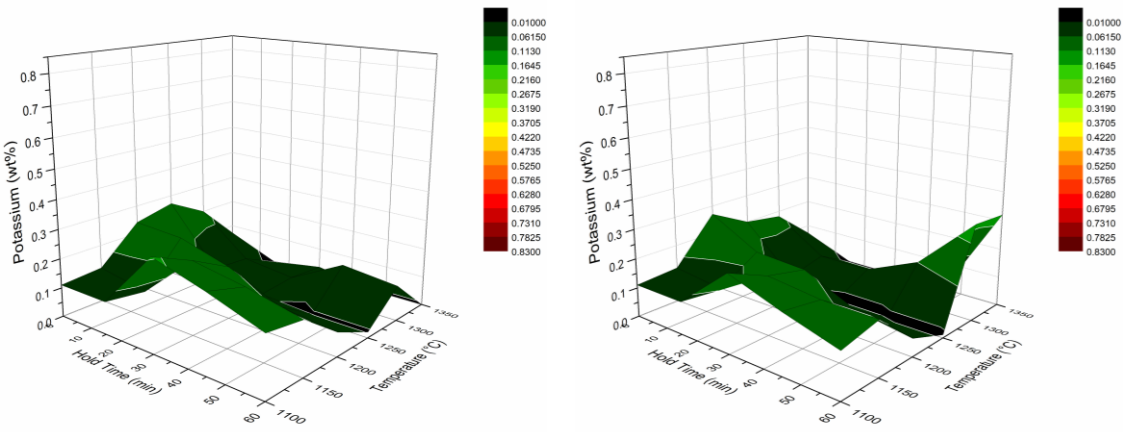

(a)

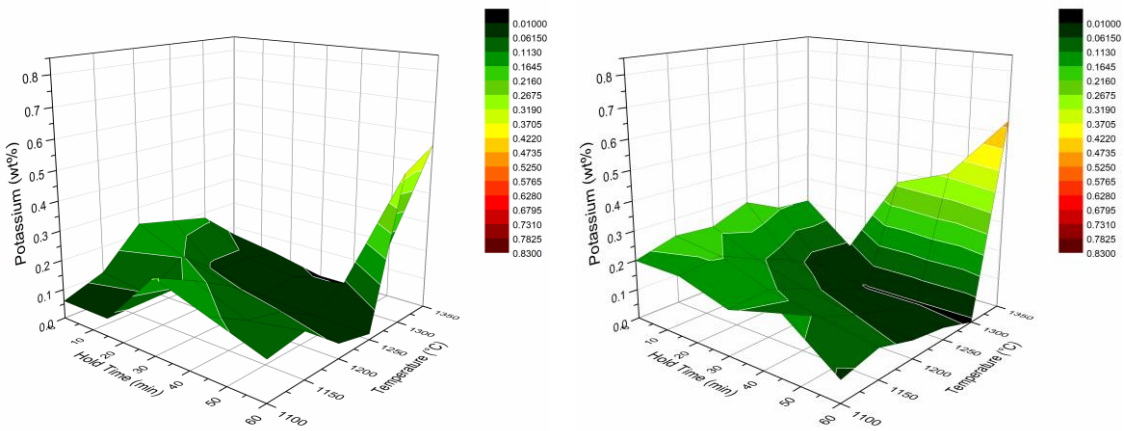

(b)

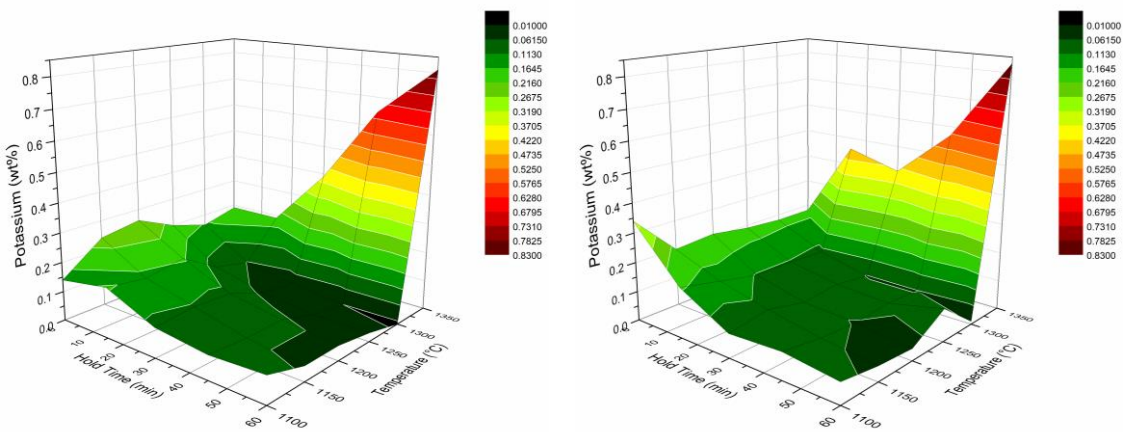

(c)

(d)

(e)

(f)

Figure 5.15. 3D surface plots of the potassium content (wt. %) of fired pellets with respect to hold time (min) and temperature (°C). C/O = 1.0 (a), C/O = 0.9 (b), C/O = 0.8 (c), C/O = 0.7 (d), C/O = 0.6 (e), and C/O = 0.5 (f).

A similar effect is observed when observing the sodium removal performance at extended hold times and temperatures (Figure 5.16), with Na diffusing into the pellet at high T and hold time for blends with lower initial carbon.

Very little detail on the mechanisms of removal of volatile metals other than zinc in the RHF exists in the literature at the time of writing, and this is certainly an area that deserves greater attention due to the potential process benefits to the BF of reducing the alkali metal content of DRI.

The most in-depth study on the removal of Na and K from steelmaking by-product dusts via the RHF at the time of writing is She et al.'s 2011 work on a blend of four unspecified by-product dusts from an integrated works to produce cold bonded briquettes which were reduced under an inert gas atmosphere (N_2) [147].

In that work, rather efficient removal of Na and K were reported for pellet blends with a C/O ratio of 1.0, with removal percentages between 1200 °C and 1330 °C approaching 90% after 30 minutes.

For comparison, in this work for a pellet with C/O ratio of 1.0 after 15 minutes of hold time at 1300 °C showed an Na removal % of 66% compared with approximately 80% in She et al.'s work. However, some critical discrepancies between the methodology used in that work and the experimental work herein exist such as the use of an exceptionally high flow rate of inert gas (5 $Lmin^{-1}$), which may affect diffusion rate of metal vapour away from the pellet, and a significantly higher initial sodium content of the self-reducing agglomerates (0.63 wt. %) in that work.

The largest and most significant difference in experimental methodology however was the suspension of samples on a cradle of Fe-Cr-Mo wire rather than containment within a crucible, as such the enrichment of Na and K in pellets at extended hold times and high temperatures was not observed.

Nevertheless, the results at modest temperatures of 1200 – 1300 °C for short periods between 0 and 30 minutes are broadly comparable, although Na and K removal appear slightly slower under uncontrolled atmosphere which stands to reason given the dependence on transport of the metal vapors away from the briquette to remove them.

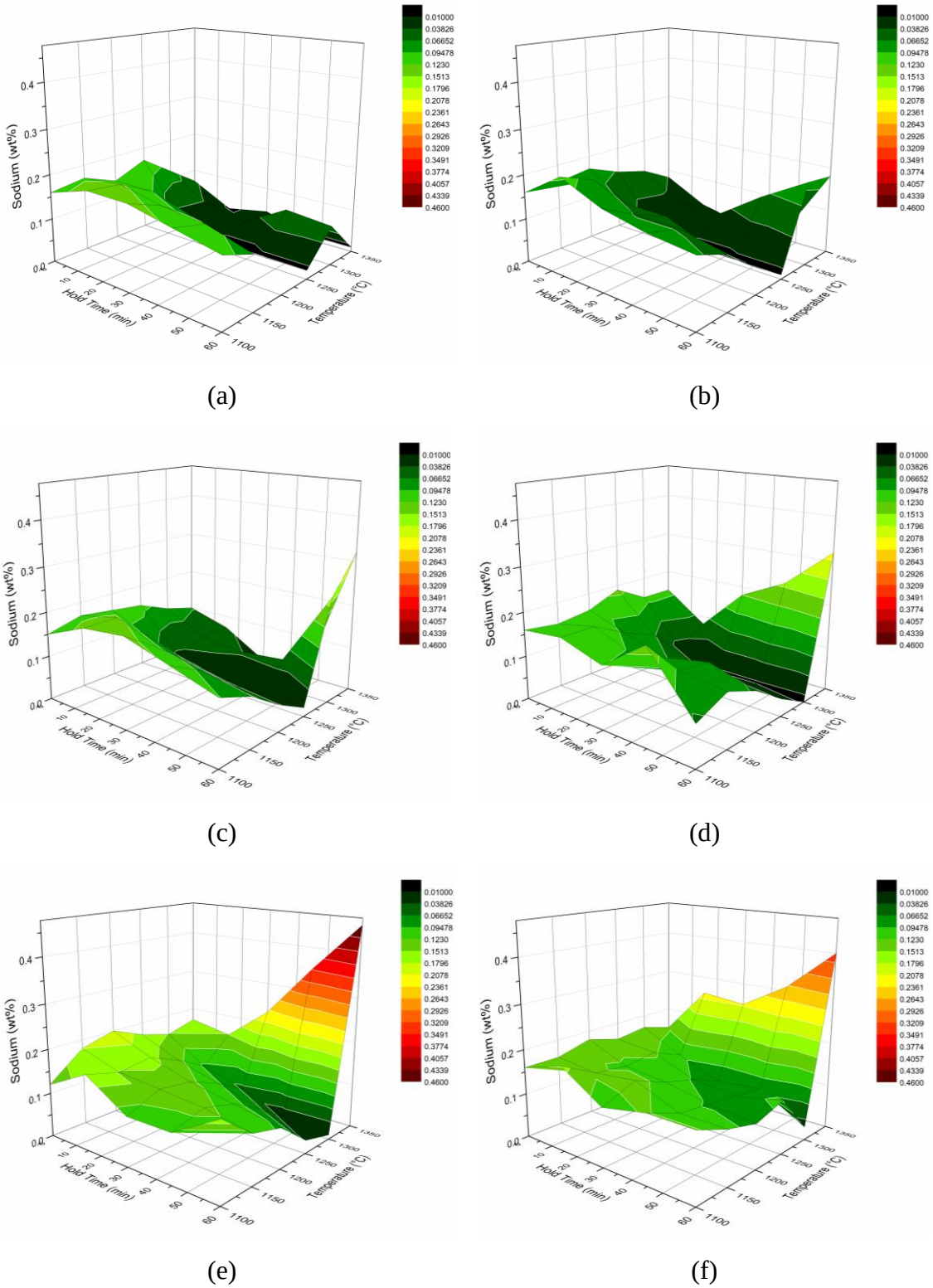

Figure 5.16. 3D surface plots of the sodium content (wt. %) of fired pellets with respect to hold time (min) and temperature (°C). C/O = 1.0 (a), C/O = 0.9 (b), C/O = 0.8 (c), C/O = 0.7 (d), C/O = 0.6 (e), and C/O = 0.5 (f).

5.3.3.3 Lead Removal

Based on thermodynamic assessment in 5.1 and as evidenced by analysis of RHF off-gas dust from an operating RHF in 5.1.1, it was expected that some level of lead removal from the fired pellets would be observed.

Lead content of pellets of varying C/O ratio ramped between 1100 – 1350 °C at 20 °Cmin^{-1} before withdrawal and quenching is shown in

Figure **5.17** and even with minimal hold time, elimination of Pb from the pellets is extremely rapid with levels of Pb for all pellets at approximately 0.01 wt. % at typical RHF temperatures of 1250 °C, even without holding the pellets at temperature.

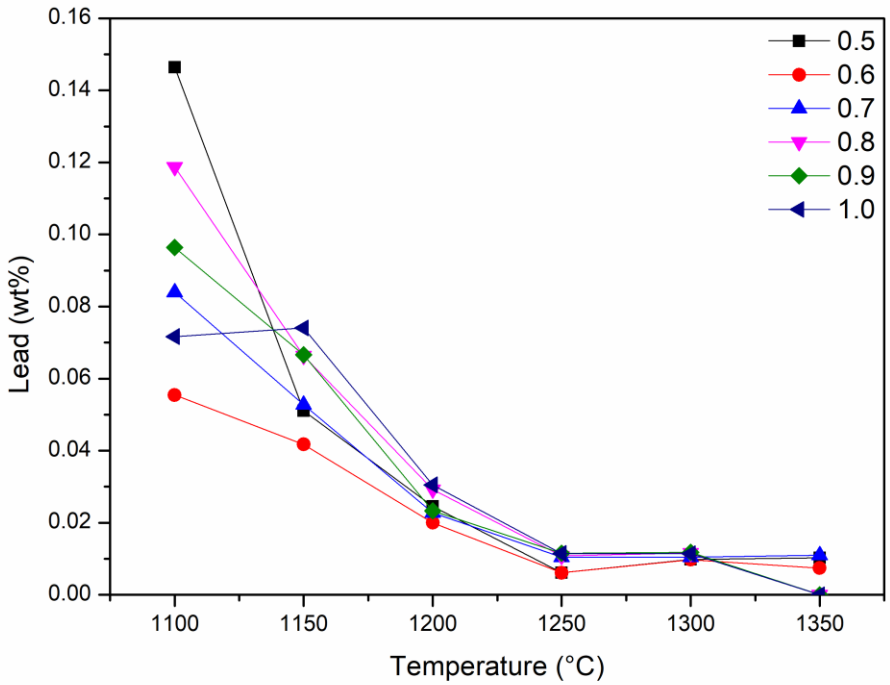

Figure 5.17. Lead (wt. %) content of pellet blends C/O = 0.5 - 1.0 from 1100 °C - 1350 °C of fired pellets heated to reaction temperature at 20 °C/min and immediately withdrawn and quenched (t = 0).

This observation may seem counterintuitive, given that the boiling point of metallic Pb is significantly higher than 1250 °C but given the extremely low concentration of Pb in the pellets made from UK material it is certainly plausible that extremely low partial pressures of Pb vapour may be eliminated from the pellet via the gas phase at RHF temperatures, given the apparent presence of lead in commercial RHF dust seen in Figure 5.5.

It is also possible that the reaction is proceeding due to lead existing as a chloride rather than an oxide in the pellet, although direct speciation of the crystalline phases of lead within BOS dust and BF dust was not possible due via XRD to the extremely low levels of Pb present (Figure 4.5).

The chloride salt of lead is significantly more volatile than the oxide, and volatilization occurs independently of a reducing agent at T > 950 °C. The volatile nature of chloride salts has been utilized previously to encourage lower temperature separation of contaminant metals from BOS dusts [51] and also EAF dusts [178].

In the work of Yoo et al. studying the removal mechanisms of lead from EAF dust containing PbO as the principle lead phase, it was observed that a synergistic chlorination of PbO via the NaCl was the driving force for low temperature lead removal via Equation 5.8 [178].

$$2\mathrm{NaCl(s)} + \mathrm{PbO(s)} + 2\mathrm{SiO_2(s)} + \mathrm{Al_2O_3(s)} \longrightarrow \mathrm{PbCl_2(g)} + \mathrm{NaAlSiO_4(s)} \qquad (5.8)$$

The effect of extended hold times at high temperature for each blend on the overall lead content is shown in Figure 5.18 and it's clear that even extremely short residence times at temperatures for all blends show comprehensive lead removal. The effect of varying carbon content of the blends appears to be minimal for the removal of lead, with all blends removing Pb to the levels approaching the detection limit of the analysis merely by heating to 1250 °C with no hold time. Based on the observation that the carbon content of the blends made minimal impact on lead removal during heat treatment, this may suggest that lead removal is happening via a solid-state chlorination reaction as in Equation 5.8 rather than the predicted carbothermal mechanism.

The results are comparable in terms of Pb removal to She et al.'s work, where comprehensive Pb removal was also achieved at modest temperatures and hold times. Leads negative effect on the blast furnace is especially hostile due to the unique metallurgical properties of lead within the furnace, therefore efficient elimination from fired pellets in the RHF is very desirable.

The presence of molten lead can ingress into refractory bricks and inflict damage via oxidative expansion or in extreme cases where lead loading to the furnace is especially excessive, molten lead can form a layer of molten liquid against the hearth of the furnace owing to the high relative density and immiscibility with the Fe-slag system.

This can cause rapid corrosion of the hearth lining, floatation of bricks and open up cracks allowing for hot metal ingress into the furnace lining [179].

As such the relative ease of removal of Pb from pellets in this study, when compared to Zn and other volatile metals is promising for minimizing the input of Pb into the furnace during recycling.

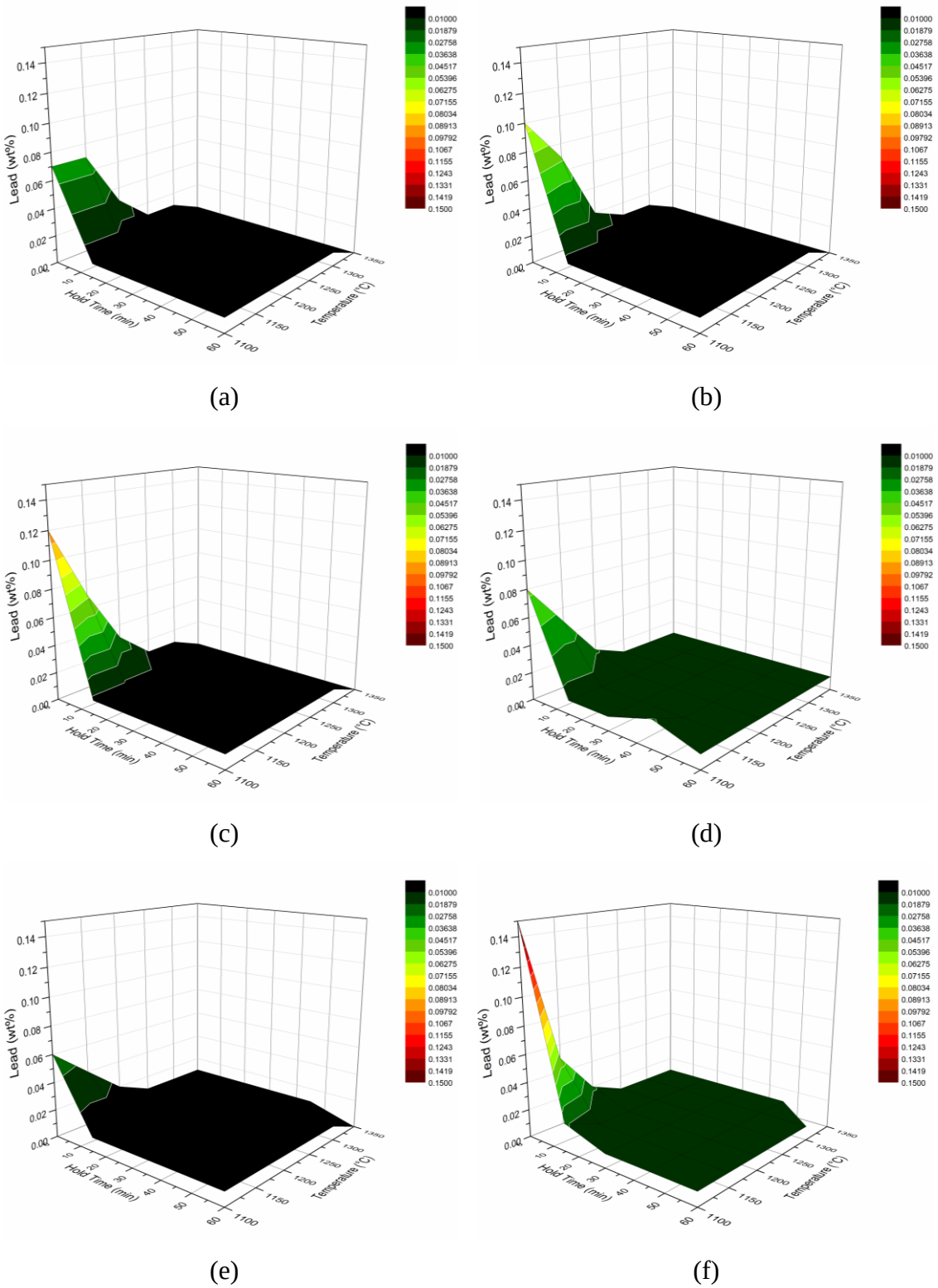

Figure 5.18. 3D surface plots of the lead content (wt. %) of fired pellets with respect to hold time (min) and temperature (°C). C/O = 1.0 (a), C/O = 0.9 (b), C/O = 0.8 (c), C/O = 0.7 (d), C/O = 0.6 (e), and C/O = 0.5 (f).

5.3.3.4 Metallization of Iron

Metallization of iron in fired DRI is arguably the second most important factor, after zinc removal, in generating a high value in use product from the RHF, very high metallization DRI can be utilized in the BOF as an alternative source of ferrous units either as a scrap substitute or as a coolant supplied during the blow, where iron ore pellets are typically used in most plants.

Highly metallized DRI can lead to fuel demand reductions in the BF [66] due to the reduced need for reduction reactions to occur in the BF itself. DRI is typically higher in Fe by weight than some of the richest ore concentrates available [180].

During direct reduction, direct measurement of metallic Fe content alone is not sufficient to monitor reduction progress. Figure 5.19 shows the variation of Fe_{Tot} (wt. %) and Fe_{met} (wt. %) of pellets during the ramping stage (t = 0) of furnace treatment and while reduction is occurring with increasing temperature due to the associated increasing content of metallic iron in the samples.

However, as can be observed in Figure 5.19a, the overall iron content by weight of the pellet also simultaneously increases as the heating process proceeds. This stands to reason due to elimination of bound oxygen in the pellets in the form of metal oxides, elimination of volatile metals and combustion and gasification of carbon.

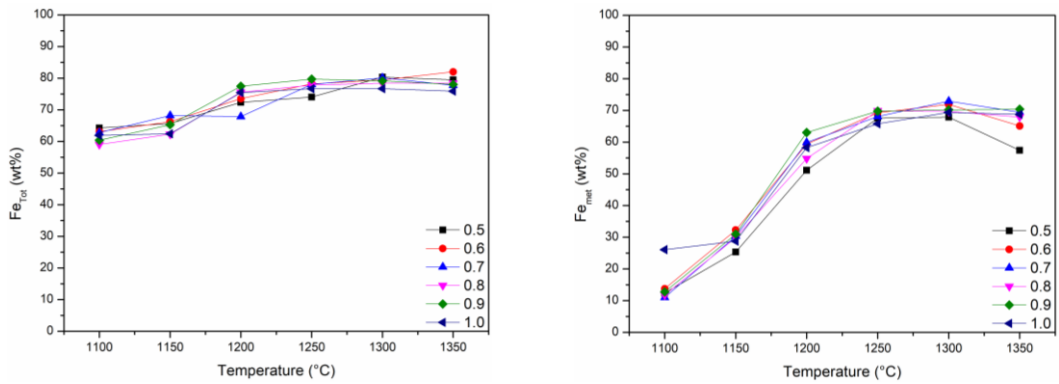

(a) (b)

Figure 5.19. Total Fe content (a) and metallic Fe content (b) of pellet blends C/O = 0.5 - 1.0 from 1100 °C - 1350 °C of fired pellets heated to reaction temperature at 20 °C/min and immediately withdrawn and quenched (t = 0).

Fe_{Tot} and Fe_{met} weight percentages are still extremely valuable metrics for assessing DRI quality however, mostly from a value-in-use perspective in terms of industrial material selection, but the Fe reduction ratio as used in Equation 4.2 on page 84 of this thesis becomes the far more useful metric for monitoring the reduction

reactions progress due to the ability to account for concentration of Fe in the solid phase as other components volatilize or combust.

Figure 5.20 shows the change in metallization for each blend during ramping from 1100 – 1350 °C. It's clear that most of the reduction for all blends occurs rapidly as the pellet is heated from 1100 to 1200 °C, with reduction appearing to slow down and approach a plateau of approximately 90% metallization for C/O = 0.7 – 1.0 blends.

Metallization is observed to decrease for C/O = 0.5 is seen to decrease from 84.5% to 72.2% during heating from 1250 °C to 1350 °C. Similarly, for C/O = 0.6 metallization decreases from 90.5% at 1300 °C to 79.4% at 1350 °C.

This is evidence of overfiring and subsequent reoxidation of iron in the lower carbon pellets and is supported by the depletion of carbon in the C/O = 0.5 and 0.6 blends at 1350 °C shown in Figure 5.7.

Nevertheless, achieving a metallization % of 88% for C/O = 0.7 during the ramping period to 1200 °C with no hold time demonstrates an extremely efficient reduction process.

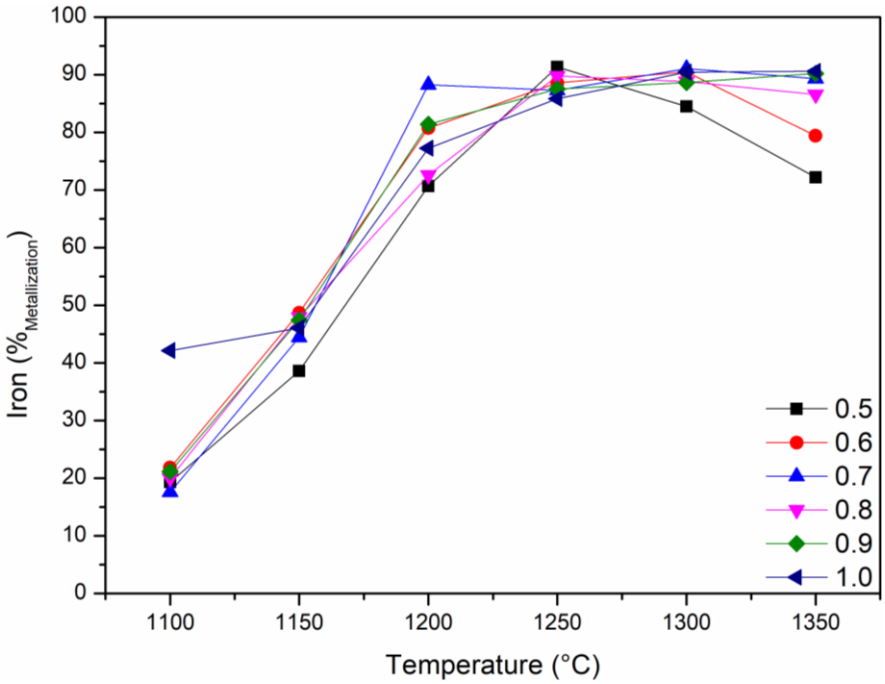

Figure 5.20. Metallization of pellet blends C/O = 0.5 - 1.0 from 1100 °C - 1350 °C of fired pellets heated to reaction temperature at 20 °C/min and immediately withdrawn and quenched (t = 0).

The effect of increasing hold time on iron metallization for each blend is shown in Figure 5.21. The highest overall metallization of iron across the range of conditions

was for 1200 °C, t = 15 min and C/O = 0.7 with a $\%_{metallization}$ of 96.7 ± 2.89 %, generally for all blends metallization peaked at t = 0 – 15 min at T =1200 – 1300 °C.

Interestingly, metallization behavior at 1100 °C behaved anomalously to higher temperatures. At 1100 °C peak iron metallization was achieved after 15 minutes, between 79.8% for C/O = 1.0 and 55.07% for C/O = 0.5 before beginning to decline at longer hold times.

Due to very little examination of direct reduction of self-reducing agglomerates without the use of a controlled atmosphere in the literature there is no clear reasoning behind this observation as the higher carbon blends (C/O = 0.7 – 1.0) still contain sufficient carbon to sustain a reducing environment.

Instead, it may be the case that as the carbon in the outer layer of the pellet depletes and generated direct reduced iron at the pellet boundary the lower temperature supplied to the center of the pellet is not sufficient to gasify the carbon contained in the interior of the pellet to protect the freshly formed metallic iron from reoxidation in the atmosphere.

At higher temperatures, this reoxidation effect appears less significant even in pellet blends that are severely carbon depleted. Gas DRI produced via shaft furnace at comparatively low temperatures (900 – 1000 °C) possess an extremely porous morphology and a high propensity to reoxidize [65]. It appears extended high temperature heating may reduce this reoxidation process even when carbon levels are depleted such that maintenance of a localized reducing atmosphere is no longer possible. This may be related to closure of surface pores on the DRI at higher temperatures and hold times reducing the available pellet surface area for oxidative attack by the furnace atmosphere.

The results show a surprisingly high level of metallization of Fe in the blends following comparatively mild treatment conditions. Mombelli et al. reported metallization ratios for BF sludge – BOS sludge self-reducing for samples heated to 1200 °C for 15 minutes before cooling in the furnace of 50 – 60% under an air atmosphere and 60 - 80% under inert gas cover [124].

Based on the reoxidation of pellets observed at extended hold times in this study, reoxidation of pellets during cooling in that study appears extremely likely and therefore the maximum metallization rate achieved may have been slightly higher than the final reported value.

A sweep gas of unspecified flow rate was also utilized in that work, whereas this work was carried out without the use of a continuous gas supply. The pellets used were

also substantially heavier (60 g) which likely has a significant effect on the reaction kinetics and heat transfer from the surface of the pellet to the interior.

Notably, complete reduction of Fe to metallic Fe was not observed in this study. Chatterjee observed that the mechanism of direct iron reduction shifts to an extremely slow rate-limiting step at high (>85%$_{metallization}$) levels of metallization as FeO becomes increasingly difficult for reducing gases to access due to coalescence of metallic Fe around cores of unreacted Wüstite [66].

At low hold times, the results are in good agreement with Wang et al.'s work on the reduction behaviour of mixed BOF fine dust agglomerates which was carried out in an N_2 atmosphere [181] showing similar metallization of >90% for furnace temperatures of 1300 °C. In that work, the lack of comprehensive metallization was attributed partially to the reduced FeO surface area available at high metallization percentages and the formation of Fayalite (Fe_2SiO_4) from unreacted FeO and siliceous gangue in the pellets which is much more resistant to carbothermal reduction by CO. In this work however, the primary gangue constituent in the pellets is CaO rather than SiO_2.

Overall, the results suggest that highly metallized DRI can be produced from BOS dust and BF dust of comparable metallization to other laboratory studies can be prepared without the use of an inert atmosphere. Pellets were able to self-reduce through the formation of a localized reducing atmosphere generated by the gasification of carbon in the pellet.

It was found that a C/O ratio of 0.7 is sufficient for excellent metallization in short residence times of 0 – 15 minutes between 1200 – 1300 °C without supplying needless excess carbon with the associated additional sulfur input.

Reoxidation of during heat treatment was also observed, with lower initial carbon content pellets exhibiting a decrease in metallization following depletion of the carbon present in the pellet.

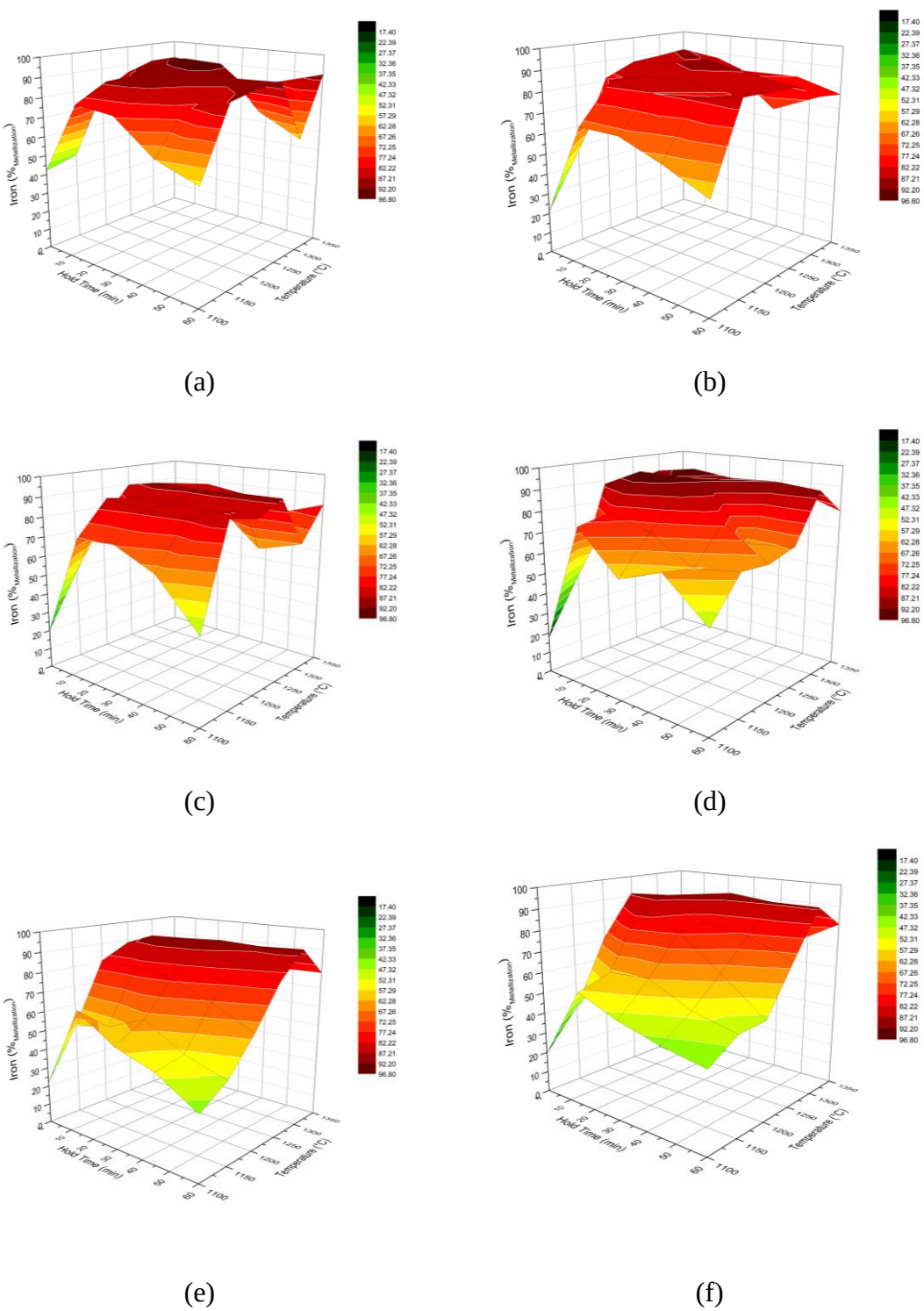

Figure 5.21. 3D surface plots of the iron metallization % of fired pellets with respect to hold time (min) and temperature (°C). C/O = 1.0 (a), C/O = 0.9 (b), C/O = 0.8 (c), C/O = 0.7 (d), C/O = 0.6 (e), and C/O = 0.5 (f).

5.3.4 Powder X-Ray Diffraction of Fired Pellets

XRD analysis of pellet blend C/O = 0.5 heated from 1100 °C to 1350 °C at a rate of 20 °C min^{-1} is shown in Figure 5.22. Counts are displayed as the square root of the measured value to allow for simultaneous display of major and minor phase constituents.

Based on the XRD semi-quantitative phase analysis, the maximum relative amount of metallic Fe relative to other components is at 1250 °C, in agreement with the metallic iron analysis in Figure 5.20. As T increases further to 1350 °C a secondary Wüstite phase emerges, likely to be the result of reoxidized metallic iron in the oxidizing furnace atmosphere.

A small peak is observed at ~31 ° for the 1100 °C corresponding to crystalline carbon, as expected this peak disappears as the temperature increases further as carbon participates in reduction reactions.

Calcium aluminoferrite (CAF), known naturally as Brownmillerite ($Ca_2(Al,Fe)_2O_5$) was seen to form in the samples. Based on the CaO-FeO phase diagram it's likely that this is a result of crystallization out of a semi-molten slag phase given the eutectic temperature of approximately 1125 °C [182]. CAF has a lower reducibility than pure iron oxide compounds which may be a contributory factor to the plateau in iron reduction observed during laboratory tests at approximately 90% metallization.

The crystalline components in C/O = 1.0 pellets (Figure 5.23) showed substantial differences compared with the lower carbon blend. The peak corresponding to graphitic carbon at ~31 ° remains visible in the X-Ray diffractogram until T = 1200 °C, in good agreement with the carbon analysis of fired pellets suggesting the C/O = 1.0 blend still contains substantial carbon under these conditions. Furthermore, in C/O = 1.0 pellets the presence of Wüstite is eliminated at T = 1250 °C, with Fe_3O_4 being the dominant remaining oxide.

Significant reoxidation of the C/O = 1.0 pellets is not observed in the x-ray diffraction data at higher temperatures, as the residual carbon in the pellet is still sufficient to sustain a reducing atmosphere.

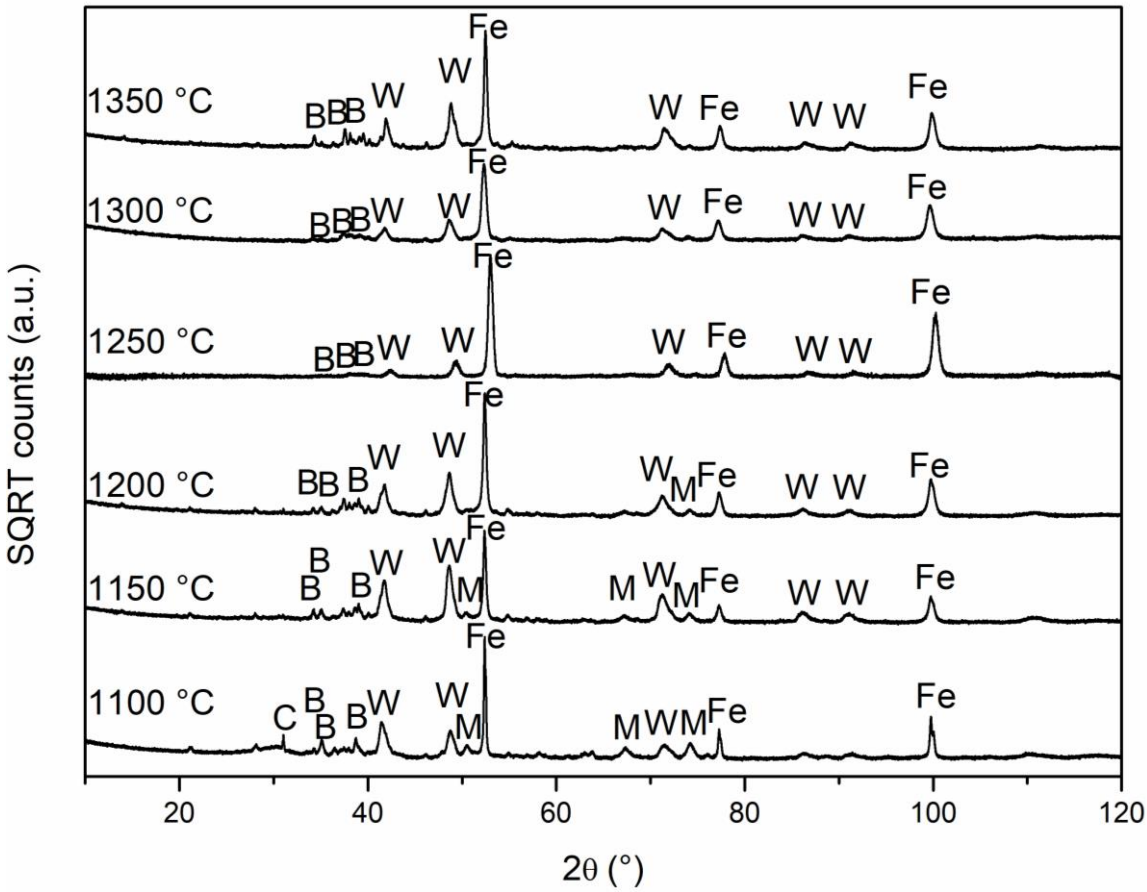

Figure 5.22. Powder XRD analyses of C/O = 0.5 of fired pellets heated to reaction temperature at 20 °C/min and immediately withdrawn and quenched (t = 0). C = graphite (C), M = Magnetite (Fe_3O_4 - COD# 9006920),), W = Wüstite (FeO - COD# 1011167), Fe = α-iron (Fe – COD# 9006595),), B = Brownmillerite ($Ca_2(Al,Fe)_2O_5$ - COD# - 1008777).

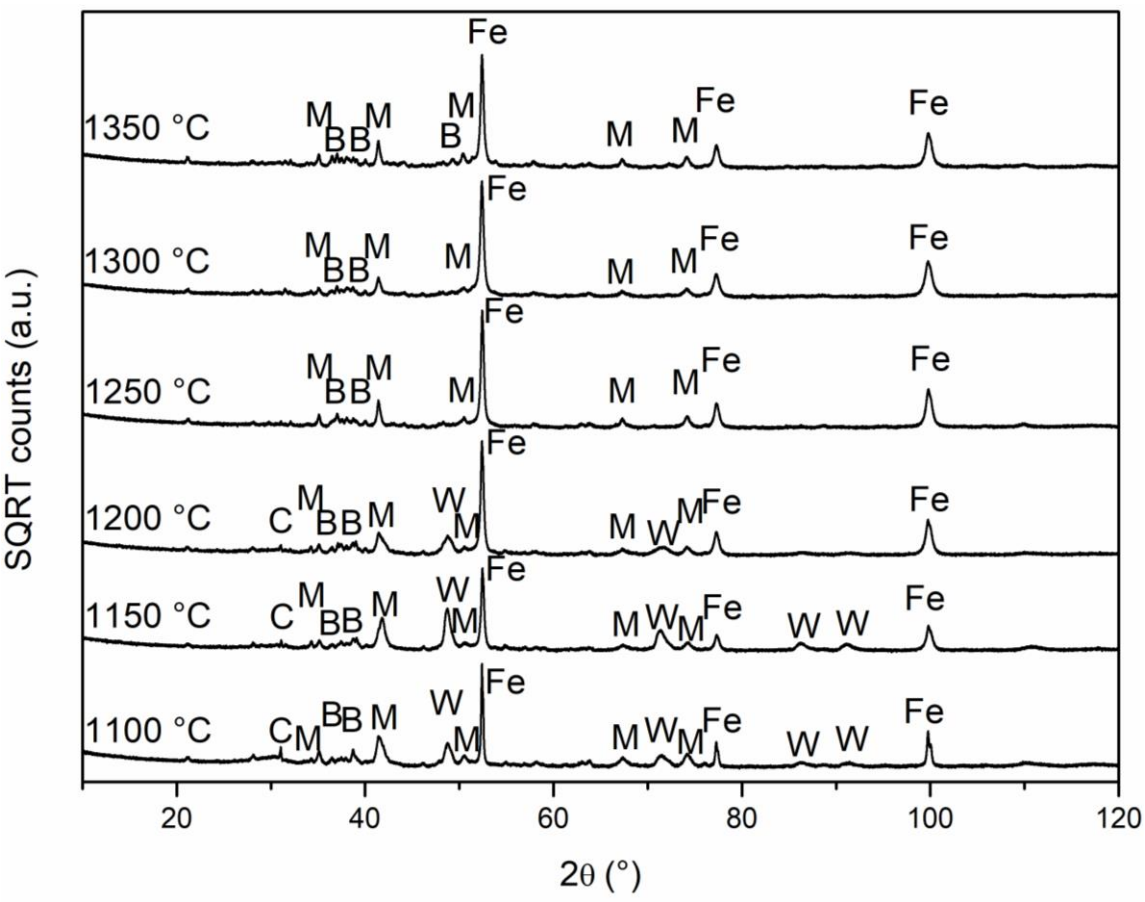

Figure 5.23. Powder XRD analyses of C/O = 1.0 of fired pellets heated to reaction temperature at 20 °C/min and immediately withdrawn and quenched (t = 0). C = graphite (C), M = Magnetite (Fe_3O_4 - COD# 9006920),), W = Wüstite (FeO - COD# 1011167), Fe = α-iron (Fe – COD# 9006595),), B = Brownmillerite ($Ca_2(Al,Fe)_2O_5$ – COD# - 1008777).

5.4 The Separated Zinc Product

It was found to be possible to collect vaporized metallic vapour from the experiments by using an overturned alumina combustion boat laid across the top of the crucible. The Al_2O_3 surface acted as a nucleation point for condensation of the vapors which could then be collected for further analysis. Zinc was found to condense into thin wires of zinc oxide on the crucible surface, as can be seen in Figure 5.24, which could be dislodged from the combustion boats surface by pressure with a sample brush.

Figure 5.24. Arrangement of inverted alumina boat rested on top of Si-C crucible used to collect metal vapour in-situ.

Analysis of the collected zinc product by SEM-EDX is shown in Figure 5.25. The EDX spectrum showed zinc and oxygen in an atomic ratio of 0.78 which is in reasonable agreement with zinc (II) oxide (ZnO). The carbon detected was ascribed to the carbon tape used for mounting of the sample for SEM-EDX. Interestingly, Na, Pb and K were not detected in this captured oxide via EDX in sufficient amounts to be parsed from the background signal, this was attributed to comparatively small amounts of those elements relative to Zn in the unfired pellets.

The prismatic hexagonal crystalline structure is characteristic of zinc oxide in the Wurtzite form [183] , and suggests a high purity collected ZnO product.
It's likely in a commercial plant the amount of iron in the off-gas dust of the RHF would be contaminated with substantially more Fe than observed in laboratory trials due to fines generation during handling, more turbulent gas flow conditions and substantially faster heating rates than were achievable in laboratory tests, which may decrease the quality of the ZnO product somewhat.

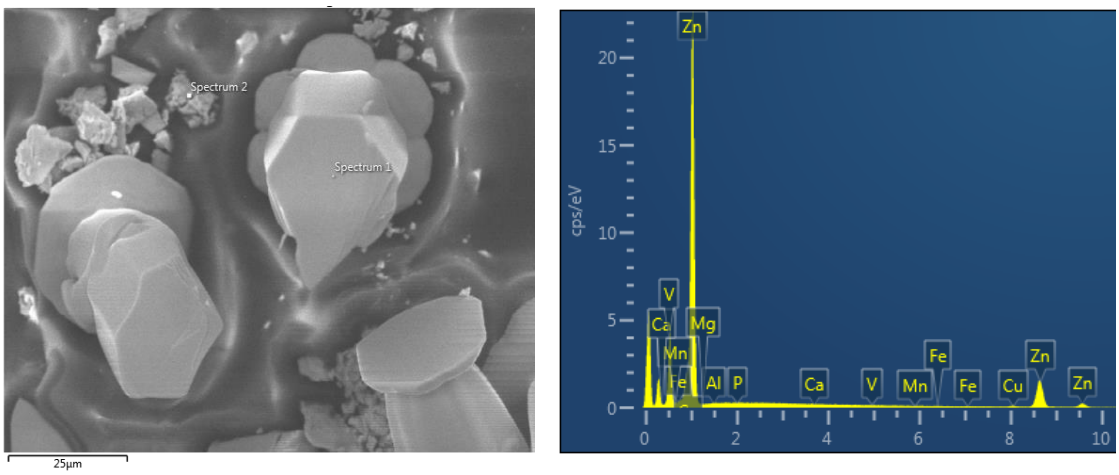

(a) **(b)**

Figure 5.25. SEM micrograph (a) and EDX spectrum (b) for condensed ZnO collected during benchmarking experiments. Calculated elemental composition 60.0 wt. % Zn, 18.7 wt. % O, bal. C

The ZnO product in this laboratory trial would be easily recyclable by a zinc smelter [99] or electrowinning operation[100] based on its high zinc content and low tramp element content.

5.5 Recycling Routes – BF, BOF or Sinter Plant?

The obvious recycling routes for DRI from the RHF following reduction and zinc removal are the BOF, the BF and the sinter plant, and each of them possesses different value drivers and raw material chemistry limitations.

Preferably, DRI produced via an RHF would be charged to the BOF as a coolant, where it would displace a portion of the steel scrap utilized as a coolant or as an auxiliary metallic iron unit supply.

The next best option for deriving high value-in-use from the DRI product would be the BF. DRI could displace a small portion of either iron ore pellets or sinter which carries a small financial benefit but primarily the value generated using DRI in the BF is in the concordant energy usage and coke rate reductions through its use. Approximately 45% of the energy input to iron ore in the BF contributes to reduction of iron oxide rather than melting [90], therefore by supplying pre-reduced material to the furnace an energy input saving per tonne of hot metal produced is achievable. Due to the high Fe (Wt. %) content of DRI, productivity benefits are also achievable using DRI when compared to ore and sinter.

Finally, DRI could be supplied to the sinter plant where it would displace fine ore concentrate or low zinc by-product materials such as mill scale. The high metallic Fe content would supply some additional heat to the sintering process via oxidation, but this is by far the least preferable option for a value-added standpoint.

Value-in-use is derived from a complicated calculation involving a large amount of data intrinsic to the material (chemical composition, size etc.) as well as extrinsic factors such as energy prices, other raw material prices, or operation factors such as plant availability and production bottlenecks (hot metal availability for example). While value-in-use is by its nature transient as economic and operational conditions change, general rules can be established that hold true under most reasonable circumstances.

For the BF, by far the most important factors are volatile metal removal from DRI pellets and the mechanical strength of the produced pellets. High metallization does provide a process benefit but is not critical for operation, in fact if low volatile metal content and high mechanical strength is achievable without driving Fe reduction reactions to completion this is often more economical as a large-scale BF is extremely efficient at carrying out final stage reduction and melting.

This is what was observed during the benchmarking visit to China, low metallization DRI was charged direct to the BF as it is more efficient at iron reduction than the RHF (Section 5.1.1).

For BF usage, it would be preferable to optimize for Fe throughput to the RHF and zinc removal with as short a hold time and as low of a temperature as possible. For BF use, C/O = 0.7, T = 1150 °C, t = 15 min allows for excellent zinc and lead removal (0.05 wt. % and 0.01 wt. % respectively) with very little residual carbon (0.92 wt. %) which may affect pellet strength while still producing DRI of 80% Fe metallization.

However, for the BOF two critical factors related to the chemistry of the fired pellets may render recycling in this manner uneconomical. Firstly the pellets contain significant gangue (80 – 85% Fe_{Tot}) when compared to gas DRI/HBI produced from virgin ore (90-94% Fe_{Tot} [184]) which increases slag generation and flux demands to furnace.

Secondly, the sulfur content of the DRI produced in this work is significantly higher (0.1 – 0.2 wt. %) than gas DRI which typically has a sulfur content of <0.03 wt. %. It's likely that a sulfur content this high would preclude the inclusion of DRI produced from BF dust and BOS dust from most applications as the ability for desulfurization to occur in the BOF is limited at best [167].

Chemical reasoning aside, another fundamental reason why RHF DRI charging to the BOF is challenging relates to the melting behavior of DRI in the furnace. The typical loading of DRI to a BOF is around 10% by weight of the cold scrap charge [185], as when higher levels of DRI are introduced so-called 'icebergs' of DRI can form within the melt [186]. These icebergs are agglomerations of DRI lumps that are insulated from the heat of the melt by a layer of molten slag adhered to the outer surface. This can lead to several negative process implications such as high C at the end of the blowing period and therefore requiring reblowing, slag slopping, and excessive flame generation. While information in the literature is sparse, it appears most commercial operations feed DRI produced via the RHF from BOS dust and BF dust to the BF rather than the BOF [156,166,169]. This is due to a combination of factors that will be calculated by each steel producer based on economic and commercial conditions, but the sulfur and gangue content is likely the driver behind this reasoning.

Inevitably during DRI production, there will be some generation of fine material that is unsuitable for charging to the BOF or BF. Estimates range between 5 – 15% of undersize fines during RHF production [169]. Due to their low volatile metal content and high metallic Fe content these would be suitable for recycling through the sinter plant or cold-bonded into briquettes for use in the BF or the BOF [187].

Using Port Talbot works as a hypothetical case study for an RHF based on this experimental work. Approximately 3.5 mt/annum of liquid steel is produced in Port Talbot annually, which corresponds approximately to 10,500 blows of 330 t in the steel plant. An RHF producing 200 kt/annum of DRI per year based on a C/O = 0.7, T = 1250 °C, t = 15 min blend of BF dust and BOS dust to be solely recycled to the BOF would therefore be an average of approximately 19 tonnes of DRI per blow at 0.2 wt. % S. For comparison, typical ore S content used for cooling in the BOF is 0.015 – 0.025 wt. % [167].

Based on a 330-tonne heat size, this would contribute an additional 0.012 % S to the total steel composition. In the converter approximately 45% of S in the hot metal reports to the slag and a further 10 -15 % is directly oxidized to SO_2 in the highest oxygen potential (near the oxygen jet impact zone) region of the melt, leaving approximately 40% of the input sulfur to report to the hot metal [167].
This would approximate to a 0.04 wt. % increase in S in the hot metal following the blow. Obviously, the tolerance for S in the hot metal following the blow varies by grade but typically S levels of 0.001 – 0.01 wt. % are desired in the liquid steel.

Therefore, it seems highly likely based on S content alone that certainly not all the DRI generated from an RHF utilizing BF dust and BOS dust could be utilized in the BOF in this hypothetical scenario, where it presents the highest value-in-use as a raw material.

The BF is significantly less sensitive to S than the BOF and any balance of DRI that cannot be economically utilized in the BOF would be recycled through that process route.

5.6 Conclusions

Self-reducing agglomerates prepared from BF dust and BOS dust can be effectively recycled via co-processing through an RHF. Realistic RHF conditions of 1200 – 1300 °C for 0 – 15 minutes reduced Zn and Pb levels sufficiently for recycling to the BF. Excellent metallization of iron was observed, even under an oxidizing atmosphere. This was ascribed to the formation of a localized reducing atmosphere generated by the carbon within the self-reducing agglomerates.

The removal of Na and K from the self-reducing agglomerates at low hold times was poor, this was ascribed to the solubility of reduced activity of the oxides of Na and K through competing reaction with the semi-molten gangue system in the pellets. Na and K was seen to increase at extended high temperature firing, although this was attributed to reaction with the binder in the crucibles utilized in the study. The findings suggest extended hold times are undesirable due to the potential interaction between pellets and the furnace hearth.

The residual level of sulfur within the pellets remains high after processing, due to the high sulfur content of the BF dust used in the work, although some sulfur is lost to combustion during firing the majority remains physically bound in the fired pellets. The DRI produced would likely be more suitable for recycling via the BF where the high metallic iron content could provide process benefits such as lower reductant requirements and higher productivity.

Small amounts could be utilized in the BOF subject to grade chemistry requirements, but the high sulfur and gangue content mean it is unlikely all the DRI produced from a commercial size RHF in Port Talbot could be utilized in the BOF and some if not most would be recycled to the BF.

The zinc oxide product produced in this trial was of good quality and would be ideal feedstock for a zinc recycler but likely the quality of the ZnO product would be

significantly less in an operating RHF due to more aggressive heating rates, gas turbulence and fines generation from the handling of pellets between forming and firing. Ultimately the question as to whether an RHF is an economical option for recovery of these materials is highly dependent on local factors which must be considered on a case-by-case basis factoring in local cost of liquid steel calculations, energy pricing and the availability of capex for plant construction.

Generally, the greater the utilization of the produced DRI in the BOF rather than the BF the more economic value to the steelmaker the process is producing. Ultimately, the inability for the RHF as a process as described herein to desulfurize the high S BF dust used as a reductant mean the prospect may be uneconomical in many cases.

6. Next Generation RHFs: Pig Iron Nugget Production

6.1 Introduction

Based on the work in the previous chapter, DRI produced from BF dust and BOS dust in a typical RHF process would not be completely recyclable to the BOF. High gangue content due to the nature of the input materials is inevitable and carries penalties such as increased slag volumes, but another key value driver of DRI is sulfur content. As DRI is substantially metallized, it can also be used to displace scrap within a BOS vessel or an electric arc furnace (EAF). Scrap steel is substantially more expensive per unit of iron than virgin ore [189] and DRI that is of high enough quality to be recycled to the BOS vessel rather than the BF will have substantially higher value in use (VIU) to the steelmaker.

The BOS process is sensitive to sulfur addition in the scrap charge, because despite the presence of a basic slag, the high oxygen activity in the converter makes the dissolution of sulfur into the HM thermodynamically favorable [167]. Many high-performance steels require extremely low levels of residual sulfur within the HM, with the production costs sharpening steeply as ultralow sulfur concentrations (<0.001 wt. %) become necessary [190]. As such, low sulfur scrap substitutes are expensive and thus low residual sulfur levels within DRI are desirable for the DRI producer.

Next generation RHF processes such as ITmk3 go one step further than the purely solid-state reduction of iron oxides. Through careful manipulation of slag chemistry, the iron in the ITmk3 process is sufficiently carburized to liquify and coalesce into pig iron nuggets (Figure 6.1), separate from an immiscible, liquid slag phase [82,191].

Similar nugget making processes include E-Iron, which uses an adapted linear tunnel furnace to produce iron nuggets from non-zinc bearing mill wastes [192] and Hi-QIP which uses an un-agglomerated feed on a bed of carbonaceous reductant [87]. The production of pig iron nuggets from zinc bearing mill wastes has been reported previously [193–195], implying the feasibility of the production of nuggets based on experimental laboratory conditions in inert gas atmospheres.

Sulfur control in DRI production is mostly achieved by raw material input. DRI produced using coal as a reductant is too high in sulfur (0.44 wt. %) to be utilized in a BOS/EAF melt shop [196] in many cases and thus is usually utilized via a blast furnace, which is less sensitive to sulfur. However, the addition of a melting step and a molten

slag, such as in ITmk3, offers an opportunity to sequester sulfur from the metallic iron within a distinct slag phase.

Figure 6.1. Iron nuggets produced via a large scale ITmk3 pilot plant[82]. Reproduced with permission from the Kobe Steel Engineering Report Editorial Board.

This is not dissimilar to the mechanism by which sulfur is removed within the blast furnace [167]. Another potential avenue to add value to iron nugget production is by the simultaneous reduction of manganese oxides often found in BOS dust in small, but not insignificant amounts, into the pig iron nugget product [124,197].

Manganese is a common alloying element in the production of steel and is often added on a supplementary basis with the scrap charge to a BOS vessel or EAF in the form of ferromanganese alloys. This is a cost to the steel producer, therefore simultaneously reducing Mn into the hot metal produced during pig iron nugget making would be economically desirable. Srivastava reported the reduction of Mn_xO_y to the liquid iron phase during nugget making reactions using a manganiferous ore with minimal losses of Mn to the slag phase (18% at 1450 °C for 40 min) [198].However, this was performed using a high manganese iron ore rather than with steelmaking by-products and used graphite and polyethylene as a reducing agent.

Herein, an exploration of the thermodynamics of the complicated slag-iron system present in nugget production is undertaken, and the ability for the nugget making

process to desulfurize the produced pig iron and reduce manganese into the hot metal at a range of temperatures, slag chemistries and reductant levels can be determined. Three conditions need to be met to produce pig iron nuggets in a manner similar to the ITmk3 process or E-Iron;

- a low liquidus temperature slag, to allow for molten iron droplets to coalesce,
- sufficient carbon to reduce iron and zinc oxides to their elemental form, and
- sufficient carbon to further carburize the metallic iron such that the melting point is low enough to form molten pig iron at the reaction temperature.

Using BF dust and BOS dust from Tata Steel Port Talbot in the United Kingdom as a case study, the effect of various blends and temperatures is explored with respect to the thermodynamics of the chemical system. The study is limited in its scope to thermodynamics, without exploring the complicated reaction kinetics of the multiphase system and a comparison is made to experimental studies from literature performed on similar material.

By comparing results of a thermodynamic study such as this to the experimental observations made in the literature to determine whether the relatively short reaction times in pig iron nugget making (<60 min) are sufficient to allow the slag-metal system to reach equilibrium or whether kinetic factors play a substantial role in determining Fe yield and Mn/S partition between the hot metal and the slag. The resultant recommendations of the computational portion of the work was also followed by a brief laboratory study to validate the core concepts of the work.

The objective of this research was to determine whether iron nugget making processes such as ITmk3 or E-Iron could be applied to integrated steel plant by-product dusts to produce a higher value product more suitable for use in the BOF than conventional RHF DRI.

6.2 Computational Methods

Calculations were performed using the equilib module of FactSage 7.3. This module uses the Gibbs free energy minimization method to determine the equilibrium composition of complex heterogeneous systems. A generalized input chemistry of the model for BOS dust and BF dust is shown in Table 6.1, based on material obtained from Tata Steel Port Talbot UK. Reducible oxygen associated to the iron within the material

is denoted by O_{Fe}. For equilibrium calculations, all pure solid and gaseous species possible from the input chemistry were considered, as well as all applicable solid-state solutions from the FTOxid database. For the liquid phase two alloy solutions were considered from the FSstel and FToxid databases, FSstel-liqu#1 to as the molten pig iron phase and FToxid-SLAGA#1 as the molten oxide slag system formed from the gangue.

Phase diagrams were generated using the phase diagram module of FACTSAGE 7.3, using FToxid-SLAGA#1 as the target alloy solution phase for thermal projections. The equilibrium composition calculations are normalized to 100 g of input material. For clarity's sake in Figures, the FSstel-liqu#1 liquid alloy solution is referred to as 'Pig Iron' and the FTOxid_SLAGA#1 liquid alloy solution is referred to as 'Slag'.

Table 6.1. Chemical composition of the two zinc contaminated steelmaking by-products BF dust and BOS dust.

	Chemical Composition (wt. %)												
Material	**Fe**	**SiO_2**	**Al_2O_3**	**TiO_2**	**$CaCO_3$**	**CaO**	**MgO**	**P_2O_5**	**MnO**	**S**	**ZnO**	**O_{Fe}**	**C**
BF dust	26.79	5.61	2.63	0.14	6.89	0.77	0.159	0.62	0	0.62	0.87	14.41	40.49
BOS dust	59.14	2.31	0.34	0.06	13.08	4.44	1.16	0.088	0.74	0.001	4.14	14.50	0

6.3 The conditions of Nugget Making

6.3.1 Low Liquidus Temperature Slag

The Al_2O_3-SiO_2-CaO-FeO system is well studied, due to its usefulness in describing the behaviour of slags within the blast furnace. In blast furnace ironmaking, siliceous ores are fluxed with limestone to reduce the overall liquidus temperature of the gangue to encourage lower temperature separation from the iron [199].

The calculated ternary phase diagram of the SiO_2-CaO -Al_2O_3 system is shown in Figure 6.2. The projection shows the liquidus projection front at temperatures 1000–1800 °C, at atmospheric pressure. The minimal liquidus temperature for this system as described is 1184 °C. It can be seen from Figure 6.2 that the CaO-Al2O3-SiO2 system for BF dust alone, 1700 °C > $T_{liquidus}$ > 1600 °C. For BOS dust the system is not molten even at 1800 °C. The solid line between the two points indicates the composition of the

system as the ratio of BOS dust to BF dust is changed. This line passes through regions of much lower liquidus temperature (~1200 °C) at a ratio of 2:1 BF dust to BOS dust.

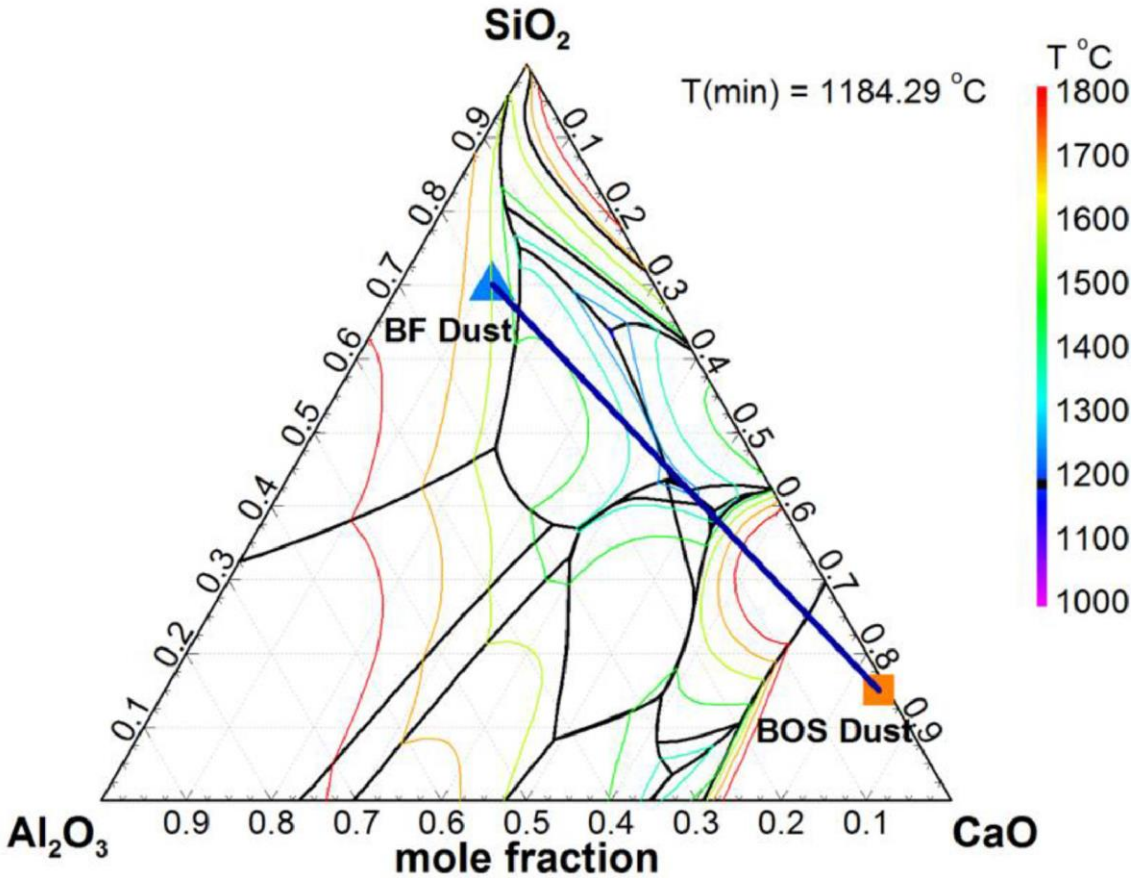

Figure 6.2. Ternary phase diagram of the CaO-Al_2O_3-SiO_2 oxide system. Liquidus projection lines from 1000 – 1800 °C indicate under which compositions the oxide system is molten. The composition of BF dust and BOS dust are marked.

FeO has a fluidizing effect on the CaO-Al2O3-SiO2 as can be seen in Figure 6.3. The minimum liquidus temperature of the system decreases dramatically with increased FeO addition, and at 0.2 mol fraction FeO the minimum liquidus temperature is 1013 °C, a substantial decrease from the pure CaO-Al2O3-SiO2 system.

As the reduction of FeO occurs during the iron nugget making process occurs, the activity (concentration) of FeO within the slag phase will reduce and liquidus temperature of the slag system will increase as the reduction reactions progress. There is a trade-off in processing iron nuggets to allow for some FeO to remain within the slag post-reduction, increased slag fluidity may reduce the demand for auxiliary fluxing agent additions, lower theoretical plant operating temperatures and promote the kinetics of slag-metal desulfurization reactions which are diffusion controlled [200]. These benefits

are of course offset by the loss of iron, the primary product of iron nugget making to the slag phase.

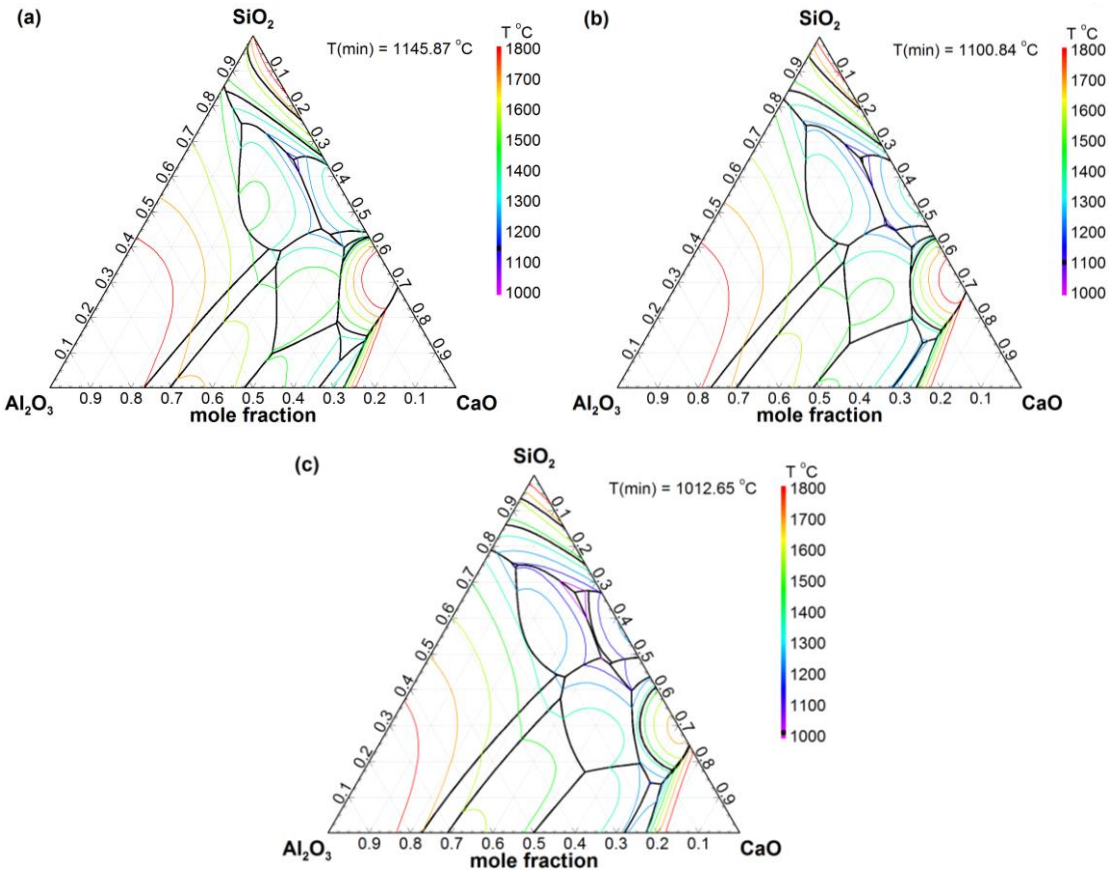

Figure 6.3. Liquidus projections between 1000 °C – 1800 °C of the calculated temperature dependent CaO-Al2O3-SiO2-FeO system at fixed FeO mole fraction compositions of (a) 0.05, (b) 0.1 and (c) 0.2.

6.3.2 Carbonaceous Reduction of Ferrous and Zinc Oxides

The role of carbon in the reduction of iron oxide and zinc oxide with regards to the processing of zinc bearing steel plants dusts has been recently reviewed [11]. BF dust has a super-stoichiometric amount of carbon present within the material with regards to reduction, even after reducing the Fe and Zn oxides in the material there is substantial remaining carbon. This can be seen clearly in Fig. 4 showing equilibrium iron species compositions of BF dust at increasing temperature. As T increases carbon reacts with the iron oxides present in the dust to form FeO at 650 °C, the iron is fully reduced to its metallic form at 700 °C. Due to the large excess of carbon the iron completely carburizes to Fe_3C at 850 °C before melting at around 1050 °C. A small proportion of the molten slag phase is present between 450 °C and 1050 °C due to the fluidizing

effects of FeO but as the reduction proceeds and more Fe is stripped from the slag phase into the molten pig iron phase it solidifies as the liquidus temperature increases. The calculations in Figure 6.4 suggest a large proportion of solid carbon is still present within the system even at 1800 °C, indicating the liquid pig iron phase is saturated with carbon.

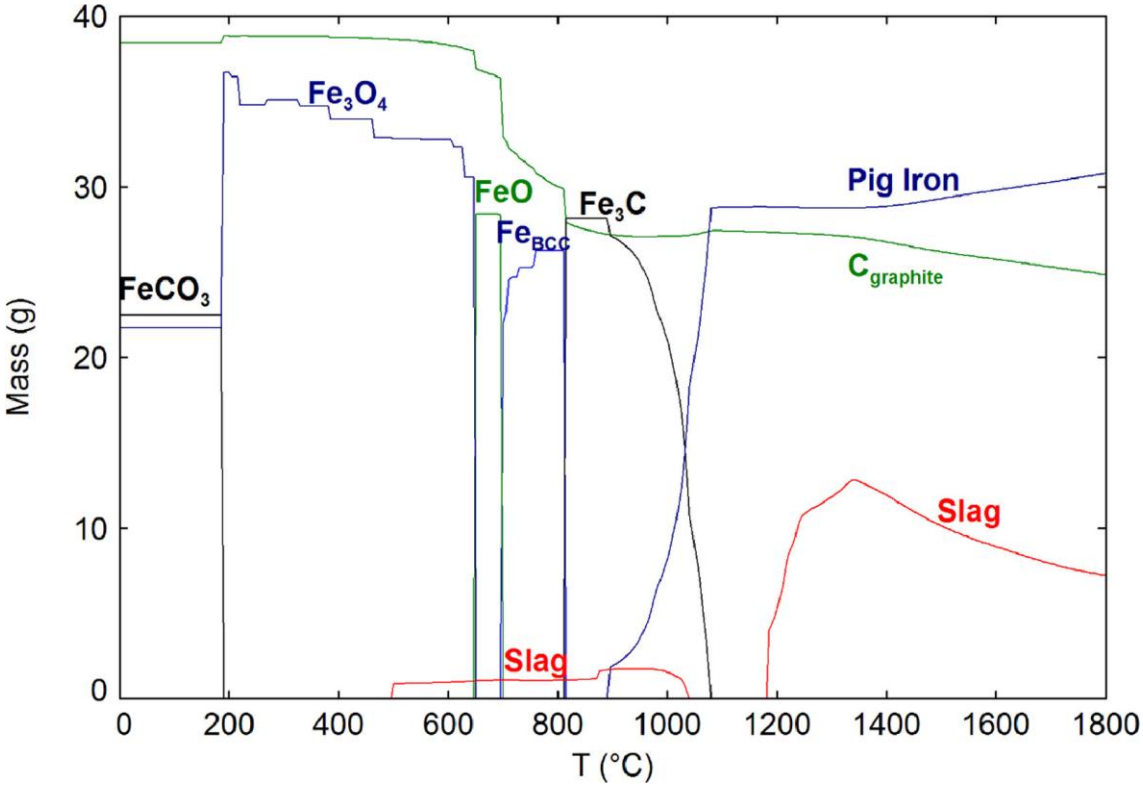

Figure 6.4. The reduction of iron oxides within BF dust from 0 °C to 1800 °C. Pig iron and slag are both liquid phases.

Figure 6.5 explores the behaviour of zinc up to a temperature range of 1800 °C. The calculations indicate that zinc is present within the dust in the form of sphalerite (ZnS) at ambient conditions, this conflicts with experimental characterization of the dust [201], which suggests it is present in the zinc oxide form in the material as received. It is likely as T increases the ZnO present at ambient conditions would react to form ZnS as a high excess of carbon and the presence of Fe_2O_3 promote sulfidation of zincite during roasting (Han et al., 2017). Studies of the sulfidation of ZnO using FeS as a sulfidization agent and demonstrated experimentally at temperatures > 450 °C [202] suggests that ZnS would indeed form preferentially to FeS during the heating of BF dust as ZnO reacts with sulfur present in the material

It is observed that a small proportion of ZnS dissolves within the small amount of molten slag phase present at T >450 °C, however the dissolved ZnS is shown to precipitate from the slag at around 875 °C. As T increases above 900 °C ZnS reduces and the zinc vaporizes, with the high residual carbon in BF dust at these temperatures sufficient to suppress the reoxidation of Zn to ZnO as oxygen activity is sufficiently low.

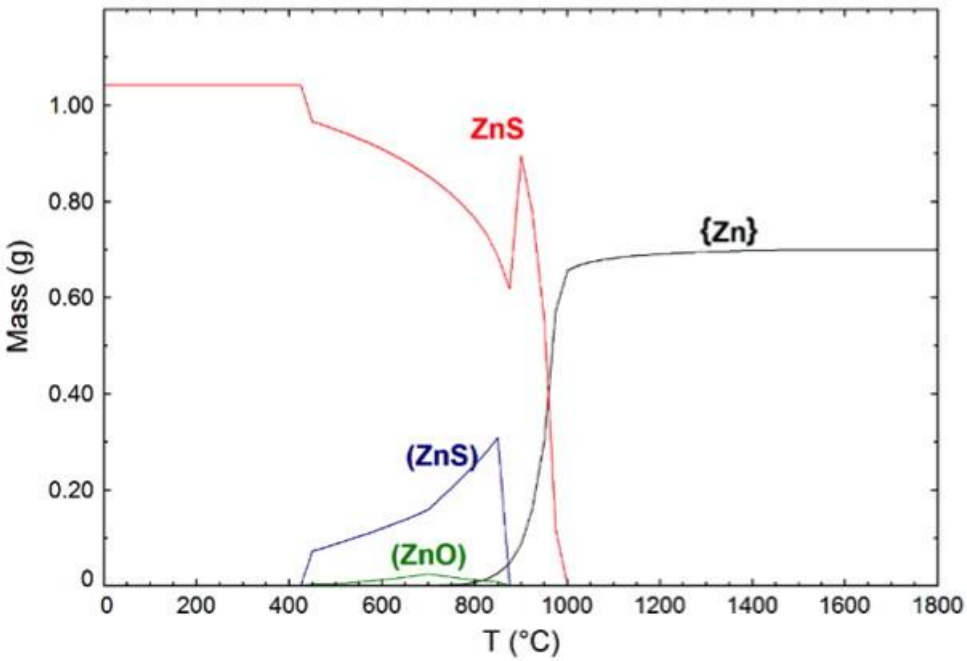

Figure 6.5. The reduction of zinc within BF dust from 0 °C to 1800 °C. Round brackets ( ) are used to denote substances dissolved within the molten slag phase, curled brackets { } are used to deonate substances in the gas phase and brace-less substances are solid.

During the heating of BOS dust as shown in Figure 6.6 however, the lack of reductant sees most of the Fe dissolving into the molten slag phase in the form of FeO. Therefore, the yield of pig iron from heating BOS dust alone would be very low. The high activity of FeO within this system means the molten slag phase is formed at low temperatures (~1000 °C). Without the excess of C it can be observed that the molten pig iron phase does not form until the melting point of elemental iron (1538 °C) as there is negligible amounts of carbon dissolved within the metallic iron.

Figure 6.7 shows the heating of BOS dust along with the addition of a super stoichiometric amount of carbon (3 mol. per 100 g of material). This addition of carbon suppresses the formation of the molten slag phase through the reduced activity of FeO and causes a large amount of solid CaO gangue to be present even at 1800 °C.

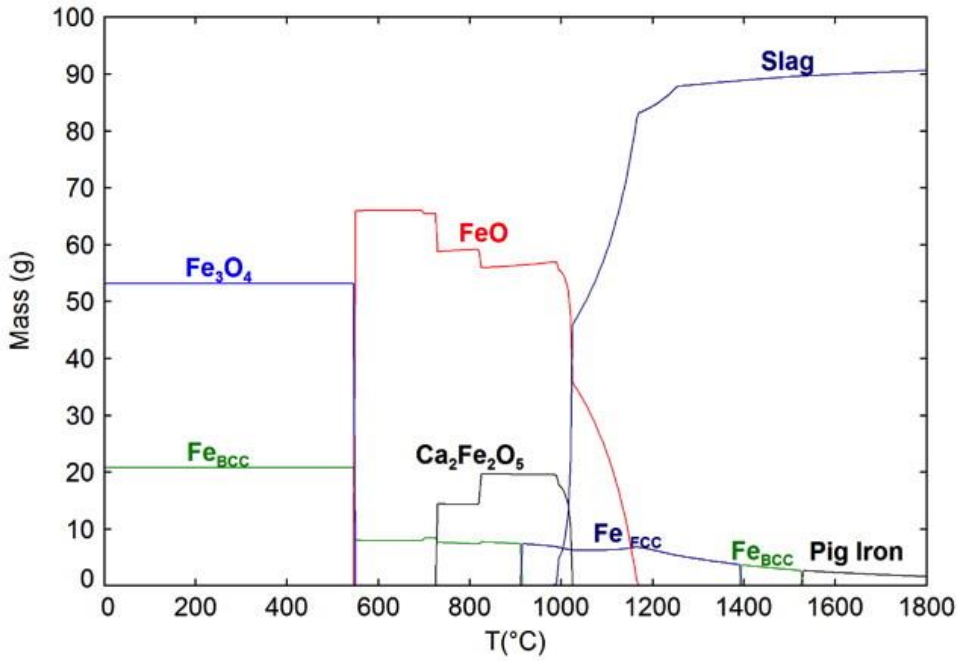

Figure 6.6. Calculated equilibrium composition of BOS dust from 0 °C to 1800 °C.

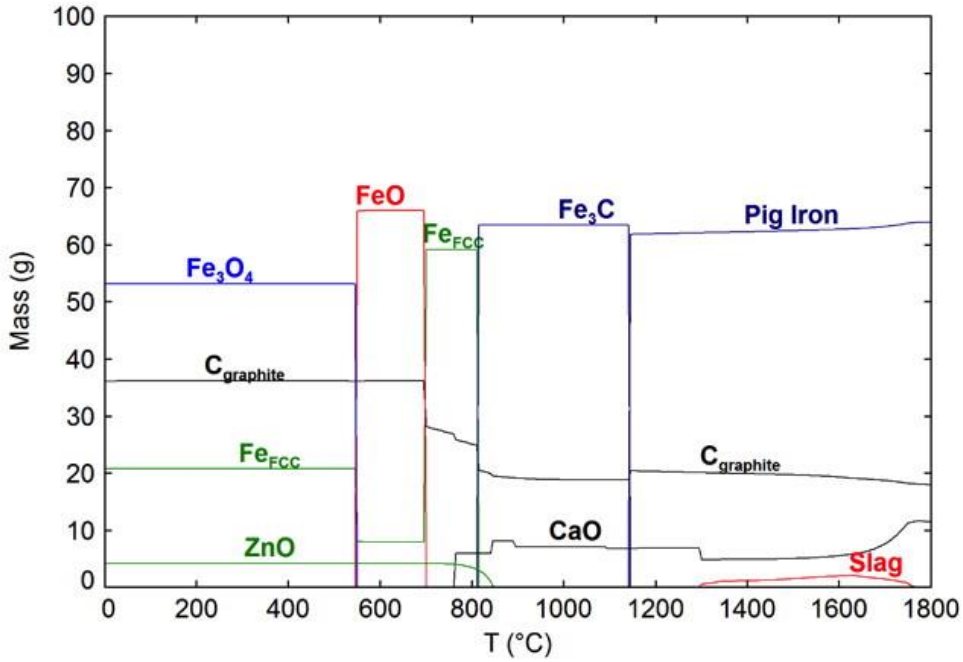

Figure 6.7 Calculated equilibrium composition of BOS dust with the addition of 3 mol of carbon from 0 °C to 1800 °C.

An excess of carbon being present post-reduction can inhibit the coalescence of molten iron droplets in pig iron nugget production as observed during experimental studies [203]. It has also been reported that work producing pig iron nuggets from jarosite waste and BF dust, with large excesses of carbon being detrimental to the coalescence

of liquid iron droplets [204]. Therefore, it is worth focusing on the optimum blend of BF dust to BOS dust to optimize for minimizing the solid fraction of the mixture at realistic process temperatures.

6.4 Varying the Ratio of BF dust to BOS dust in Pig Iron Nugget Production

6.4.1 Iron Recovery

Iron recovery is effectively the molar yield of the iron nugget making process. Some iron loss to slag in the emulsion loss (iron droplets unable to coalesce to a size separable from the immiscible slag phase) is an inevitability and controlled by kinetic factors such as reaction time, but in this context solely represents the solubility of Fe in the slag phase at a given BF dust: BOS dust ratio and temperature.

Iron recovery is calculated using Equation 6.1 with losses occurring either by the incomplete melting of the system or via dissolution of unreduced FeO into the slag.

$$\mathrm{R}_{\mathrm{Fe}_{\%}} = \frac{\mathrm{Fe}_{\mathrm{Pig\ Iron}}}{\mathrm{Fe}_{\mathrm{Pig\ Iron}} + \mathrm{Fe}_{\mathrm{Slag}}} \times 100 \tag{6.1}$$

Figure 6.8 shows the effect of temperature (T) and BF dust fraction on the recovery of Fe. Once a stoichiometric amount of carbon is present in the blend at 0.35 BF dust fraction, iron recovery sharply increases, above 90% even at lower temperatures around 1100 °C. This seems to be a general behaviour in the production of iron nuggets from a broad range of iron-bearing materials, with practical studies reporting the requirement of a stoichiometric amount of carbon relative to the total reducible oxygen content to produce iron nuggets with a high yield [124,193,203–206].

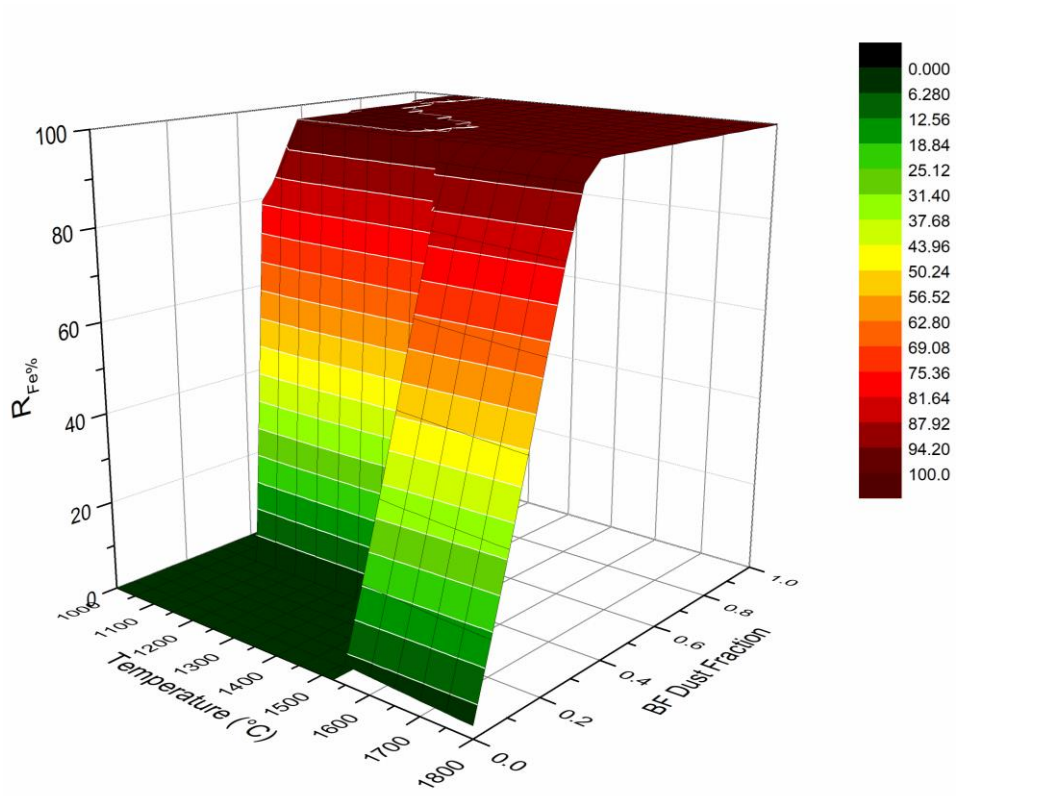

Figure 6.8. Surface plot showing $R_{Fe\%}$ at varying ratios of BF dust to BOS dust from 0 °C to 1800 °C.

Following the reduction step only a small excess of carbon is required to saturate the Fe and subsequently melt it. However, the addition of an excess of BF dust leaves significant unreacted C in the system which as well as reducing productivity of nuggets from a kinetic viewpoint, also reduces the total iron loading to the furnace and therefore reducing throughput.

Iron output is calculated from Equation 6.2 and a 3D surface plot of output against BF dust fraction and T is shown in Figure 6.9.

$$R_{Out_{\%}} = \frac{R_{Fe\%} \times Fe_{Tot}}{100} \tag{6.2}$$

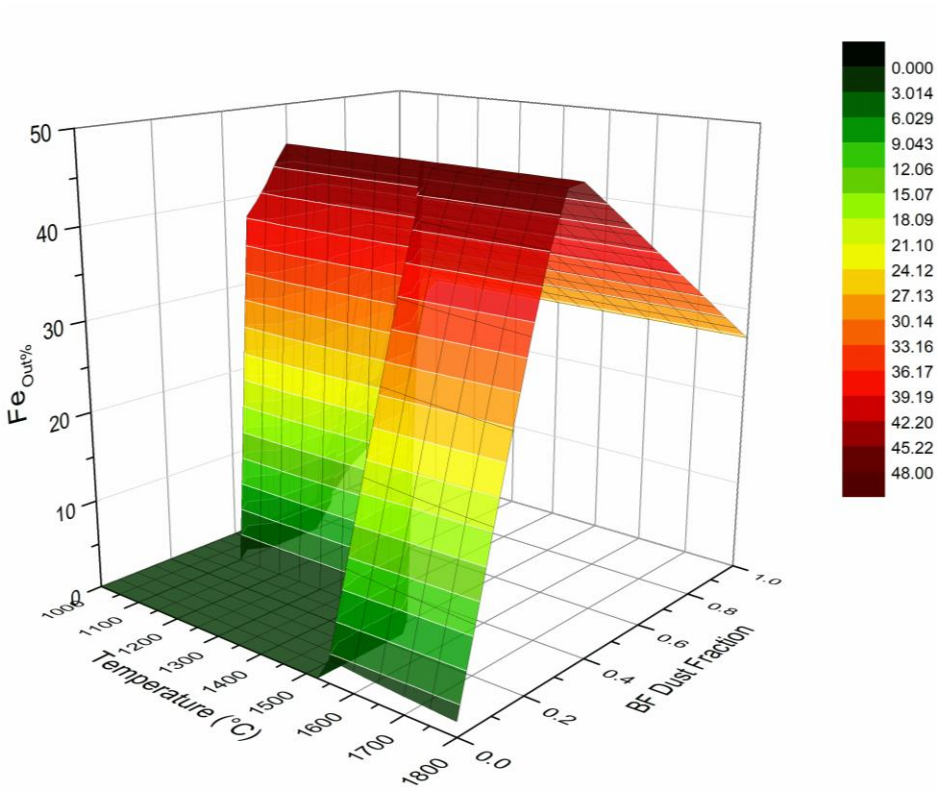

Figure 6.9. Calculated surface plot showing Fe_{out} at varying ratios of BF dust to BOS dust from 0 °C to 1800 °C.

The maximum iron throughput is achieved by heating to >1150 °C with a BF dust fraction of 0.35 but this productivity drops off as increasing BF dust is added to the system as the overall amount of Fe in the system decreases.

6.4.2 Carburization

The carbon content of the produced pig iron is of relevance for two reasons. Firstly, as already established, a greater degree of carbon dissolved within the pig iron phase reduces melting temperature and therefore lowers the energy demand of the process. Secondly, increased carbon content in the produced nuggets has process benefits for the EAF/BOF meltshop [165,207]. It has been established that the critical role carburization plays in low temperature pig iron nugget making, showing that the separation of slag and metal phases in the process was controlled by the rate of carbon dissolution into the newly formed metallic iron [205].

To fully carburize the pig iron formed, carbon must be present in excess of the stoichiometric amount required for reduction of oxides such as Fe_2O_3 and ZnO as these reactions occur preferentially to carbon dissolving into metallic iron. Figure 6.10 shows the changing carbon content calculated for the pig iron phase with relation to

temperature and BF dust fraction. As expected, high temperature and BF dust fraction favor a degree of carburization of the pig iron, this is due to the high level of carbon present in BF dust compared to the negligible amount in the BOS dust.

Very little carbon dissolves into the molten iron phase at low BF dust fractions (< 0.35), this is due to the amount of carbon in the system being insufficient to fully reduce the iron and zinc oxides. Once the BF dust fraction reaches a level at which carbon is in stoichiometric excess relative to the iron and zinc oxides in the system, further increase of BF dust fraction causes a sharp increase in the carbon content of the pig iron phase.

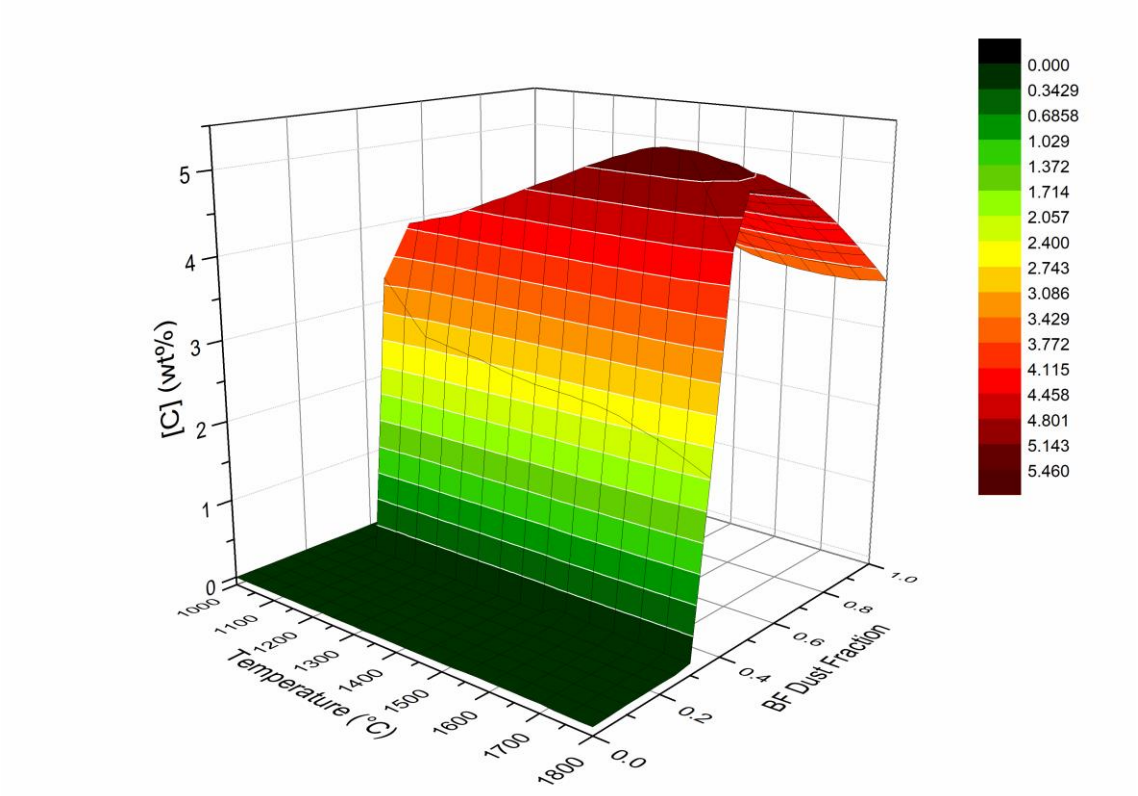

Figure 6.10. Calculated surface plot showing the dissolved carbon (wt. % [C]) in the pig iron alloy phase with varying BF dust fraction between 0 °C – 1800 °C.

6.4.3 Sulfur Control

Due to BF dust containing substantially more sulfur per unit mass than BOS dust, as the BF dust fraction increases in the blend so too does S_{Tot} for the system (Figure 6.11). High temperature favors the sequestration of S in the slag, while high BF dust fractions and low temperatures promote sulfurization of the pig iron. At BF dust fractions of 0.4 and 1200 °C the equilibrium sulfur content of the pig iron is 0.024 wt%, which reduces to 0.014 wt% at 1300 °C and 0.007 wt% at 1400 °C. This seems consistent with

experimental observations of the S seizing capacity of ironmaking slags from literature increasing with T [208,209].

As the BF dust fraction increases, the overall basicity of the slag is reduced and therefore the activity of CaO is lowered. As such, S becomes less soluble in the slag phase and more so to the pig iron phase. It is therefore desirable to maintain a basic slag chemistry with regards to sulfur removal, but the drawback of this is the higher melting temperature of more basic oxide systems as discussed below.

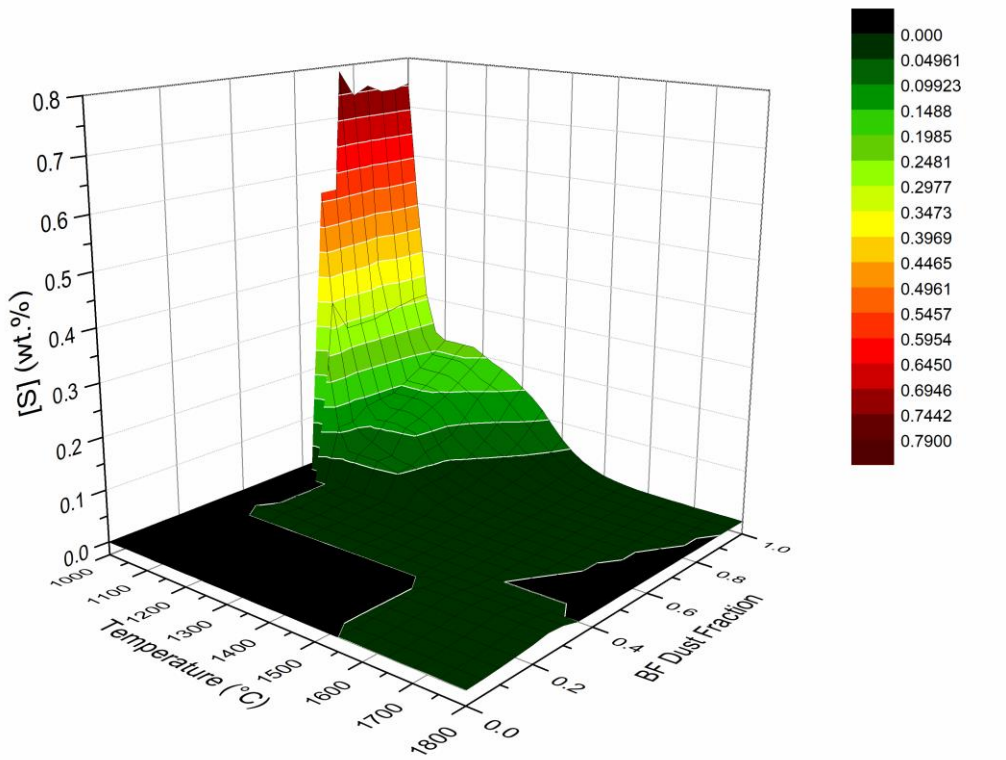

Figure 6.11. Calculated surface plot showing the dissolved sulfur (wt. % [S]) in the pig iron alloy phase with varying BF dust fraction between 0 °C - 1800 °C.

6.4.4 Manganese Recovery

Manganese reduction by solid carbon is feasible under standard conditions at 1417 °C [198]during the production of iron nuggets, but it is observed in this study that Mn dissolving into the pig iron is initiated once a stoichiometric amount of carbon in the blend is reached. This is likely due to the extremely low oxygen activity of the system once excess carbon is present as a solid in the system at equilibrium.

At all temperatures with a BF dust fraction below 0.35 Mn is present either as solid MnO or in solution in the slag phase (Figure 6.12). The total amount of Mn in the

system decreases with increasing BF dust fraction, hence the drop-off in wt% [Mn] as BF dust fraction exceeds the stoichiometrically optimal amount of carbon.

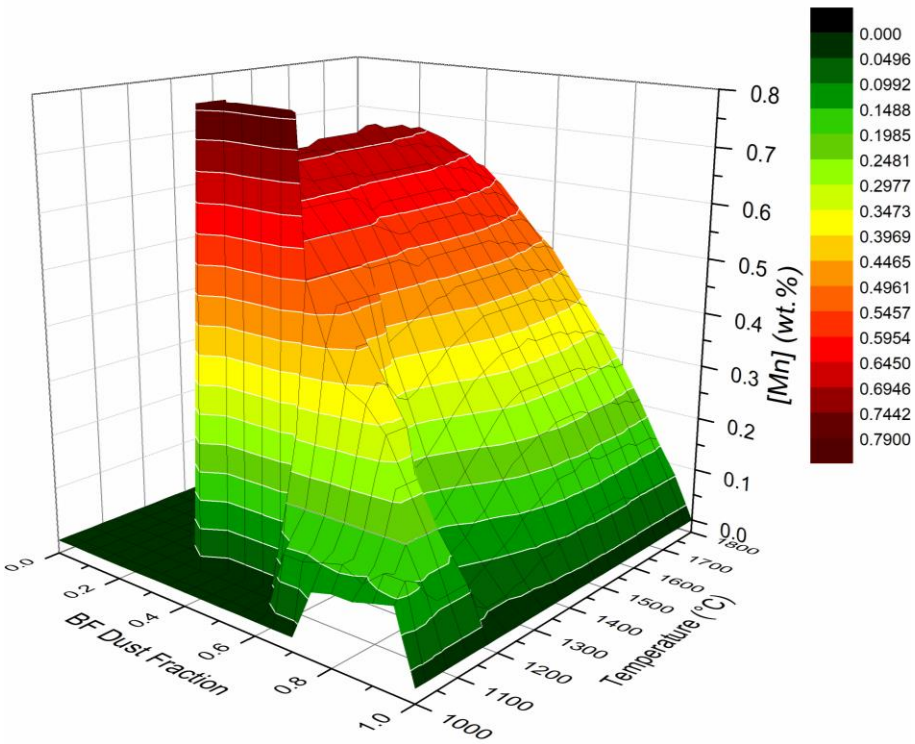

Figure 6.12. Calculated surface plot showing the dissolved manganese (wt. % [Mn]) in the pig iron alloy phase with varying BF dust fraction between 0 °C - 1800 °C.

6.4.5 Liquidity of the system

To facilitate the agglomeration of the molten pig iron phase into droplets large enough to separate easily from the slag by mechanical means, it is favourable that the system be as liquid as possible. As expected, higher temperatures lead to a decrease in solid fraction in the system. Figure 6.13 shows the fraction of the system present as solids under the given conditions. The solid fraction is defined by Equation 6.3, where mass(s), mass(m), and mass(v) are the mass of material in the solid, molten and vapor phases, respectively.

$$\text{Solid Fraction} = \frac{\text{mass(s)}}{\text{mass(s)} + \text{mass(m)} + \text{mass(v)}} \tag{6.3}$$

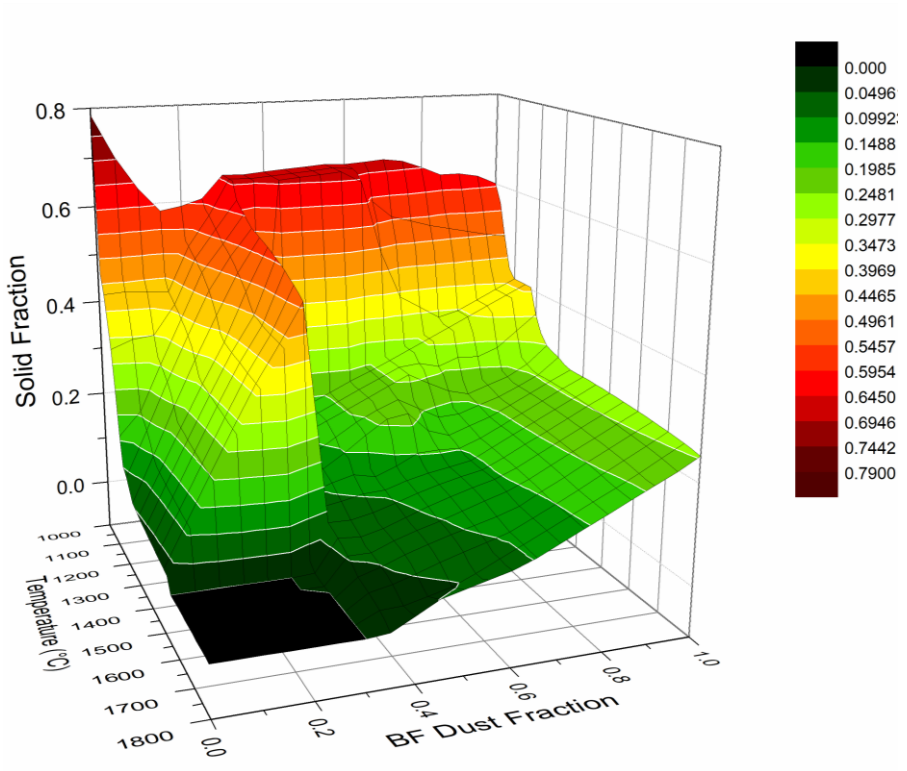

Figure 6.13. Calculated surface plot showing the fraction of the system present as a solid with varying BF dust fraction between 0 °C – 1800 °C.

The solids present in the system here can be classified as non-carbonaceous and carbonaceous. Carbonaceous material under these conditions is in the form of solid iron carbide Fe_3C and elemental carbon in the form of graphite. Non-carbonaceous material is all other solid matter, which includes gangue mineral oxides like Si, Ca and Al oxides, unreduced iron oxides and metallic but un-melted iron. By plotting these two types of solid independently of one another, a clearer picture of the process can be obtained (Figure 6.14.)

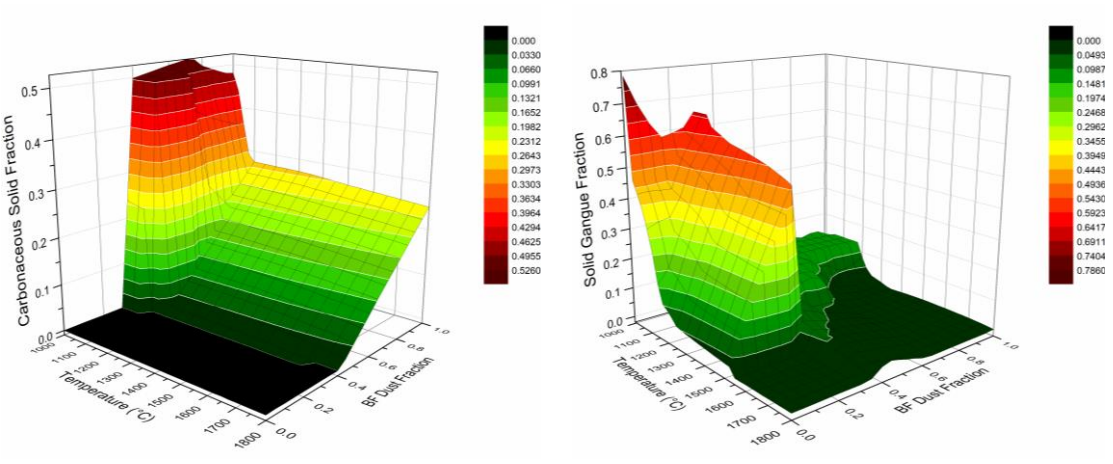

(a) (b)

Figure 6.14. Surface plots showing the fraction of the system present as solid carbonaceous material (a) and non-carbonaceous material (b) with varying BF dust fraction between 0 °C – 1800 °C.

Large proportions of solid carbonaceous matter are only present in significant proportions at large BF dust fractions. The region confined between 0.4 – 0.6 BF dust fraction and 1000 °C – 1150 °C in Figure 6.14a is due to the solid carburization of Fe to Fe_3C but at temperatures not sufficient to melt the iron carbide. It can be seen that at high temperatures large amounts of solid graphite is present when the BF dust fraction is high. This is due to the pig iron phase being saturated with carbon and the low activity of oxygen means the carbon is not simply oxidized to form gasses.

In Figure 6.14b the solid non-carbonaceous material is present at low BF dust fractions and temperatures. As BF dust fraction moves from 0 to 0.3 the solid non-carbonaceous fraction begins to increase as FeO is reduced from the slag and the liquidus temperature of the CaO-SiO_2-Al_2O_3 system increases. The solid fraction drops substantially as the BF dust fraction exceeds 0.35, as iron is reduced and melts but at temperatures below 1500 °C the system still contains substantial calcium oxide minerals which would impede the coalescence of iron nuggets. Once the amount of carbon in the system exceeds the required amount to reduce all reducible oxides (Zn, Mn, Fe etc.) and carburize the iron, additional carbon would be detrimental to the productivity of the process.

6.5 Introduction of Fluxing Agents

As explored above, the optimum ratio to produce iron nuggets from BF dust and BOS dust appear to be in a proportion of 37:63. This provides sufficient carbon to reduce and carburize iron oxides present, reduces oxygen activity sufficiently to promote desulfurization and simultaneously recover Mn in the pig iron without incorporating excess carbon into the system which may impede the kinetics of production. However, the temperatures required to fully fluidize the gangue in the system to produce a molten slag are high, the system at these conditions is not fully liquid at 1450 °C. Limestone is often used as a flux to promote fluidization of the acidic silica impurities found in iron ore in blast furnace ironmaking, but at 37% BF dust: 63% BOS dust the gangue chemistry is very basic with a wt. % CaO/SiO_2 ratio of 2.59. As such the slag produced is fully saturated with CaO and excess amounts of CaO exists as a solid at nugget making temperatures of ~1450 °C. Two criteria must be met for nugget making to be feasible with regards to fluidizing the oxide gangue present. Firstly, the liquidus temperature of the gangue must be decreased sufficiently with additions to become molten at reaction temperatures. Secondly, the molten slag that is produced must be compatible with a refractory surface that is suitable for an RHF.

6.5.1 Flux Additions

Under the assumption that all MnO and FeO is reduced from the slag, the slag system can be simplified to a $CaO\text{-}SiO_2\text{−}MgO\text{-}Al_2O_3$ quaternary system, and the temperatures at which this system is fully fluid can be projected via a phase diagram as shown in Figure 6.15. To fluidize the system, SiO_2 can be added to the blend to flux the excess CaO and bring the liquidus temperature of the system down. It would be desirable to add only enough SiO2 to form a slag that is only just CaO saturated, as a fully fluid slag with a high CaO activity would be favorable for the sequestration of S and P from the pig iron into the slag phase.

Figure 6.15 suggests that an addition of 3.307 wt% SiO_2 would be sufficient to fully fluidize the $CaO\text{-}SiO_2\text{−}MgO\text{-}Al_2O_3$ system for a 37:63 BF dust: BOS dust blend at proposed nugget making temperatures of 1450 °C. The phase diagram below, however, is limited to only four components. To consider all the components present in the BF dust: BOS dust mixture, the addition of SiO_2 to the 37:63 BF dust: BOS dust system is explored through FactSage's equilib module. Using the precipitate target function, it was determined that at 1450 °C the minimum SiO_2 addition required to flux the CaO present

and generate a fully molten slag was 5.4 g SiO_2 per 100 g of the blend. This which is in reasonable agreement with Fig. 15 but accounts for the interaction with the pig iron alloy as well as minor constituents not considered in the phase diagram such as TiO_2 and S which of course affect the slags properties.

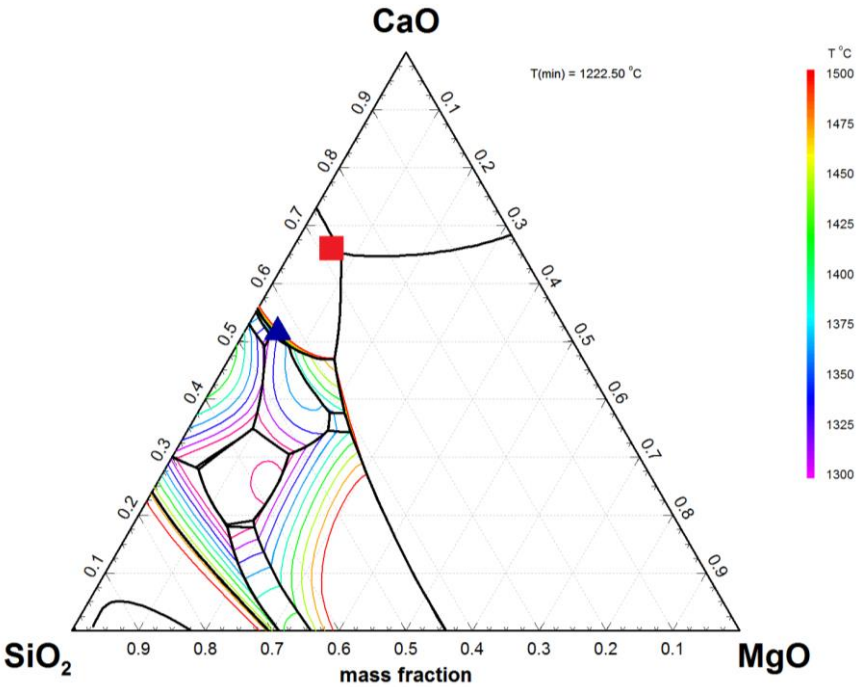

Figure 6.15. Melting projection for the CaO-SiO2−MgO-Al2O3 system at fixed 9 wt% Al2O3 between 1300 – 1500 °C. The red square corresponds to the CaO-SiO2−MgO-Al2O3 composition in a 37:63 BF dust:BOS dust blend. The blue triangle corresponds to a blend with 3.307 wt. % SiO_2 added.

Figure 6.16a shows the effect that this SiO_2 addition has on the Mn, S and Si levels in the pig iron phase as this addition is made. The concentration of Si increases dramatically as SiO_2 is added to the mixture as expected, and S also increases with SiO_2 addition to 0.155 wt%; however, with only SiO_2 addition, this type of slag would be extremely aggressive to refractories. It is highly basic, meaning it would readily attack and dissolve acidic refractories. The slag is also not MgO saturated, meaning basic refractories such as those used on the slag line of a basic oxygen converter would also be attacked and corroded by this slag. Saturating slag with MgO is common practice in EAF and BOS steelmaking as a means of prolonging vessel lining lifetime [210,211], by mitigating the interaction between the liquid slag and the basic furnace lining.

Beggs describes the mechanism of corrosion by the charge to an MgO refractory in an RHF in their 1969 patent for a vitrified refractory surface designed to impede

corrosion by the aggressive FeO-SiO_2 liquid eutectic [212]. The unsaturated nature of the slag with respect to the MgO refractory allowed ingress of liquid into the surface, whereby thermal expansion causes catastrophic spalling. To mitigate this, the MgO capacity of the slag system was explored using Factsage's equilib function.

Again, using the precipitate target function, calculations showed that 1.51 g MgO could be added to the system before it becomes saturated and a Merwinite, $Ca_3Mg(SiO_4)_2$, precipitate would begin to form with increasing MgO inclusion. This addition would render the slag less aggressive to an MgO or dolomite based refractory and thus prolong refractory lifetime in a production environment. Fig. 16b shows the effect this MgO addition has on dissolved elemental composition within the pig iron phase. The levels of dissolved Si in the Pig Iron dramatically decrease to 0.92 wt% and the MgO addition also resulted in a lower total of dissolved S in the pig iron phase. Mn levels in the pig iron were almost unchanged by the addition of MgO.

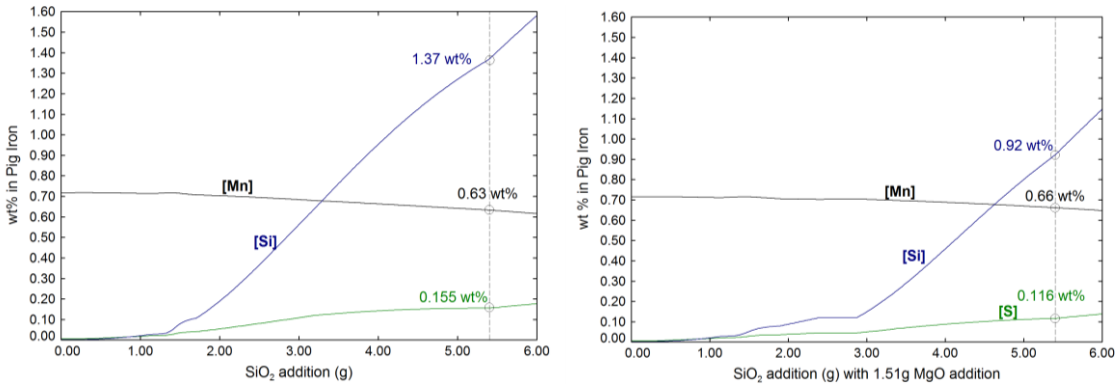

(a) (b)

Figure 6.16. Changing manganese, silicon and sulfur content of the pig iron phase with SiO2 addition at 1450 °C with 0 g MgO added (a) and 1.51 g added (b). The dashed line corresponds to the saturation point of the slag, the minimum addition of SiO2 needed to fully fluidize the system.

The calculated chemical composition of the pig iron nuggets and slag formed at 1450 °C with addition of 5.4 g SiO2 and 1.51 g MgO per 100 g of blend is shown in Table 6.2. The calculated pig iron sulfur content of 0.116 wt% S is relatively high meaning pig iron nuggets produced from waste would have to be utilized as part of a mix of scrap sources to supplement steel production, however their lack of gangue, complete metallization, high carbon and manganese content and partial desulfurization would mean they have a higher value in use than DRI in a steel plant.

Table 6.2. Calculated pig iron and slag compositions for 100g 37:63 BF dust to BOS dust ratio at 1450 °C, with the addition of 5.4 g SiO_2 and 1.51 g MgO. Under these conditions the system is fully fluidized, the remaining balance of the system is gaseous, or a minor constituent dissolved into the slag or pig iron.

Calculated Pig Iron Composition		Calculated Slag Composition	
Element	**Composition (wt. %)**	**Component**	**Composition (wt. %)**
Fe	93.75	FeO	0.01
C	4.30	Al_2O_3	5.67
P	0.24	SiO_2	37.85
S	0.116	CaO	43.53
Si	0.92	MgO	10.95
Mn	0.66	Ti_2O_3	0.22
		SiS_2	0.61
		CaS	0.58
		MnO	0.18

The present study is thermodynamic in scope to act as a guide for future experimental work to fully gage the feasibility of processing BF dust and BOS dust in this manner; however, pig iron nuggets produced at similar temperatures in laboratory studies appear to be somewhat consistent with the results of this study, as shown in Table 6.3. These experimental studies suggest a reaction time of 15–20 min may be suitable to produce iron nuggets, though it appears higher total gangue content increases reaction times [193].

Table 6.3. Comparison of input materials and pig iron nugget chemistry used in experimental studies.

Study	Temp. (°C)	Reaction Time (min)	Materials	Composition (Wt. %)				
				Fe_{Tot}	C	Si	P	S
Ishiwata et al. [87]	1500	15	Ore	57.3	-	3.29	-	-
			Coal	-	85.7	-	-	0.54
			Pig Iron Nugget	Bal.	2.5	0.08	0.04	0.21
Birol [193]	1400	15	BF Dust	25.27	37.1	3.87	-	0.40
			Mill Scale	66.19	-	0.26	-	0.01
			Pig Iron Nugget	94.80	3.24	0.259	0.004	0.209
Wang et al. [194]	1400	10	BOF Sludge	71.48	1.32	1.86	0.13	0.04
			BF Dust	30.87	34.25	2.73	0.052	-
			Pig Iron Nugget	92.91	3.61	-	0.094	0.023

The study by Wang et al. utilizes very similar methods to the ones suggested herein, demonstrating that using a basic Ca_2SiO_4 saturated slag to produce nuggets from BF dust and BOS dust is experimentally possible [194]. The levels of S in the product pig iron nuggets are extremely low in that work however, and this may be related to a few factors. The input materials used in the work appear to have substantially lower S content than this study and the work of Birol et al. and a Ca_2SiO_4 saturated slag as used in the study has significantly better sulfur capacity than an acidic slag as used in the other studies [193].

Most of the work that has been carried out producing pig iron nuggets from by-product dusts has focused principally on the properties of the pig iron nuggets produced, while the chemistry and morphology of the slag generated has been somewhat neglected. Wang et al. reported iron content of slags for the purposes of calculating iron recovery, but the mineralogical properties of the produced slag are not reported [194] .

The Scheil-Gulliver solidification model is a useful tool for projecting the mineralogy of slags as they solidify [213]. The model assumes diffusion rates of infinity for the liquid phase and zero for the solid phase, which can limit the model's accuracy under circumstances such as extremely high viscosity liquid solidification.

Table 6.4 shows a calculated Scheil-Gulliver composition of the slag phase from the conditions set out in Table 6.2. to estimate the phase composition of the cooled slag product. The slag is predominately estimated to be comprised of merwinite, melilite minerals such as Åkermanite and gehlenite, and anorthite. The lack of free periclase

(MgO) and lime (CaO) in the cooled slag is desirable if the slag were to be utilized in the construction sector due to the volumetric stability issues posed by the formation of hydroxides from CaO and MgO [4].

Table 6.4. Scheil-Gulliver cooling projection for slag produced by addition of 37:63 BF dust to BOS dust with the addition of 5.4 wt. % SiO2 and 1.51 wt. % MgO. Phases <0.01 wt% have been omitted. The temperature of final disappearance of liquid slag was calculated to be 953 °C.

Phase	Formula	Calculated wt. %
Åkermanite	$Ca_2MgSi_2O_7$	41.13
Merwinite	$Ca_3MgSi_2O_8$	39.90
Anorthite	$Ca_2Al_2Si_2O_8$	9.56
Gehlenite	$Ca_2Al_2SiO_7$	5.60
Calcium sulfide	CaS	1.53
Wollastonite	$CaSiO_3$	1.12
Perovskite	$CaTiO_3$	0.36
Spinel	$(Mg, Fe)(Al, Cr)_2O_4$	0.06
Diopside	$CaMgSi_2O_6$	0.03

Microstructure of steelmaking slags is of great importance for the control of leaching of heavy metals which can render slags untenable for recycling. Mombelli et al. discussed the influence of microstructure on heavy metal leaching characteristics in electric arc furnace slag [214], suggesting phases such as spinel and gehlenite suppress leaching of Ba, V and Cr from slag, while larnite (β–Ca2SiO4) is more prone to leaching metals. The method by which slag is cooled can also manipulate the mineralogy of the final product, and thus the leaching behaviour [215].

In order to develop a nugget making process from by-products with zero solid waste, slag leaching, and weathering behaviour will require more in-depth study to ensure a usable product.

6.5.2 Recovery of Zinc

The quality of the zinc oxide produced from such a process is challenging to predict using a purely thermodynamic methodology, and often neglected in practical studies.

Zhao et al. studied Zn removal rates in nugget production from steelmaking by-products [195] but focused on removal rates from the iron rather than on the quality of the zinc oxide product. The bag filter dust from a RHF plant (sometimes referred to as secondary rotary hearth furnace dust) typically contains any volatile elements from the input material such as Zn, Pb, Cd, Cl, Na and K, and is therefore heavily dependent on the quality of input materials. RHF secondary dusts are usually collected by means of a dry fabric dedusting filter system in the off-gas treatment portion of the plant [154]. In terms of recycling, elements such as Cl and Cd are considered impurities, and can be controlled through material input chemistry control.

One element that is also considered undesirable for zinc recyclers is iron [100], and contamination by this element is much more closely tied to the manner in which a rotary hearth furnace is operated. Poor mechanical strength of pellets and fines generation during processing are the major contributors to iron contamination in the secondary dust product from an RHF. There does not appear to be any fundamental reason the secondary dust produced from an RHF producing iron nuggets would be significantly different in terms of quality than the secondary dust produced from an RHF producing DRI from recycled materials such as a Fastmet plant. A comparison between Waelz oxide (secondary dust from a Waelz kiln), secondary RHF dust and the off-gas product from producing nuggets from blast furnace dust in a laboratory study is show in Table 6.5.

Table 6.5. Comparison of secondary zinc containing dusts from a Waelz Kiln, RHF and a laboratory study producing iron nuggets from BF dust.

	Composition (Wt. %)								
Material	**C**	**Fe**	**Zn**	**Pb**	**Na**	**K**	**Cl**	**SiO_2**	**Source**
Waelz Oxide	0.5 – 1.0	3.1 – 5.4	55.0 – 58.0	7.0 – 10.0	0.1	0.1	4.0 – 8.0	0 – 1.0	Mager et al. [72]
RHF Secondary Dust	-	3.73	22.78	-	7.92	12.77	-	2.23	Liang et al. [158]
Hi-QIP nugget production (laboratory scale)	0.68	6.66	47.1	7.02	0.22	1.95	13.2	0.2	Sawa et al. [85]

As can be seen in Table 6.5, the materials are quite variable but made up of similar elements. It is difficult to draw direct comparisons from the laboratory study to the industrially produced samples as production conditions will be dramatically different. It is worth noting however, that the Hi-QIP study was with a loose, agglomerated feed, which may go some way to explaining the higher iron contamination in the material from that work [85].

It is likely, based on the chemical composition of input material as well as the composition suggested by Sawa et al.'s study that a cleaning step would be required to remove halides and soluble alkali metals such as Na and K as is common for waelz oxide [216] before the product is considered suitable for use in the production of zinc via electrowinning. It may be feasible to source SiO_2 from sustainable sources for the purposes of this work, this may include wastes from other industries such as coal fly ash [217] or rice husk ash [218]. MgO could potentially be sourced from spent refractory linings from BOFs or EAFs [219] as an environmentally favorable alternative to virgin material.

This work suggests that modification of emerging RHF and linear tunnel furnace based may potentially be adapted to process zinc contaminated by-products, recovering a higher value pig iron nugget product than established DRI recovery routes such as

FASTMET. Technical considerations such as refractory design, off-gas dedusting system design would require modification to accommodate high volatile metal content and a basic slag.

6.6 Practical Validation of Computational Experiments

To validate the recommendations of the computational study, a blend of 37% BF dust and 63% BOS dust with 5.4 wt. % SiO_2 addition and 1.51 wt% MgO was prepared in the same manner as 5.2.

SiO_2 was supplied in the form of laboratory grade sand supplied by Sigma Aldrich and MgO was supplied in the form of reagent grade MgO powder supplied by Sigma Aldrich. Pellets were fired at 1450 °C for 15 minutes to replicate reaction conditions in literature examples [87,193,194].

Upon discharge from the furnace, the product was still molten but was allowed to cool to approximately 1000 °C (as measured by an infrared thermometer) before removal from the crucible using a pair of furnace tongs. The result was a pig iron nugget loosely bonded to a glassy black slag (Figure 6.17) whereby the slag and the pig iron nugget were easily separable by hand.

Figure 6.17. Pig iron nugget (left) and fused slag (right) produced by firing 37:63 BF dust: BOS dust + 5.14 wt. % SiO_2 + 1.51 wt% MgO at 1450 °C in air for 15 minutes.

Chemical analysis of the pig iron nuggets proved challenging. Milling of the iron nuggets proved impossible, their exceptional hardness precluded them from traditional milling via a ball mill.

XRF analysis typically requires an appropriate sample geometry and consistent matrix for accurate analysis. The granulated iron was found to be too small and inconsistent in dimension (Figure 6.18) to be easily analyzed as produced via XRF.

Figure 6.18. Size distribution of pig iron nuggets produced from 13.5 g briquettes.

Fusion via lithium tetraborate which is typical for XRF analysis into a bead [220] was also deemed to be unpractical due to the propensity of metallic iron to alloy with the platinum crucibles used to prepare the fused glass disks for analysis. This would obviously be extremely cost-prohibitive.

Commonly, analysis on BF pig iron or samples from the BOF or BF are cast into disks and ground to produce a flat surface before being subjected to spark-optical emission spectroscopy (S-OES), where a spark is generated against a sample heating the surface to thousands of degrees Celsius via an electrode forming an arc against the sample. This causes atomization and excitation of the atoms bound within the samples surface [221]. As these atoms decay back to the electronic ground state, they emit photons with wavelengths in the visible light region of the electromagnetic spectrum.

The wavelength of the emitted photons is characteristic to elements in the sample and can be detected and quantified in a very similar operating principle to the atomic emission spectrometer portion of the MP-AES utilized in this work as described in 3.2.

In an S-OES instrument, the substrate to be analyzed acts as the cathode for the high voltage arc and hence must be conductive, flat, homogenous and a large enough cross-sectional area to ensure the electrical arc is contained to the sample to be analyzed.

To prepare samples of pig iron nuggets produced in this study for analysis the methods of Zenngrebe et al. were adapted [222]. They were first mounted in a conductive Bakelite phenolic resin typically used for SEM-EDX studies. Samples were ground using 80 grit sandpaper until the appropriate geometry was achieved, and then ground using successively finer grades of sandpaper before a 1200 grit finishing sandpaper was used to achieve the final finish before analysis.

S-OES analysis was performed on samples of pig iron nuggets produced from 37:63 BF:BOS dust with the addition of 5.14 wt. % SiO_2 and 1.51 wt. % MgO produced at 1450 °C for 15 minutes at Tata Steel Port Talbot with the assistance of the Basic Oxygen Steelmaking Laboratories team.

The composition of the produced pig iron nuggets as determined by S-OES is compared to the calculated composition from the computational thermodynamic prediction shown in Table 6.2 is shown in Table 6.6.

The results are in good agreement with the calculated chemical composition of the pig iron nuggets. The pig iron nuggets are extremely high in metallic Fe, meaning they would be an excellent source of iron units in the BOF or the EAF.

The carbon content of the pig iron nuggets is slightly lower than calculated, likely due to incomplete carburization in the relatively short reaction time at high temperature. It’s also likely that some proportion of carbon was lost from the pellet due to combustion during the heat treatment which the calculations generated using FactSage fails to account for. Increased carbon content is preferable for the purposes of recycling the pig iron nuggets via the BOF/EAF due to the reduced cooling capacity of the material on account of the associated reduction in melting temperature with increasing carbon.

Using the precipitate target function on FactSage, the calculated melting temperature at 1 bar of the experimentally produced pig iron nuggets specified in Table 6.6 is projected to be 1294.9 °C. This melting temperature is much more comparable with carbon steel scrap than DRI, which translates to reduced cooling capacity in the BOF, reduced energy consumption in the EAF per unit Fe [223].

S content of the pig iron nuggets was slightly lower than projected, it may be the case that some S left the pellet in the gas phase in a similar manner to the behavior observed during RHF benchmarking trials in Section 5.3.2.

Nevertheless, approximately 36% of S present in the initial pellet reported to the pig iron nugget, which when compared with miniscule reductions in sulfur shown in 5.3.2 prior to pellet burnout represents a substantially improved Sulfur removal capacity.

The FactSage calculations also overestimated the proportion of Mn that would report to the pig iron phase under these conditions. Based on observations by Srivastava, this may be related to direct carburization by solid carbon driving the reduction of MnO to Mn which is kinetically a rather slow reaction comparatively to iron reduction [198].

A similar explanation may also explain the lower than anticipated Si content of the pig iron nuggets comparatively, although a lower than anticipated Si content has associated process benefits in the BOF/EAF with regards to recycling. Increased Si content can be related to increased demand for flux (principally CaO) in the steel plant, thus increasing slag volumes and therefore lowering the materials value-in-use [224]. Zinc removal is seen to be comprehensive, as predicted via the FactSage calculation and in good agreement with experimentation on high carbon RHF blends at in 5.3.3.1 which showed excellent zinc removal with little no hold time at 1350 °C. This supports the notion that zinc removal occurs well before the melting step of pig iron nugget production. The pig iron nuggets are also Na and K free, with those elements either volatilizing away from the pellet or being entrained in the slag.

Table 6.6. Calculated (via FactSage) and experimental composition of a 37:63 BF dust:BOS dust + 5.14 wt. % SiO_2 + 1.51 wt. % MgO briquette fired at 1450 °C for 15 min.

Component	Calculated	Experimental
Fe_{Tot}	93.75	96.53
C	4.3	2.71
Si	0.92	0.33
S	0.12	0.083
P	0.24	0.116
Mn	0.66	0.147
Zn	<0.001	BDL

6.6.1 SEM-EDX

6.6.1.1 SEM-EDX of Pig Iron Nuggets

SEM-EDX analysis of pig iron nuggets produced as above is shown in Figure 6.19. The material presents as a matrix of ferritic iron with thin graphitic inclusions (identified as carbon rich areas via EDX). This structure is typical of hypoeutectic gray cast iron [225], with the relatively moderate cooling rate of the pig iron nuggets in the methodology facilitating an equilibrium microstructure in the pig iron rather than a pearlitic or white cast iron structure that may be expected with a more rapid cooling rate.

Critically, the pig iron nuggets are free of gangue which makes them much more attractive for steelmaking application as described in 5.5. The grey cast iron structure also provides excellent mechanical strength and hardness meaning that transportation and storage is very unlikely to generate fines.

The pig iron nuggets are also extremely dense, with no pores observed in the grey cast iron microstructure. Due to this the pig iron nuggets are extremely space efficient with regards to transportation and storage but may also be less sensitive to oxidative degradation during storage.

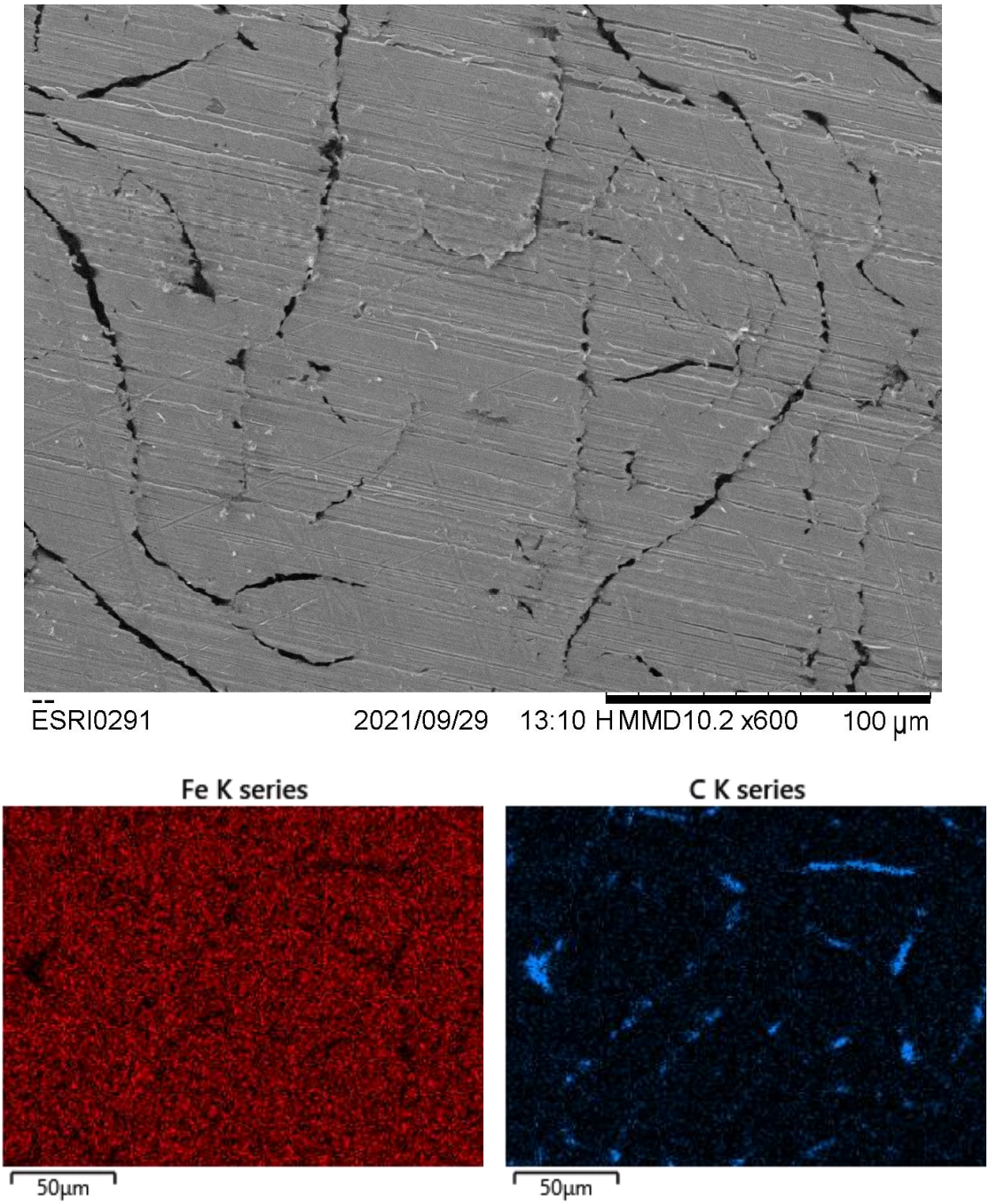

Figure 6.19. SEM-EDX maps for pig iron nuggets produced at 1450 °C for 15 minutes from a briquette composition of 37:63 BF dust:BOS dust + 5.14 wt. % SiO2 + 1.51 wt. % MgO.

6.6.1.2 SEM-EDX of Slag Generated from Pig Iron Nugget Production

Analysis of the glassy fusible slag produced from pig iron nugget production showed a continuous slag matrix containing Mg, Si and Ca oxides, with small droplets of solidified metallic iron suspended within it (Figure 6.20) at the boundary where the pig iron nugget broke away from the fused slag (the bottom of the image). These droplets

caught in the slag phase represent an emulsion loss – the molten iron was unable to fully separate from the molten slag in the 15-minute reaction time. It's likely that this iron loss can be controlled via engineering of slag viscosity through flux addition changes, or increased reaction temperature.

Little Fe appears to remain in the bulk of the solidified slag based on EDX analysis, which would represent a solution loss as FeO. This implies that it is the coalescence of the molten pig iron phase that would be the primary driver of yield loss rather than incomplete reduction of FeO from the slag phase.

Srivastava, via a mass balance methodology, studied the yield of pig iron nuggets produced from ore [198] and found that hold time was the primary driver of iron losses to the slag. However, the losses of iron to slag (0 – 2 wt. %) were dwarfed by losses to dust or transfer losses moving pellets between primary and secondary furnaces. Total iron nugget yields versus initial Fe input at 1450 °C for 15 minutes in that study was 76.66 ± 3.95 % increasing to 83.72 ± 1.82 % at 40 minutes.

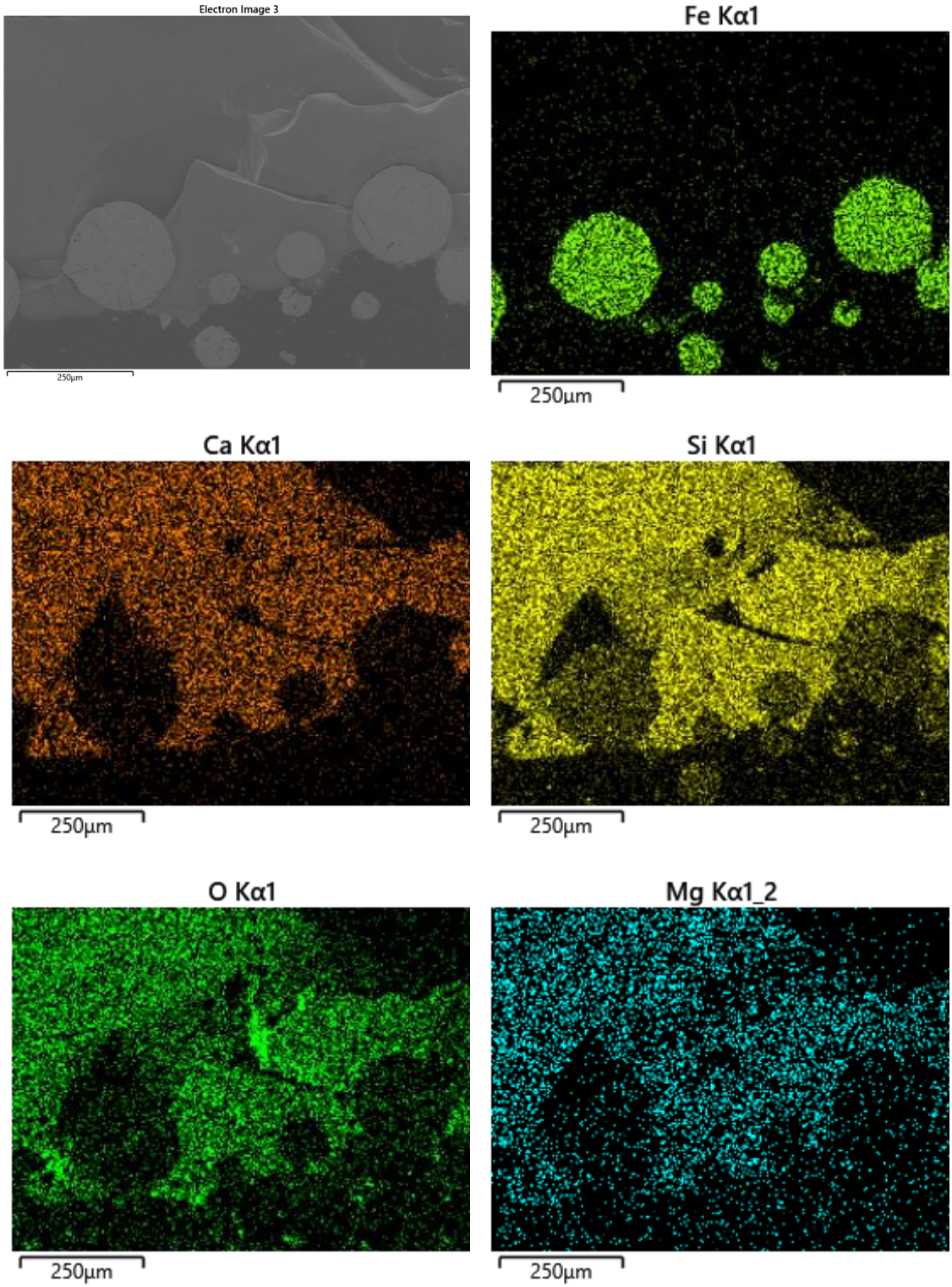

Figure 6.20. SEM-EDX analysis of slag product from pig iron nugget production, showing entrained droplets of metallic iron.

Some loss of yield of Fe in the production of pig iron nuggets seems inevitable, although some magnetic recovery of entrained iron may be possible. Yield of iron with respect to process conditions will form a vital part of assessing the process economy of an upscaled pig iron nugget production process from BOS dust and BF dust.

Detailed study on the mechanical and leaching properties of the slag product would be a key area for further study, as for an environmentally friendly iron production route it would be desired that the slag is reusable as aggregate and not pose any environmental hazards [4,226].

6.6.2 Oxidative behaviour of Pig Iron Nuggets versus Direct Reduced Iron

The relatively high surface area and porosity of DRI means that it has a high propensity for reoxidation during storage [227] , shipping [90] and during recycling via ironmaking and steelmaking [228] by reaction with process gases at elevated temperature.

The shipping of uncompacted DRI via sea freight, while perhaps slightly exaggerated in terms of risk on occasion is still nevertheless an important issue. DRIs low thermal conductivity means localized hotspots caused by oxidation in the saline, moist marine environment can develop into fires if not carefully monitored and rigid loading practices are not adhered to [229]. This hazard is exacerbated by the potential risk of generating explosive volumes of hydrogen upon application of water to a DRI fire.

Often DRI will be compacted at temperatures more than 600 °C to form hot briquetted iron (HBI) before transit to reduce this risk to reduce porosity, increase thermal conductivity (thus mitigating ‘hot-spotting’) and reduce available surface area, which obviously bears additional production expense.

The likelihood is that an RHF based process in the UK would be based at an operating integrated works to benefit from proximity to raw material and recycling routes (BF/BOF/EAF), rather than preparing DRI or pig iron nuggets for export therefore some of these considerations are less significant.

Nevertheless, Figure 6.21 shows the differences in oxidation behavior for pig iron nuggets produced as above and a DRI sample (1250 °C, t = 15 min, C/O = 0.7) as prepared in Chapter 5 as determined via thermogravimetric analysis. Samples were introduced to the TGA without pulverization, with a fragment of a fired DRI briquette taken with a fine point chisel and a single pig iron nugget instead being used.

Significant oxidation is seen to initiate in the DRI fragment above 700 °C, whereas the pig iron nugget sample does not exhibit substantial oxidation until T > 1100

°C. The results suggest that the continuous metallic, non-porous structure of the pig iron nuggets are significantly less vulnerable to high temperature oxidation than DRI.

Pig iron nuggets appear much more suitable for outdoor storage than DRI and would be much less likely to degrade in quality if charged to the BOF with scrap, where material is held at high temperatures prior to the charging of hot metal onto the scrap charge.

Should it be more commercially attractive to export pig iron nuggets rather than utilize them internally at the production site, their increased total Fe content, lack of gangue, high density and lower reoxidation potential would make them easier to transport and handle.

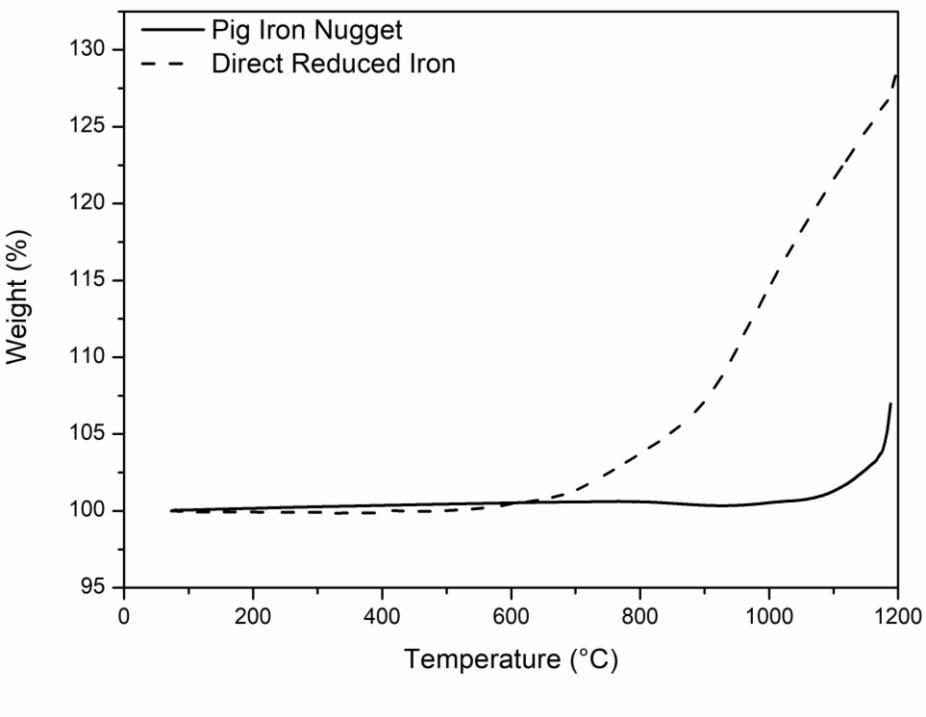

Figure 6.21. TGA oxidation behavior of pig iron nuggets and DRI (100 mLmin^{-1} air, 20 °Cmin^{-1}).

6.7 Conclusions

This study was undertaken to determine the feasibility of an adapted pig iron nugget process as a viable recycling route for BOS dust and BF dust from an integrated steel plant, from a thermodynamic perspective.

The main outcomes of the work are:

- The production of pig iron nuggets from steelmaking by-products is thermodynamically feasible at reasonable operating conditions of 1450 °C.
- The addition of SiO_2 and MgO as fluxing agents allows for a reduction in process temperature and has benefits for control of sulfur sequestration by the slag phase.
- Zinc from the input materials could be captured from the process as a crude oxide in a similar manner to FASTMET [120] and sold to recyclers as an additional revenue source.
- SiO_2 and MgO used to supplement production via a pig iron nugget process could potentially be sourced from industrial by-products.
- Iron nuggets produced are of an appropriate quality to supplement scrap in BOS/EAF processes.
- If the slag produced from such a process is found to be volumetrically stable, it may be utilized as an aggregate leading to a process with little to no solid waste generation.

The results were then validated experimentally using box furnace trials, and pig iron nuggets of good quality with microstructure similar to gray cast iron and in reasonable agreement with calculated composition. The S (wt. %) content of the pig iron nuggets was only 35% of the input material S (wt. %), increasing the value in use of the pig iron nuggets as a scrap substitute. Zinc was removed to levels below the detectable limit of the S-OES analysis used to characterize the produced pig iron nuggets.

Some loss of Fe in the form of entrained Fe droplets within the molten slag phase constitute a yield loss, but a full mass balance comparison between pig iron nugget production and DRI production via an RHF would highlight the significance of losses

By modifying an RHF or utilizing a linear tunnel furnace to operate with a basic refractory, higher temperatures of 1450 °C and careful control of pellet flux content and basicity the RHF could produce higher value in use pig iron nuggets than DRI and potentially improve the process economics of recycling BF dust and BOS dust from integrated steel plants in this manner.

Further work on production of pig iron nuggets would include studies on appropriate refractory selection, optimization of flux addition on a cost-benefit basis factoring in product value-in-use including yield, energy costs etc.

A computational process study similar to the work of Fisher et al. would also allow for realization of energy demand, CO_2 emissions and productivity of such a process for the recycling of BOS and BF dusts [230].

7. UTILIZATION OF FACEMASK PLASTIC WASTE RESULTING FROM THE COVID-19 PANDEMIC IN RHF IRONMAKING

7.1 Introduction

As part of the response to the global COVID-19 pandemic caused by the coronavirus SARS-CoV-2 and its variants, many governments and the World Health Organization recommended or required the use of face coverings to suppress transmission of the virus. Although often politically controversial, the benefit of facemasks in mitigating the spread of COVID-19 has led to wide scale adoption [231,232].

Although the UK government specifically recommended non-medical grade [233], reusable fabric face masks many members of the public opted for single use plastic medical-style facemasks. The North London Waste Authority projected UK citizens were discarding 102 million masks a week during the height of the pandemic [234]. At an average mass of 3 g per mask this approximates to a staggering 300 tonnes per week of non-recyclable plastic waste being generated in the UK alone. On a greater scale, during state-wide lockdowns in China it was estimated the Chinese public were using 900 million facemasks per day [235].

Much of this plastic facemask waste is expected to end up in rivers and oceans in the form of microplastic pollution with disastrous effects on aquatic ecosystems [236–239]. At present, the vast majority of this unrecyclable plastic facemask waste is landfilled; however, alternative waste management strategies include gasification to syngas (CO and H_2) and pyrolysis for direct energy recovery [240,241].

The recyclability of facemasks is complicated by their blended composition, and also the presence of iron wire designed to improve the seal against the wearers nose. Given the scope of the environmental impact, what is needed is a process of recycling or repurposing facemasks as well as related PPE (disposable gowns, hospital bed pads, and privacy curtains), if the process can use essentially whole items without pre-treatment.

The use of plastic waste in ironmaking and steelmaking to reduce demand for extraction of fossil fuel reductants like coal is a promising area of study and application; however, to-date the two key areas where plastics have seen application at commercial scale for steelmaking have been the inclusion of a small component of waste plastic in the coke oven process [242] and injection at the tuyere of the BF [243].

The rotary hearth furnace (RHF) is an emerging technology for the separation of volatile metals (Zn, Pb etc.) from steelmaking by-product dusts that are too high in volatile metals for direct recycling into the ironmaking process [78,83,154]. Self-reducing agglomerates prepared from ferrous by-product dusts and a carbon source (coal, coke

breeze, blast furnace dust) are charged into a rotating turntable furnace and heated to 1200 – 1300 °C for a period between 10 and 30 minutes.

The metal oxides in the agglomerate such as Fe and Zn are reduced via carbothermic reduction to yield pellets of direct reduced iron (DRI) and a separated recyclable secondary oxide dust containing the volatile metal components [244].

Previous studies have indicated the CO_2 gasification reaction is the rate determining step in the reduction process of cold bonded self-reducing iron-carbon agglomerates[170] although with extremely high reactivity carbon sources heat transfer effects become more significant [245]. An increased gasification reactivity of the carbon source in self-reducing agglomerates for the RHF can therefore lead to improved reduction rates and therefore improved productivity.

Studies into the inclusion of waste plastics into self-reducing agglomerates as a feedstock for RHFs have yielded promising results, showing good reactivity and reduced CO_2 emission as a result of the hydrogen content of the plastic [246]. Unfortunately, a key issue in the inclusion of waste plastic in self-reducing agglomerates is particle sizing, where fine particle sizes (~115 µm) are required to form a composite pellet with adequate strength for processing [150]. Milling of fibrous plastic materials such as facemasks to appropriate sizing for application in the RHF is extremely challenging, due to their ductility and relatively low softening temperature. Furthermore, the low density of conventionally milled plastic waste makes storage and transport difficult.

Herein a new scalable process is reported, in which entire plastic facemasks are blended with a Welsh ground coal injection (GCI) coal and the subsequent change in the CO_2 gasification reactivity of the material is explored. Gasification reactivity of the material was measured using thermogravimetric techniques, as this allowed for direct observation of the reaction without simultaneous metal reduction reactions occurring. If the gasification reactivity of low volatile content coal can be substantially improved by pre-treatment with waste facemask plastic, it may be applicable as a means of economically increasing the productivity of RHF plants through reduced pellet hold times.

7.2 Instrumental Methods

Thermogravimetric experiments were carried out using a TA Instruments SDT Q600 analyser. Experiments were performed on 20 mg ±0.5 mg of sample, using alumina sample crucibles. For non-isothermal tests, samples were ramped to reaction temperature (900 °C) under protective cover of argon (100 cm^3/min) at a rate of 20 °C/min and held isothermally for a period of 10 minutes at reaction temperature. The purge gas was then changed to CO_2 at a rate of 120 cm^3/min to initiate the reaction before ramping the analysis temperature from 900 °C to 1200 °C at a range of heating rates (1, 5, 8 and 10 °C/min) [247]. Surface area analysis was performed using a Quantachrome Nova 2000e analyzer using N_2 as an adsorbate gas. Around 130 mg of sample was degassed under vacuum at 130 °C for 12 hr. BET surface area was calculated in the 0.09237-0.24399 P/P_0 range for each of the samples. FTIR measurements were taken using a Thermofisher Scientific Nicolet iS10. Scanning electron microscopy was performed on a Hitachi TM3030. Carbon and sulfur were determined via combustion analysis using an ELTRA CS500 C/S Analyzer as in Chapter 3.5. Proximate analysis of coal was determined using the SDT Q600 by ramping the sample at 10 °$Cmin^{-1}$ under 100 cm^3min^{-1} pureshield argon to 900 °C and holding for 7 min, the reaction gas was then switched to compressed air to ash the sample.

Ball milling of samples was performed in a Fritsch Pulverisite 6 ball mill at 500 rpm. Bulk pyrolysis experiments were performed using a carbolite MTF 12/38/400 controlled atmosphere tube furnace heated to 500 °C at a rate of 5 °$Cmin^{-1}$ under the protection of 1 dm^3min^{-1} pureshield argon to heat a pellet of material (16mm diameter, 2.5 g, 975 bar, 60s residence time) produced using a Retsch PP 25 Pellet Press. Samples were cooled in the furnace to ambient temperature for pulverizing and further analysis.

7.3 Materials and Milling Protocol

Disposable, non-medical grade face coverings were used for the purpose of this study. Masks produced by the Changzhou Huangshi Packaging Printing Co. Ltd. were coarsely chopped into squares using scissors without any prior disassembly. Charcoal was purchased from Fisher Scientific, and the coal used was a typical BF injection coal. Both materials were dried at 90 °C for 12 hours and pulverized and sieved to <215 μm.

Proximate analysis of the GCI coal and charcoal samples[248], along with the carbon and sulfur analysis results are shown in Table 7.1 and Table 7.2 respectively.

Table 7.1. Proximate analysis of the GCI coal and charcoal samples.

Material	Moisture (Wt %)	Volatile Matter (Wt %)	Fixed Carbon (Wt %)	Ash (Wt %)
GCI coal	0.67	12.71	78.75	7.77
Charcoal	3.91	23.71	53.46	18.64

Table 7.2. Carbon and sulfur analysis of GCI coal, charcoal, and coarse facemasks.

Material	Carbon (Wt %)	Sulfur (Wt %)
GCI coal	90.08	1.308
Charcoal	63.69	<0.01
Facemasks	85.68	<0.01

Whole facemasks were coarsely chopped into squares using scissors without any prior disassembly. The manufacturer specifies the non-metallic composition of the masks is non-woven plastic (60 Wt. %), melt-blown plastic (30 Wt. %), spandex (7 Wt. %) and polyolefin resin (3 Wt. %). The masks also contained a small steel wire (ca. 6 Wt. % of the total mask) designed to improve the seal against the wearers nose, this wire was not removed during initial processing to better replicate an upscaled process where that would not be feasible. A photographic image of the components is shown in Figure 7.1a, while scanning electron microscopy (SEM) images of the layers allowed for better visualization of their fibrous nature. The dense interlocking fibres of the filtration layer can be observed in Figure 7.1c, compared with the comparatively less tightly woven fibres in the external (hydrophobic splash resistant) and internal (comfort) layers of the mask in Figure 7.1b and 1d, respectively.

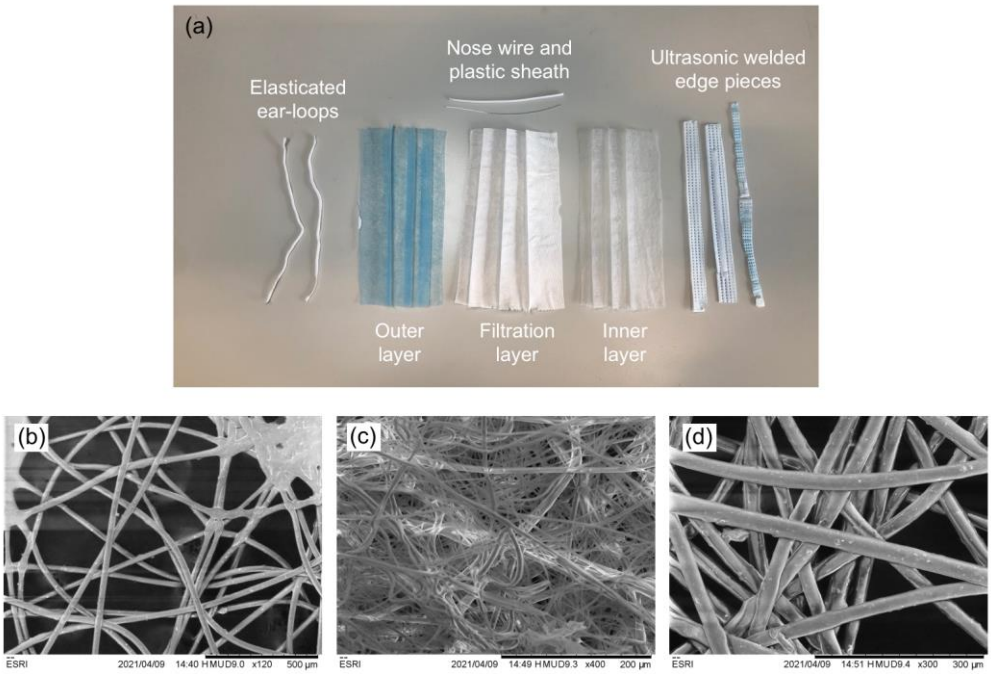

Figure 7.1. Components of the disposable mask. (a) A photograph of a fully disassembled mask with the component pieces labelled. (b) SEM image of the untreated mask outer layer. (c) SEM image of the untreated mask filtration layer. (d) SEM image of the untreated mask inner layer.

Single use facemasks such as the ones used in this study are typically made of polypropylene fabric. The FTIR spectra of untreated facemask (Figure 7.2) is in reasonable agreement with Aragaw's work [249] characterizing facemask plastic, with the exception that a broad absorbance that was ascribed to cellulose O-H bonding is not observed in the masks used in this study. It appears that the masks used in this work contained no paper component, which given the tremendous variation in manufacturing processes for face coverings in the COVID-19 era and lack of widespread standardization seems likely.

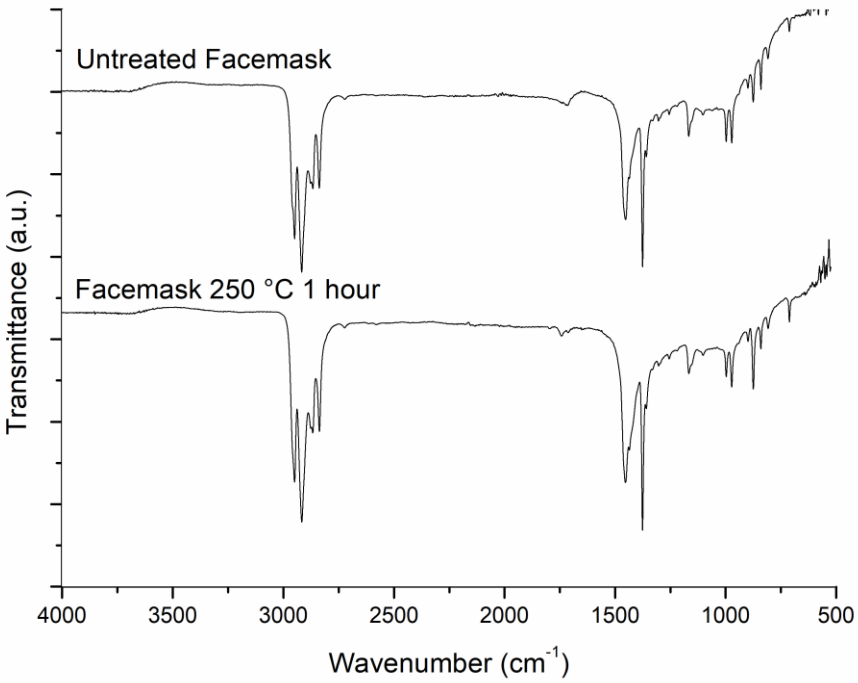

Figure 7.2. FTIR spectra for untreated facemasks (top) and facemasks that have been held at 250 °C for 1 hour (bottom).

Pulverization of the masks, even by cryogenic ball milling, was found to be totally ineffective. In a similar manner, physically mixing the cut pieces of mask with coal (or charcoal), as per the approach of Wang et al. [250], did not create a homogeneous mixture. Dankwah et al. [122] have previously reported that by melting it was possible to physically pelletize iron oxide with a plastic powder. This was done by pulverizing plastic after it had been separately heated to 300 °C and embrittled via quenching. This suggested that the correct physical form for the plastic could be obtained through melt processing. However, to obtain a granular material suitable for producing cold bonded briquettes, melt processing was performed by mixing the waste facemasks with coal fines.

In the process, coarsely cut untreated facemasks (Figure 7.3a) were added to GCI coal fines and charcoal (Figure 7.3b) in a 20:80 weight ratio, and physically mixed (Figure 7.3c). The resulting mixture was heat treated at 250 °C in a laboratory oven (in air) for one hour and then removed. While still hot, the mixture was stirred allowing the molten plastic to wet the carbon source and form a coarse powder (Figure 7.3d).

The effect of mixing molten plastic with coal is an embrittling of the polymer, rendering it much more receptive to conventional milling methods such as ball milling.

Once cooled to room temperature, the coarse powder was ball milled for 5 min at 500 rpm, whereby the powder fully passed a <215 μm mesh, except for fragments of nose wire that remained in the mixture. These fragments may easily be recovered via screening or magnetic separation or can be left in place as an Fe source.

The texture of the GCI coal/facemask sample after melt processing is that of a granular powder, which makes it suitable to be stored and transported, in particular via a conveyor belt, without creating an airborne powder hazard. Visually the facemask treated coal and charcoal is nearly indistinguishable from the untreated material.

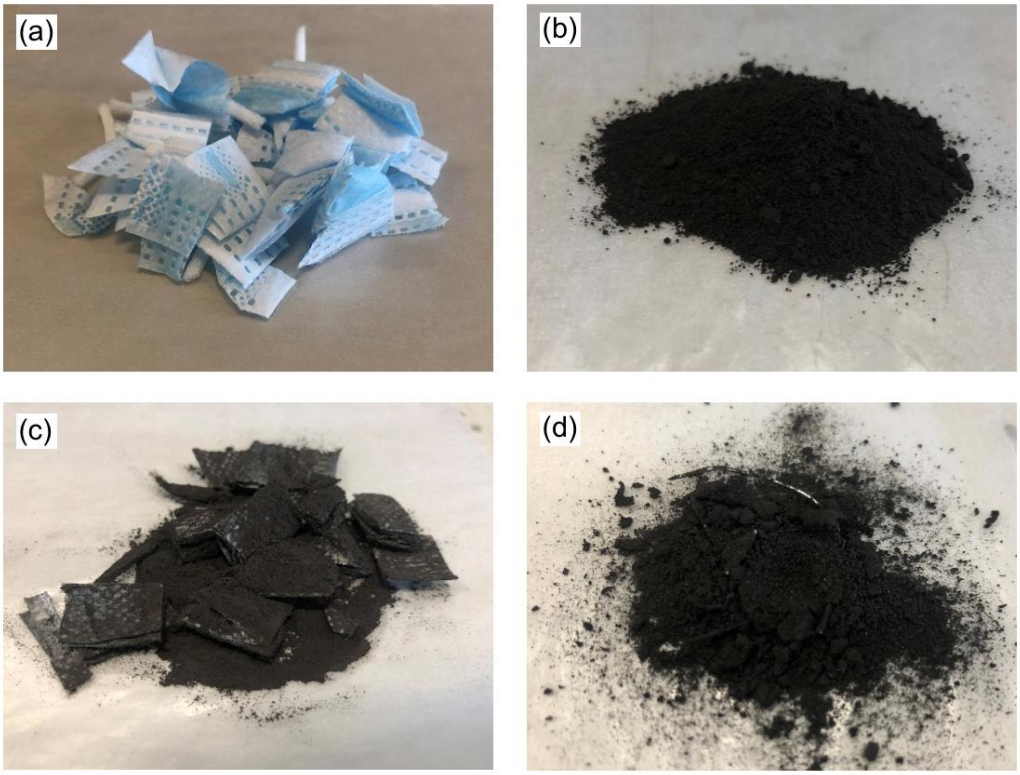

Figure 7.3. Materials at various stages of the milling process. (a) Coarsely cut untreated facemasks, (b) GCI coal, (c) cut facemasks and GCI coal before heat treatment and (d) facemasks and GCI coal after 1 hour at 250 °C and before milling.

7.4 Thermogravimetric Analysis

TGA-DTG of the untreated facemasks shows that melting of the facemask occurs at 167 °C without significant decomposition (Figure 7.4a). The lack of decomposition in air upon heating to 250 °C as in the milling process which can be seen in Figure 7.4a is supported by the unchanged FTIR spectra of material held at 250 °C for 1 hr as in Figure 7.2. This indicates that the process of heating the facemask with GCI coal (or charcoal) simply involves the melting of the plastic with the carbon. An important observation is that the oxidative degradation mass loss of the facemask plastic begins at T > 250 °C, therefore this is the highest realistic temperature at which the milling procedure can be performed without substantial degradation of the mask material.

TGA shows combustion of the facemask occurs at 382 °C in air (Figure 7.4a); as may be expected this decomposition temperature is increased to 447 °C under inert atmosphere (Figure 7.4b). In both cases a second smaller decomposition occurs at 700 °C leaving a residue of 3.06% (4.84% under Ar). As decomposition occurred under both oxidizing and inert conditions it is likely that this is a carbonate decomposition. Under the CO_2 atmosphere (Figure 7.4c) the second decomposition step observed did not occur until 955 °C suggesting that a high partial pressure of CO_2 suppressed the decomposition step, supporting the observation that this is a carbonate decomposition.

The ash content following oxidation at 1,000 °C as determined in Fig. 3a was 2.20%, and by subtracting this value from the 4.84% mass remaining after heating under inert conditions to 1,000 °C suggests that 2.64% of the total mass of the facemasks is available as fixed carbon (the solid, combustible, carbonaceous residue that remains after heating coal or organic material to high temperatures, after the pyrolysis of all volatile matter has taken place).

The results suggest very little fixed carbon remains after the pyrolysis process for facemask plastic under inert conditions, in good agreement with pyrolysis tests performed by Jung et al. on the polypropylene layer of N95 masks[240]. Fixed carbon content is commonly used as a comparative metric in iron production, as it is effectively a measure of the solid carbon available for reduction of oxides at ironmaking reaction temperatures.

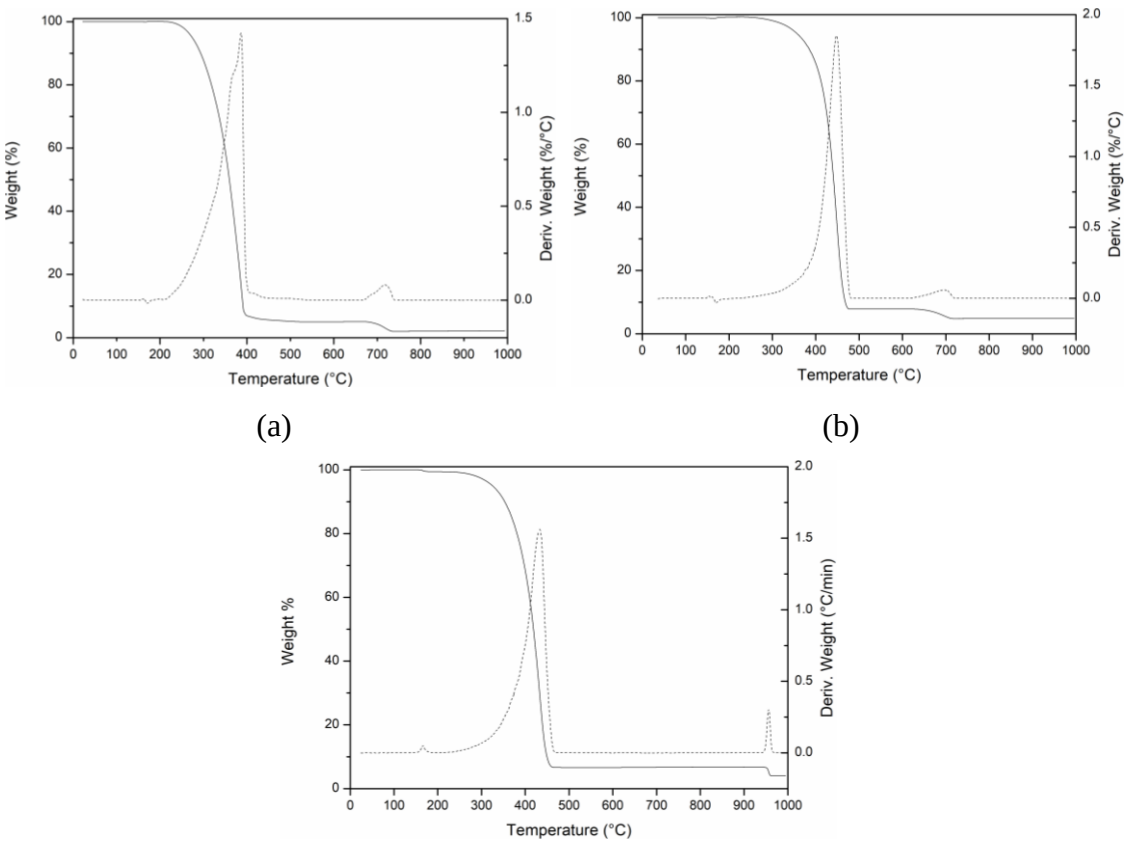

Figure 7.4. TGA-DTG curve for (a) untreated facemasks under a 100 cm3/min flow air, (b) untreated facemasks under a 100 cm3/min flow argon, and untreated facemasks under a 100 cm3/min flow CO_2. DTG signals are denoted as dashed lines.

Analysis of the ash residue left from combustion under oxidizing conditions by SEM-EDX (Figure 7.5 and Table 7.3) indicates it to be primarily calcium(II) oxide (CaO) and calcium carbonate ($CaCO_3$) which is consistent with the use of calcium carbonate as a filler to polypropylene and to enhance rheological properties during the manufacturing process[251,252]. This supports the observation that the mass loss at ~700 °C observed in Figure 7.4 is decomposition of $CaCO_3$. Calcium carbonate is commonly used within steelmaking as a supplementary flux[253], so a CaO based ash from the facemask plastic would not present a major issue for steelmaking application from the standpoint of the introduction of far more undesirable elements in ash such as K, Na and Zn.

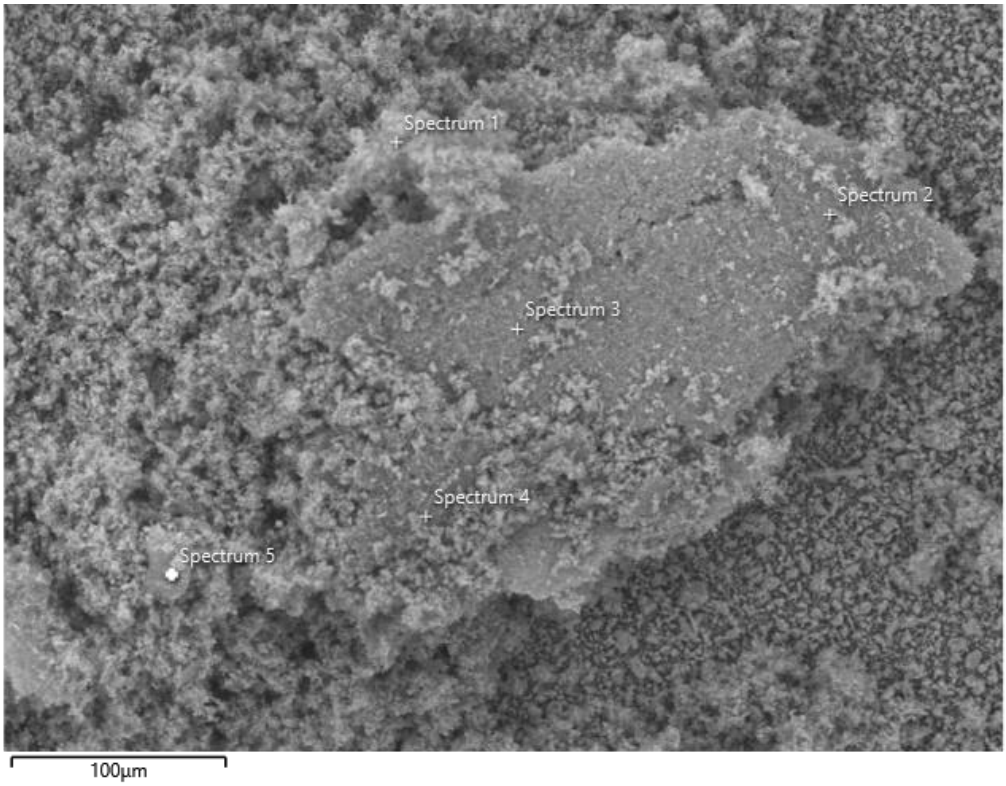

Figure 7.5 SEM-EDX analysis of ash produced by combustion of untreated facemasks

Table 7.3. EDX analysis of facemask ash

Element	Composition (Wt. %)	σ (Wt%)
Al	0.34	0.04
C	9.64	1.20
Ca	50.24	9.49
Cu	0.01	0.02
Mg	0.10	0.09
O	38.52	8.50
Si	0.17	0.07
Ti	0.79	0.49
Zn	0.08	0.18

To replicate the oxidative behavior of chars in the RHF the TGA of facemask blends was collected under an experimental program was utilized in which the initial

rapid ramping period from ambient temperature to 900 °C occurs under inert atmosphere.

After a stabilization period of 10 minutes at 900 °C, to allow for samples to equilibrate, the gas flow was switched to CO_2 to initiate the gasification reaction and the samples were ramped to 1200 °C at various rates between 1-10 °C/min. The TGA plots of GCI coal/20 wt. % facemask blend, in comparison with that of the untreated GCI coal are shown in Figure 7.6b. The comparable plots for charcoal and charcoal/facemask blend are shown in Figure 7.6a. The GCI coal samples shows pyrolysis of volatile organic compounds beginning at 382 °C with a mass loss of 13.8%, which is likely a complex mixture of volatile organic compounds present in the coal.

However, for the facemask treated samples of GCI coal a far greater pyrolysis mass loss can be observed (29.1%) which is related to the simultaneous pyrolysis of the facemask plastic alongside the coal volatiles. Similarly, the facemask treated charcoal shows a greater mass loss compared to the untreated material at pyrolytic temperatures, but the difference is less stark (29.6% vs 20.6%). This observation suggests that the plastic has volatilized, and the products have departed from the reaction zone of the analyzer long before CO_2 oxidation is initiated.

It can be seen from Figure 7.6b that the rate of CO_2 oxidation of GCI coal was substantially increased by melt-blending with the facemask, with the untreated coal fully converting at 1155 °C compared to 993 °C for the facemask treated material. Interestingly, the treated charcoal performance is essentially unchanged compared to the untreated material, except for additional ash content. The samples completely reacted at 936 °C (untreated charcoal) and 917 °C (charcoal/facemask blend), respectively.

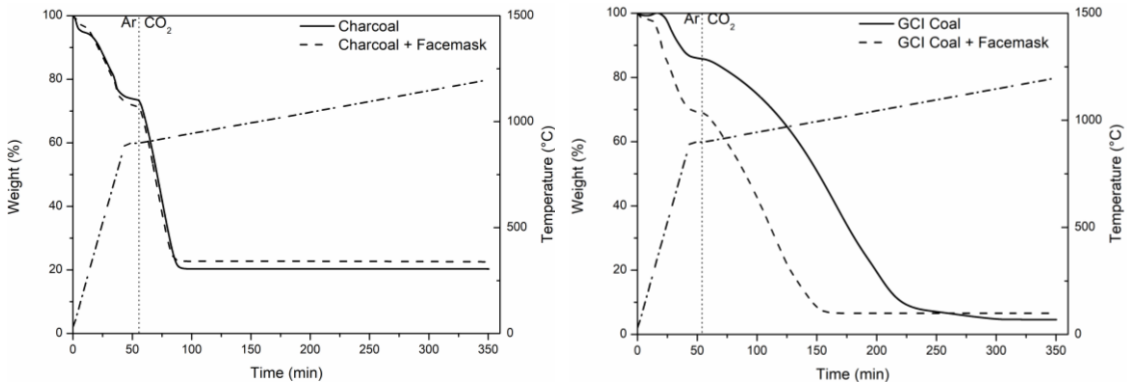

(a) **(b)**

Figure 7.6. TGA measurements to 900 °C under Ar and to 1200 °C under CO2 atmospheres for (a) charcoal (solid line) compared to charcoal/20 wt. % facemask blend (dashed line) and (b) GCI coal (solid line) compared to GCI coal/20 wt. % facemask blend (dashed line).

7.5 Kinetic Analysis

To gain further insight into the behavior of the coal/facemask blend with regard to its potential application in a RHF, the kinetics of the CO_2 gasification step were investigated in detail. In this regard, CO_2 gasification is an extremely complicated chemical process, many different chemical compounds in the complex starting material are reacting simultaneously and the mechanism of reaction likely changes with the degree of conversion. However, model-free kinetics allow for estimation of Arrhenius parameters without the assumption of a specific reaction mechanism and has previously been utilized to characterize the kinetics of pyrolysis of waste facemasks.[254]

Methods such as the Friedman method[255], Flynn-Wall-Ozawa method (FWO)[256,257], and the Kissinger Akahira Sunose method (KAS)[258] are all commonly used iso-conversional methods of determining kinetic factors, primarily activation energy (E_a). Boudouard reaction energy for CO_2 gasification of carbon materials has been shown to vary substantially with conversion degree[259]. For this reason, the Friedman method was selected as the FWO and KAS methods are derived from systems where activation energy does not vary with reaction progress.

As changes in mechanism can be factored into the model free method used, CO_2 is presumed to be in large excess, and the reverse Boudouard reaction is assumed to be

negligible due to the high purge flow rate through the thermogravimetric analyzer. As such the CO_2 gasification of biomass/char/coal can be simplified to Equation 7.1.

$$C_{Fix}(s) + CO_2(g) \longrightarrow 2CO(g) \tag{7.1}$$

The general kinetic expression for decomposition gas-solid reactions is described in Equation 7.2 [258], where *t* is time, *k*(T) is the temperature dependent kinetic constant, f(α) is the expression of the reaction model, dα/dt is the rate of conversion with respect to time and α is the conversion degree as described in Equation 7.3, where m_o is the samples initial mass before reaction initiation, m_t is the mass of the sample at time t and m_f is the final mass of the sample after the reaction has abated.

$$\frac{d\alpha}{dt} = k(T)f(\alpha) \tag{7.2}$$

$$\alpha = \frac{m_0 - m_t}{m_0 - m_f} \tag{7.3}$$

By substituting the Arrhenius equation into Equation 7.2, a general expression to calculate kinetic factors E_a and A is given in Equation 7.4, where A is the preexponential factor (min^{-1}), E_a is the activation energy of the conversion ($kJmol^{-1}$) and T is absolute temperature (K).

$$\frac{d\alpha}{dt} = f(\alpha)A \cdot \exp\left(\frac{E_a}{RT}\right) \tag{7.4}$$

The expression as proposed by Friedman involves taking the natural logarithm of Equation 7.4 to yield Equation 7.5 [151,255,260].

$$\ln\left(\frac{d\alpha}{dt}\right) = \ln[Af(\alpha)] - \frac{E_a}{RT} \tag{7.5}$$

The values of E_a with respect to conversion degree α can be determined the plot of ln(dα/dt) against 1000/T at a constant conversion value for several experiments with varying heating rate β (°C/min), where the slope of each iso-conversional line corresponds to $-E_a/R$.

A typical plot of α versus T for GCI coal and the GCI coal/facemask melt blend is shown in Figure 7.7a and b, respectively, while the analogous plots for the charcoal samples are given in Figure 7.7c and d. Charcoal is seen to be significantly more reactive to CO_2 than GCI coal, likely owing to the materials high degree of intrinsic porosity.

By plotting dα/dt against T for the samples, the difference in maximum rates between the samples is clearer and is shown in Fig. 5e-h. The gasification of charcoal (Figure 7.7g) appears to take place in a single stage whereas the twin peaks observed in the GCI coal (Figure 7.7e) and GCI coal with 20 wt% added facemask (Figure 7.7f) suggests a more complicated multi-step mechanism of CO_2 gasification.

Charcoal and facemask treated charcoal show extreme similarity in terms of CO_2 reactivity, with the DTG signals appearing nearly identical. This is in stark contrast to the GCI coal samples where maximal rate and reaction completion temperature are significantly improved (lowered) by addition of facemask plastic.

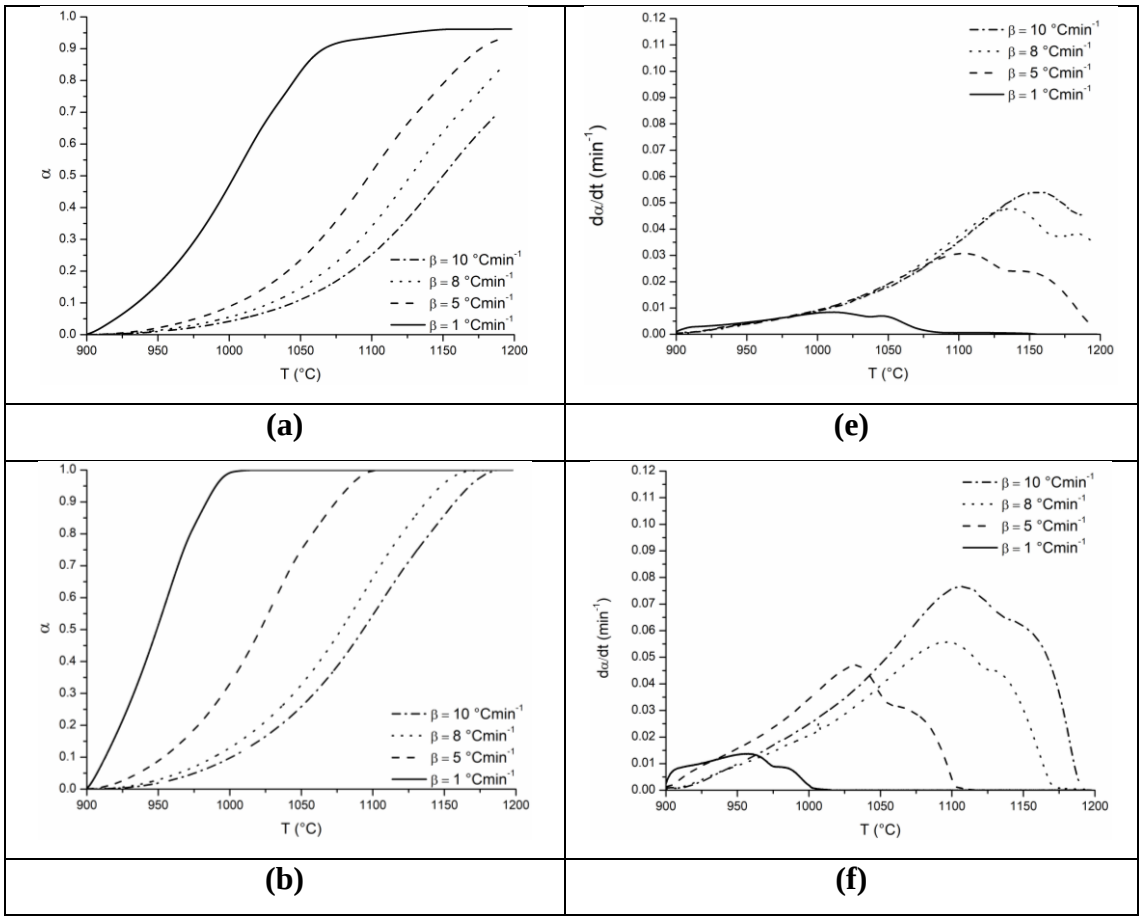

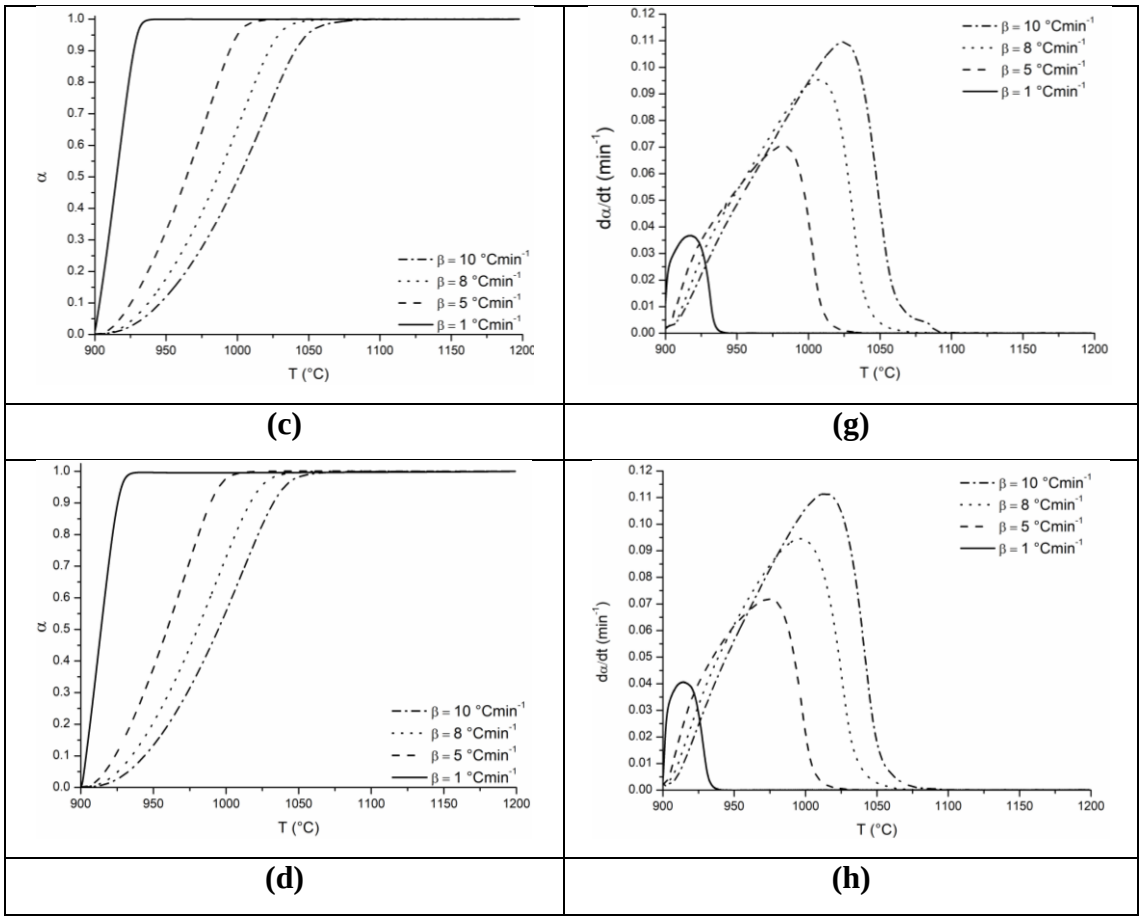

Figure 7.7. Plots of α and dα/dt against T (°C) for different heating rates. (a) GCI coal, α against T. (b) GCI coal melt-blended with 20 wt. % facemask material, α against T. (c) Charcoal, α against T. (d) Charcoal melt-blended with 20 wt. % facemask material, α against T. (e) GCI coal, dα/dt against T. (f) GCI coal melt-blended with 20 wt. % facemask material, dα/dt against T. (g) Charcoal, dα/dt against T. (h) Charcoal melt-blended with 20 wt. % facemask material, dα/dt against T.

Friedman plots of ln(dα/dt) against 1000/T at iso-conversions of α = 0.1-0.9 for each sample are shown in Figure 7.8a-d. and calculated activation energies for each of the samples based on the iso-conversional line slopes in Figure 7.8c and Figure 7.8f.

Activation energies for CO_2 gasification of charcoal ranged from 133 – 147 kJ/mol compared with 136 – 142 kJ/mol for facemask treated charcoal in reasonable agreement with Dai et al.'s calculated CO_2 gasification activation energies for various biomass chars[261]. The tight range of activation energies at different stages of conversion suggests a consistent gasification mechanism for both treated and untreated charcoal.

The results imply that the treatment with facemask plastic for charcoal has little to no effect on CO_2 gasification reactivity.

Activation energies for GCI coal ranged from 184 – 246 $kJmol^{-1}$, with an apparent shift in the reaction mechanism at higher levels of conversion, where a sharp increase in E_a is observed for $\alpha = 0.9$. These results are broadly similar to calculated activated energies for Indian coals[262] and coal chars[151] but the range of reported values for the Boudouard reaction is extremely wide in literature, due to its dependence on structural factors in the material. GCI coal treated with facemask plastic showed a marked decrease in activation energy across the entire conversion range when compared with the untreated material, with values spanning 134 -160 kJ/mol.

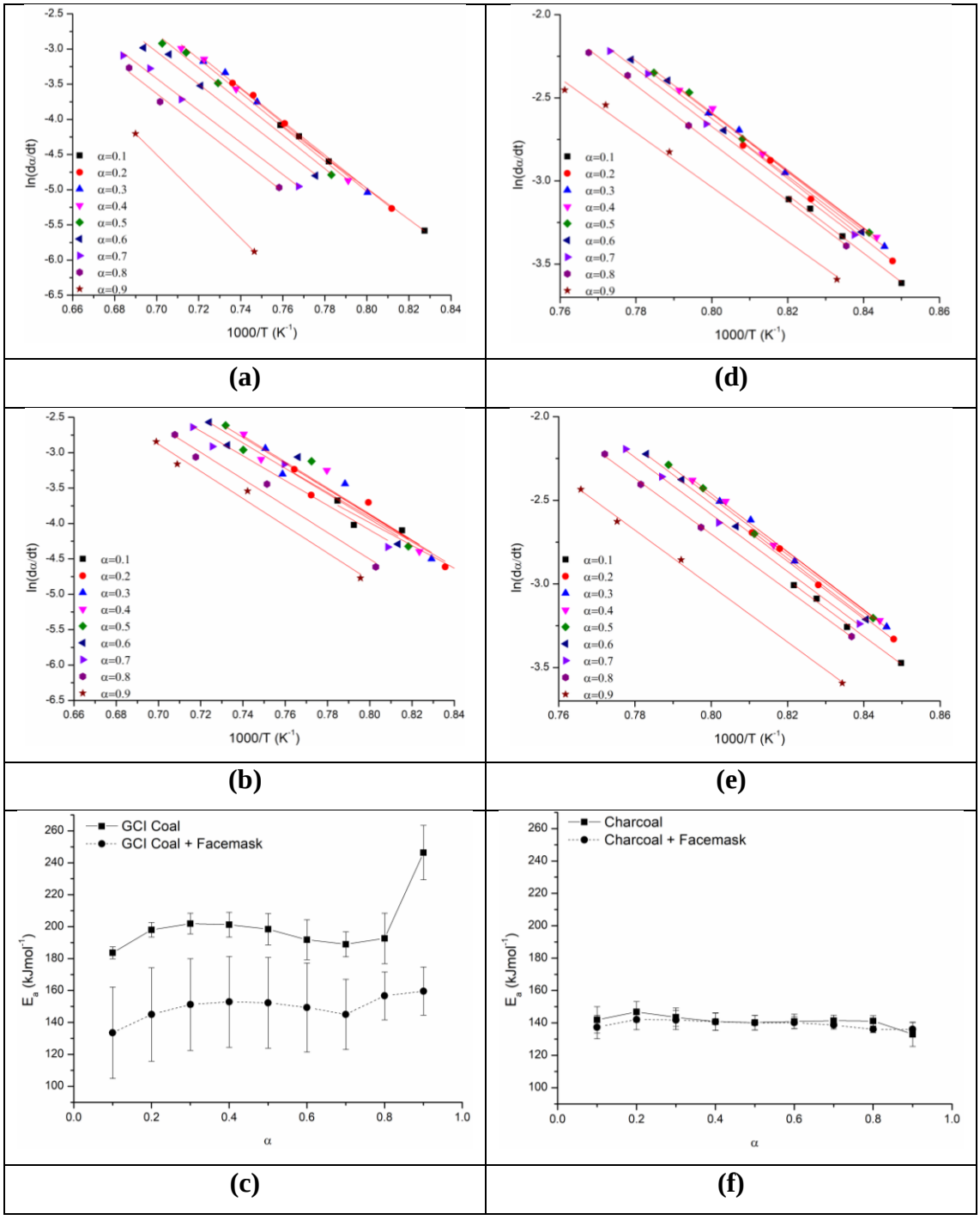

Figure 7.8. Friedman plots and calculated activation energy (E_a) against α for the combustion of carbon and carbon/facemask melt blends in CO_2 atmosphere. (a) Friedman plot for GCI coal. (b) Friedman plot for GCI coal/facemask melt blend. (c) Activation energy against α for GCI coal and GCI coal/facemask melt blend. (e) Friedman plot for charcoal. (e) Friedman plot for charcoal/facemask melt blend. (f) Activation energy against α for charcoal and charcoal/facemask melt blend.

That the addition of facemask plastic to coal can increase its reactivity so decidedly, even though the plastic has long since decomposed and volatilized before the reaction gas was introduced to the thermogravimetric analyzer implies that either, the ash residue of the facemasks is acting in a catalytic manner to accelerate CO_2 gasification or that the action of the plastic in the material vaporizing and diffusing away from the solid is introducing some form of chemical or structural change in the material that is leading to increased CO_2 gasification reactivity (Figure 7.8c and 6f).

7.6 Pyrolysis Experiments and Structural Changes

To better understand the structural changes that occur within the facemask treated and untreated material. Samples of material were pyrolyzed at 500 °C in a tube furnace under cover of an inert atmosphere to volatilize the plastic component of the facemask treated materials, as described in 7.2.

7.6.1 SEM analysis

The morphology of the facemask plastic melt-blend materials as prepared, was compared to that of the untreated carbon materials by SEM as shown in Figure 7.9. The GCI coal samples (Figure 7.9a) shows the flaky structure typical of raw coals with limited porosity [263]. The charcoal sample (Figure 7.9c) appears significantly more porous as the material retains some of the cellular structure of the wood which it is derived from. Comparing the untreated coal and charcoal to the samples treated with facemask plastic (Figure 7.9b and d respectively) it can be seen that the plastic readily wets and coats the coal particles while in the molten phase. Further to this, the mixing step disperses the molten polymer across the coal surface.

SEM images of the materials following pyrolysis at 500 °C are also shown in Figure 7.9. Little difference in the structure is observed between the charcoal (Figure 7.9g) and facemask treated charcoal (Figure 7.9h), both materials still exhibit the cellular structure and large pores characteristic of charcoal. In contrast, the pyrolyzed GCI coal sample treated with facemask plastic (Figure 7.9f) appears significantly more amorphous than the GCI coal that was not treated (Figure 7.9e). This change in surface morphology suggests that the action of plastic pyrolyzing from the surface of the coal during heat treatment is altering the surface structure of the coal. This textural change

on the surface of the material may be responsible for the differences observed in CO_2 reactivity.

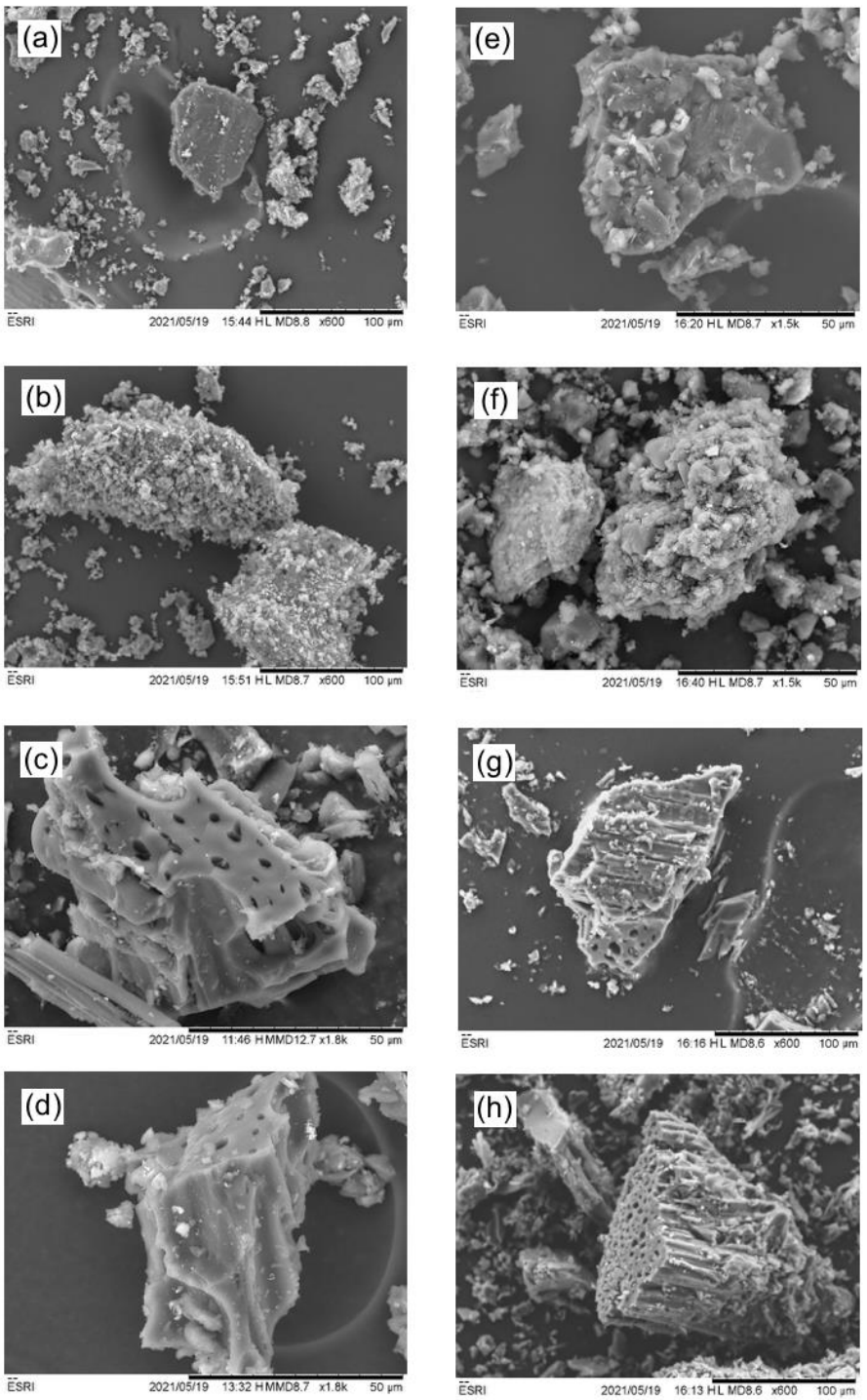

Figure 7.9. SEM images of samples of carbon and carbon/facemask melt blends. (a) GCI coal, (b) GCI coal with 20 wt. % facemask plastic, (c) charcoal, and (d) charcoal with 20 wt% added facemask plastic. (e) GCI coal after pyrolysis to 500 °C, (f) GCI coal with 20 wt. % facemask plastic after pyrolysis to 500 °C, (g) charcoal after pyrolysis to 500 °C, and (h) charcoal with 20 wt% added facemask plastic after pyrolysis to 500 °C.

7.6.2 Surface Area Analysis

Surface area analysis of the samples (Table 7.4) provides important insight into the mechanism of the increased reactivity observed in the GCI coal. Firstly, it is seen that pre-pyrolysis the samples mixed with facemasks have a dramatically increased surface area.

This may be related to the adhesion of polymer particles to either the coal or charcoal particles creating a rough surface on the carbon particles. Following pyrolysis, however, the increased porosity observed in the pre-pyrolysis charcoal samples is eliminated and the charcoal and facemask treated charcoal exhibit essentially identical surface areas (Table 7.4).

For the GCI coal however, it appears the mechanical and/or chemical action of the plastic pyrolysis has had a roughening effect on the relatively non-porous surface of the material leaving the post pyrolysis facemask treated sample significantly more porous than the sample without facemask plastic addition, in agreement with observations made using SEM in Figure 7.9. A similar trend is seen in pore volume analysis performed using DFT, as the pyrolyzed GCI coal sample with 20 wt. % added facemask shows substantially higher pore volume than the untreated sample.

Table 7.4. Surface area (BET) and pore volume (DFT) analysis for pre- and post-pyrolysis of samples carbon and carbon/facemask samples. [a]20 wt. % facemask added to the carbon source. [b] 500 °C in argon.

	Surface area (m^2g^{-1})		**Pore volume (cm^3g^{-1})**	
Sample	**Pre-pyrolysis**	**Post-pyrolysis**	**Pre-pyrolysis**	**Post-pyrolysis**
GCI coal	5.498	6.265	0.036	0.032
GCI coal/facemask[a]	12.789	13.544	0.048	0.046
Charcoal	33.517	31.056	0.034	0.067
Charcoal/facemask[a]	75.238	31.067	0.055	0.071

Pore development of coals as volatile compounds are lost from the material is a critical factor in gasification reactivity [264], and thus surface area measurements can be useful for estimating reactivity. However, it is important to note, from the work of Sexton et al., that this relationship between surface area and CO_2 activity was not found

to be absolute and that the intrinsic chemical structure of the char material plays a substantial role in CO_2 gasification reactivity.

The chemical composition of the ash in the material also plays a key role: alkali and alkaline earth metals such as Na, K and Ca are extremely catalytically significant in CO_2 gasification of coals [263,265].

7.7 Producing DRI from Facemask Plastic

Many studies on the production of DRI from self-reducing agglomerates utilizing plastics either employ reagent grade plastic powders unrepresentative of plastic waste [246] or elaborate milling methods [122] which may not be feasible at scale. By adopting the melt-blending protocol from Section 7.3 to process COVID-19 face coverings with coal fines into a fine powder, the performance of facemask plastic in self-reducing agglomerates for the RHF can be evaluated.

To prepare DRI from facemask plastic, reagent grade Fe_2O_3 (99%, <5 μm) was obtained from Fisher Scientific and mixed in a ratio of 7:3 with GCI coal and facemask treated GCI coal (FC) to give blend Fe_2O_3-C and Fe2O3-FC respectively.

Pellets of material were prepared in a hydraulic press (20 wt. % added water, 200 mg sample, 5 mm, 1 t, 30s) for reduction reactions in a Carbolite MTF 12/38/400 controlled atmosphere tube furnace heated to reaction temperature at a rate of 5 °C/min under the protection of 1 dm^3/min of N_2 before holding for 1 hr. Samples were cooled under a flow N_2 within the furnace to prevent reoxidation. All samples were stored in a vacuum desiccator following drying/heat treatment to prevent oxidation.

7.7.1 Thermogravimetric Analysis

Thermogravimetric analysis of the Fe_2O_3, coal and facemask treated coal (FC) used in this study is shown in Figure 2. The Fe_2O_3 used showed minimal degradation over the experimental temperature range, only losing 2.70 wt. % over the course of the heat treatment. The coal utilized in the study gradually loses mass over the course of the experiment as expected as volatile organic compounds vaporize. The FC sample initially behaves very similarly to the untreated coal until approximately 400 °C where the pyrolysis of the facemask plastic occurs causing a sudden mass drop of 9.1% in good agreement with the behavior of facemask plastic in Figure 7.10.

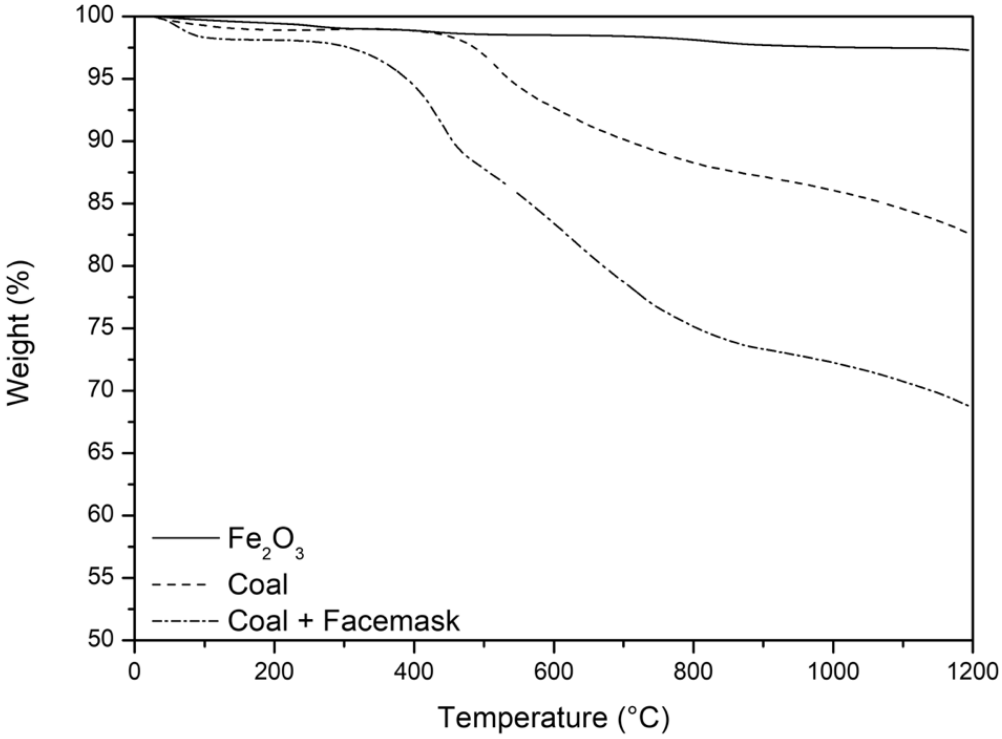

Figure 7.10 TGA curves for Fe_2O_3 coal and facemask treated coal (FC) from room temperature to 1200 °C under argon with a heating of 10 °C/min.

Reference TGA curves for the blends were calculated using Equation 7.4 adapted from Ubando et al. [266] to offer a baseline TGA curve for the blends to compare experimental data to, to allow examination of iron reduction and other synergistic effects. TGA and Y represent the TGA curve and the mass fraction of the component in the blend respectively, with the subscript Fe_2O_3 representing the Fe_2O_3 used in the study and C representing the carbon source (Coal or FC). By plotting the experimental TGA curves for the Fe_2O_3-Coal and Fe_2O_3-FC blends in comparison to the theoretical curves as determined by studying the reactants individually, their interaction can be visualized and is shown in Figure 7.11.

$$\mathrm{TGA}_{\mathrm{theoretical}} = \left(\mathrm{Y}_{\mathrm{Fe_2O_3}}\mathrm{TGA}_{\mathrm{Fe_2O_3}}\right) + \left(\mathrm{Y}_{\mathrm{C}}\mathrm{TGA}_{\mathrm{C}}\right) \tag{7.4}$$

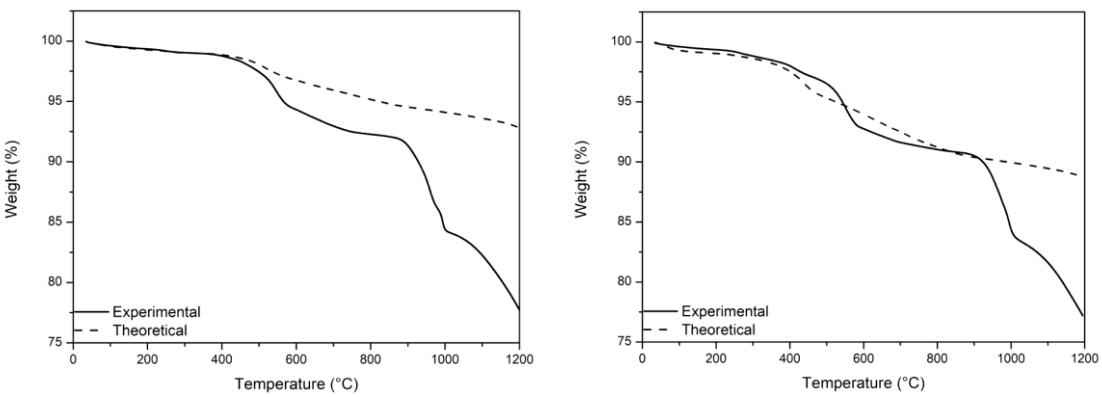

(a) **(b)**

Figure 7.11. Experimental TGA curves versus theoretical curves for (a) Fe_2O_3-C and (b) Fe_2O_3-FC.

Three clear transitions can be seen for both the Fe_2O_3-Coal and Fe_2O_3-FC samples. The first transition between 400-600 °C is likely to be the reduction of Fe_2O_3 to Fe_3O_4, the transition between 900-1000 °C is the further reduction of Fe_3O_4 to FeO and the final transition initiating at 1000 °C is reduction of FeO to metallic Fe. This is in reasonable agreement with the work of Willm's et al. who observed reduction behavior of briquetted self-reducing agglomerates where heat transfer and external diffusion become more significant than the TGA experiments here [267].

An interesting observation from comparing the experimental results to the theoretical TGA curves based on the raw materials is a potentially synergistic interaction between the Fe_2O_3 in the Fe_2O_3-FC sample and the pyrolysis products released as the facemask plastic material decomposes.

The theoretical curve is 1.08 wt. % greater than the experimental results for Fe_2O_3-FC at 450 °C which suggests that less than the expected amount of volatile matter from the facemask plastic decomposition volatilized and vacated the sample. Fe_2O_3 may be acting as a nucleation site for soot by interacting with the pyrolysis products, as Fe_2O_3 is well known to be an active catalyst for alkane reformation to syngas [268] and pyrolysis of polypropylene as in disposable face coverings is known to generate simple alkanes as gaseous products [269].

The relationship between increasing fixed carbon (carbon that is available for reduction at ironmaking temperatures) and reduction rates in self-reducing agglomerates are well established in both literature [123] and the earlier portions of this thesis (Section 5.3.3.4). Therefore, it is promising that mixing waste plastic (in this case facemasks) that

contain almost no fixed carbon may be able to supply additional carbon into pellets in a form that is useful for reduction in an RHF, solely through interaction with the oxides present within the pellets.

7.7.2 Tube Furnace Experiments

Pellets of Fe_2O_3-C and Fe_2O_3-FC as described in the experimental methods were heat treated to 650, 1000 and 1200 °C prior to XRD and SEM analysis. It was observed that in samples heated to 650 °C, a color change was observed in the Fe_2O_3-FC sample but not the Fe_2O_3-C sample, the Fe_2O_3-FC sample had a dull grey luster and appeared to be coated in fine black powder (Figure 7.12).

Figure 7.12. Images of Fe_2O_3-FC (left) and Fe_2O_3-C (right) briquettes reduced at 650 °C for 1 hr under N_2.

7.7.2.1 Scanning Electron Microscopy

SEM micrographs of the untreated Fe_2O_3-C and Fe_2O_3-FC blends (Figure 7.13) show fine iron oxide material (the bright particles) mixed and adhered to darker, angular coal and facemask treated coal particles. Following heat treatment to 650 °C, the Fe_2O_3-FC sample appears to show substantially more extremely fine carbon material throughout the iron oxide matrix, alongside angular coal particles like those seen in Fe_2O_3-C at 650 °C, supporting the notion of soot deposition observed in TGA experiments.

Samples treated at 1000 °C begin to show cracking within the structure of the briquettes, this is typical for self-reducing agglomerates due to internal stresses within the briquettes caused by volumetric changes during the reduction of Fe_2O_3 [157,270] and the internal generation of gas within the briquette.

At 1200 °C clear grains of metallic iron are visible in both samples; some unreacted carbon still clearly remains and is visible as porous black particles embedded within the matrix of metallic Fe. The morphology of reduced iron is directly related to the

gas conditions of reduction, specifically the reducing potential and CO/CO_2 ratio in the reactive gas phase. Whisker-like formations of metallic iron is common in more oxidizing gas mixtures, while porous iron is expected at higher CO/CO_2 ratios [157], and the morphology seen in both 1200 °C samples is characteristic of porous metallic iron, though the coalescence of iron grains through necking appears more significant in the Fe_2O_3-FC sample.

(a)

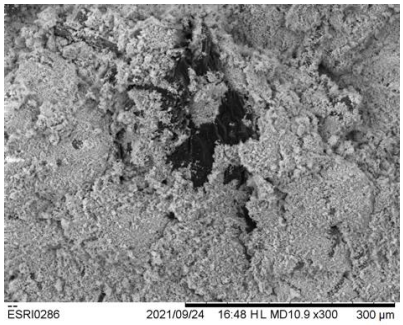

(e)

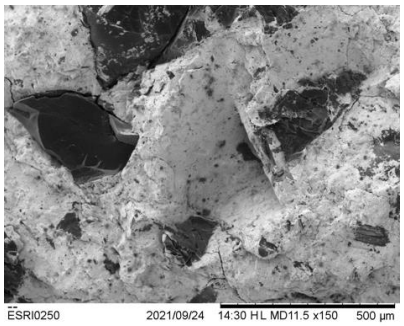

(b)

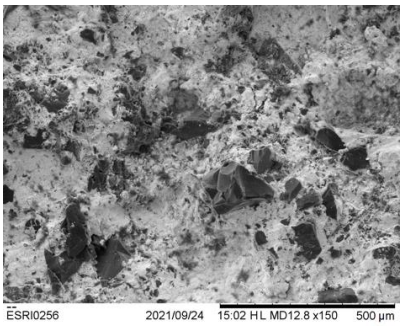

(f)

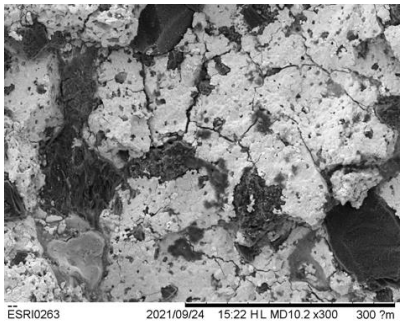

(c)

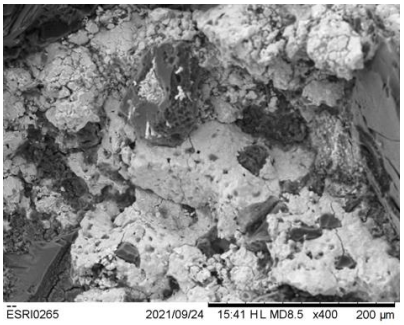

(g)

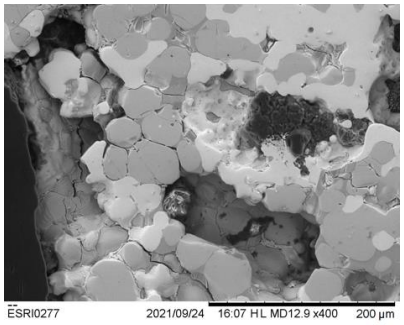

(d)

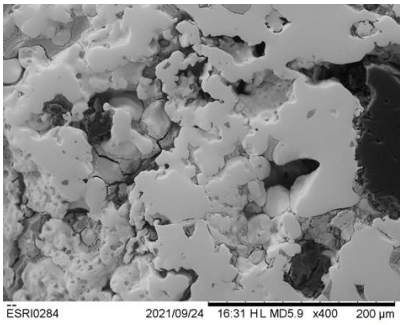

(h)

Figure 7.13. SEM micrographs for briquettes: (a) untreated Fe_2O_3-C; (b) Fe_2O_3-C heated to 650 °C under N_2 for 1 hr; (c) Fe_2O_3-C heated to 1000 °C under N_2 for 1 hr; (d) Fe_2O_3-C heated to 1200 °C under N_2 for 1 hr; (e) untreated Fe_2O_3-FC; (f)

Fe_2O_3-FC heated to 650 °C under N_2 for 1 hr; (g) Fe_2O_3-FC heated to 1000 °C under N_2 for 1 hr; (h) Fe_2O_3-FC heated to 1200 °C under N_2 for 1 hr.

7.7.2.2 Powder X-Ray Diffraction

XRD data for heat treated samples of the two blends (Figure 7.14 and Figure 7.15) supports the decompositions observed in thermogravimetric analysis. Both untreated samples show a characteristic diffraction pattern of hematite (Fe_2O_3) as expected but following treatment at 650 °C significant but incomplete reduction to Fe_3O_4 is observed.

At 1000 °C both samples are further reduced to a mixture of FeO and Fe_3O_4 with a small amount of metallic iron. At 1200 °C both samples are highly metalized, containing predominantly iron in the metallic form with small amounts of FeO. Interestingly in both samples > 1000 °C, a broad peak emerges between 25 – 35 ° which corresponds well with semi-crystalline carbonaceous phases that emerge during the carbonization process in coking [24].

Rietveld refinement of diffractograms for Fe_2O_3-C and Fe_2O_3-FC at 1200 °C, discounting the broad carbonaceous peak from fitting show that for crystalline components, the Fe_2O_3-C sample is 94.8% metallic Fe and 5.2 % FeO and the Fe_2O_3-FC sample is 97.0% metallic Fe and 3.0% FeO. The result suggests Fe_2O_3-FC is marginally better reduced than the non-plastic treated Fe_2O_3-C.

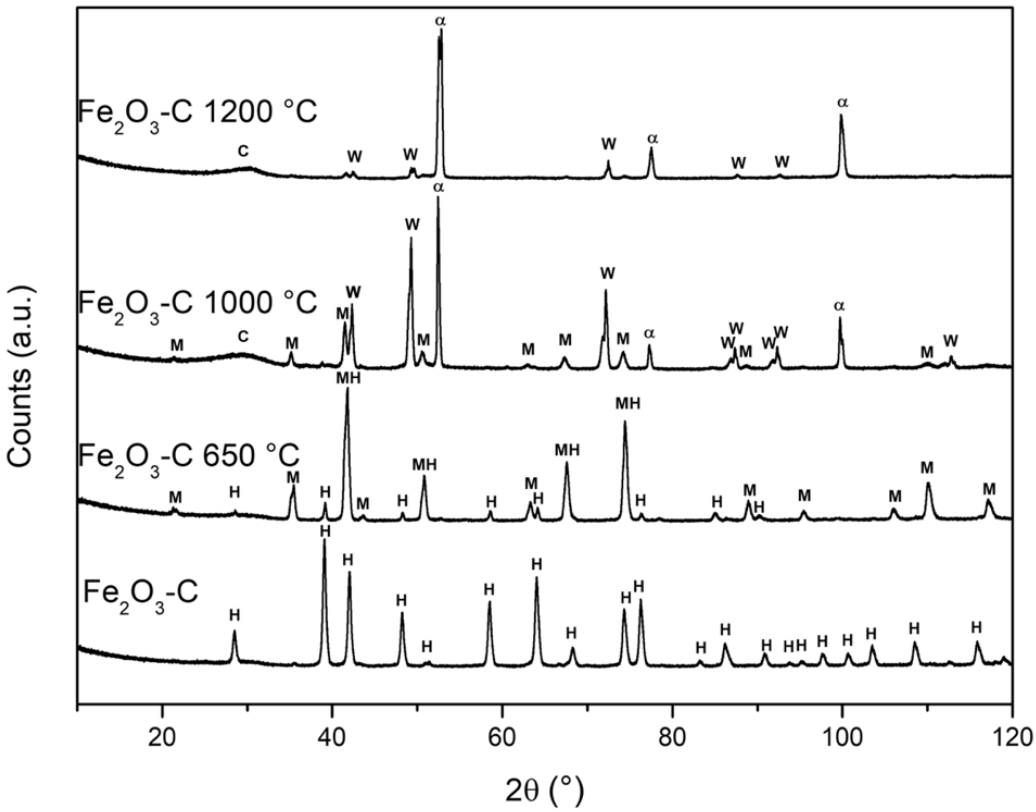

Figure 7.14 Powder XRD for Fe_2O_3-C as prepared, and heat treated for 1 hr at 650 °C, 1000 °C, and 1200 °C. H = Hematite (Fe_2O_3 – COD# 9009782), M = Magnetite (Fe_3O_4 -COD# 9006920), W = Wüstite (FeO – COD# 1011167), α = Iron (Fe – COD# 9006595), C = coke (C – [271]).

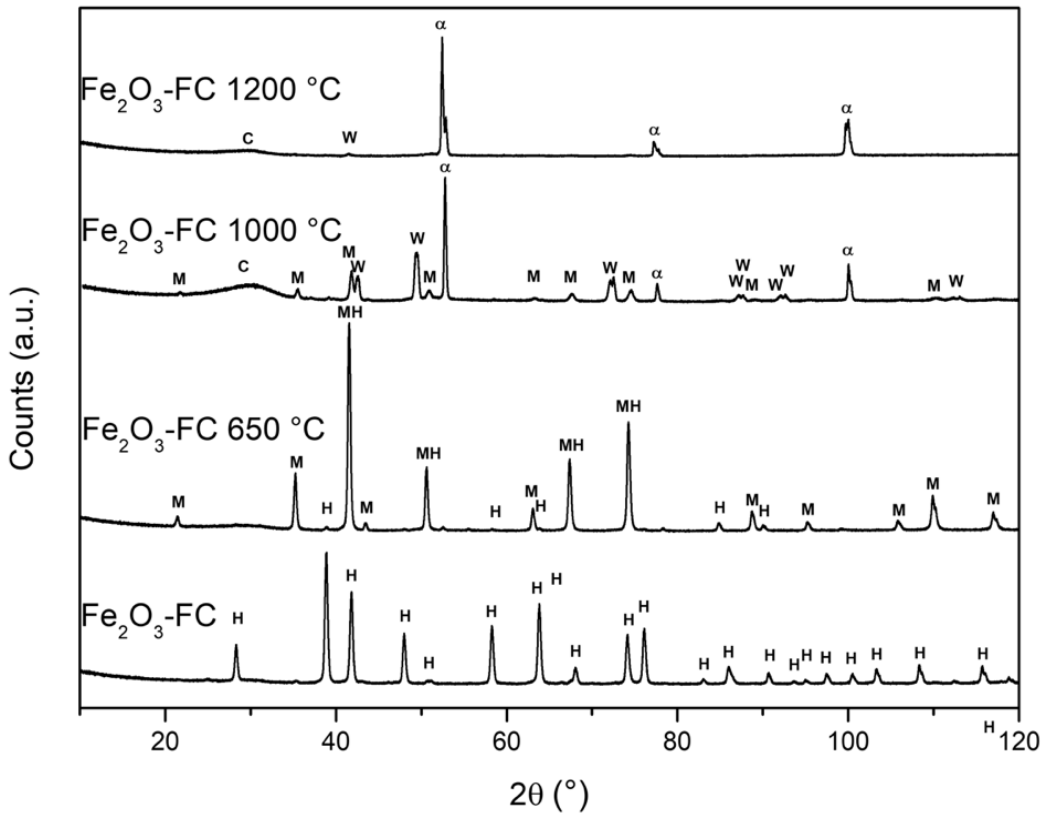

Figure 7.15. Powder XRD for Fe_2O_3-C as prepared, and heat treated for 1 hr at 650 °C, 1000 °C, and 1200 °C. H = Hematite (Fe_2O_3 – COD# 9009782), M = Magnetite (Fe_3O_4 -COD# 9006920), W = Wüstite (FeO – COD# 1011167), α = Iron (Fe – COD# 9006595), C = coke (C – [271]).

7.8 Discussion

The observation that charcoal is not seen to increase in CO_2 reactivity with the addition of facemask plastic, but the GCI coal sample does, has two potential explanations. The first is that the far higher initial porosity of the facemask treated charcoal sample led to the facemask treatment doing little to increase porosity further, and therefore have no tangible effect on CO_2 gasification reactivity. Secondly, if the deposition of catalytic CaO ash following pyrolysis of the facemask plastic is the dominant mechanism of increased CO_2 reactivity, this may be masked due to the high ash content of the charcoal (18.7%) having such a significant catalytic effect on CO_2 reactivity that the further small addition of facemask ash has no tangible effect.

It is likely there is a combination of catalytic and pore development factors responsible for the observed increase in reactivity of facemask treated GCI coal. Nevertheless, the CO_2 gasification reactivity of a sample of a low volatile content coal

was dramatically improved by the addition of waste facemask plastic, as determined through non-isothermal thermogravimetric measurements. This was not observed in a substantially more porous, higher volatile content and higher ash content charcoal material. The results suggest a potentially synergistic mechanism where the deposition of CaO based ash following the pyrolysis of the facemask plastic, as well as a physical change in the structure of the coal causing increased porosity both play a role in increasing the reactivity of the material in the CO_2 gasification reaction. Further study is required to fully parse these two competing explanations.

Steer et al. described a close relationship between increasing volatile matter content of injection coals and reduced burnout time (and therefore improved combustion reactivity) using a drop tube furnace (DTF) to emulate the conditions of the raceway of a BF and attributed this increase to increasing particle surface area and additional heat supplied by combustion of coal volatiles [272]. It can be proposed that the action of dispersing molten facemask plastic across the surface of low volatile content coal is acting in a manner similar to intrinsic volatile matter within the coals, opening pores in the material and increasing the reactive surface area of the particles. An overall schematic for the process is shown in Figure 7.16.

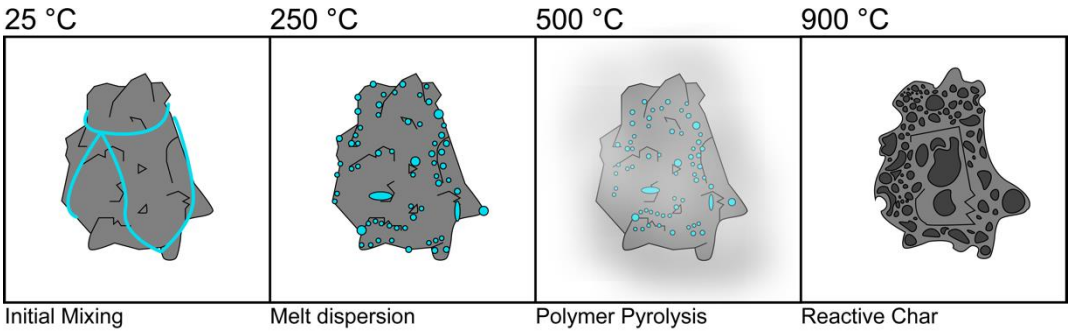

Figure 7.16. Proposed process schematic showing the effect of the polymer fabric of facemasks on a coal particle as it undergoes heat treatment

The results are favorable for the purposes of increasing CO_2 reactivity of low-quality carbonaceous materials for RHF processing of steelmaking by-product sludges. Increased char reactivity may lead to improved iron and zinc reduction rates in self-reducing agglomerates and the additional reducing gases provided by the facemask plastic would also contribute additional reductant. The synergistic effect of plastic decomposition products interacting with iron oxide particles in pellets of DRI leading to additional fixed carbon within the pellet is promising from a process perspective, as it

However, through exploring the properties of the facemask treated GCI coal for RHF application it became apparent that the material may be a good candidate for direct injection at the BF tuyere as well.

The injection of coal through the tuyeres into the blast furnace has become extremely commonplace in the global steel industry as a means of reducing demand for expensive and environmentally costly coke in iron production [272,273]. BF coal injection rates have been steadily increasing for decades, from 60-80 $kgtHM^{-1}$ in the 1980s to over 200 $kgtHM^{-1}$ in some plants [274].

An extremely important consideration when selecting candidate coals for injection to the BF is the reactivity of the char produced following injection. Coal that enters the furnace via a tuyere experiences oxidizing conditions and an extremely high heating rate as the material enters the raceway. Any coal particles that are not completely reacted at this stage leave the raceway region as a partially burnt-out char where gasification under the prevailing gas condition of the furnace becomes dominant.

In order to achieve the maximum possible injection rate, it is critical that the injected material reacts and gasifies in as short a time period as possible [275], de Lourdes Ilha Gomez et al. stipulated that “The more reactive a char is, the better is the effect in the replacement of coke” [276] with respect to pulverized coal injection and the BF.

Char that is not completely consumed during PCI is obviously economically unfavorable as it is underutilized for the purposes of iron reduction, but much more significantly, unburnt material can accumulate within the furnace burden. This can have substantial negative effects on burden permeability, furnace stability, temperature distribution, coke erosion and char carryover [277]. Injection rates to a BF can be limited by a number of other factors such as S and ash input but one of the key reactivity criteria that has an established effect on burden permeability is the insufficient gasification of chars formed after injection to the furnace [264].

However, there is some debate as to whether the effect of increased gasification reactivity of chars leads to decreased coke rates in the literature. Steer et al. suggested that based on data from an operating BF that high gasification chars actually lead to an increased coke rate rather than a decrease and attributed this to the endothermic nature of CO_2 gasification leading to the cooling effect on the thermal reserve temperature of the BF [278].

Therefore, the increase in CO_2 gasification reactivity caused by the introduction of facemask plastic to the GCI coal here may or may not be beneficial from a direct BF injection perspective and warrants further study.

Globally, plastic injection systems are also emerging capable of injecting plastic to the furnace, reducing fossil fuel requirements and sparing plastic waste from landfill or entering the ocean [279]. However these modified plants are capital intensive, requiring specialist support plant and tuyere modifications to be capable of handling the extreme heterogeneity of a recycled plastic feed [279], subject to further trials the method of melt-blending described herein may present a way of introducing plastics to a BF with minimal plant modification.

As waste facemask plastic is unfortunately, readily available in the wake of the pandemic of SARS-CoV-2 and its variants, its application in the iron and steelmaking industry is a positive avenue of disposal to prevent material being introduced into rivers and oceans while displacing environmentally damaging fossil fuels from the steelmaking process.

Drop tube furnace trials designed to replicate the unique chemical conditions of the BF tuyere would allow for examination of burnout behavior of the facemask treated coal, which is a much better indicator of the maximal injection rates achievable with a material [274], especially when combined with calorimetry.

7.9 Conclusions

Waste COVID-19 face coverings were found to be a potential low-sulfur reductant in ironmaking processes, but due to their physical form are extremely challenging to process.

A melt-dispersion milling process was developed to process waste COVID-19 face coverings rapidly and economically into a granular powder, through co-processing with coal or charcoal.

The resultant material exhibits good handling characteristics similar to the original coal and is of appropriate size and homogeneity for inclusion in self-reducing agglomerates in RHF ironmaking.

As well as providing additional reductant to the iron reduction process, the facemask treated coal became significantly more reactive in the CO_2 gasification

reaction due to increased porosity in the material generated by the action of the facemask plastic undergoing pyrolysis.

This increased CO_2 reactivity for the resultant chars formed from the coal could lead to improved iron reduction and volatile metal removal in the RHF, subject to further study. The increased CO_2 reactivity of the facemask treated coal was ascribed to pyrolysis of the facemask plastic at lower temperatures increasing the coals surface area and thus the area available for reaction with carbon dioxide.

DRI pellets prepared from self-reducing agglomerates containing facemask treated material showed very similar quality to DRI prepared from untreated coal, and a synergistic interaction between the facemask plastic pyrolysis products and the iron oxides in the self-reducing agglomerate led to deposition of soot within the agglomerate. This soot could provide additional fixed carbon for high temperature iron reduction.

The facemask plastic treated coal may be a promising candidate for direct injection to the BF as well as inclusion in RHF feed, owing to it's extremely similar material handling characteristics to untreated coal, and is a promising avenue for further study.

8. CONCLUSIONS

8.1 Summary

This research aimed to identify an effective and scalable process for the recovery of zinc contaminated by-products produced during the ironmaking and steelmaking process.

An in-depth literature review suggested that the RHF is an attractive commercialised process for the recovery of zinc contaminated by-products when placed locally to an integrated site to allow for the recycling of the produced DRI.

A materials characterization study carried out on material from around the UK identified that the variability in zinc morphology in stockpiled material might make hydrometallurgical recovery less viable than pyrometallurgical extraction which is less sensitive to the chemical form of zinc within the materials. It was found that BF dust is a suitable reductant for the RHF due to its high fixed carbon content and therefore could allow for co-processing of BF dust and BOS dust simultaneously without additional reductants.

A benchmarking study was undertaken, imitating the RHF process using a benchtop furnace. Excellent zinc removal, lead removal and iron metallization were found to be achievable in realistic RHF process conditions of 15 minutes at 1250 °C. While the produced DRI was highly metallized, the S content of the BF dust used as a reductant and the high gangue content of the DRI would likely limit the amount that is recyclable via the BOF.

Excessive carbon in the pellets was found to provide little additional benefit in terms of zinc removal and metallization and should be avoided due to the high sulfur content of the BF dust used as a reductant which is not removed through processing through a conventional RHF.

Thermodynamic studies using FactSage suggested a potentially viable process of producing pig iron nuggets via an RHF in a manner similar to ITmk3[82], E-Iron [192,230] or Hi-QIP [86,87] by the addition of an SiO_2 and MgO flux. The recommendations made via the computational portion of the study and were validated experimentally, with 15 minutes at 1450 °C being found to be sufficient to produce granulated pig iron nuggets from BOS dust and BF dust with below detectable levels of zinc.

The melting step and generation of a fusible slag allowed for partial desulfurization of the pig iron, and the lack of gangue present makes the iron nuggets more attractive for use in the BOF than DRI. The pig iron nuggets produced were found to be more oxidatively stable than DRI making them a more attractive option for outdoor storage or export.

A new process was devised for the milling of the fibrous plastic present in waste COVID-19 facemasks to render them more recyclable via the RHF, via a melt dispersion milling process using another carbon source such as coal or charcoal.

The addition of facemask plastic to coal not only provided supplementary reductant, as the facemasks are a low sulfur source of carbon and hydrogen for direct reduction, but the action of plastic facemask decomposition was found to enhance the CO_2 reactivity of the coal.

This increased CO_2 reactivity was attributed to a combination of the catalytic action of the CaO ash content of the facemasks and also to an increase in porosity in the coal, allowing for greater accessible surface area to reaction gases.

The increase in CO_2 reactivity may relate to an increase in iron reduction rate in self-reducing agglomerates, due to carbon gasification controlling reaction rate during a large portion of the reduction process.

DRI prepared from facemask treated coal appears to be of similar quality to DRI prepared from untreated coal and a soot deposition mechanism caused by an interaction between the facemask pyrolysis products and the iron oxide present in the self-reducing agglomerate leads to an increase of carbon available for higher temperature reduction.

The thesis provides a framework for the production of DRI from BF dust and BOS dust in Port Talbot via currently available ‘off-the-shelf’ RHF technology and therefore generating valuable ferrous feedstock by co-processing two challenging materials, a mechanism for increasing the value of the ferrous product through the addition of fluxes to generate pig iron nuggets rather than DRI, and a method for incorporating waste plastic resulting from the COVID-19 global pandemic into RHF production through an economical milling process.

8.2 Recommendations for Future Work

There is ample scope to expand on the work contained within this thesis, as with any research it was constrained by time and by resource.

A more representative furnace rig such as that described in Figure 5.1 would allow for study into the effect of gas atmosphere on DRI production and also for more representative heating rates. Thermogravimetric monitoring of iron reduction *in-situ* is also much more preferable to the expansive and time-consuming wet chemical analyses carried out herein. Study into multi-layer pellet beds in the RHF and their effects on

zinc removal are also relatively sparse in the literature and provide scope for further work imitating and optimizing operational RHF production.

An expanded study into producing pig iron nuggets from waste would allow for a more thorough process optimization, but the good agreement between computational and experimental results shown herein bode well for future work. Mass balance studies would allow for much more accurate estimations of yield, raw material utilization and thus process economics, and refractory trials would be required to understand wear mechanisms in the unique chemical conditions of an RHF producing pig iron nuggets using a basic slag.

The use of waste plastic in the RHF has previously been limited by the physical form of readily available plastic waste streams – the heterogeneity in terms of size and geometry boding poorly for preparing self-reducing agglomerates from the material. The method of preparing a granular powder from plastic in a relatively easy process such as that proposed herein could be applied outside the application of COVID-19 face coverings and into environments that generate large volumes of single use plastic waste at a central location such as a hospital, where such material is typically incinerated anyway.

The application of plastic treated coal in BF ironmaking would also be a ripe avenue of future research. The similarity in handling characteristics between the treated and untreated coal mean it may be usable directly into existing injection systems in older BFs without expensive tuyere modifications and support plants that steelmakers are often reluctant to install onto older furnace.

REFERENCES

1. Bureau of International Recycling - Ferrous Division. *World Steel Recycling in Figures 2015 - 2019*. https://www.bir.org/publications/facts-figures/download/643/175/36?method=view (2019).
2. Griffin, P. W. & Hammond, G. P. The prospects for ‘green steel’ making in a net-zero economy: A UK perspective. *Glob. Transitions* **3**, 72–86 (2021). doi: 10.1016/j.glt.2021.03.001.
3. Branca, T. A. *et al.* Reuse and recycling of by-products in the steel sector: Recent achievements paving the way to circular economy and industrial symbiosis in europe. *Metals* vol. 10 (2020). doi: 10.3390/met10030345.
4. Fisher, L. V & Barron, A. R. The recycling and reuse of steelmaking slags — A review. *Resources, Conservation and Recycling* vol. 146 244–255 (2019). doi: 10.1016/j.resconrec.2019.03.010.
5. World Steel Association. *Steel - the Permanent Material in the Circular Economy*. https://www.worldsteel.org/en/dam/jcr:7e0dc90a-3efe-41bc-9fb4-85f9e873dfc7/Steel%2520-%2520The%2520Permanent%2520Material%2520in%2520the%2520Circular%2520Economy.pdf (2016).
6. Parry, S. History of the Steel Industry in the Port Talbot Area 1900-1988. (University of Leeds, 2011).
7. Welsh Government. Wales Commits to Net Zero by 2050, but sets out ambitions to get there sooner. https://gov.wales/wales-commits-net-zero-2050-sets-out-ambitions-get-there-sooner.
8. Macha, V. The Beauty of Steel Project. https://www.viktormacha.com/foto/beauty-of-steel-project/.
9. Umadevi, T. *et al.* Recycling of steel plant mill scale via iron ore sintering plant. *Ironmak. Steelmak.* **39**, 222–227 (2013). doi: 10.1179/1743281211Y.0000000063.
10. Shibli, S. M. A., Meena, B. N. & Remya, R. A review on recent approaches in the field of hot dip zinc galvanizing process. *Surface and Coatings Technology* vol. 262 210–215 (2015). doi: 10.1016/j.surfcoat.2014.12.054.
11. Stewart, D. J. C. & Barron, A. R. Pyrometallurgical removal of zinc from basic oxygen steelmaking dust – A review of best available technology. *Resour. Conserv. Recycl.* **157**, 104746 (2020). doi: 10.1016/j.resconrec.2020.104746.
12. World Steel Association. *World Steel in Figures 2017*. (2017).
13. Singh, A. K. P. & Raju, M. T. Recycling of Basic Oxygen Furnace (BOF)

sludge in iron and steel works Usha Jha. **14**, 19–32 (2011).

14. Narita, K. *et al.* Effects of Alkalis and Zinc on the Wear of Blast Furnace Refractories and the Tuyere Displacement. *Trans. Iron Steel Inst. Japan* **21**, 839–845 (1981). doi: 10.2355/isijinternational1966.21.839.
15. Daigo, I., Osako, S., Adachi, Y. & Matsuno, Y. Time-series analysis of global zinc demand associated with steel. *Resour. Conserv. Recycl.* **82**, 35–40 (2014). doi: 10.1016/j.resconrec.2013.10.013.
16. Lin, X. *et al.* Pyrometallurgical recycling of electric arc furnace dust. *Journal of Cleaner Production* vol. 149 1079–1100 (2017). doi: 10.1016/j.jclepro.2017.02.128.
17. Shawabkeh, R. A. Hydrometallurgical extraction of zinc from Jordanian electric arc furnace dust. *Hydrometallurgy* **104**, 61–65 (2010). doi: 10.1016/j.hydromet.2010.04.014.
18. Dutra, A. J. B., Paiva, P. R. P. & Tavares, L. M. Alkaline leaching of zinc from electric arc furnace steel dust. *Miner. Eng.* **19**, 478–485 (2006). doi: 10.1016/j.mineng.2005.08.013.
19. Gargul, K., Jarosz, P. & Małecki, S. Alkaline leaching of low zinc content iron-bearing sludges. *Archives of Metallurgy and Materials* vol. 61 43–50 (2016). doi: 10.1515/amm-2016-0013.
20. Sun, X., Hwang, J. & Huang, X. The Microwave Processing of Electric Arc Furnace Dust.pdf. *Jom* vol. 60 34–39 (2008).
21. Jaafar, I. Chlorination for the removal of zinc from basic oxygen steelmaking (bos) by-product. (2014).
22. Allwood, J. M., Cullen, J. M. & Milford, R. L. Options for achieving a 50% cut in industrial carbon emissions by 2050. *Environ. Sci. Technol.* **44**, 1888–1894 (2010). doi: 10.1021/es902909k.
23. Kim, Y. & Worrell, E. International comparison of CO2 emission trends in the iron and steel industry. *Energy Policy* vol. 30 827–838 (2002). doi: 10.1016/S0301-4215(01)00130-6.
24. Lobato, N. C. C., Villegas, E. A. & Mansur, M. B. Management of solid wastes from steelmaking and galvanizing processes: A brief review. *Resources, Conservation and Recycling* vol. 102 49–57 (2015). doi: 10.1016/j.resconrec.2015.05.025.
25. De Buzin, P. J. W. K., Heck, N. C. & Vilela, A. C. F. EAF dust: An overview on

the influences of physical, chemical and mineral features in its recycling and waste incorporation routes. *J. Mater. Res. Technol.* **6**, 194–202 (2017). doi: 10.1016/j.jmrt.2016.10.002.

26. Onnen, J. H. Wet scrubbers tackle pollution. *Environ. Sci. Technol.* **6**, 994–998 (1972). doi: 10.1021/es60071a007.
27. Henschen, H. C. Wet vs dry gas cleaning in the steel industry. *J. Air Pollut. Control Assoc.* **18**, 338–342 (1968). doi: 10.1080/00022470.1968.10469138.
28. Kohlmeyer, E. & Spandau, H. Ueber die Vergasung von Eisen (About the Gasification of Iron). *Arch. für das Eisenhüttenwes.* **18**, 1–6 (1944). doi: https://doi.org/10.1002/srin.194401336.
29. Santos, J., Phillips, J. & Dumesic, J. A. Metal-support interactions between iron and titania for catalysts prepared by thermal decomposition of iron pentacarbonyl and by impregnation. *J. Catal.* **81**, 147–167 (1983). doi: 10.1016/0021-9517(83)90154-9.
30. Turkdogan, E. & Leake, L. Preliminary Studies on the Evolution of Fumes from Iron at High Temperatures. *J Iron Steel Inst* (1959).
31. Nedar, L. Dust formation in a BOF converter. *Steel Res.* **67**, 320–327 (1996). doi: DOI:10.1002/srin.199605497.
32. Goetz, F. The Mechanism Of BOF Fume Formation. (McMaster University, 1980).
33. Hoskins, B. J., Draghici, I. & Davies, H. C. A new look at the cause of fuming. *JOM* **18**, 803–810 (1966).
34. Steer, J., Griffiths, A., Heinrich, T., Thomas, A. & Barnes, C. Correlation of BOS process variables with dust mass formation and zinc content. *Ironmaking and Steelmaking* vol. 41 (2014). doi: 10.1179/1743281213Y.0000000152.
35. Tsujino, R., Hirai, M., Ohno, T., Ishiwata, N. & Inoshita, T. Mechanism of dust generation in a converter with minimum slag. *ISIJ Int.* **29**, 291–299 (1989). doi: 10.2355/isijinternational.29.291.
36. Okhotskii, V. B. Formation of Iron Oxide Dust in Steel Smelting. *Steel in Translation* vol. 37 979–981 (2007).
37. Gritzan, A. & Neuschütz, D. Rates and mechanisms of dust generation in oxygen steelmaking. *Steel Res.* **72**, 324–330 (2001). doi: 10.1002/srin.200100126.
38. Oustadakis, P., Tsakiridis, P. E., Katsiapi, A. & Agatzini-Leonardou, S. Hydrometallurgical process for zinc recovery from electric arc furnace dust (EAFD). Part I: Characterization and leaching by diluted sulfuric acid. *J. Hazard.*

Mater. **179**, 1–7 (2010). doi: 10.1016/j.jhazmat.2010.01.059.

39. Kelebek, S., Yörük, S. & Davis, B. Characterization of basic oxygen furnace dust and zinc removal by acid leaching. in *Minerals Engineering* vol. 17 285–291 (2004). doi: 10.1016/j.mineng.2003.10.030.
40. Ma, N. Recycling of basic oxygen furnace steelmaking dust by in-process separation of zinc from the dust. *J. Clean. Prod.* **112**, 4497–4504 (2016). doi: 10.1016/j.jclepro.2015.07.009.
41. Heinrich, T. Reducing zinc contamination in basic oxygen steelmaking dust. (Cardiff University, 2015).
42. Vereš, J., Šepelák, V. & Hredzák, S. Chemical, mineralogical and morphological characterisation of basic oxygen furnace dust. *Miner. Process. Extr. Metall.* **124**, 1–8 (2015). doi: 10.1179/1743285514Y.0000000069.
43. Hahn, I. & Neuschütz, D. Ejection of steel and slag droplets from gas stirred steel melts. *Ironmaking and Steelmaking* vol. 29 219–223 (2002). doi: 10.1179/030192302225004115.
44. Orbaek, A. & Barron, A. R. ICP-AES analysis of nanoparticles. in *Physical Methods in Chemistry and Nano Science* (2009).
45. Mikhail, S. a & Turcotte, A.-M. Thermal reduction of steel-making secondary materials. *Thermochim. Acta* **311**, 113–119 (1998). doi: 10.1016/S0040-6031(97)00430-9.
46. Steer, J. *et al.* Characterisation of BOS steelmaking dust and techniques for reducing zinc contamination. *Ironmaking & Steelmaking* vol. 41 61–66 (2014). doi: 10.1179/1743281213Y.0000000106.
47. Cantarino, M. V., De Carvalho Filho, C. & Borges Mansur, M. Selective removal of zinc from basic oxygen furnace sludges. *Hydrometallurgy* **111**–**112**, 124–128 (2012). doi: 10.1016/j.hydromet.2011.11.004.
48. BRAGG, W. H. The Structure of Magnetite and the Spinels. *Nature* **95**, 561–561 (1915). doi: 10.1038/095561a0.
49. Levy, D., Pavese, A. & Hanfland, M. Phase transition of synthetic zinc ferrite spinel (ZnFe2O4) at high pressure, from synchrotron X-ray powder diffraction. *Phys. Chem. Miner.* **27**, 638–644 (2000). doi: 10.1007/s002690000117.
50. Sammut, M. L. *et al.* Determination of zinc speciation in basic oxygen furnace flying dust by chemical extractions and X-ray spectroscopy. *Chemosphere* vol. 70 1945–1951 (2008). doi: 10.1016/j.chemosphere.2007.09.063.

51. Jaafar, I. *et al.* An evaluation of chlorination for the removal of zinc from steelmaking dusts. *Minerals Engineering* vol. 24 1028–1030 (2011). doi: 10.1016/j.mineng.2011.04.026.

52. Ray, S. K., Chattopadhyay, G. & Ray, A. K. Evaluation of Dust Generated from Basic Oxygen Furnace Steel Making. *J. Air Waste Manag. Assoc.* **47**, 716–721 (1997). doi: 10.1080/10473289.1997.10463929.

53. Krishnamurthy, K. R., Gopalakrishnan, J., Aravamudan, G. & Sastri, M. V. C. STUDIES ON THE FORMATION OF ZINC FERRITE. *J. inorg. nucl. Chem.* **36**, 569–573 (1974).

54. Liu, S. & Loper, C. R. The formation of kish graphite. *Carbon N. Y.* **29**, 547–555 (1991).

55. Salama, W., El Aref, M. & Gaupp, R. Spectroscopic characterization of iron ores formed in different geological environments using FTIR, XPS, Mössbauer spectroscopy and thermoanalyses. *Spectrochim. Acta - Part A Mol. Biomol. Spectrosc.* **136**, 1816–1826 (2015). doi: 10.1016/j.saa.2014.10.090.

56. Zboril, R., Mashlan, M. & Petridis, D. Iron(III) oxides from thermal processes-synthesis, structural and magnetic properties, Mössbauer spectroscopy characterization, and applications. *Chem. Mater.* **14**, 969–982 (2002). doi: 10.1021/cm0111074.

57. Kuzmann, E., Nagy, S. & Vértes, A. Critical review of analytical applications of Mössbauer spectroscopy illustrated by mineralogical and geological examples (IUPAC Technical Report). *Pure Appl. Chem.* **75**, (2003). doi: 10.1351/pac200375060801.

58. Rose, J. *et al.* Synthesis and characterization of carboxylate - FeOOH nanoparticles (ferroxanes) and ferroxane-derived ceramics. *Chem. Mater.* **14**, 621–628 (2002). doi: 10.1021/cm010583r.

59. Jha, M. K., Kumar, V. & Singh, R. J. Review of hydrometallurgical recovery of zinc from industrial wastes. *Resour. Conserv. Recycl.* **33**, 1–22 (2001). doi: 10.1016/S0921-3449(00)00095-1.

60. Hay, S. M. & Rankin, W. J. Recovery of iron and zinc from blast furnace and basic oxygen furnace dusts: A thermodynamic evaluation. *Miner. Eng.* **7**, 985–1001 (1994). doi: 10.1016/0892-6875(94)90028-0.

61. Lin, B. & Wang, X. Carbon emissions from energy intensive industry in China: Evidence from the iron & steel industry. *Renewable and Sustainable Energy Reviews* vol. 47 746–754 (2015). doi: 10.1016/j.rser.2015.03.056.

62. Gielen, D. & Moriguchi, Y. CO2 in the iron and steel industry: An analysis of Japanese emission reduction potentials. *Energy Policy* vol. 30 849–863 (2002). doi: 10.1016/S0301-4215(01)00143-4.

63. Lee, J., Lin, C. & Chen, H. Carbothermal Reduction of Zinc Ferrite. *Metall. Mater. Trans. B* **32**, 1033–1040 (2001).

64. Stephenson, R. L. & Smailer, R. M. *Direct Reduced Iron: Technology and economics of production and use*. (United States, 1980).

65. Anameric, B. & Kawatra, S. K. Properties and features of direct reduced iron. *Miner. Process. Extr. Metall. Rev.* **28**, 59–116 (2007). doi: 10.1080/08827500600835576.

66. Chatterjee, A. *Sponge Iron Production by Direct Reduction of Iron Oxide*. (2012).

67. Atsushi, M., Uemura, H. & Sakaguchi, T. MIDREX Processes. *Kobelco Technol. Rev.* **29**, 50–57 (2010).

68. Fruehan, R. J. New steelmaking processes: Drivers, requirements and potential impact. *Ironmak. Steelmak.* **32**, 3–8 (2005). doi: 10.1179/irs.2005.32.1.3.

69. Ahmed, H. New Trends in the Application of Carbon-Bearing materials in blast furnace iron-making. *Minerals* **8**, 1–20 (2018). doi: 10.3390/min8120561.

70. Porter, F. & International Lead Zinc Research Organization. *Zinc handbook : properties, processing, and use in design*. (1991).

71. Mager, K., Meurer, U. & Wirling, J. Minimizing Dioxin and Furan Emissions during Zinc Dust Recycle by the Waelz Process. *Jom* vol. 55 20–25 (2003). doi: 10.1007/s11837-003-0099-6.

72. Mager, K. *et al.* Recovery of Zinc Oxide from Secondary Raw Materials: New Developments of the Waelz Process. *Fourth Int. Symp. Recycl. Met. Eng. Mater.* 329–344 (2000).

73. Masson, N., Briol, P. & Zinc One Resources Inc. *A Brief Summary of Zinc Oxide Processing Methods Available for the Bongará Deposit*.

74. Lu, L., Pan, J. & Zhu, D. Chapter 16. Quality Requirements of Iron Ore for Iron Production. in *Iron Ore* (Elsevier, 2015).

75. Kobelco. Fastmet® Process. http://www.kobelco.co.jp/english/products/fastmet/.

76. Espinosa, D. C. R., Bernardes, A. M. & Tenório, J. A. S. An overview on the current processes for the recycling of batteries. *Journal of Power Sources* vol. 135 311–319 (2004). doi: 10.1016/j.jpowsour.2004.03.083.

77. Money, K. L., Hanewald, R. H. & Bleakney, R. R. Processing steel wastes pyrometallurgically at INMETCO. in *4th International Symposium on Recycling of Metals and Engineered Materials* 397–408 (2000). doi:10.1002/9781118788073.ch34. doi: 10.1002/9781118788073.ch34.

78. Hanewald, R. H., Munson, W. A. & Schweyer, D. L. Processing Steel Wastes Pyrometallurgically at INMETCO. *Mining, Metall. Explor.* **9**, 169–173 (1992).

79. Seetharaman, S. Chapter IV: Environmental Aspects and the Future of Process Metallurgy. in *Treatise on Process Metallurgy, Vol. 3: Industrial Processes* vol. 3 (Elsevier Ltd, 2013).

80. Rinker, F. G. Using the DRylron ™ process to produce value-added iron units. *Miner. Metall. Process.* **18**, 45–48 (2001).

81. Lehtinen, L. The Mesabi Nugget Project: New Iron Making Technology of the Future. *Direct from MIDREX Q2* 3–8 (2003).

82. Kikuchi, S. *et al.* ITmk3 process. *Kobelco Technol. Rev.* **29**, 69–77 (2010).

83. Zhang, Y. Y., Qi, Y. H., Zou, Z. S. & Li, Y. G. Development prospect of rotary hearth furnace process in China. *Adv. Mater. Res.* **746**, 533–538 (2013). doi: 10.4028/www.scientific.net/AMR.746.533.

84. MacKillop, F. The Construction of ‘Waste’ in the UK Steel Industry. *J. Environ. Plan. Manag.* **52**, 177–194 (2009). doi: 10.1080/09640560802666529.

85. Sawa, Y., Yamamoto, T., Takeda, K. & Itaya, H. New coal based process to produce high quality DRI for the EAF. *ISIJ Int.* **41**, 17–21 (2001).

86. Murao, A. *et al.* Hi-QIP, a new ironmaking process. in *Iron and Steel Technology* vol. 5 87–94 (2008).

87. Ishiwata, N. *et al.* Investigation of Reduction and Smelting Mechanism in the Hi-QIP Process. **80**, 523–529 (2009). doi: 10.2374/SRI09SP040.

88. Steffen, R. & Lüngen, H. B. Etat de l’art de la réduction directe et de la fusion-réduction de minerai de fer. *Rev. Metall. Cah. D’Informations Tech.* **101**, 171–182 (2004). doi: 10.1051/metal:2004131.

89. Holappa, L. E. & Kekkonen, M. *Comparison of Different Coal Based Direct Reduction Processes*. (2000).

90. Chatterjee, A. *Sponge Iron Production by Direct Reduction of Iron Oxide*. (PHI Private Learning Limited, 2012).

91. Zunkel, D. What to do with your EAF Dust. *Steel Times Int.* **20**, 46 (1996).

92. Schoukens, A. F. S., Abdel-Latif, M. A., Freeman, M. J. & Barcza, N, A. The Enviroplas Process for the Recovery of Zinc, Chromium and Nickel from Steel-

Plant Dust. in *Electric Furnace Conference Proceedings* 341–351 (1996).

93. Assis, G. *Emerging Pyrometallurgical Processes for Zinc and Lead Recovery from Zinc-Bearing Waste Materials*. (1998).
94. Southwick, L. M. Still No Simple Solution to Processing EAF dust. *Steel Times International* 43–45 (2010) doi:10.1109/TDEI.2009.5211872. doi: 10.1109/TDEI.2009.5211872.
95. Keegel, J. F. 5538532 Methods for recycling electric arc furnace dust. (1996) doi:10.1016/s0959-6526(97)88898-1. doi: 10.1016/s0959-6526(97)88898-1.
96. Meijer, K., Zeilstra, C., Teerhuis, C., Ouwehand, M. & Van Der Stel, J. Developments in alternative ironmaking. *Trans. Indian Inst. Met.* **66**, 475–481 (2013). doi: 10.1007/s12666-013-0309-z.
97. Dry, R. J., Bates, C. P. & Price, D. P. HIsmelt - the future in direct ironmaking. in *Proceedings of the 58th Ironmaking Conference* 361–366 (1999).
98. Peters, A. G. . Zinc vapourisation from sludge wastes under thermal processing conditions. (Delft University of Technology, 2019).
99. Morgan, S. W. K. & Greenwood, D. A. The metallurgical and economic behavior of lead in the imperial smelting furnace. *Jom* **20**, 31–35 (1968). doi: 10.1007/bf03378767.
100. Antuñano, N., Cambra, J. F. & Arias, P. L. Hydrometallurgical processes for Waelz oxide valorisation – An overview. *Process Saf. Environ. Prot.* **129**, 308–320 (2019). doi: 10.1016/j.psep.2019.06.028.
101. Wu, X., Liu, Z. & Liu, X. The effects of additives on the electrowinning of zinc from sulphate solutions with high fluoride concentration. *Hydrometallurgy* vol. 141 31–35 (2014). doi: 10.1016/j.hydromet.2013.09.007.
102. Díaz, G. & Martín, D. Modified Zincex process: the clean, safe and profitable solution to the zinc secondaries treatment. *Resour. Conserv. Recycl.* **10**, 43–57 (1994). doi: 10.1016/0921-3449(94)90037-X.
103. Nogueira, E. D. The Zinclor process: Simultaneous production of zinc and chlorine. in *Proceedings of the 13th Annual Hydrometallurgy Conference* 1–23 (1983).
104. Van Den Bekerom, D. *et al.* Non-equilibrium microwave plasma for efficient high temperature chemistry. *J. Vis. Exp.* **2017**, 1–11 (2017). doi: 10.3791/55066.
105. McQuaker, N. R., Brown, D. F. & Kluckner, P. D. Digestion of Environmental Materials for Analysis by Inductively Coupled Plasma-Atomic Emission

Spectrometry. *Anal. Chem.* **51**, 1082–1084 (1979). doi: 10.1021/ac50043a071.

106. Al-Harahsheh, M., Kingman, S., Somerfield, C. & Ababneh, F. Microwave-assisted total digestion of sulphide ores for multi-element analysis. *Anal. Chim. Acta* **638**, 101–105 (2009). doi: 10.1016/j.aca.2009.02.030.
107. Muse, L. A. Safety in the chemical laboratory: XCV. Safe handling of perchloric acid in the laboratory. *J. Chem. Educ.* **49**, 465–467 (1972). doi: 10.1021/ed049pa463.
108. Sastri, V. S. Determination of metallic iron in a mixture of lime, calcium sulphide and pyrrhotite. *Talanta* **25**, 702–704 (1978). doi: 10.1016/0039-9140(78)80178-7.
109. Morcali, M. H. Development of a method for determination of metallic iron content within hot briquette iron (HBI) for steelmaking. *J. Min. Metall. Sect. B Metall.* **52**, 151–155 (2016). doi: 10.2298/JMMB150606017M.
110. Sant, B. R. & Prasad, T. P. Determination of metallic iron, iron(II) oxide, and iron(III) oxide in a mixture. *Talanta* **15**, 1483–1486 (1968). doi: 10.1016/0039-9140(68)80211-5.
111. Beauchamp, I. L. & Tebbens, B. D. Mercury Vapor Hazards in the University Laboratories. *Am. Ind. Hyg. Assoc. Q.* **12**, 171–174 (1951). doi: 10.1080/00968205109343848.
112. Xu, Z. *et al.* Quantitative Determination of Metallic Iron Content in Steel-Making Slag. *J. Miner. Mater. Charact. Eng.* **02**, 65–70 (2003). doi: 10.4236/jmmce.2003.21006.
113. Beverskog, B. & Puigdomenech, I. Revised Pourbaix diagrams for iron at 25-300°C. *Corrosion Science* vol. 38 2121–2135 (1996). doi: 10.1016/S0010-938X(96)00067-4.
114. Halt, J. A., Nitz, M. C., Kawatra, S. K. & Dube, M. Iron Ore Pellet Dustiness Part I : Factors Affecting Dust Generation. *Miner. Process. Extr. Metall. Rev.* **36**, 258–266 (2015). doi: 10.1080/08827508.2014.928876.
115. Bagatini, M. C., Zymla, V., Osório, E., Cezar, A. & Vilela, F. Characterization and Reduction Behavior of Mill Scale. *ISIJ Int.* **51**, 1072–1079 (2011). doi: https://doi.org/10.2355/isijinternational.51.1072.
116. Nyridena, R. L. The Processing of Steelmaking Flue-Dust: A Review. *Miner. Eng.* **4**, 1003–1025 (1991). doi: https://doi.org/10.1016/0892-6875(91)90080-F.
117. Klut, P., Tesselaar, E., Barel, J., Engel, E. & Corus, D. Blast furnace zinc control. in *Millenium Steel 2016* 46–52 (2016).

118. Besta, P. *et al.* The cycle and effect of zinc in the blast-furnace process. *Metalurgija* vol. 52 197–200 (2013).
119. Onoye, T., Satoh, Y., Manabu, T. & Kamatani, K. S. Effects of Alkalis and Zinc on the Wear of the Blast Furnace Refractories and the Tuyere Displacement. *Trans. ISIJ* **21**, 839–845 (1981).
120. McClelland, J. M. & Metius, G. E. Recycling Ferrous and Nonferrous Waste Streams with FASTMET. *Jom* **55**, 30–34 (2003). doi: 10.1007/s11837-003-0101-3.
121. Ichikawa, H. & Morishige, H. Effective use of steelmaking dust and sludge by use of rotary hearth furnace. *Nippon Steel Technical Report* 35–38 (2002).
122. Dankwah, J. R., Amoah, T., Dankwah, J. & Fosu, A. Y. Recycling Mixed Plastics Waste as Reductant in Ironmaking *. *Ghana Min. J.* **15**, 73–80 (2015).
123. Yuan, P. *et al.* Study on the formation of direct reduced iron by using biomass as reductants of carbon containing pellets in RHF process. *Energy* **141**, 472–482 (2017). doi: 10.1016/j.energy.2017.09.058.
124. Mombelli, D., Di Cecca, C., Mapelli, C., Barella, S. & Bondi, E. Experimental analysis on the use of BF-sludge for the reduction of BOF-powders to direct reduced iron (DRI) production. *Process Saf. Environ. Prot.* **102**, 410–420 (2016). doi: 10.1016/j.psep.2016.04.017.
125. HM Revenue & Customs. Excise Notice LFT1. https://www.gov.uk/government/publications/excise-notice-lft1-a-general-guide-to-landfill-tax/excise-notice-lft1-a-general-guide-to-landfill-tax#mining-and-quarrying-material (2020).
126. ENDS Report. Scottish steel works leaves massive clean-up bill. *ENDS Report* (1992).
127. British Steel. The History of British Steel. https://britishsteel.co.uk/media/323481/history-of-british-steel.pdf.
128. Rhodes, C. *UK steel industry : statistics and policy*. (2018).
129. Trung, Z. H. *et al.* Acidic leaching both of zinc and iron from basic oxygen furnace sludge. *J. Hazard. Mater.* **192**, 1100–1107 (2011). doi: 10.1016/j.jhazmat.2011.06.016.
130. Ruíz-Baltazar, A., Esparza, R., Rosas, G. & Pérez, R. Effect of the Surfactant on the Growth and Oxidation of Iron Nanoparticles. *Journal of Nanomaterials* vol. 2015 (2015). doi: 10.1155/2015/240948.

131. Zhang, Y. & Xu, X. Machine learning lattice constants for spinel compounds. *Chemical Physics Letters* vol. 760 (2020). doi: 10.1016/j.cplett.2020.137993.

132. Yang, Y. *et al.* Synthesis of nonstoichiometric zinc ferrite nanoparticles with extraordinary room temperature magnetism and their diverse applications. *J. Mater. Chem. C* **1**, 2875–2885 (2013). doi: 10.1039/c3tc00790a.

133. Kmita, A. *et al.* Effect of Thermal Treatment at Inert Atmosphere on Structural and Magnetic Properties of Non-stoichiometric Zinc Ferrite Nanoparticles. *Metall. Mater. Trans. A Phys. Metall. Mater. Sci.* **52**, 1632–1648 (2021). doi: 10.1007/s11661-021-06154-3.

134. Souza, F. De & Braganc, S. R. Thermogravimetric analysis of limestones with different contents of MgO and microstructural characterization in oxy-combustion. *Thermochim. Acta* **561**, 19–25 (2013).

135. Zhang, W. *et al.* Experimental study on the thermal volatilization and condensation of zinc at 10 Pa and 200 Pa. *J Mater Res Technol.* **9**, 3590–3597 (2020). doi: https://doi.org/10.1016/j.jmrt.2020.01.097.

136. DONALD, J. & PICKLES, C. Reduction of electric arc furnace dust with solid iron powder. *Canadian Metallurgical Quarterly* vol. 35 255–267 (1996). doi: 10.1016/0008-4433(96)00009-2.

137. Pickles, C. A. Thermodynamic analysis of the separation of zinc and lead from electric arc furnace dust by selective reduction with metallic iron. *Sep. Purif. Technol.* **59**, 115–128 (2008). doi: 10.1016/j.seppur.2007.05.032.

138. Lysenko, E. N. *et al.* The oxidation kinetics study of ultrafine iron powders by thermogravimetric analysis. *J Therm Anal Calorim* **115**, 1447–1452 (2014). doi: 10.1007/s10973-013-3456-x.

139. Trinkel, V., Mallow, O., Aschenbrenner, P., Rechberger, H. & Fellner, J. Characterization of Blast Furnace Sludge with Respect to Heavy Metal Distribution. *Ind. Eng. Chem. Res.* **55**, 5590–5597 (2016). doi: 10.1021/acs.iecr.6b00617.

140. Narita, C. Y., Mourao, M. B. & Takano, C. Development of composite briquettes of iron ore and coal hardened by heat treatment. *Ironmak. Steelmak.* **42**, 548–552 (2015). doi: 10.1179/1743281214Y.0000000260.

141. Kuwauchi, Y. & Barati, M. A mathematical model for carbothermic reduction of dust-carbon composite agglomerates. *ISIJ Int.* **53**, 1097–1105 (2013). doi: 10.2355/isijinternational.53.1097.

142. Vereš, J., Jakabský, Š. & Šepelák, V. Chemical, physical, morphological and

structural characterization of blast furnace sludge. *Diffus. Fundam.* **12**, 88–91 (2010).

143. Jabłońska, M. *et al.* Mineralogical and chemical specificity of dusts originating from iron and non-ferrous metallurgy in the light of their magnetic susceptibility. *Minerals* **11**, 1–20 (2021). doi: 10.3390/min11020216.
144. Stevens, J. G., Khasanov, A. M., Miller, J. W., Pollak, H. & Li, Z. *Mössbauer Mineral Handbook.* (Mössbauer Effect Data Center, 2005).
145. Vicente, A., Picon, A. & Barco, E. New method for estimating the economic penalties of ferrous scraps in the steelmaking industry due to material degradation during its storage in scrap yards. *Ironmak. Steelmak.* **47**, 473–481 (2020). doi: 10.1080/03019233.2020.1748433.
146. Inaba, S. & Kimura, Y. Behavior of sulfur in the carbon-bearing iron oxide pellet during heating. *ISIJ Int.* **44**, 2112–2114 (2004). doi: 10.2355/isijinternational.44.2112.
147. She, X. . F., Wang, J. S., Wang, G., Xue, Q. G. & ZHang, X. X. Removal Mechanism of Zn, Pb and Alkalis from Metallurgical Dusts in Direct Reduction Process. *J. Iron Steel Res. Int.* **21**, 488–495 (2011).
148. El-Hussiny, N. A. & Shalabi, M. E. H. A self-reduced intermediate product from iron and steel plants waste materials using a briquetting process. *Powder Technol.* **205**, 217–223 (2011). doi: 10.1016/j.powtec.2010.09.017.
149. Dey, K. & Jana, B. Coal Mixed Pellets under Nitrogen Gas Atmosphere. **33**, 735–739 (1993).
150. Nikai, I. & Garbers-Craig, A. M. Use of Iron Ore Fines in Cold-Bonded Self-Reducing Composite Pellets. *Miner. Process. Extr. Metall. Rev.* **37**, 42–48 (2016). doi: 10.1080/08827508.2015.1104506.
151. Bagatini, M. C., Zymla, V., Osório, E. & Vilela, A. C. F. Carbon gasification in self-reducing mixtures. *ISIJ Int.* **54**, 2687–2696 (2014). doi: 10.2355/isijinternational.54.2687.
152. Ahmed, H. M., Persson, A., Sundqvist, L. & Bjorkman, B. Utilization of Steelmaking Industry Waste Materials in Producing Direct Reduced Iron. in *European Steel Environment & Energy Congress (ESEC)* (2014).
153. Lu, W. K. & Huang, D. F. Mechanisms of reduction of iron ore/coal agglomerates and scientific issues in RHF operations. *Miner. Process. Extr. Metall. Rev.* **24**, 293–324 (2003). doi: 10.1080/714856826.

154. Tsutsumi, H., Yoshida, S. & Tetsumoto, M. Features of FASTMET Process. *Kobelco Technol. Rev.* **29**, 85–92 (2010).

155. Rodebush, W. H. & Dixon, A. L. The vapor pressures of metals; A new experimental method. *Phys. Rev.* **26**, 851–858 (1925). doi: 10.1103/PhysRev.26.851.

156. Huitu, K., Helle, H., Helle, M., Kekkonen, M. & Saxén, H. Optimization of steelmaking using fastmet direct reduced iron in the blast furnace. *ISIJ Int.* **53**, 2038–2046 (2013). doi: 10.2355/isijinternational.53.2038.

157. Gudenau, H. W., Senk, D., Wang, S., De Melo Martins, K. & Stephany, C. Research in the reduction of iron ore agglomerates including coal and C-containing dust. *ISIJ Int.* **45**, 603–608 (2005). doi: 10.2355/isijinternational.45.603.

158. Liang, S., Liang, X. & Tang, Q. Treatment of secondary dust produced in rotary hearth furnace through alkali leaching and evaporation-crystallization processes. *Processes* **8**, 1–15 (2020). doi: 10.3390/PR8040396.

159. Zhu, J. *et al.* An assessment of metal recycling worker lead exposure associated with cutting uncoated new steel scrap. *J. Occup. Environ. Hyg.* **6**, D18–D21 (2009). doi: 10.1080/15459620902810117.

160. Tzouganatos, N., Dell'Amico, M., Wieckert, C., Hinkley, J. & Steinfeld, A. On the development of a zinc vapor condensation process for the solar carbothermal reduction of zinc oxide. *Jom* vol. 67 1096–1109 (2015). doi: 10.1007/s11837-015-1356-1.

161. Cox, A. & Fray, D. J. Zinc reoxidation in the shaft of a zinc-lead imperial smelting furnace - 1: zinc-carbon-oxygen system with deposition initiated on a quartz substrate and subsequent propagation on zinc oxide. *Trans. Institutions Min. Metall. Sect. C Miner. Process. Extr. Metall.* **109**, C97–C104 (2000). doi: 10.1179/mpm.2000.109.2.97.

162. Raghavan, V. Al-Fe-O (Aluminum-iron-oxygen). *J. Phase Equilibria Diffus.* **31**, 367 (2010). doi: 10.1007/s11669-010-9712-x.

163. Zhang, J., Zhang, Y., Wang, H. & Meng, M. Effect of SiC on the oxidation resistance of graphite crucible for aluminium melting. *Spec. Cast. Nonferrous Alloy.* (2012).

164. Bagaikov, Y. S., Krukmaleva, G. P. & Kulakova, L. D. Clay-graphite refractory crucibles containing variable amounts of silicon carbide. *Refractories* **32**, 87–89 (1991). doi: doi.org/10.1007/BF01295636.

165. Memoli, F. Behavior and benefits of high-Fe3C DRI in the EAF. in *AISTech - Iron and Steel Technology Conference Proceedings* 1928–1945 (2015).

166. Lee, Y. S., Ri, D. W., Yi, S. H. & Sohn, I. Relationship between the reduction degree and strength of DRI pellets produced from iron and carbon bearing wastes using an RHF simulator. *ISIJ Int.* **52**, 1454–1462 (2012). doi: 10.2355/isijinternational.52.1454.

167. Schrama, F. N. H., Beunder, E. M., Van den Berg, B., Yang, Y. & Boom, R. Sulfur removal in ironmaking and oxygen steelmaking. *Ironmak. Steelmak.* **44**, 333–343 (2017). doi: 10.1080/03019233.2017.1303914.

168. Shishin, D., Jak, E. & Decterov, S. A. Critical Assessment and Thermodynamic Modeling of the Fe-O-S System. *J. Phase Equilibria Diffus.* **36**, 224–240 (2015). doi: 10.1007/s11669-015-0376-4.

169. Michishita, H. & Tanaka, H. Prospects for Coal-based Direct Reduction Process. *Kobelco Technol. Rev.* **29**, 69–76 (2010).

170. Coetsee, T., Pistorius, P. C. & De Villiers, E. E. Rate-determining steps for reduction in magnetite-coal pellets. *Miner. Eng.* **15**, 919–929 (2002). doi: 10.1016/S0892-6875(02)00120-6.

171. Moon, J. Kinetics of the self-reduction reactions occurring within fine iron oxide and carbon mixtures . (University of New South Wales, 2002).

172. Xia, L. *et al.* Reduction process and zinc removal from composite briquettes composed of dust and sludge from a steel enterprise. **22**, 122–131 (2015). doi: 10.1007/s12613-015-1052-8.

173. Peng, C., Zhang, F., Huifang, L. I. & Guo, Z. Removal behavior of Zn, Pb, K and Na from cold bonded briquettes of metallurgical dust in simulated RHF. *ISIJ Int.* **49**, 1874–1881 (2009). doi: 10.2355/isijinternational.49.1874.

174. Geerdes, M. *et al.* Standards for alkali input in blast furnaces 1. in *6th International Congress on the Science and Technology of Ironmaking* 788–797 (2012).

175. Eze, E. O. & Iyeke, S. D. Field Characteristics and other Properties of a Fireclay. *Global Journal of Engineering Research* vol. 10 27–34 (2011).

176. Li, Z., Ma, G., Liu, M. & Zou, J. Calculation model for activity of FeO in quaternary slag system SiO2-CaO-Al2 O3-FeO. *Metals* vol. 8 (2018). doi: 10.3390/met8090714.

177. Song, J., Liu, Y., Lv, X. & You, Z. Corrosion behavior of Al2O3 substrate by

SiO2-MgO-FeO-CaO-Al2O3 slag. *Journal of Materials Research and Technology* vol. 9 314–321 (2020). doi: 10.1016/j.jmrt.2019.10.060.

178. Yoo, J. M., Kim, B. S., Lee, J. C., Kim, M. S. & Nam, C. W. Kinetics of the volatilization removal of lead in electric arc furnace dust. *Mater. Trans.* **46**, 323–328 (2005). doi: 10.2320/matertrans.46.323.
179. Mustafa, S., Luo, L., Zheng, B. T., Wei, C. X. & Christophe, N. Effect of lead and zinc impurities in ironmaking and the corresponding removal methods: A review. *Metals (Basel).* **11**, 1–19 (2021). doi: 10.3390/met11030407.
180. Houot, R. Beneficiation of iron ore by flotation - Review of industrial and potential applications. *Int. J. Miner. Process.* **10**, 183–204 (1983). doi: 10.1016/0301-7516(83)90010-8.
181. Wang, G. *et al.* Strength and high temperature behaviour of carbon composite pellets containing BOF fine dust Strength and high temperature behaviour of carbon composite pellets containing BOF fine dust. **9233**, (2014). doi: 10.1179/1743281213Y.0000000171.
182. Shornikov, S. I. & Shornikova, M. S. Thermodynamic Properties of the CaO-FeO Melts. *Exp. Geosci.* **25**, 82–85 (2019).
183. Das, S., Dutta, K. & Pramanik, A. Morphology control of ZnO with citrate: A time and concentration dependent mechanistic insight. *CrystEngComm* **15**, 6349–6358 (2013). doi: 10.1039/c3ce40822a.
184. Jiang, X., Wang, L. & Shen, F. M. Shaft furnace direct reduction technology --- Midrex and Energiron. *Adv. Mater. Res.* **805**–**806**, 654–659 (2013). doi: 10.4028/www.scientific.net/AMR.805-806.654.
185. Satish Kumar, D., Prasad, G., Ghorui, P. K. & Ranjan, M. Coolant strategies for BOF steelmaking. *Ironmak. Steelmak.* **35**, 539–544 (2008). doi: 10.1179/174328108X335159.
186. Hornby, S. & Brooks, G. Impact of Hydrogen DRI on EAF Steelmaking. *Direct from MIDREX Q2* 3–11 (2021).
187. Barisetty, S., Kalshetty, S., Ramakrishna, S., Vishwanath, S. C. & Balachandran, G. Cold Briquetting of DRI Fines for Use in Steel Making Process. *Trans. Indian Inst. Met.* **73**, 449–455 (2019). doi: 10.1007/s12666-019-01856-0.
188. Stewart, D. J. C., Thomson, D. & Barron, A. R. The production of high value pig iron nuggets from steelmaking by-products – A thermodynamic evaluation. *Resour. , Conserv. Recycl.* **170**, 105592 (2021). doi: https://doi.org/10.1016/j.resconrec.2021.105592.

189. Yellishetty, M., Mudd, G. M., Ranjith, P. G. & Tharumarajah, A. Environmental life-cycle comparisons of steel production and recycling: Sustainability issues, problems and prospects. *Environ. Sci. Policy* **14**, 650–663 (2011). doi: 10.1016/j.envsci.2011.04.008.

190. Pehlke, R. D. & Fuwa, T. Control of sulfur in liquid iron and steel. *Int. Met. Rev.* **30**, 125–140 (1985). doi: https://doi.org/10.1179/imtr.1985.30.1.125.

191. Kobe Steel ltd. World's first commercial ITmk3 plant successfully begins production. http://www.kobelco.co.jp/english/releases/2010/1182907_14776.html (2010).

192. Simmons, J. E-Iron Nugget Process. in *CIM Montreal* (Canadian Institute of Mining, Metallurgy and Petroleum, 2015).

193. Birol, B. Investigating the utilization of blast furnace flue dusts and mill scale as raw materials in iron nugget production. *Mater. Res. Express* **6**, 1–8 (2019). doi: https://doi.org/10.1088/2053-1591/ab243b.

194. Wang, W. *et al.* Producing iron nuggets with steel making wastes. in *2010 4th International Conference on Bioinformatics and Biomedical Engineering, iCBBE 2010* 1–4 (2010). doi:10.1109/ICBBE.2010.5518019. doi: 10.1109/ICBBE.2010.5518019.

195. Zhao, D. N., Xue, Z. L., Wang, W., Li, Y. S. & Song, S. Q. Process analysis of Pb and Zn during producing iron nuggets by iron bearing dust. in *Advanced Materials Research* vol. 402 173–178 (2012). doi: 10.4028/www.scientific.net/AMR.402.173.

196. Seetharaman, S. Chapter 4.5 - Future of Process Metallurgy. in *Treatise on Process Metallurgy, Vol. 3: Industrial Processes* vol. 3 1563–1726 (2014). doi: 10.1016/B978-0-08-096988-6.00037-7.

197. Longbottom, R., Monaghan, B. J., Zhang, G., Chew, S. & Pinson, D. J. Characterization of Steelplant By-Products to Realise the Value of Fe and Zn. 1017–1026 (2016).

198. Srivastava, U. Sustainable Iron Making Process. (2014).

199. Geerdes, M., Chaigneau, R., Kurunov, I., Lingiardi, O. & Ricketts, J. *Modern Blast Furnace Ironmaking: An Introduction*. (IOS PRESS, 2015).

200. Feild, A. The Viscosity of Blast-Furnace Slag and its Relation to Iron Metallurgy, Including a Description of a New Method of Measuring Slag Viscosity at High Temperatures. *Trans. Faraday Soc.* **13**, 3–35 (1917). doi:

https://doi.org/10.1039/TF9171300003.

201. Zeydabadi, B. A., Mowla, D., Shariat, M. H. & Kalajahi, J. F. Zinc recovery from blast furnace flue dust. *Hydrometallurgy* **47**, 113–125 (1997). doi: https://doi.org/10.1016/S0304-386X(97)00039-X.

202. Zheng, Y. X., Lv, J. F., Wang, H., Wen, S. M. & Pang, J. Formation of zinc sulfide species during roasting of ZnO with pyrite and its contribution on flotation. *Sci. Rep.* **8**, 1–10 (2018).

203. Han, H., Duan, D., Chen, S. & Yuan, P. Mechanism and Influencing Factors of Iron Nuggets Forming in Rotary Hearth Furnace Process at Lower Temperature. *Metall. Mater. Trans. B Process Metall. Mater. Process. Sci.* **46**, 2208–2217 (2015). doi: 10.1007/s11663-015-0420-0.

204. Mombelli, D., Mapelli, C., Barella, S., Gruttadauria, A. & Spada, E. Jarosite wastes reduction through blast furnace sludges for cast iron production. *J. Environ. Chem. Eng.* **7**, (2019). doi: 10.1016/j.jece.2019.102966.

205. Anameric, B., Rundman, K. B. & Kawatra, S. K. Carburization effects on pig iron nugget making. *Miner. Metall. Process. 139* **23**, 139–150 (2006).

206. Archambo, M. S. & Kawatra, S. K. Utilization of Bauxite Residue: Recovering Iron Values Using the Iron Nugget Process. *Miner. Process. Extr. Metall. Rev.* **7508**, (2020). doi: 10.1080/08827508.2020.1720982.

207. Wei, G., Zhu, R., Tang, T. & Dong, K. Study on the melting characteristics of steel scrap in molten steel. *Ironmak. Steelmak.* **46**, 609–617 (2019). doi: 10.1080/03019233.2019.1609738.

208. Sosinsky, D. J. & Sommerville, I. D. The composition and temperature dependence of the sulfide capacity of metallurgical slags. *Metall. Trans. B* **17**, 331–337 (1986). doi: 10.1007/BF02655080.

209. Taniguchi, Y., Wang, L., Sano, N. & Seetharaman, S. Sulfide Capacities of CaO-Al 2O 3-SiO 2 Slags in the Temperature Range 1673 K to 1773 K (1400 °C to 1500 °C). *Metall. Mater. Trans. B Process Metall. Mater. Process. Sci.* **43**, 477–484 (2012). doi: 10.1007/s11663-011-9621-3.

210. Bennett, J. & Kwong, K. S. Thermodynamic studies of MgO saturated EAF slag. *Ironmak. Steelmak.* **37**, 529–535 (2010). doi: 10.1179/030192310X12706364542669.

211. Song, S., Zhao, J. & Pistorius, C. P. MgO Refractory Attack by Transient Non-saturated Slag. *Metall. Mater. Trans. B* **51**, 891–897 (2020). doi: https://doi.org/10.1007/s11663-020-01788-x.

212. Beggs, D. Furnace Hearth. (1969).

213. Durinck, D. *et al.* Slag solidification modeling using the Scheil-Gulliver assumptions. *J. Am. Ceram. Soc.* **90**, 1177–1185 (2007). doi: 10.1111/j.1551-2916.2007.01597.x.

214. Mombelli, D. *et al.* The effect of microstructure on the leaching behaviour of electric arc furnace (EAF) carbon steel slag. *Process Saf. Environ. Prot.* **102**, 810–821 (2016). doi: 10.1016/j.psep.2016.05.027.

215. Strandkvist, I. *et al.* Minimizing chromium leaching from low-alloy electric arc furnace (EAF) slag by adjusting the basicity and cooling rate to control brownmillerite formation. *Appl. Sci.* **10**, (2020). doi: 10.3390/app10010035.

216. Mager, K. *et al.* Recovery of zinc oxide from secondary raw materials: New developments of the Waelz process. *Proc. TMS Fall Extr. Process. Conf.* **4th Intern**, 329–344 (2000). doi: 10.1002/9781118788073.ch29.

217. Yao, Z. T. *et al.* A comprehensive review on the applications of coal fly ash. *Earth-Science Rev.* **141**, 105–121 (2015). doi: https://doi.org/10.1016/j.earscirev.2014.11.016.

218. Srivastava, V. C., Mall, I. D. & Mishra, I. M. Characterization of mesoporous rice husk ash (RHA) and adsorption kinetics of metal ions from aqueous solution onto RHA. *J Hazard Mater.* **134**, 257–267 (2006). doi: 10.1016/j.jhazmat.2005.11.052.

219. Horckmans, L., Nielsen, P., Dierckx, P. & Ducastel, A. Recycling of refractory bricks used in basic steelmaking: A review. *Resources, Conservation and Recycling* vol. 140 297–304 (2019). doi: 10.1016/j.resconrec.2018.09.025.

220. Sieber, J. R. Matrix-Independent XRF Methods for Certification of Standard Reference Materials. in *Advances in X-ray analysis* vol. 45 493–504 (2002).

221. Zhou, Z., Zhou, K., Hou, X. & Luo, H. Arc/spark optical emission spectrometry: Principles, instrumentation, and recent applications. *Appl. Spectrosc. Rev.* **40**, 165–185 (2005). doi: 10.1081/ASR-200052001.

222. Zinngrebe, E., Hoek, C. Van, Visser, H., Westendorp, A. & Jung, I. H. Inclusion population evolution in ti-alloyed al-killed steel during secondary steelmaking process. *ISIJ Int.* **52**, 52–61 (2012). doi: 10.2355/isijinternational.52.52.

223. Kirschen, M., Hay, T. & Echterhof, T. Process Improvements for Direct Reduced Iron Melting in the Electric Arc Furnace with Emphasis on Slag Operation. *Processes* **9**, (2021). doi: 10.3390/pr9020402.

224. Klimczyk, A., Bernasowski, M., Stachura, R. & Ledzki, A. Reduction of silicon in blast furnace. *Met. 2014 - 23rd Int. Conf. Metall. Mater. Conf. Proc.* 159–164 (2014).

225. Li, Q. *et al.* Influence of Sn and Nb additions on the microstructure and wear characteristics of a gray cast iron. *Appl. Phys. A Mater. Sci. Process.* **126**, 1–8 (2020). doi: 10.1007/s00339-020-03468-8.

226. Matsumiya, T. Steel research and development in the aspect for a sustainable society. *Scand. J. Metall.* **34**, 256–267 (2005). doi: 10.1111/j.1600-0692.2005.00746.x.

227. Bandopadhyay, A., Ganguly, A., Gupta, K. N. & Ray, H. S. Investigations on the anomalous oxidation behaviour of high-carbon gas-based direct reduced iron (DRI). *Thermochim. Acta* **276**, 199–207 (1996). doi: 10.1016/0040-6031(95)02738-6.

228. Kaushik, P. & Fruehan, R. J. Behavior of direct reduced iron and hot briquetted iron in the upper blast furnace shaft: Part I. Fundamentals of kinetics and mechanism of oxidation. *Metall. Mater. Trans. B Process Metall. Mater. Process. Sci.* **37**, 715–725 (2006). doi: 10.1007/s11663-006-0055-2.

229. Sammt, F. L. & Hunter, R. L. Handling & shipping of DRI/HBI - Will it burn? *Steel Times Int.* **24**, 42–43 (2000).

230. Fisher, A., Llnl, C. W., Zhou, C., Silaen, A. & Civs, H. M. Utilizing simulations to guide furnace designs for the E-Iron ™ Nugget process. in *HPC4Mfg Industry Day* (2017). doi:10.13140/RG.2.2.35443.73764. doi: 10.13140/RG.2.2.35443.73764.

231. Lyu, W. & Wehby, G. L. Community use of face masks and COVID-19: Evidence from a natural experiment of state mandates in the US. *Health Aff.* **39**, 1419–1425 (2020). doi: 10.1377/hlthaff.2020.00818.

232. Panovska-Griffiths, J. *et al.* Modelling the potential impact of mask use in schools and society on COVID-19 control in the UK. *Sci. Rep.* **11**, 1–12 (2021). doi: 10.1038/s41598-021-88075-0.

233. UK Department of Health & Social Care. Face Coverings: When to Wear One, Exemptions, and how to make your own. https://www.gov.uk/government/publications/face-coverings-when-to-wear-one-and-how-to-make-your-own/face-coverings-when-to-wear-one-and-how-to-make-your-own (2020).

234. North London Waste Authority. 102 Million Disposible Facemasks Thrown

Away in the UK Each Week Would Cover Wembley Pitch 232 Times Over. https://www.nlwa.gov.uk/news/102-million-disposable-facemasks-thrown-away-uk-each-week-would-cover-wembley-pitch-232-times (2020).

235. Wang, M. W. *et al.* Mask crisis during the COVID-19 outbreak. *Eur. Rev. Med. Pharmacol. Sci.* **24**, 3397–3399 (2020). doi: 10.26355/eurrev_202003_20707.

236. Ragazzi, M., Rada, E. C. & Schiavon, M. Municipal solid waste management during the SARS-COV-2 outbreak and lockdown ease: Lessons from Italy. *Science of the Total Environment* vol. 745 1–6 (2020). doi: 10.1016/j.scitotenv.2020.141159.

237. Adyel, T. M. Accumulation of plastic waste during COVID-19. *Science (80-.).* **369**, 1314–1315 (2020). doi: 10.1126/SCIENCE.ABD9925.

238. Fadare, O. O. & Okoffo, E. D. Covid-19 face masks: A potential source of microplastic fibers in the environment. *Sci. Total Environ.* **140279**, 1–4 (2020). doi: 10.1016/j.scitotenv.2020.140279.

239. Torres, F. G. & De-la-Torre, G. E. Face mask waste generation and management during the COVID-19 pandemic: An overview and the Peruvian case. *Sci. Total Environ.* **147628**, 1–11 (2021). doi: 10.1016/j.scitotenv.2021.147628.

240. Jung, S., Lee, S., Dou, X. & Kwon, E. E. Valorization of disposable COVID-19 mask through the thermo-chemical process. *Chem. Eng. J.* **405**, 126658 (2021). doi: 10.1016/j.cej.2020.126658.

241. Anuar Sharuddin, S. D., Abnisa, F., Wan Daud, W. M. A. & Aroua, M. K. A review on pyrolysis of plastic wastes. *Energy Conversion and Management* vol. 115 308–326 (2016). doi: 10.1016/j.enconman.2016.02.037.

242. Sekine, Y., Fukuda, K., Kato, K., Adachi, Y. & Matsuno, Y. CO2 reduction potentials by utilizing waste plastics in steel works. *Int. J. Life Cycle Assess.* **14**, 122–136 (2009). doi: 10.1007/s11367-008-0055-3.

243. Babich, A., Senk, D., Knepper, M. & Benkert, S. Conversion of injected waste plastics in blast furnace. *Ironmak. Steelmak.* **43**, 11–21 (2016). doi: 10.1179/1743281215Y.0000000042.

244. Stewart, D. J. C. & Barron, A. R. Pyrometallurgical removal of zinc from basic oxygen steelmaking dust – A review of best available technology. *Resour. Conserv. Recycl.* **157**, 104746 (2020). doi: 10.1016/j.resconrec.2020.104746.

245. Fortini, O. M. & Fruehan, R. J. Rate of reduction of ore-carbon composites: Part II. Modeling of reduction in extended composites. *Metall. Mater. Trans. B*

Process Metall. Mater. Process. Sci. **36**, 709–717 (2005). doi: 10.1007/s11663-005-0074-4.

246. Murakami, T. & Kasai, E. Reduction mechanism of iron oxide-carbon composite with polyethylene at lower temperature. *ISIJ Int.* **51**, 9–13 (2011). doi: 10.2355/isijinternational.51.9.
247. Andreoli, E., Cullum, L. & Barron, A. R. Carbon dioxide absorption by polyethylenimine-functionalized nanocarbons: A kinetic study. *Ind. Eng. Chem. Res.* **54**, 878–889 (2015). doi: 10.1021/ie504277s.
248. Donahue, C. J. & Rais, E. A. Proximate analysis of coal. *J. Chem. Educ.* **86**, 222–224 (2009). doi: 10.1021/ed086p222.
249. Aragaw, T. A. Surgical face masks as a potential source for microplastic pollution in the COVID-19 scenario. *Mar. Pollut. Bull.* **159**, 111517 (2020). doi: 10.1016/j.marpolbul.2020.111517.
250. Wang, G., Wang, J. & Xue, Q. Efficient utilization of waste plastics as raw material for metallic iron and syngas production by combining heat treatment pulverization and direct reduction. *Process Saf. Environ. Prot.* **137**, 49–57 (2020). doi: 10.1016/j.psep.2020.02.017.
251. Wang, Y. & Wang, J. J. Shear yield behavior of calcium carbonate-filled polypropylene. *Polym. Eng. Sci.* **39**, 190–198 (1999). doi: 10.1002/pen.11407.
252. Samsudin, M. S. F., Ishak, Z. A. M., Jikan, S. S., Ariff, Z. M. & Ariffin, A. Effect of filler treatments on rheological behavior of calcium carbonate and talc-filled polypropylene hybrid composites. *J. Appl. Polym. Sci.* **102**, 5421–5426 (2006). doi: 10.1002/app.25054.
253. Eisele, T. C. & Kawatra, S. K. A review of binders in iron ore pelletization. *Miner. Process. Extr. Metall. Rev.* **24**, 1–90 (2003). doi: 10.1080/08827500306896.
254. Yousef, S., Eimontas, J., Striūgas, N. & Abdelnaby, M. A. Pyrolysis kinetic behaviour and TG-FTIR-GC–MS analysis of Coronavirus Face Masks. *J. Anal. Appl. Pyrolysis* **156**, (2021). doi: 10.1016/j.jaap.2021.105118.
255. Friedman, H. L. Kinetics of thermal degradation of char-forming plastics from thermogravimetry. Application to a phenolic plastic. *J. Polym. Sci. Part C Polym. Symp.* **6**, 183–195 (2007). doi: 10.1002/polc.5070060121.
256. Flynn, J. H. & Wall, L. A. General Treatment of the Thermogravimetry of Polymers. *J Res Natl Bur Stand A Phys Chem* **70A**, 487–523 (1966). doi: 10.6028/jres.070A.043.

257. Ozawa, T. A New Method of Analyzing Thermogravimetric Data. *Bull. Chem. Soc. Jpn.* **38**, 1881–1886 (1965). doi: 10.1246/bcsj.38.1881.

258. Kissinger, H. E. Reaction Kinetics in Differential Thermal Analysis. *Anal. Chem.* **29**, 1702–1706 (1957). doi: 10.1021/ac60131a045.

259. Fidalgo, B. *et al.* Non-isothermal thermogravimetric kinetic analysis of the thermochemical conversion of human faeces. *Renew. Energy* **132**, 1177–1184 (2019). doi: 10.1016/j.renene.2018.08.090.

260. Heydari, M., Rahman, M. & Gupta, R. Kinetic study and thermal decomposition behavior of lignite coal. *Int. J. Chem. Eng.* **2015**, (2015). doi: 10.1155/2015/481739.

261. Dai, B. *et al.* Kinetic analysis of CO2gasification of biochar and anthracite based on integral isoconversional nonlinear method. *High Temp. Mater. Process.* **39**, 527–538 (2020). doi: 10.1515/htmp-2020-0086.

262. Das, T., Saikia, A., Mahanta, B., Choudhury, R. & Saikia, B. K. Thermogravimetric and model-free kinetic studies on CO2 gasification of low-quality, high-sulfur Indian coals. *J. Earth Syst. Sci.* **125**, 1365–1377 (2016). doi: 10.1007/s12040-016-0743-5.

263. Nie, B., Liu, X., Yang, L., Meng, J. & Li, X. Pore structure characterization of different rank coals using gas adsorption and scanning electron microscopy. *Fuel* **158**, 908–917 (2015). doi: 10.1016/j.fuel.2015.06.050.

264. Sexton, D. C., Steer, J. M., Marsh, R. & Greenslade, M. Investigating char agglomeration in blast furnace coal injection. *Fuel Process. Technol.* **178**, 24–34 (2018). doi: 10.1016/j.fuproc.2018.05.013.

265. Quyn, D. M., Hayashi, J. I. & Li, C. Z. Volatilisation of alkali and alkaline earth metallic species during the gasification of a Victorian brown coal in CO2. *Fuel Process. Technol.* **86**, 1241–1251 (2005). doi: 10.1016/j.fuproc.2004.08.008.

266. Ubando, A. T., Chen, W. H. & Ong, H. C. Iron oxide reduction by graphite and torrefied biomass analyzed by TG-FTIR for mitigating CO2 emissions. *Energy* vol. 180 968–977 (2019). doi: 10.1016/j.energy.2019.05.149.

267. Willms, T. *et al.* Investigation on the chemical and thermal behavior of recycling agglomerates from EAF by-products. *Appl. Sci.* **10**, 1–14 (2020). doi: 10.3390/app10228309.

268. Majumder, A. Fe2O3-based Oxygen Carriers for Gaseous and Solid-Fueled Chemical Looping Processes. (The Ohio State University, 2016).

269. Tsuchiya, Y. & Sumi, K. Thermal decomposition products of Polypropylene. *J. Polym. Sci.* **7**, 1599–1607 (1969). doi: https://doi.org/10.1002/pol.1969.150070704.

270. Chen, Z. yuan *et al.* Prediction of density and volume variation of hematite ore particles during in-flight melting and reduction. *J. Iron Steel Res. Int.* **26**, 1285–1294 (2019). doi: 10.1007/s42243-019-00265-3.

271. Manoj, B. A comprehensive analysis of various structural parameters of Indian coals with the aid of advanced analytical tools. *Int. J. Coal Sci. Technol.* **3**, 123–132 (2016). doi: 10.1007/s40789-016-0134-1.

272. Steer, J. M., Marsh, R., Greenslade, M. & Robinson, A. Opportunities to improve the utilisation of granulated coals for blast furnace injection. *Fuel* vol. 151 40–49 (2015). doi: 10.1016/j.fuel.2014.12.060.

273. Maki, A. *et al.* High rate coal injection of 218kg/t at Fukuyama No. 4 Blast Furnace. *ISIJ Int.* **36**, 650–657 (1996). doi: 10.2355/isijinternational.36.650.

274. Nomura, S. & Callcott, T. G. Maximum rates of pulverized coal injection in ironmaking blast furnaces. *ISIJ Int.* **51**, 1033–1043 (2011). doi: 10.2355/isijinternational.51.1033.

275. Schott, R. Optimization strategies for pulverized coal injection into the blast furnace. *Stahl und Eisen* **136**, 39–47 (2016).

276. de Lourdes Ilha Gomes, M., Osório, E. & Vilela, A. C. F. Thermal analysis evaluation of the reactivity of coal mixtures for injection in the blast furnace. *Mater. Res.* **9**, 91–95 (2006). doi: 10.1590/s1516-14392006000100017.

277. Osório, E. *et al.* Evaluation of petrology and reactivity of coal blends for use in pulverized coal injection (PCI). *International Journal of Coal Geology* vol. 68 14–29 (2006). doi: 10.1016/j.coal.2005.11.007.

278. Steer, J., Greenslade, M. & Marsh, R. A comparison of laboratory coal testing with the blast furnace process and coal injection. *Metals (Basel).* **11**, (2021). doi: 10.3390/met11091476.

279. Yoji, O. *et al.* Recycling of waste plastic packaging in a blast furnace system. *NKK Tech. Rev.* 1–7 (2001).

APPENDICES

APPENDIX 1. RAW DATA FROM RHF BENCHMARKING STUDY IN CHAPTER 5 267
APPENDIX 2. RAW DATA FROM FACTSAGE CALCULATIONS IN CHAPTER 6 271

APPENDIX 1. RAW DATA FROM RHF BENCHMARKING STUDY IN CHAPTER 5

Temp (°C)	Hold Time (min)	C/O	C (Wt. %)	S (Wt. %)	Zn (Wt. %)	Pb (Wt. %)	Na (Wt. %)	K (Wt. %)	Fe (Wt. %)	Fe_{met} (Wt. %)
1350	30	0.9	1.67	0.2	0.02	0	0.01	0	83.08	66.67
1350	45	0.9	2.05	0.24	0.02	0	0.01	0	83.04	68.9
1350	30	0.8	1.18	0.19	0.02	0	0.01	0	82.61	70.36
1350	15	0.9	1.82	0.17	0.02	0	0.03	0	81.67	71.52
1350	45	0.8	1.95	0.18	0.02	0	0	0	81.49	63.13
1350	45	1	1.86	0.37	0.02	0	0.01	0	81.09	68.01
1350	60	1	3.41	0.28	0.02	0	0.01	0	80.68	72.6
1350	60	0.9	0.13	0.18	0.02	0	0.18	0.32	80.38	61.88
1350	0	0.8	1.77	0.23	0.03	0	0.1	0.07	78.41	67.89
1350	0	0.9	2.78	0.16	0.02	0	0.08	0.07	78.05	70.4
1350	15	1	3.22	0.24	0.02	0	0.02	0	78	68.68
1350	15	0.8	0.9	0.19	0.02	0	0.07	0.04	77.85	68.78
1350	0	0.7	1.29	0.22	0.04	0.01	0.15	0.21	77.77	69.45
1350	30	1	1.61	0.24	0.02	0	0.04	0.03	77.63	61.36
1350	15	0.7	0.59	0.21	0	0.01	0.08	0.07	76.46	56.78
1350	30	0.7	0.27	0.15	0	0.01	0.18	0.36	76.13	57.52
1350	0	1	4.68	0.2	0.02	0	0.07	0.07	75.89	68.75
1350	45	0.7	0.15	0.08	0	0.01	0.23	0.43	74.81	63.9
1200	0	0.9	4.61	0.18	1.11	0.02	0.17	0.27	77.44	63.02
1350	60	0.8	0.1	0.2	0.01	0	0.32	0.56	74.72	63.05
1350	45	0.5	0.06	0.01	0.01	0.01	0.31	0.57	74.55	51.55
1200	0	1	6.87	0.14	1.32	0.03	0.14	0.24	75.45	58.28
1200	0	0.8	4.51	0.11	1.48	0.03	0.16	0.24	75.54	54.81
1350	60	0.7	0.13	0.05	0.01	0.01	0.32	0.64	74.54	58.39
1350	45	0.6	0.08	0.02	0	0.01	0.35	0.65	74.45	57.74
1350	15	0.6	0.22	0.14	0.02	0.01	0.15	0.19	74.43	53.11
1150	0	1	9.04	0.11	1.93	0.07	0.17	0.12	62.42	28.76
1150	0	0.8	6.61	0.11	1.94	0.07	0.17	0.11	62.33	29.87
1150	0	0.9	7.76	0.11	1.97	0.07	0.16	0.12	65.3	30.98
1100	0	1	11.25	0.13	2.1	0.07	0.16	0.11	61.91	26.1
1350	30	0.6	0.23	0.04	0.01	0.01	0.23	0.39	74.42	57.13
1100	0	0.9	9.52	0.12	2.15	0.1	0.16	0.11	60.41	12.78
1350	15	0.5	0.24	0.04	0.07	0.01	0.26	0.46	73.37	52.01
1100	0	0.8	9.3	0.11	2.28	0.12	0.15	0.06	59.03	11.8
1350	30	0.5	0.1	0.04	0.02	0.01	0.25	0.41	73.1	55.4
1350	60	0.6	0.08	0	0.02	-0.01	0.46	0.81	67.45	52.62
1350	60	0.5	0.08	0.01	0.01	0.01	0.4	0.83	66.61	54.13
1300	45	0.5	0.34	0.1	0.01	0.01	0.09	0.06	86.32	79.19
1300	60	0.5	0.27	0.18	0	0.01	0.03	0.01	86.06	78.93
1300	0	0.7	1.97	0.16	0.1	0.01	0.15	0.22	80.1	72.93

1300	45	0.6	0.28	0.05	0	0.01	0.02	0.01	84.84	77.52
1300	15	0.8	1.51	0.2	0	0.01	0.07	0.07	84.61	73.06
1350	0	0.6	0.48	0.02	0.1	0.01	0.17	0.19	82.01	65.1
1200	15	0.5	0.42	0.15	0.14	0.01	0.14	0.11	71.13	62.55
1150	15	0.6	0.23	0.04	0.18	0.01	0.15	0.15	76.41	40.05
1300	30	0.6	0.28	0.13	0.01	0.01	0.06	0.03	83.37	76.93
1300	60	0.7	1.52	0.26	0	0.01	0	0	82.69	74.83
1300	60	0.6	0.21	0.15	0	0.01	0.01	0	82.35	76.05
1300	15	0.6	0.28	0.06	0.01	0.01	0.09	0.06	82.18	74.94
1300	45	0.7	1.43	0.14	0.01	0.01	0.01	0.01	81.53	75.33
1300	30	0.7	0.27	0.13	0.01	0.01	0.01	0.01	81.09	74.22
1250	0	0.7	2.24	0.16	0.24	0.01	0.19	0.28	78.02	68.09
1300	30	0.5	0.24	0.1	0.01	0.01	0.08	0.06	80.93	75.94
1300	15	0.9	1.41	0.2	0	0.01	0.06	0.07	79.69	71.93
1150	15	0.5	0.23	0.08	0.31	0.01	0.15	0.14	76.32	46.12
1300	30	1	1.94	0.24	0	0.01	0.04	0.04	79.68	74.12
1300	0	0.5	0.52	0.17	0.37	0.01	0.17	0.18	80.34	67.86
1300	15	0.7	1.49	0.09	0.01	0.01	0.04	0.04	79.51	74.77
1250	0	0.6	0.7	0.12	0.41	0.01	0.17	0.2	78.21	69.27
1350	0	0.5	0.58	0.12	0.49	0.01	0.15	0.18	79.51	57.39
1100	15	0.7	1.2	0.11	0.72	0.01	0.17	0.2	77.27	58.87
1300	0	0.6	0.96	0.21	0.09	0.01	0.15	0.16	79.44	71.88
1150	15	0.8	1.38	0.13	0.1	0.01	0.19	0.09	76.7	68.81
1300	0	0.9	3.09	0.18	0.05	0.01	0.12	0.18	79.14	70.17
1100	15	1	3.66	0.14	0.17	0.01	0.19	0.11	76.52	61.08
1250	0	0.5	0.89	0.13	1.07	0.01	0.16	0.19	74.03	67.6
1100	15	0.9	2.44	0.12	0.21	0.01	0.22	0.11	74.12	49.91
1300	15	0.5	0.32	0.09	0.05	0.01	0.12	0.1	78.46	70.35
1100	15	0.8	1.68	0.12	0.68	0.01	0.19	0.06	74.36	54.04
1200	0	0.6	1.89	0.14	1.2	0.02	0.2	0.26	73.52	59.37
1200	0	0.7	3.97	0.17	1.24	0.02	0.16	0.23	67.85	59.87
1300	0	0.8	2.99	0.14	0.09	0.01	0.12	0.18	78.44	69.66
1300	30	0.9	0.75	0.14	0	0.01	0.06	0.07	77.6	66.87
1300	30	0.8	0.58	0.22	0	0.01	0.06	0.05	77.55	61.45
1300	45	0.8	0.21	0.08	0	0.01	0.07	0.08	77.19	47.11
1300	15	1	2.52	0.23	0	0.01	0.06	0.06	76.84	72.15
1300	0	1	5.32	0.19	0.05	0.01	0.12	0.2	76.67	69.35
1300	45	1	0.71	0.25	0	0.01	0.1	0.14	75.42	53.19
1300	45	0.9	0.54	0.23	0	0.01	0.13	0.15	74.01	51.39
1300	60	1	0.19	0.18	0	0.01	0.09	0.12	72.96	43.7
1300	60	0.9	0.18	0.16	0	0.01	0.19	0.33	72.75	57.28
1300	60	0.8	0.1	0.08	0	0.01	0.24	0.5	71.62	48.21
1250	0	0.8	3.02	0.18	0.2	0.01	0.15	0.21	77.81	69.86
1250	30	0.8	1.5	0.21	0	0.01	0.03	0.03	83.7	76.98
1250	60	0.8	1.54	0.19	0	0.01	0.02	0.02	83	76.81
1250	60	0.7	0.51	0.15	0.01	0.01	0.04	0.04	82.71	56.32
1250	60	0.9	2.16	0.2	0	0.01	0.01	0.01	81.67	70.23

1250	45	0.8	1.35	0.21	0	0.01	0.02	0.02	81.62	75.47
1250	45	0.9	2.49	0.21	0	0.01	0.01	0.01	81.34	72.32
1250	60	0.6	0.2	0.09	0.01	0.01	0.03	0.03	80.78	64.1
1250	45	1	3.5	0.24	0	0.01	0.02	0.02	80.75	72.76
1250	15	0.8	2.43	0.21	0.01	0.01	0.05	0.07	80.73	74.98
1250	60	1	2.68	0.22	0	0.01	0.02	0.02	80.53	73.28
1100	15	0.6	6.59	0.02	1.38	0.01	0.17	0.17	76.46	49.48
1250	15	0.9	3.19	0.19	0.01	0.01	0.03	0.04	79.94	70.91
1250	0	0.9	3.16	0.11	0.09	0.01	0.14	0.2	79.71	69.77
1250	30	0.9	2.99	0.2	0.01	0.01	0.01	0.01	78.88	73.57
1150	0	0.6	3.77	0.1	1.52	0.04	0.18	0.24	66.25	32.26
1250	15	1	4.45	0.28	0.01	0.01	0.05	0.07	77.98	71.55
1250	30	0.7	1.66	0.19	0.01	0.01	0.06	0.05	77.53	71.96
1250	60	0.5	0.25	0.15	0.05	0.01	0.12	0.11	77.03	53.9
1250	30	1	4.23	0.22	0.01	0.01	0.02	0.03	76.76	71.5
1250	45	0.6	0.19	0.15	0.01	0.01	0.07	0.03	75.85	64.88
1250	45	0.5	0.23	0.12	0.02	0.01	0.1	0.07	75.32	58.96
1250	45	0.7	0.44	0.14	0.01	0.01	0.05	0.04	74.58	48.72
1200	0	0.5	1.51	0.13	1.69	0.02	0.18	0.21	72.35	51.12
1100	30	0.6	0.3	0.02	0.2	0.01	0.11	0.1	75.4	38.9
1250	15	0.7	0.86	0.2	0.02	0.01	0.1	0.11	74.57	68.69
1250	15	0.6	0.23	0.15	0.02	0.01	0.13	0.09	73.18	67.82
1100	0	0.6	6.09	0.1	1.73	0.06	0.12	0.14	63.11	13.77
1250	30	0.6	0.33	0.12	0.01	0.01	0.1	0.05	72.42	65.35
1150	0	0.5	3.98	0.1	2.14	0.05	0.16	0.2	65.64	25.32
1250	30	0.5	0.3	0.13	0.03	0.01	0.11	0.08	70.91	57.93
1250	15	0.5	0.3	0.09	0.05	0.01	0.15	0.11	69.74	64.62
1200	60	0.9	0.43	0.19	0	0.01	0.06	0.06	84.34	73.21
1200	60	1	0.77	0.2	0	0.01	0.07	0.08	84.11	76.13
1200	45	1	1.46	0.22	0.01	0.01	0.07	0.1	84.07	70.14
1200	30	0.8	0.95	0.17	0.01	0.01	0.09	0.12	83.84	73.58
1200	45	0.9	1.97	0.2	0	0.01	0.07	0.09	83.73	68.77
1200	45	0.8	0.62	0.19	0.01	0.01	0.07	0.09	83.7	72.9
1200	60	0.8	0.49	0.16	0	0.01	0.06	0.05	82.53	70.77
1200	15	0.8	2.95	0.2	0.03	0.01	0.12	0.17	82.08	71.64
1200	15	0.9	2.51	0.21	0.05	0.01	0.11	0.18	82.07	69.43
1200	30	0.9	1.56	0.2	0.01	0.01	0.11	0.17	81.27	71.02
1200	30	1	3.02	0.22	0.01	0.01	0.11	0.18	78.68	71.05
1250	0	1	4.68	0.14	0.13	0.01	0.17	0.27	76.67	65.8
1200	15	1	4.42	0.21	0.02	0.01	0.14	0.23	77.82	69.26
1200	30	0.6	0.28	0.16	0.06	0.01	0.13	0.1	77.77	60.35
1200	60	0.5	0.28	0.03	0.02	0.01	0.1	0.04	76.14	36.38
1200	30	0.7	0.71	0.2	0.04	0.01	0.1	0.11	75.49	66.19
1200	15	0.6	0.32	0.15	0.06	0.01	0.16	0.17	74.58	59.88
1200	45	0.6	0.21	0.14	0.02	0.01	0.11	0.07	74.15	51.3
1200	60	0.7	0.34	0.09	0.01	0.01	0.09	0.06	73.94	47.39
1200	45	0.7	0.31	0.08	0.01	0.01	0.12	0.08	72.86	57.14

1200	15	0.7	1.01	0.2	0.04	0.01	0.13	0.16	70.57	68.22
1200	30	0.5	0.28	0.12	0.05	0.01	0.13	0.07	68.91	54.99
1200	45	0.5	0.27	0.08	0.06	0.01	0.11	0.06	66.01	42.59
1200	60	0.6	0.21	0.08	0.01	0.01	0.09	0.05	64.41	37.78
1150	60	1	1.19	0.18	0.01	0.01	0.12	0.18	79.51	69.75
1150	30	0.5	0.36	0.11	0.17	0.01	0.16	0.1	73.13	45.21
1150	15	0.7	0.92	0.19	0.05	0.01	0.17	0.22	78.83	62.94
1100	0	0.7	8.18	0.1	2.27	0.08	0.16	0.2	62.81	11.05
1100	45	0.6	0.2	0	0.27	0.01	0.11	0.08	64.98	29.31
1100	15	0.5	0.68	0.06	2.64	0.02	0.19	0.17	74.6	41.08
1150	45	0.8	0.69	0.17	0.03	0.01	0.13	0.12	78.26	66.79
1150	30	0.8	0.79	0.16	0.06	0.01	0.15	0.19	77.69	67.45
1150	30	0.7	0.86	0.21	0.06	0.01	0.13	0.16	77.5	57.27
1150	45	0.5	0.33	0.03	0.1	0.01	0.12	0.07	74.94	38.77
1150	60	0.8	1.2	0.18	0.01	0.01	0.11	0.15	77.07	70.72
1150	45	0.7	0.68	0.11	0.01	0.01	0.13	0.13	76.76	47.53
1150	45	0.9	0.59	0.18	0.01	0.01	0.14	0.18	76.6	64.29
1100	30	0.5	0.23	0.01	0.7	0.01	0.13	0.08	72.15	33.9
1150	60	0.9	0.75	0.19	0.01	0.01	0.12	0.18	76.23	66.61
1150	30	0.9	1.49	0.13	0.02	0.01	0.14	0.2	75.72	62.74
1150	30	1	1.67	0.17	0.02	0.01	0.16	0.25	75.5	65.39
1150	15	0.9	2.31	0.2	0.04	0.01	0.19	0.1	75.27	64.3
1150	60	0.6	0.31	0.03	0.05	0.01	0.11	0.05	74.9	31.14
1150	15	1	2.8	0.16	0.05	0.01	0.18	0.09	74.88	66.1
1150	45	1	1.97	0.18	0.01	0.01	0.15	0.22	74.6	60.51
1150	60	0.5	0.24	0.03	0.06	0.01	0.12	0.05	73.41	34.46
1150	30	0.6	0.38	0.02	0.07	0.01	0.14	0.11	70.72	42.85
1150	45	0.6	0.28	0.02	0.06	0.01	0.13	0.07	68.88	33.28
1150	60	0.7	0.51	0.08	0.01	0.01	0.12	0.1	68.12	44.37
1100	30	0.7	0.98	0.18	0.09	0.01	0.14	0.15	77.64	44.13
1100	30	1	2.43	0.2	0.05	0.01	0.19	0.31	75.17	58.63
1100	45	0.9	0.96	0.03	0.03	0.01	0.16	0.2	74.75	44.69
1100	45	0.5	0.19	0.02	0.74	0.01	0.15	0.09	72.06	30.04
1100	60	0.7	0.49	0.03	0.01	0.01	0.09	0.07	74.42	34.86
1100	60	0.8	0.61	0.03	0.04	0.01	0.14	0.13	74.31	31.59
1100	30	0.8	1.18	0.1	0.08	0.01	0.2	0.25	72.76	53.63
1150	0	0.7	6.05	0.14	2.72	0.05	0.15	0.24	68.21	30.33
1100	60	0.9	1.01	0.02	0.02	0.01	0.15	0.15	72.4	36.72
1100	45	0.8	0.52	0.03	0.05	0.01	0.17	0.19	72.13	46.49
1100	45	1	1.38	0.02	0.04	0.01	0.17	0.26	71.96	44.99
1100	60	1	0.94	0.03	0.02	0.01	0.15	0.2	71.94	40.03
1100	30	0.9	1.39	0.18	0.07	0.01	0.18	0.26	71.5	48.12
1100	45	0.7	0.7	0.06	0.09	0.02	0.21	0.2	68.54	44.37
1100	60	0.5	0.28	0	0.44	0.01	0.15	0.07	65.63	24.95
1100	60	0.6	0.33	0.01	0.42	0.01	0.17	0.09	65.59	21.26
1100	0	0.5	5.81	0.11	3.92	0.15	0.16	0.34	64.28	12.45

APPENDIX 2. RAW DATA FROM FACTSAGE CALCULATIONS IN CHAPTER 6

[1] – Solid Fraction
[2] – Non-carbonaceous Solid Fraction
[3] – Carbonaceous Solid Fraction

Temperature (°C)	BF Dust Fraction	R_{Fe} (%)	[S] (Wt. %)	[Mn] (Wt. %)	[C] (Wt. %)	Fe_{Out} (%)	SF [1]	NCSF [2]	CSF [3]
1000	0.00	0.00	0.00	0.00	0.00	0.00	0.79	0.79	0.00
1025	0.00	0.00	0.00	0.00	0.00	0.00	0.46	0.46	0.00
1050	0.00	0.00	0.00	0.00	0.00	0.00	0.43	0.43	0.00
1075	0.00	0.00	0.00	0.00	0.00	0.00	0.38	0.38	0.00
1100	0.00	0.00	0.00	0.00	0.00	0.00	0.33	0.33	0.00
1125	0.00	0.00	0.00	0.00	0.00	0.00	0.25	0.25	0.00
1150	0.00	0.00	0.00	0.00	0.00	0.00	0.16	0.16	0.00
1175	0.00	0.00	0.00	0.00	0.00	0.00	0.10	0.10	0.00
1200	0.00	0.00	0.00	0.00	0.00	0.00	0.09	0.09	0.00
1225	0.00	0.00	0.00	0.00	0.00	0.00	0.07	0.07	0.00
1250	0.00	0.00	0.00	0.00	0.00	0.00	0.05	0.05	0.00
1275	0.00	0.00	0.00	0.00	0.00	0.00	0.05	0.05	0.00
1300	0.00	0.00	0.00	0.00	0.00	0.00	0.05	0.05	0.00
1325	0.00	0.00	0.00	0.00	0.00	0.00	0.04	0.04	0.00
1350	0.00	0.00	0.00	0.00	0.00	0.00	0.04	0.04	0.00
1375	0.00	0.00	0.00	0.00	0.00	0.00	0.04	0.04	0.00
1400	0.00	0.00	0.00	0.00	0.00	0.00	0.04	0.04	0.00
1425	0.00	0.00	0.00	0.00	0.00	0.00	0.03	0.03	0.00
1450	0.00	0.00	0.00	0.00	0.00	0.00	0.03	0.03	0.00
1475	0.00	0.00	0.00	0.00	0.00	0.00	0.03	0.03	0.00
1500	0.00	0.00	0.00	0.00	0.00	0.00	0.03	0.03	0.00
1525	0.00	0.00	0.00	0.00	0.00	0.00	0.03	0.03	0.00
1550	0.00	4.19	0.00	0.00	0.01	2.48	0.00	0.00	0.00
1575	0.00	3.99	0.00	0.00	0.01	2.36	0.00	0.00	0.00
1600	0.00	3.80	0.00	0.00	0.01	2.25	0.00	0.00	0.00
1625	0.00	3.63	0.00	0.01	0.01	2.15	0.00	0.00	0.00
1650	0.00	3.46	0.00	0.01	0.01	2.05	0.00	0.00	0.00
1675	0.00	3.30	0.00	0.01	0.01	1.95	0.00	0.00	0.00
1700	0.00	3.15	0.00	0.01	0.01	1.86	0.00	0.00	0.00
1725	0.00	3.00	0.00	0.01	0.00	1.77	0.00	0.00	0.00
1750	0.00	2.87	0.00	0.01	0.00	1.70	0.00	0.00	0.00
1775	0.00	2.73	0.00	0.01	0.00	1.61	0.00	0.00	0.00
1800	0.00	2.61	0.00	0.01	0.00	1.54	0.00	0.00	0.00
1000	0.05	0.00	0.00	0.00	0.00	0.00	0.70	0.70	0.00
1025	0.05	0.00	0.00	0.00	0.00	0.00	0.46	0.46	0.00
1050	0.05	0.00	0.00	0.00	0.00	0.00	0.43	0.43	0.00
1075	0.05	0.00	0.00	0.00	0.00	0.00	0.39	0.39	0.00
1100	0.05	0.00	0.00	0.00	0.00	0.00	0.34	0.34	0.00
1125	0.05	0.00	0.00	0.00	0.00	0.00	0.28	0.28	0.00
1150	0.05	0.00	0.00	0.00	0.00	0.00	0.21	0.21	0.00

1175	0.05	0.00	0.00	0.00	0.00	0.00	0.19	0.19	0.00
1200	0.05	0.00	0.00	0.00	0.00	0.00	0.18	0.18	0.00
1225	0.05	0.00	0.00	0.00	0.00	0.00	0.17	0.17	0.00
1250	0.05	0.00	0.00	0.00	0.00	0.00	0.15	0.15	0.00
1275	0.05	0.00	0.00	0.00	0.00	0.00	0.13	0.13	0.00
1300	0.05	0.00	0.00	0.00	0.00	0.00	0.13	0.13	0.00
1325	0.05	0.00	0.00	0.00	0.00	0.00	0.13	0.13	0.00
1350	0.05	0.00	0.00	0.00	0.00	0.00	0.13	0.13	0.00
1375	0.05	0.00	0.00	0.00	0.00	0.00	0.12	0.12	0.00
1400	0.05	0.00	0.00	0.00	0.00	0.00	0.12	0.12	0.00
1425	0.05	0.00	0.00	0.00	0.00	0.00	0.12	0.12	0.00
1450	0.05	0.00	0.00	0.00	0.00	0.00	0.12	0.12	0.00
1475	0.05	0.00	0.00	0.00	0.00	0.00	0.11	0.11	0.00
1500	0.05	0.00	0.00	0.00	0.00	0.00	0.11	0.11	0.00
1525	0.05	0.00	0.00	0.00	0.00	0.00	0.11	0.11	0.00
1550	0.05	19.14	0.00	0.00	0.01	11.01	0.00	0.00	0.00
1575	0.05	18.94	0.00	0.00	0.01	10.89	0.00	0.00	0.00
1600	0.05	18.75	0.00	0.01	0.01	10.79	0.00	0.00	0.00
1625	0.05	18.57	0.00	0.01	0.01	10.68	0.00	0.00	0.00
1650	0.05	18.39	0.00	0.01	0.01	10.58	0.00	0.00	0.00
1675	0.05	18.23	0.00	0.01	0.01	10.49	0.00	0.00	0.00
1700	0.05	18.07	0.00	0.01	0.01	10.39	0.00	0.00	0.00
1725	0.05	17.92	0.00	0.01	0.01	10.31	0.00	0.00	0.00
1750	0.05	17.77	0.00	0.01	0.01	10.22	0.00	0.00	0.00
1775	0.05	17.63	0.00	0.01	0.01	10.14	0.00	0.00	0.00
1800	0.05	17.50	0.00	0.01	0.00	10.07	0.00	0.00	0.00
1000	0.10	0.00	0.00	0.00	0.00	0.00	0.63	0.63	0.00
1025	0.10	0.00	0.00	0.00	0.00	0.00	0.45	0.45	0.00
1050	0.10	0.00	0.00	0.00	0.00	0.00	0.43	0.43	0.00
1075	0.10	0.00	0.00	0.00	0.00	0.00	0.39	0.39	0.00
1100	0.10	0.00	0.00	0.00	0.00	0.00	0.35	0.35	0.00
1125	0.10	0.00	0.00	0.00	0.00	0.00	0.31	0.31	0.00
1150	0.10	0.00	0.00	0.00	0.00	0.00	0.30	0.30	0.00
1175	0.10	0.00	0.00	0.00	0.00	0.00	0.29	0.29	0.00
1200	0.10	0.00	0.00	0.00	0.00	0.00	0.28	0.28	0.00
1225	0.10	0.00	0.00	0.00	0.00	0.00	0.26	0.26	0.00
1250	0.10	0.00	0.00	0.00	0.00	0.00	0.24	0.24	0.00
1275	0.10	0.00	0.00	0.00	0.00	0.00	0.22	0.22	0.00
1300	0.10	0.00	0.00	0.00	0.00	0.00	0.22	0.22	0.00
1325	0.10	0.00	0.00	0.00	0.00	0.00	0.21	0.21	0.00
1350	0.10	0.00	0.00	0.00	0.00	0.00	0.21	0.21	0.00
1375	0.10	0.00	0.00	0.00	0.00	0.00	0.21	0.21	0.00
1400	0.10	0.00	0.00	0.00	0.00	0.00	0.21	0.21	0.00
1425	0.10	0.00	0.00	0.00	0.00	0.00	0.20	0.20	0.00
1450	0.10	0.00	0.00	0.00	0.00	0.00	0.20	0.20	0.00
1475	0.10	0.00	0.00	0.00	0.00	0.00	0.20	0.20	0.00
1500	0.10	0.00	0.00	0.00	0.00	0.00	0.20	0.20	0.00
1525	0.10	0.00	0.00	0.00	0.00	0.00	0.20	0.20	0.00
1550	0.10	34.92	0.00	0.01	0.01	19.52	0.00	0.00	0.00

1575	0.10	34.71	0.00	0.01	0.01	19.40	0.00	0.00	0.00
1600	0.10	34.50	0.00	0.01	0.01	19.29	0.00	0.00	0.00
1625	0.10	34.30	0.00	0.01	0.01	19.18	0.00	0.00	0.00
1650	0.10	34.12	0.00	0.01	0.01	19.07	0.00	0.00	0.00
1675	0.10	33.94	0.00	0.01	0.01	18.97	0.00	0.00	0.00
1700	0.10	33.77	0.00	0.01	0.01	18.88	0.00	0.00	0.00
1725	0.10	33.61	0.00	0.01	0.01	18.79	0.00	0.00	0.00
1750	0.10	33.45	0.00	0.01	0.01	18.70	0.00	0.00	0.00
1775	0.10	33.30	0.00	0.01	0.01	18.62	0.00	0.00	0.00
1800	0.10	33.16	0.00	0.01	0.01	18.54	0.00	0.00	0.00
1000	0.15	0.00	0.00	0.00	0.00	0.00	0.58	0.58	0.00
1025	0.15	0.00	0.00	0.00	0.00	0.00	0.44	0.44	0.00
1050	0.15	0.00	0.00	0.00	0.00	0.00	0.42	0.42	0.00
1075	0.15	0.00	0.00	0.00	0.00	0.00	0.42	0.42	0.00
1100	0.15	0.00	0.00	0.00	0.00	0.00	0.41	0.41	0.00
1125	0.15	0.00	0.00	0.00	0.00	0.00	0.40	0.40	0.00
1150	0.15	0.00	0.00	0.00	0.00	0.00	0.39	0.39	0.00
1175	0.15	0.00	0.00	0.00	0.00	0.00	0.38	0.38	0.00
1200	0.15	0.00	0.00	0.00	0.00	0.00	0.37	0.37	0.00
1225	0.15	0.00	0.00	0.00	0.00	0.00	0.36	0.36	0.00
1250	0.15	0.00	0.00	0.00	0.00	0.00	0.34	0.34	0.00
1275	0.15	0.00	0.00	0.00	0.00	0.00	0.31	0.31	0.00
1300	0.15	0.00	0.00	0.00	0.00	0.00	0.30	0.30	0.00
1325	0.15	0.00	0.00	0.00	0.00	0.00	0.30	0.30	0.00
1350	0.15	0.00	0.00	0.00	0.00	0.00	0.30	0.30	0.00
1375	0.15	0.00	0.00	0.00	0.00	0.00	0.29	0.29	0.00
1400	0.15	0.00	0.00	0.00	0.00	0.00	0.29	0.29	0.00
1425	0.15	0.00	0.00	0.00	0.00	0.00	0.29	0.29	0.00
1450	0.15	0.00	0.00	0.00	0.00	0.00	0.29	0.29	0.00
1475	0.15	0.00	0.00	0.00	0.00	0.00	0.28	0.28	0.00
1500	0.15	0.00	0.00	0.00	0.00	0.00	0.28	0.28	0.00
1525	0.15	0.00	0.00	0.00	0.00	0.00	0.28	0.28	0.00
1550	0.15	51.41	0.00	0.01	0.01	27.91	0.00	0.00	0.00
1575	0.15	51.18	0.00	0.01	0.01	27.78	0.00	0.00	0.00
1600	0.15	50.96	0.00	0.01	0.01	27.66	0.00	0.00	0.00
1625	0.15	50.75	0.00	0.01	0.01	27.55	0.00	0.00	0.00
1650	0.15	50.56	0.00	0.01	0.01	27.45	0.00	0.00	0.00
1675	0.15	50.37	0.00	0.01	0.01	27.34	0.00	0.00	0.00
1700	0.15	50.18	0.00	0.01	0.01	27.24	0.00	0.00	0.00
1725	0.15	50.01	0.00	0.01	0.01	27.15	0.00	0.00	0.00
1750	0.15	49.85	0.00	0.01	0.01	27.06	0.00	0.00	0.00
1775	0.15	49.69	0.00	0.01	0.01	26.98	0.00	0.00	0.00
1800	0.15	49.53	0.00	0.02	0.01	26.89	0.00	0.00	0.00
1000	0.20	0.00	0.00	0.00	0.00	0.00	0.59	0.59	0.00
1025	0.20	0.00	0.00	0.00	0.00	0.00	0.52	0.52	0.00
1050	0.20	0.00	0.00	0.00	0.00	0.00	0.52	0.52	0.00
1075	0.20	0.00	0.00	0.00	0.00	0.00	0.51	0.51	0.00
1100	0.20	0.00	0.00	0.00	0.00	0.00	0.50	0.50	0.00
1125	0.20	0.00	0.00	0.00	0.00	0.00	0.49	0.49	0.00
1150	0.20	0.00	0.00	0.00	0.00	0.00	0.48	0.48	0.00

1175	0.20	0.00	0.00	0.00	0.00	0.00	0.47	0.47	0.00
1200	0.20	0.00	0.00	0.00	0.00	0.00	0.46	0.46	0.00
1225	0.20	0.00	0.00	0.00	0.00	0.00	0.44	0.44	0.00
1250	0.20	0.00	0.00	0.00	0.00	0.00	0.42	0.42	0.00
1275	0.20	0.00	0.00	0.00	0.00	0.00	0.39	0.39	0.00
1300	0.20	0.00	0.00	0.00	0.00	0.00	0.38	0.38	0.00
1325	0.20	0.00	0.00	0.00	0.00	0.00	0.38	0.38	0.00
1350	0.20	0.00	0.00	0.00	0.00	0.00	0.38	0.38	0.00
1375	0.20	0.00	0.00	0.00	0.00	0.00	0.37	0.37	0.00
1400	0.20	0.00	0.00	0.00	0.00	0.00	0.37	0.37	0.00
1425	0.20	0.00	0.00	0.00	0.00	0.00	0.37	0.37	0.00
1450	0.20	0.00	0.00	0.00	0.00	0.00	0.37	0.37	0.00
1475	0.20	0.00	0.00	0.00	0.00	0.00	0.36	0.36	0.00
1500	0.20	0.00	0.00	0.00	0.00	0.00	0.36	0.36	0.00
1525	0.20	0.00	0.00	0.00	0.00	0.00	0.36	0.36	0.00
1550	0.20	68.34	0.01	0.01	0.01	35.99	0.00	0.00	0.00
1575	0.20	68.11	0.01	0.01	0.01	35.87	0.00	0.00	0.00
1600	0.20	67.88	0.01	0.01	0.01	35.75	0.00	0.00	0.00
1625	0.20	67.67	0.01	0.01	0.01	35.64	0.00	0.00	0.00
1650	0.20	67.47	0.01	0.02	0.01	35.54	0.00	0.00	0.00
1675	0.20	67.27	0.01	0.02	0.01	35.43	0.00	0.00	0.00
1700	0.20	67.09	0.01	0.02	0.01	35.34	0.00	0.00	0.00
1725	0.20	66.91	0.01	0.02	0.01	35.24	0.00	0.00	0.00
1750	0.20	66.74	0.01	0.02	0.01	35.15	0.00	0.00	0.00
1775	0.20	66.57	0.01	0.02	0.01	35.06	0.00	0.00	0.00
1800	0.20	66.41	0.01	0.02	0.01	34.98	0.00	0.00	0.00
1000	0.25	0.00	0.00	0.00	0.00	0.00	0.60	0.60	0.00
1025	0.25	0.00	0.00	0.00	0.00	0.00	0.59	0.59	0.00
1050	0.25	0.00	0.00	0.00	0.00	0.00	0.58	0.58	0.00
1075	0.25	0.00	0.00	0.00	0.00	0.00	0.57	0.57	0.00
1100	0.25	0.00	0.00	0.00	0.00	0.00	0.56	0.56	0.00
1125	0.25	0.00	0.00	0.00	0.00	0.00	0.55	0.55	0.00
1150	0.25	0.00	0.00	0.00	0.00	0.00	0.54	0.54	0.00
1175	0.25	0.00	0.00	0.00	0.00	0.00	0.53	0.53	0.00
1200	0.25	0.00	0.00	0.00	0.00	0.00	0.52	0.52	0.00
1225	0.25	0.00	0.00	0.00	0.00	0.00	0.52	0.52	0.00
1250	0.25	0.00	0.00	0.00	0.00	0.00	0.50	0.50	0.00
1275	0.25	0.00	0.00	0.00	0.00	0.00	0.49	0.49	0.00
1300	0.25	0.00	0.00	0.00	0.00	0.00	0.48	0.48	0.00
1325	0.25	0.00	0.00	0.00	0.00	0.00	0.46	0.46	0.00
1350	0.25	0.00	0.00	0.00	0.00	0.00	0.45	0.45	0.00
1375	0.25	0.00	0.00	0.00	0.00	0.00	0.44	0.44	0.00
1400	0.25	0.00	0.00	0.00	0.00	0.00	0.44	0.44	0.00
1425	0.25	0.00	0.00	0.00	0.00	0.00	0.44	0.44	0.00
1450	0.25	0.00	0.00	0.00	0.00	0.00	0.44	0.44	0.00
1475	0.25	0.00	0.00	0.00	0.00	0.00	0.43	0.43	0.00
1500	0.25	0.00	0.00	0.00	0.00	0.00	0.43	0.43	0.00
1525	0.25	0.00	0.00	0.00	0.00	0.00	0.43	0.43	0.00
1550	0.25	84.44	0.01	0.03	0.02	43.11	0.00	0.00	0.00

1575	0.25	84.26	0.01	0.03	0.02	43.02	0.00	0.00	0.00
1600	0.25	84.09	0.01	0.03	0.02	42.93	0.00	0.00	0.00
1625	0.25	83.92	0.01	0.03	0.02	42.84	0.00	0.00	0.00
1650	0.25	83.76	0.01	0.03	0.02	42.76	0.00	0.00	0.00
1675	0.25	83.60	0.01	0.04	0.01	42.68	0.00	0.00	0.00
1700	0.25	83.45	0.01	0.04	0.01	42.60	0.00	0.00	0.00
1725	0.25	83.30	0.01	0.04	0.01	42.53	0.00	0.00	0.00
1750	0.25	83.16	0.01	0.05	0.01	42.46	0.00	0.00	0.00
1775	0.25	83.02	0.01	0.05	0.01	42.38	0.00	0.00	0.00
1800	0.25	82.88	0.01	0.05	0.01	42.31	0.00	0.00	0.00
1000	0.30	0.00	0.00	0.00	0.00	0.00	0.65	0.65	0.00
1025	0.30	0.00	0.00	0.00	0.00	0.00	0.65	0.65	0.00
1050	0.30	0.00	0.00	0.00	0.00	0.00	0.65	0.65	0.00
1075	0.30	0.00	0.00	0.00	0.00	0.00	0.65	0.65	0.00
1100	0.30	0.00	0.00	0.00	0.00	0.00	0.62	0.62	0.00
1125	0.30	0.00	0.00	0.00	0.00	0.00	0.61	0.61	0.00
1150	0.30	0.00	0.00	0.00	0.00	0.00	0.60	0.60	0.00
1175	0.30	0.00	0.00	0.00	0.00	0.00	0.59	0.59	0.00
1200	0.30	0.00	0.00	0.00	0.00	0.00	0.58	0.58	0.00
1225	0.30	0.00	0.00	0.00	0.00	0.00	0.58	0.58	0.00
1250	0.30	0.00	0.00	0.00	0.00	0.00	0.57	0.57	0.00
1275	0.30	0.00	0.00	0.00	0.00	0.00	0.57	0.57	0.00
1300	0.30	0.00	0.00	0.00	0.00	0.00	0.56	0.56	0.00
1325	0.30	0.00	0.00	0.00	0.00	0.00	0.56	0.56	0.00
1350	0.30	0.00	0.00	0.00	0.00	0.00	0.55	0.55	0.00
1375	0.30	0.00	0.00	0.00	0.00	0.00	0.55	0.55	0.00
1400	0.30	0.00	0.00	0.00	0.00	0.00	0.54	0.54	0.00
1425	0.30	0.00	0.00	0.00	0.00	0.00	0.53	0.53	0.00
1450	0.30	0.00	0.00	0.00	0.00	0.00	0.52	0.52	0.00
1475	0.30	0.00	0.00	0.00	0.00	0.00	0.52	0.52	0.00
1500	0.30	0.00	0.00	0.00	0.00	0.00	0.51	0.51	0.00
1525	0.30	96.61	0.01	0.20	0.10	47.76	0.02	0.02	0.00
1550	0.30	96.44	0.01	0.21	0.10	47.68	0.00	0.00	0.00
1575	0.30	96.38	0.01	0.22	0.09	47.65	0.00	0.00	0.00
1600	0.30	96.33	0.01	0.23	0.08	47.62	0.00	0.00	0.00
1625	0.30	96.28	0.01	0.23	0.07	47.60	0.00	0.00	0.00
1650	0.30	96.25	0.01	0.24	0.07	47.58	0.00	0.00	0.00
1675	0.30	96.22	0.01	0.25	0.06	47.57	0.00	0.00	0.00
1700	0.30	96.19	0.01	0.26	0.06	47.55	0.00	0.00	0.00
1725	0.30	96.15	0.01	0.27	0.05	47.53	0.00	0.00	0.00
1750	0.30	96.11	0.01	0.28	0.05	47.51	0.00	0.00	0.00
1775	0.30	96.07	0.01	0.28	0.04	47.49	0.00	0.00	0.00
1800	0.30	96.01	0.01	0.29	0.04	47.46	0.00	0.00	0.00
1000	0.35	0.00	0.00	0.00	0.00	0.00	0.65	0.41	0.24
1025	0.35	0.00	0.00	0.00	0.00	0.00	0.65	0.42	0.23
1050	0.35	0.00	0.00	0.00	0.00	0.00	0.65	0.42	0.23
1075	0.35	0.00	0.00	0.00	0.00	0.00	0.65	0.42	0.23
1100	0.35	82.37	0.01	0.90	3.52	39.39	0.24	0.24	0.00
1125	0.35	86.16	0.01	0.86	3.36	41.20	0.22	0.22	0.00
1150	0.35	90.48	0.01	0.83	3.20	43.27	0.20	0.20	0.00

1175	0.35	95.65	0.01	0.75	3.03	45.74	0.15	0.15	0.00
1200	0.35	99.99	0.01	0.72	2.89	47.81	0.13	0.13	0.00
1225	0.35	99.99	0.00	0.72	2.87	47.81	0.13	0.13	0.00
1250	0.35	99.99	0.00	0.72	2.84	47.81	0.13	0.13	0.00
1275	0.35	99.98	0.00	0.71	2.82	47.81	0.12	0.12	0.00
1300	0.35	99.98	0.00	0.71	2.79	47.81	0.12	0.12	0.00
1325	0.35	99.97	0.00	0.70	2.77	47.80	0.10	0.10	0.00
1350	0.35	99.97	0.00	0.70	2.73	47.80	0.10	0.10	0.00
1375	0.35	99.97	0.00	0.71	2.70	47.80	0.10	0.10	0.00
1400	0.35	99.97	0.00	0.71	2.67	47.80	0.09	0.09	0.00
1425	0.35	99.97	0.00	0.71	2.65	47.80	0.09	0.09	0.00
1450	0.35	99.96	0.00	0.71	2.63	47.80	0.09	0.09	0.00
1475	0.35	99.96	0.00	0.71	2.62	47.80	0.08	0.08	0.00
1500	0.35	99.96	0.00	0.72	2.61	47.80	0.08	0.08	0.00
1525	0.35	99.96	0.00	0.72	2.60	47.80	0.07	0.07	0.00
1550	0.35	99.96	0.00	0.71	2.58	47.80	0.07	0.07	0.00
1575	0.35	99.96	0.00	0.71	2.57	47.80	0.06	0.06	0.00
1600	0.35	99.95	0.00	0.71	2.54	47.79	0.05	0.05	0.00
1625	0.35	99.95	0.00	0.70	2.51	47.79	0.05	0.05	0.00
1650	0.35	99.94	0.00	0.70	2.45	47.79	0.04	0.04	0.00
1675	0.35	99.94	0.00	0.69	2.40	47.79	0.03	0.03	0.00
1700	0.35	99.93	0.00	0.68	2.35	47.78	0.03	0.03	0.00
1725	0.35	99.92	0.00	0.67	2.29	47.78	0.03	0.03	0.00
1750	0.35	99.90	0.00	0.65	2.22	47.77	0.02	0.02	0.00
1775	0.35	99.88	0.00	0.64	2.15	47.76	0.01	0.01	0.00
1800	0.35	99.85	0.00	0.62	2.08	47.75	0.00	0.00	0.00
1000	0.40	0.00	0.00	0.00	0.00	0.00	0.65	0.16	0.50
1025	0.40	0.00	0.00	0.00	0.00	0.00	0.65	0.16	0.50
1050	0.40	0.00	0.00	0.00	0.00	0.00	0.65	0.16	0.50
1075	0.40	0.00	0.00	0.00	0.00	0.00	0.65	0.16	0.50
1100	0.40	0.00	0.00	0.00	0.00	0.00	0.65	0.16	0.50
1125	0.40	46.63	0.00	1.50	4.18	21.54	0.42	0.15	0.27
1150	0.40	100.00	0.00	0.71	4.21	46.20	0.16	0.15	0.01
1175	0.40	100.00	0.00	0.70	4.27	46.20	0.15	0.14	0.01
1200	0.40	100.00	0.00	0.70	4.31	46.20	0.15	0.14	0.01
1225	0.40	100.00	0.00	0.70	4.35	46.20	0.16	0.15	0.01
1250	0.40	100.00	0.00	0.70	4.41	46.20	0.16	0.15	0.01
1275	0.40	100.00	0.00	0.70	4.48	46.20	0.14	0.13	0.01
1300	0.40	100.00	0.00	0.70	4.55	46.20	0.13	0.12	0.01
1325	0.40	100.00	0.00	0.70	4.62	46.20	0.13	0.12	0.01
1350	0.40	100.00	0.00	0.70	4.68	46.20	0.12	0.11	0.01
1375	0.40	100.00	0.00	0.69	4.75	46.20	0.12	0.11	0.01
1400	0.40	100.00	0.00	0.69	4.82	46.20	0.11	0.10	0.01
1425	0.40	99.99	0.00	0.69	4.89	46.20	0.10	0.09	0.01
1450	0.40	99.99	0.00	0.69	4.95	46.20	0.09	0.08	0.01
1475	0.40	99.99	0.00	0.69	5.02	46.20	0.08	0.08	0.01
1500	0.40	99.99	0.00	0.69	5.09	46.20	0.08	0.07	0.01
1525	0.40	99.99	0.00	0.69	5.16	46.20	0.07	0.06	0.01
1550	0.40	99.99	0.00	0.68	5.22	46.20	0.06	0.06	0.01

1575	0.40	99.99	0.00	0.68	5.29	46.20	0.05	0.05	0.01
1600	0.40	99.99	0.00	0.68	5.34	46.20	0.05	0.05	0.01
1625	0.40	99.99	0.00	0.67	5.40	46.20	0.05	0.05	0.00
1650	0.40	99.98	0.00	0.67	5.44	46.19	0.05	0.04	0.00
1675	0.40	99.98	0.00	0.66	5.46	46.19	0.04	0.04	0.00
1700	0.40	99.97	0.00	0.65	5.45	46.19	0.04	0.04	0.00
1725	0.40	99.96	0.00	0.65	5.34	46.18	0.03	0.03	0.00
1750	0.40	99.95	0.00	0.64	5.05	46.18	0.02	0.02	0.00
1775	0.40	99.94	0.00	0.62	4.76	46.17	0.02	0.02	0.00
1800	0.40	99.91	0.00	0.61	4.48	46.16	0.03	0.03	0.00
1000	0.45	0.00	0.00	0.00	0.00	0.00	0.66	0.15	0.50
1025	0.45	0.00	0.00	0.00	0.00	0.00	0.66	0.15	0.50
1050	0.45	0.00	0.00	0.00	0.00	0.00	0.66	0.15	0.50
1075	0.45	0.00	0.00	0.00	0.00	0.00	0.66	0.15	0.50
1100	0.45	0.00	0.00	0.00	0.00	0.00	0.66	0.15	0.50
1125	0.45	47.86	0.01	1.39	4.17	21.34	0.43	0.15	0.28
1150	0.45	100.00	0.01	0.67	4.19	44.58	0.18	0.15	0.04
1175	0.45	100.00	0.01	0.67	4.20	44.58	0.18	0.15	0.03
1200	0.45	100.00	0.01	0.67	4.27	44.58	0.18	0.15	0.03
1225	0.45	100.00	0.01	0.67	4.33	44.58	0.18	0.15	0.03
1250	0.45	100.00	0.00	0.67	4.40	44.58	0.18	0.15	0.03
1275	0.45	100.00	0.00	0.66	4.47	44.58	0.17	0.14	0.03
1300	0.45	100.00	0.00	0.66	4.54	44.58	0.16	0.13	0.03
1325	0.45	100.00	0.00	0.66	4.60	44.58	0.15	0.12	0.03
1350	0.45	100.00	0.00	0.66	4.67	44.58	0.15	0.12	0.03
1375	0.45	100.00	0.00	0.66	4.74	44.58	0.15	0.11	0.03
1400	0.45	100.00	0.00	0.65	4.80	44.58	0.12	0.09	0.03
1425	0.45	100.00	0.00	0.65	4.87	44.58	0.11	0.08	0.03
1450	0.45	100.00	0.00	0.65	4.94	44.58	0.10	0.07	0.03
1475	0.45	99.99	0.00	0.65	5.00	44.58	0.09	0.06	0.03
1500	0.45	99.99	0.00	0.65	5.07	44.58	0.08	0.05	0.03
1525	0.45	99.99	0.00	0.65	5.13	44.58	0.07	0.05	0.03
1550	0.45	99.99	0.00	0.65	5.19	44.58	0.07	0.04	0.03
1575	0.45	99.99	0.00	0.65	5.24	44.58	0.07	0.04	0.03
1600	0.45	99.99	0.00	0.64	5.28	44.58	0.07	0.04	0.03
1625	0.45	99.99	0.00	0.64	5.32	44.58	0.07	0.04	0.03
1650	0.45	99.98	0.00	0.63	5.35	44.57	0.07	0.04	0.02
1675	0.45	99.98	0.00	0.63	5.38	44.57	0.06	0.04	0.02
1700	0.45	99.97	0.00	0.62	5.40	44.57	0.05	0.03	0.02
1725	0.45	99.96	0.00	0.61	5.38	44.56	0.04	0.02	0.02
1750	0.45	99.95	0.00	0.60	5.28	44.56	0.03	0.01	0.02
1775	0.45	99.94	0.00	0.59	5.16	44.56	0.04	0.03	0.02
1800	0.45	99.93	0.00	0.58	5.06	44.55	0.05	0.04	0.01
1000	0.50	0.00	0.00	0.00	0.00	0.00	0.66	0.15	0.51
1025	0.50	0.00	0.00	0.00	0.00	0.00	0.66	0.15	0.51
1050	0.50	0.00	0.00	0.00	0.00	0.00	0.66	0.15	0.51
1075	0.50	0.00	0.00	0.00	0.00	0.00	0.66	0.15	0.51
1100	0.50	0.00	0.00	0.00	0.00	0.00	0.66	0.15	0.51
1125	0.50	49.35	0.01	1.27	4.15	21.20	0.43	0.15	0.28
1150	0.50	100.00	0.01	0.63	4.16	42.97	0.20	0.15	0.06

1175	0.50	100.00	0.01	0.63	4.18	42.97	0.20	0.15	0.06
1200	0.50	100.00	0.01	0.63	4.25	42.97	0.20	0.15	0.06
1225	0.50	100.00	0.01	0.63	4.32	42.97	0.20	0.15	0.06
1250	0.50	100.00	0.01	0.63	4.39	42.97	0.20	0.15	0.06
1275	0.50	100.00	0.00	0.63	4.46	42.97	0.20	0.15	0.05
1300	0.50	100.00	0.00	0.63	4.52	42.97	0.19	0.14	0.05
1325	0.50	100.00	0.00	0.63	4.59	42.97	0.19	0.13	0.05
1350	0.50	100.00	0.00	0.62	4.66	42.97	0.18	0.13	0.05
1375	0.50	100.00	0.00	0.60	4.72	42.97	0.12	0.07	0.05
1400	0.50	100.00	0.00	0.61	4.79	42.97	0.11	0.06	0.05
1425	0.50	100.00	0.00	0.61	4.85	42.97	0.11	0.05	0.05
1450	0.50	99.99	0.00	0.61	4.92	42.96	0.10	0.05	0.05
1475	0.50	99.99	0.00	0.61	4.98	42.96	0.10	0.05	0.05
1500	0.50	99.99	0.00	0.61	5.03	42.96	0.10	0.05	0.05
1525	0.50	99.99	0.00	0.61	5.09	42.96	0.09	0.04	0.05
1550	0.50	99.99	0.00	0.61	5.13	42.96	0.09	0.04	0.05
1575	0.50	99.99	0.00	0.61	5.16	42.96	0.09	0.04	0.05
1600	0.50	99.99	0.00	0.60	5.19	42.96	0.08	0.04	0.05
1625	0.50	99.99	0.00	0.60	5.21	42.96	0.08	0.04	0.05
1650	0.50	99.98	0.00	0.59	5.23	42.96	0.08	0.03	0.05
1675	0.50	99.98	0.00	0.59	5.25	42.96	0.07	0.03	0.04
1700	0.50	99.97	0.00	0.58	5.27	42.95	0.07	0.02	0.04
1725	0.50	99.96	0.00	0.58	5.29	42.95	0.06	0.01	0.04
1750	0.50	99.95	0.00	0.57	5.27	42.94	0.04	0.00	0.04
1775	0.50	99.94	0.00	0.55	5.15	42.94	0.05	0.01	0.04
1800	0.50	99.92	0.00	0.54	5.03	42.93	0.06	0.03	0.04
1000	0.55	0.00	0.00	0.00	0.00	0.00	0.66	0.15	0.51
1025	0.55	0.00	0.00	0.00	0.00	0.00	0.66	0.15	0.51
1050	0.55	0.00	0.00	0.00	0.00	0.00	0.66	0.15	0.51
1075	0.55	0.00	0.00	0.00	0.00	0.00	0.66	0.15	0.51
1100	0.55	0.00	0.00	0.00	0.00	0.00	0.66	0.15	0.51
1125	0.55	51.35	0.02	1.15	4.13	21.23	0.44	0.15	0.29
1150	0.55	100.00	0.01	0.59	4.16	41.35	0.22	0.15	0.08
1175	0.55	100.00	0.01	0.59	4.17	41.35	0.22	0.14	0.08
1200	0.55	100.00	0.01	0.59	4.24	41.35	0.22	0.14	0.08
1225	0.55	100.00	0.01	0.59	4.31	41.35	0.22	0.14	0.08
1250	0.55	100.00	0.00	0.59	4.37	41.35	0.22	0.14	0.08
1275	0.55	100.00	0.00	0.59	4.44	41.35	0.22	0.14	0.08
1300	0.55	100.00	0.00	0.59	4.51	41.35	0.21	0.14	0.08
1325	0.55	100.00	0.00	0.59	4.58	41.35	0.21	0.13	0.08
1350	0.55	100.00	0.00	0.58	4.64	41.35	0.21	0.13	0.08
1375	0.55	100.00	0.00	0.57	4.71	41.35	0.18	0.10	0.08
1400	0.55	100.00	0.00	0.56	4.77	41.35	0.13	0.05	0.07
1425	0.55	100.00	0.00	0.56	4.83	41.35	0.12	0.05	0.07
1450	0.55	100.00	0.00	0.57	4.88	41.35	0.12	0.04	0.07
1475	0.55	99.99	0.00	0.57	4.94	41.34	0.12	0.04	0.07
1500	0.55	99.99	0.00	0.57	4.98	41.34	0.11	0.04	0.07
1525	0.55	99.99	0.00	0.57	5.02	41.34	0.11	0.04	0.07
1550	0.55	99.99	0.00	0.57	5.05	41.34	0.11	0.03	0.07

1575	0.55	99.99	0.00	0.57	5.07	41.34	0.10	0.03	0.07
1600	0.55	99.99	0.00	0.56	5.08	41.34	0.10	0.03	0.07
1625	0.55	99.99	0.00	0.56	5.09	41.34	0.10	0.03	0.07
1650	0.55	99.98	0.00	0.55	5.10	41.34	0.09	0.03	0.07
1675	0.55	99.98	0.00	0.55	5.12	41.34	0.09	0.02	0.07
1700	0.55	99.97	0.00	0.54	5.13	41.34	0.08	0.02	0.06
1725	0.55	99.96	0.00	0.53	5.14	41.33	0.07	0.01	0.06
1750	0.55	99.95	0.00	0.53	5.15	41.33	0.06	0.00	0.06
1775	0.55	99.94	0.00	0.52	5.13	41.32	0.06	0.00	0.06
1800	0.55	99.92	0.00	0.50	5.00	41.31	0.07	0.02	0.06
1000	0.60	0.00	0.00	0.00	0.00	0.00	0.66	0.14	0.52
1025	0.60	0.00	0.00	0.00	0.00	0.00	0.66	0.14	0.52
1050	0.60	0.00	0.00	0.00	0.00	0.00	0.66	0.14	0.52
1075	0.60	1.26	0.23	0.18	3.66	0.50	0.66	0.14	0.51
1100	0.60	6.23	0.11	0.29	3.79	2.48	0.64	0.15	0.49
1125	0.60	100.00	0.06	0.54	4.01	39.73	0.24	0.14	0.10
1150	0.60	100.00	0.06	0.54	4.08	39.73	0.24	0.14	0.10
1175	0.60	100.00	0.06	0.54	4.14	39.73	0.24	0.14	0.10
1200	0.60	100.00	0.06	0.54	4.21	39.73	0.24	0.14	0.10
1225	0.60	100.00	0.06	0.54	4.27	39.73	0.24	0.14	0.10
1250	0.60	100.00	0.05	0.54	4.34	39.73	0.24	0.14	0.10
1275	0.60	100.00	0.04	0.53	4.40	39.73	0.23	0.14	0.10
1300	0.60	100.00	0.03	0.53	4.47	39.73	0.23	0.13	0.10
1325	0.60	100.00	0.02	0.53	4.54	39.73	0.22	0.13	0.10
1350	0.60	100.00	0.02	0.53	4.60	39.73	0.22	0.12	0.10
1375	0.60	100.00	0.01	0.52	4.67	39.73	0.20	0.10	0.10
1400	0.60	100.00	0.01	0.51	4.74	39.73	0.15	0.05	0.10
1425	0.60	99.99	0.01	0.52	4.79	39.73	0.14	0.04	0.10
1450	0.60	99.99	0.00	0.52	4.83	39.73	0.13	0.03	0.10
1475	0.60	99.99	0.00	0.52	4.87	39.73	0.13	0.03	0.09
1500	0.60	99.99	0.00	0.52	4.90	39.73	0.12	0.03	0.09
1525	0.60	99.99	0.00	0.52	4.93	39.73	0.12	0.03	0.09
1550	0.60	99.99	0.00	0.52	4.94	39.73	0.12	0.03	0.09
1575	0.60	99.99	0.00	0.52	4.96	39.73	0.12	0.02	0.09
1600	0.60	99.99	0.00	0.52	4.96	39.73	0.11	0.02	0.09
1625	0.60	99.99	0.00	0.51	4.96	39.73	0.11	0.02	0.09
1650	0.60	99.98	0.00	0.51	4.97	39.72	0.10	0.02	0.09
1675	0.60	99.98	0.00	0.50	4.97	39.72	0.10	0.01	0.09
1700	0.60	99.97	0.00	0.50	4.98	39.72	0.09	0.01	0.09
1725	0.60	99.96	0.00	0.49	4.99	39.71	0.08	0.00	0.08
1750	0.60	99.95	0.00	0.48	5.01	39.71	0.08	0.00	0.08
1775	0.60	99.94	0.00	0.48	5.02	39.71	0.08	0.00	0.08
1800	0.60	99.92	0.00	0.47	4.98	39.70	0.08	0.00	0.08
1000	0.65	0.00	0.00	0.00	0.00	0.00	0.66	0.14	0.52
1025	0.65	3.10	0.56	0.12	3.47	1.18	0.65	0.14	0.51
1050	0.65	20.20	0.35	0.15	3.52	7.70	0.59	0.15	0.44
1075	0.65	28.30	0.23	0.18	3.66	10.79	0.55	0.14	0.41
1100	0.65	45.00	0.11	0.29	3.79	17.15	0.49	0.14	0.34
1125	0.65	100.00	0.09	0.44	3.99	38.11	0.26	0.14	0.12
1150	0.65	100.00	0.08	0.50	4.06	38.11	0.26	0.14	0.12

1175	0.65	100.00	0.07	0.50	4.12	38.11	0.26	0.14	0.12
1200	0.65	100.00	0.06	0.50	4.19	38.11	0.26	0.14	0.12
1225	0.65	100.00	0.06	0.50	4.26	38.11	0.26	0.14	0.12
1250	0.65	100.00	0.05	0.50	4.32	38.11	0.26	0.14	0.12
1275	0.65	100.00	0.04	0.41	4.38	38.11	0.21	0.09	0.12
1300	0.65	100.00	0.03	0.42	4.45	38.11	0.20	0.09	0.12
1325	0.65	100.00	0.02	0.43	4.52	38.11	0.19	0.07	0.12
1350	0.65	99.99	0.02	0.44	4.58	38.11	0.17	0.06	0.12
1375	0.65	99.99	0.01	0.45	4.64	38.11	0.16	0.04	0.12
1400	0.65	99.99	0.01	0.46	4.69	38.11	0.15	0.03	0.12
1425	0.65	99.99	0.01	0.46	4.73	38.11	0.14	0.02	0.12
1450	0.65	99.99	0.01	0.47	4.77	38.11	0.13	0.02	0.12
1475	0.65	99.99	0.00	0.47	4.79	38.11	0.13	0.02	0.12
1500	0.65	99.99	0.00	0.47	4.81	38.11	0.13	0.02	0.12
1525	0.65	99.99	0.00	0.47	4.82	38.11	0.13	0.02	0.11
1550	0.65	99.99	0.00	0.47	4.83	38.11	0.13	0.02	0.11
1575	0.65	99.99	0.00	0.47	4.83	38.11	0.13	0.02	0.11
1600	0.65	99.99	0.00	0.47	4.83	38.11	0.13	0.01	0.11
1625	0.65	99.98	0.00	0.47	4.82	38.10	0.12	0.01	0.11
1650	0.65	99.98	0.00	0.46	4.82	38.10	0.12	0.01	0.11
1675	0.65	99.98	0.00	0.46	4.82	38.10	0.11	0.00	0.11
1700	0.65	99.97	0.00	0.45	4.82	38.10	0.11	0.00	0.11
1725	0.65	99.96	0.00	0.45	4.83	38.10	0.11	0.00	0.11
1750	0.65	99.95	0.00	0.44	4.85	38.09	0.10	0.00	0.10
1775	0.65	99.93	0.00	0.43	4.87	38.09	0.10	0.00	0.10
1800	0.65	99.92	0.00	0.42	4.87	38.08	0.10	0.00	0.10
1000	0.70	0.00	0.00	0.00	0.00	0.00	0.67	0.14	0.52
1025	0.70	7.19	0.56	0.12	3.47	2.62	0.64	0.14	0.50
1050	0.70	30.08	0.29	0.14	3.44	10.98	0.55	0.14	0.41
1075	0.70	44.02	0.20	0.18	3.61	16.07	0.50	0.14	0.36
1100	0.70	73.56	0.13	0.27	3.83	26.85	0.39	0.14	0.25
1125	0.70	100.00	0.11	0.38	3.96	36.50	0.28	0.14	0.14
1150	0.70	100.00	0.11	0.44	4.03	36.50	0.28	0.14	0.14
1175	0.70	100.00	0.11	0.44	4.09	36.50	0.28	0.14	0.14
1200	0.70	100.00	0.11	0.35	4.15	36.50	0.27	0.12	0.14
1225	0.70	100.00	0.10	0.36	4.21	36.50	0.26	0.12	0.14
1250	0.70	99.99	0.07	0.33	4.29	36.49	0.24	0.10	0.14
1275	0.70	99.99	0.05	0.32	4.36	36.49	0.21	0.07	0.14
1300	0.70	99.99	0.03	0.33	4.43	36.49	0.18	0.04	0.14
1325	0.70	99.99	0.02	0.35	4.49	36.49	0.17	0.03	0.14
1350	0.70	99.99	0.02	0.36	4.55	36.49	0.16	0.02	0.14
1375	0.70	99.99	0.02	0.38	4.60	36.49	0.16	0.02	0.14
1400	0.70	99.99	0.01	0.39	4.64	36.49	0.15	0.01	0.14
1425	0.70	99.99	0.01	0.40	4.67	36.49	0.14	0.01	0.14
1450	0.70	99.99	0.01	0.41	4.69	36.49	0.14	0.01	0.14
1475	0.70	99.99	0.01	0.42	4.70	36.49	0.14	0.00	0.14
1500	0.70	99.99	0.00	0.42	4.70	36.49	0.14	0.01	0.14
1525	0.70	99.99	0.00	0.42	4.70	36.49	0.14	0.01	0.14
1550	0.70	99.99	0.00	0.42	4.70	36.49	0.14	0.01	0.13

1575	0.70	99.99	0.00	0.42	4.69	36.49	0.14	0.01	0.13
1600	0.70	99.99	0.00	0.42	4.69	36.49	0.14	0.01	0.13
1625	0.70	99.98	0.00	0.42	4.68	36.49	0.13	0.00	0.13
1650	0.70	99.98	0.00	0.41	4.67	36.49	0.13	0.00	0.13
1675	0.70	99.97	0.00	0.41	4.66	36.48	0.13	0.00	0.13
1700	0.70	99.97	0.00	0.40	4.66	36.48	0.13	0.00	0.13
1725	0.70	99.96	0.00	0.40	4.67	36.48	0.13	0.00	0.13
1750	0.70	99.95	0.00	0.39	4.69	36.48	0.13	0.00	0.13
1775	0.70	99.93	0.00	0.38	4.70	36.47	0.12	0.00	0.12
1800	0.70	99.91	0.00	0.37	4.71	36.46	0.12	0.00	0.12
1000	0.75	1.80	0.79	0.09	3.36	0.63	0.66	0.14	0.52
1025	0.75	13.91	0.52	0.13	3.43	4.85	0.61	0.13	0.48
1050	0.75	35.87	0.29	0.14	3.44	12.51	0.54	0.14	0.40
1075	0.75	50.84	0.21	0.18	3.63	17.73	0.48	0.14	0.35
1100	0.75	84.95	0.14	0.27	3.84	29.63	0.36	0.14	0.22
1125	0.75	100.00	0.12	0.36	3.94	34.88	0.30	0.14	0.17
1150	0.75	100.00	0.12	0.39	4.01	34.88	0.30	0.14	0.17
1175	0.75	100.00	0.12	0.38	4.07	34.88	0.30	0.14	0.17
1200	0.75	99.99	0.12	0.21	4.12	34.87	0.26	0.09	0.17
1225	0.75	99.99	0.11	0.22	4.19	34.87	0.24	0.08	0.16
1250	0.75	99.99	0.07	0.22	4.26	34.87	0.22	0.05	0.16
1275	0.75	99.98	0.05	0.23	4.34	34.87	0.19	0.02	0.16
1300	0.75	99.99	0.04	0.25	4.40	34.87	0.18	0.02	0.16
1325	0.75	99.99	0.03	0.27	4.46	34.87	0.18	0.02	0.16
1350	0.75	99.99	0.03	0.29	4.51	34.87	0.18	0.01	0.16
1375	0.75	99.99	0.02	0.31	4.55	34.87	0.17	0.01	0.16
1400	0.75	99.99	0.02	0.33	4.58	34.87	0.17	0.01	0.16
1425	0.75	99.99	0.01	0.34	4.59	34.87	0.17	0.01	0.16
1450	0.75	99.99	0.01	0.35	4.59	34.87	0.16	0.01	0.16
1475	0.75	99.99	0.01	0.36	4.58	34.87	0.16	0.01	0.16
1500	0.75	99.99	0.00	0.36	4.58	34.87	0.16	0.01	0.16
1525	0.75	99.99	0.00	0.36	4.57	34.87	0.16	0.01	0.16
1550	0.75	99.99	0.00	0.37	4.56	34.87	0.16	0.00	0.16
1575	0.75	99.99	0.00	0.36	4.55	34.87	0.16	0.00	0.15
1600	0.75	99.99	0.00	0.36	4.53	34.87	0.16	0.00	0.15
1625	0.75	99.98	0.00	0.36	4.52	34.87	0.16	0.00	0.15
1650	0.75	99.98	0.00	0.36	4.51	34.87	0.15	0.00	0.15
1675	0.75	99.97	0.00	0.35	4.50	34.87	0.15	0.00	0.15
1700	0.75	99.97	0.00	0.35	4.49	34.87	0.15	0.00	0.15
1725	0.75	99.96	0.00	0.34	4.50	34.86	0.15	0.00	0.15
1750	0.75	99.95	0.00	0.34	4.51	34.86	0.15	0.00	0.15
1775	0.75	99.93	0.00	0.33	4.53	34.85	0.15	0.00	0.15
1800	0.75	99.91	0.00	0.32	4.55	34.85	0.14	0.00	0.14
1000	0.80	8.52	0.74	0.10	3.33	2.83	0.65	0.14	0.51
1025	0.80	20.58	0.49	0.14	3.40	6.84	0.60	0.13	0.46
1050	0.80	42.23	0.29	0.14	3.44	14.05	0.53	0.14	0.39
1075	0.80	58.32	0.22	0.18	3.64	19.40	0.47	0.14	0.33
1100	0.80	97.44	0.14	0.26	3.85	32.41	0.33	0.14	0.20
1125	0.80	100.00	0.14	0.32	3.92	33.26	0.32	0.14	0.19
1150	0.80	100.00	0.14	0.32	3.98	33.26	0.32	0.14	0.19

1175	0.80	100.00	0.14	0.32	4.04	33.26	0.32	0.14	0.19
1200	0.80	99.99	0.13	0.16	4.10	33.26	0.27	0.09	0.19
1225	0.80	99.98	0.12	0.14	4.16	33.25	0.23	0.04	0.19
1250	0.80	99.98	0.08	0.14	4.24	33.25	0.21	0.02	0.19
1275	0.80	99.98	0.07	0.16	4.30	33.25	0.20	0.02	0.19
1300	0.80	99.98	0.06	0.18	4.36	33.25	0.20	0.01	0.18
1325	0.80	99.98	0.04	0.20	4.42	33.25	0.19	0.01	0.18
1350	0.80	99.99	0.04	0.22	4.46	33.26	0.19	0.01	0.18
1375	0.80	99.99	0.03	0.24	4.48	33.26	0.19	0.01	0.18
1400	0.80	99.99	0.02	0.26	4.49	33.26	0.19	0.01	0.18
1425	0.80	99.99	0.02	0.28	4.48	33.26	0.19	0.01	0.18
1450	0.80	99.99	0.01	0.29	4.47	33.26	0.19	0.01	0.18
1475	0.80	99.99	0.01	0.30	4.45	33.26	0.19	0.01	0.18
1500	0.80	99.99	0.01	0.30	4.43	33.26	0.18	0.01	0.18
1525	0.80	99.99	0.00	0.30	4.41	33.26	0.18	0.01	0.18
1550	0.80	99.99	0.00	0.30	4.40	33.26	0.18	0.01	0.18
1575	0.80	99.99	0.00	0.30	4.38	33.26	0.18	0.01	0.18
1600	0.80	99.99	0.00	0.30	4.37	33.26	0.18	0.01	0.17
1625	0.80	99.98	0.00	0.30	4.35	33.25	0.18	0.00	0.17
1650	0.80	99.98	0.00	0.30	4.34	33.25	0.18	0.00	0.17
1675	0.80	99.97	0.00	0.29	4.33	33.25	0.17	0.00	0.17
1700	0.80	99.97	0.00	0.29	4.32	33.25	0.17	0.00	0.17
1725	0.80	99.96	0.00	0.28	4.32	33.25	0.17	0.00	0.17
1750	0.80	99.94	0.00	0.28	4.33	33.24	0.17	0.00	0.17
1775	0.80	99.93	0.00	0.27	4.35	33.24	0.17	0.00	0.17
1800	0.80	99.91	0.00	0.27	4.37	33.23	0.16	0.00	0.16
1000	0.85	12.91	0.75	0.10	3.34	4.09	0.63	0.13	0.50
1025	0.85	35.84	0.39	0.12	3.29	11.34	0.56	0.14	0.42
1050	0.85	48.16	0.29	0.14	3.45	15.24	0.52	0.14	0.38
1075	0.85	66.56	0.22	0.18	3.64	21.06	0.46	0.14	0.32
1100	0.85	100.00	0.16	0.25	3.83	31.64	0.34	0.14	0.21
1125	0.85	100.00	0.16	0.25	3.89	31.64	0.34	0.14	0.21
1150	0.85	100.00	0.16	0.25	3.95	31.64	0.34	0.14	0.21
1175	0.85	99.99	0.15	0.14	4.00	31.64	0.32	0.11	0.21
1200	0.85	99.98	0.14	0.10	4.07	31.64	0.27	0.06	0.21
1225	0.85	99.96	0.13	0.09	4.13	31.63	0.23	0.02	0.21
1250	0.85	99.97	0.11	0.10	4.20	31.63	0.22	0.01	0.21
1275	0.85	99.97	0.09	0.11	4.27	31.63	0.22	0.01	0.21
1300	0.85	99.97	0.07	0.13	4.32	31.63	0.21	0.01	0.21
1325	0.85	99.98	0.06	0.14	4.37	31.64	0.21	0.00	0.21
1350	0.85	99.98	0.05	0.16	4.40	31.64	0.21	0.00	0.21
1375	0.85	99.98	0.04	0.18	4.40	31.64	0.21	0.01	0.20
1400	0.85	99.99	0.03	0.20	4.39	31.64	0.21	0.01	0.20
1425	0.85	99.99	0.02	0.21	4.36	31.64	0.21	0.01	0.20
1450	0.85	99.99	0.01	0.22	4.33	31.64	0.21	0.01	0.20
1475	0.85	99.99	0.01	0.23	4.30	31.64	0.21	0.01	0.20
1500	0.85	99.99	0.01	0.23	4.27	31.64	0.21	0.01	0.20
1525	0.85	99.99	0.00	0.24	4.24	31.64	0.21	0.01	0.20
1550	0.85	99.99	0.00	0.24	4.22	31.64	0.20	0.01	0.20

1575	0.85	99.99	0.00	0.24	4.21	31.64	0.20	0.01	0.20
1600	0.85	99.99	0.00	0.24	4.19	31.64	0.20	0.01	0.20
1625	0.85	99.98	0.00	0.23	4.17	31.64	0.20	0.01	0.19
1650	0.85	99.98	0.00	0.23	4.16	31.64	0.20	0.01	0.19
1675	0.85	99.97	0.00	0.23	4.15	31.63	0.20	0.00	0.19
1700	0.85	99.97	0.00	0.23	4.14	31.63	0.19	0.00	0.19
1725	0.85	99.96	0.00	0.22	4.14	31.63	0.19	0.00	0.19
1750	0.85	99.94	0.00	0.22	4.15	31.62	0.19	0.00	0.19
1775	0.85	99.93	0.00	0.21	4.16	31.62	0.19	0.00	0.19
1800	0.85	99.91	0.00	0.21	4.18	31.61	0.19	0.00	0.19
1000	0.90	18.06	0.74	0.11	3.34	5.42	0.63	0.14	0.49
1025	0.90	31.69	0.50	0.15	3.42	9.51	0.57	0.13	0.45
1050	0.90	54.73	0.30	0.14	3.46	16.43	0.51	0.13	0.37
1075	0.90	75.68	0.22	0.18	3.65	22.72	0.44	0.13	0.31
1100	0.90	100.00	0.17	0.18	3.80	30.03	0.37	0.13	0.23
1125	0.90	100.00	0.17	0.18	3.86	30.03	0.36	0.13	0.23
1150	0.90	100.00	0.17	0.18	3.92	30.03	0.36	0.13	0.23
1175	0.90	100.00	0.17	0.14	3.97	30.03	0.35	0.12	0.23
1200	0.90	99.97	0.16	0.06	4.03	30.02	0.29	0.06	0.23
1225	0.90	99.96	0.15	0.05	4.10	30.01	0.24	0.01	0.23
1250	0.90	99.96	0.14	0.06	4.16	30.01	0.24	0.01	0.23
1275	0.90	99.96	0.11	0.07	4.22	30.01	0.23	0.00	0.23
1300	0.90	99.97	0.10	0.08	4.28	30.02	0.23	0.00	0.23
1325	0.90	99.97	0.08	0.09	4.31	30.02	0.23	0.00	0.23
1350	0.90	99.98	0.07	0.10	4.33	30.02	0.23	0.00	0.23
1375	0.90	99.98	0.05	0.12	4.31	30.02	0.23	0.01	0.23
1400	0.90	99.98	0.04	0.13	4.28	30.02	0.23	0.01	0.22
1425	0.90	99.99	0.03	0.14	4.23	30.02	0.23	0.01	0.22
1450	0.90	99.99	0.02	0.15	4.18	30.02	0.23	0.01	0.22
1475	0.90	99.99	0.01	0.16	4.13	30.02	0.23	0.01	0.22
1500	0.90	99.99	0.01	0.16	4.09	30.02	0.23	0.01	0.22
1525	0.90	99.99	0.01	0.16	4.06	30.02	0.23	0.01	0.22
1550	0.90	99.99	0.00	0.17	4.04	30.02	0.23	0.01	0.22
1575	0.90	99.99	0.00	0.17	4.02	30.02	0.22	0.01	0.22
1600	0.90	99.99	0.00	0.16	4.00	30.02	0.22	0.01	0.22
1625	0.90	99.98	0.00	0.16	3.98	30.02	0.22	0.01	0.21
1650	0.90	99.98	0.00	0.16	3.97	30.02	0.22	0.01	0.21
1675	0.90	99.97	0.00	0.16	3.95	30.02	0.22	0.01	0.21
1700	0.90	99.96	0.00	0.16	3.95	30.01	0.22	0.00	0.21
1725	0.90	99.95	0.00	0.15	3.95	30.01	0.21	0.00	0.21
1750	0.90	99.94	0.00	0.15	3.96	30.01	0.21	0.00	0.21
1775	0.90	99.93	0.00	0.15	3.97	30.00	0.21	0.00	0.21
1800	0.90	99.90	0.00	0.14	3.99	29.99	0.21	0.00	0.21
1000	0.95	23.05	0.74	0.12	3.34	6.55	0.62	0.14	0.48
1025	0.95	36.44	0.50	0.15	3.43	10.35	0.57	0.13	0.44
1050	0.95	62.04	0.31	0.14	3.47	17.62	0.50	0.13	0.37
1075	0.95	84.72	0.23	0.11	3.65	24.07	0.43	0.13	0.30
1100	0.95	100.00	0.19	0.09	3.76	28.41	0.39	0.13	0.25
1125	0.95	100.00	0.19	0.09	3.82	28.41	0.39	0.13	0.25
1150	0.95	100.00	0.19	0.09	3.88	28.41	0.38	0.13	0.25

1175	0.95	100.00	0.19	0.09	3.94	28.41	0.38	0.13	0.25
1200	0.95	99.98	0.18	0.04	4.00	28.40	0.32	0.07	0.25
1225	0.95	99.95	0.17	0.03	4.06	28.39	0.27	0.02	0.25
1250	0.95	99.95	0.16	0.03	4.12	28.39	0.26	0.01	0.25
1275	0.95	99.95	0.15	0.03	4.17	28.39	0.25	0.00	0.25
1300	0.95	99.96	0.13	0.04	4.22	28.40	0.25	0.00	0.25
1325	0.95	99.96	0.11	0.04	4.24	28.40	0.25	0.00	0.25
1350	0.95	99.97	0.09	0.05	4.24	28.40	0.25	0.00	0.25
1375	0.95	99.97	0.07	0.06	4.21	28.40	0.25	0.00	0.25
1400	0.95	99.98	0.05	0.06	4.15	28.40	0.25	0.01	0.25
1425	0.95	99.98	0.03	0.07	4.08	28.40	0.25	0.01	0.24
1450	0.95	99.99	0.02	0.08	4.01	28.40	0.25	0.01	0.24
1475	0.95	99.99	0.02	0.08	3.95	28.40	0.25	0.01	0.24
1500	0.95	99.99	0.01	0.08	3.90	28.40	0.25	0.01	0.24
1525	0.95	99.99	0.01	0.09	3.86	28.40	0.25	0.01	0.24
1550	0.95	99.99	0.00	0.09	3.83	28.40	0.25	0.01	0.24
1575	0.95	99.99	0.00	0.09	3.81	28.40	0.25	0.01	0.24
1600	0.95	99.99	0.00	0.09	3.79	28.40	0.25	0.01	0.24
1625	0.95	99.98	0.00	0.09	3.77	28.40	0.24	0.01	0.24
1650	0.95	99.98	0.00	0.08	3.76	28.40	0.24	0.01	0.23
1675	0.95	99.97	0.00	0.08	3.75	28.40	0.24	0.01	0.23
1700	0.95	99.96	0.00	0.08	3.75	28.40	0.24	0.01	0.23
1725	0.95	99.95	0.00	0.08	3.75	28.39	0.24	0.01	0.23
1750	0.95	99.94	0.00	0.08	3.75	28.39	0.23	0.00	0.23
1775	0.95	99.92	0.00	0.08	3.77	28.38	0.23	0.00	0.23
1800	0.95	99.90	0.00	0.08	3.79	28.38	0.23	0.00	0.23
1000	1.00	27.12	0.75	0.00	3.35	7.27	0.60	0.12	0.48
1025	1.00	41.46	0.50	0.00	3.42	11.11	0.56	0.12	0.44
1050	1.00	69.15	0.31	0.00	3.46	18.53	0.49	0.13	0.36
1075	1.00	94.01	0.23	0.00	3.64	25.19	0.42	0.13	0.29
1100	1.00	100.00	0.22	0.00	3.72	26.79	0.41	0.13	0.27
1125	1.00	100.00	0.21	0.00	3.78	26.79	0.41	0.13	0.27
1150	1.00	100.00	0.21	0.00	3.84	26.79	0.41	0.13	0.27
1175	1.00	100.00	0.21	0.00	3.90	26.79	0.41	0.13	0.27
1200	1.00	99.98	0.20	0.00	3.96	26.78	0.35	0.08	0.27
1225	1.00	99.96	0.19	0.00	4.02	26.78	0.32	0.04	0.27
1250	1.00	99.95	0.18	0.00	4.07	26.78	0.30	0.02	0.27
1275	1.00	99.95	0.17	0.00	4.12	26.78	0.29	0.02	0.27
1300	1.00	99.95	0.15	0.00	4.16	26.78	0.28	0.01	0.27
1325	1.00	99.96	0.14	0.00	4.17	26.78	0.28	0.01	0.27
1350	1.00	99.96	0.12	0.00	4.15	26.78	0.27	0.00	0.27
1375	1.00	99.97	0.09	0.00	4.10	26.78	0.27	0.00	0.27
1400	1.00	99.97	0.07	0.00	4.02	26.78	0.27	0.01	0.27
1425	1.00	99.98	0.05	0.00	3.92	26.78	0.27	0.01	0.27
1450	1.00	99.98	0.03	0.00	3.83	26.78	0.27	0.01	0.26
1475	1.00	99.99	0.02	0.00	3.75	26.79	0.27	0.01	0.26
1500	1.00	99.99	0.01	0.00	3.69	26.79	0.27	0.01	0.26
1525	1.00	99.99	0.01	0.00	3.64	26.79	0.27	0.01	0.26
1550	1.00	99.99	0.01	0.00	3.61	26.79	0.27	0.01	0.26

1575	1.00	99.99	0.00	0.00	3.59	26.79	0.27	0.01	0.26
1600	1.00	99.99	0.00	0.00	3.57	26.79	0.27	0.01	0.26
1625	1.00	99.98	0.00	0.00	3.55	26.78	0.27	0.01	0.26
1650	1.00	99.98	0.00	0.00	3.54	26.78	0.26	0.01	0.26
1675	1.00	99.97	0.00	0.00	3.53	26.78	0.26	0.01	0.25
1700	1.00	99.96	0.00	0.00	3.53	26.78	0.26	0.01	0.25
1725	1.00	99.95	0.00	0.00	3.53	26.78	0.26	0.01	0.25
1750	1.00	99.94	0.00	0.00	3.54	26.77	0.26	0.01	0.25
1775	1.00	99.92	0.00	0.00	3.56	26.77	0.25	0.00	0.25
1800	1.00	99.90	0.00	0.00	3.58	26.76	0.25	0.00	0.25